Cover Page

Universiteit Leiden

The handle http://hdl.handle.net/1887/81821 holds various files of this Leiden University dissertation.

Author: Cazzoletti, P.
Title: Not so smooth after all: resolving dust and gas structures in protoplanetary disks
Issue Date: 2019-12-12

Not so smooth after all: resolving dust and gas structures in protoplanetary disks

Proefschrift

ter verkrijging van
de graad van Doctor aan de Universiteit Leiden,
op gezag van Rector Magnificus prof. mr. C.J.J.M. Stolker,
volgens besluit van het College voor Promoties
te verdedigen op woensdag 12 december 2019
klokke 11:15 uur
door

Paolo Cazzoletti

geboren te Monza, Italie
in 1990

Contents

1 | Introduction

One of the most fascinating astronomical achievements of all times has been the discovery in the last couple of decades of planets outside of the Solar System, called "exoplanets", orbiting stars other than our own Sun. Since the only place known to host life in the Universe is a planet, i.e., the Earth, the detection and characterization of these objects is potentially the most promising path toward the answers to some of the most exciting and intriguing questions of mankind: "Are we alone in the Universe?", "How did life originate in the first place?" and "Are the Earth and the Solar System unique, or are they common in our galaxy?". The highly-improved capabilities of spectrometers of future astronomical facilities (e.g. ELT, JWST) will allow us to characterize the chemical composition of exoplanetary atmospheres. The detection of particular chemical elements (the so-called "bio-markers") in the atmospheres of terrestrial planets inside the habitable zone of their host star would provide strong indication for the presence of extra-terrestrial life in those systems. Even now, huge steps towards the understanding of exoplanets are already being made.

Since the discovery of the first exoplanet around a millisecond pulsar in the early 1990s (PSR1257+12, Wolszczan and Frail, 1992), and around a Solar-type star three years later (51 Peg b, Mayor and Queloz, 1995), more than 4000 new exoplanets have been found in almost 3000 planetary systems, mostly thanks to the *Kepler* space telescope (e.g., Borucki et al., 2011a,b). Not only is this a demonstration of the extraordinary technological advancements in the field of observational astronomy, but the ever-growing number of discovered exoplanets is revealing an unexpected and surprising variety of orbital properties and planetary masses (Winn and Fabrycky, 2015). This characteristic of the observed exoplanets is an indication that the planet formation process may lead to a wide variety of results.

Although understanding the origin of Earth has always been one of the overarching questions of science, many important aspects of the planet formation process are still far from being understood. This is not entirely surprising,
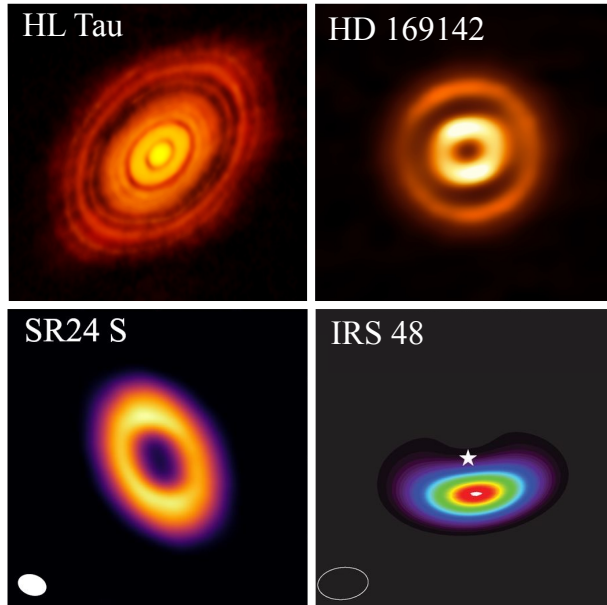
Figure 1.1: A few examples of early ALMA images of protoplanetary disks, showing an unexpected variety of rings, gaps and asymmetries, suggesting the presence of planets. Images from van der Marel et al. (2013), ALMA Partnership et al. (2015), Fedele et al. (2017), and Pinilla et al. (2017), from top-left to bottom-right.

considering the huge dynamical range involved in the making of a planet: the growth process from tiny sub-μm-sized dust particles such as those found in the interstellar medium (ISM) to full planets covers 13 orders of magnitude in size and about 40 in mass, and therefore involves many different physical processes (see Sec. 1.1.2). Moreover, the environments in which this growth occurs, called "protoplanetary disks", are also very complex because of the steep gradients in their properties and of the many physical and chemical processes shaping them. The study and understanding of protoplanetary disks and their evolution is therefore one of the pivotal aspects required to grasp the origin of planets and planetary systems, and ultimately the origin of life itself.

In recent years, the Atacama Large Millimeter/sub-millimeter Array (ALMA) has allowed an incredible breakthrough in the understanding of protoplanetary disks. Its unprecedented sensitivity, spatial and spectral resolution are allowing us to clearly observe the properties of the gaseous and mm-sized dusty components of these objects in details never imagined before (Fig. 1.1). Alongside ALMA, other new instruments such as VLT/SPHERE are allowing us to probe the smaller μm-sized grains, completing our already rich vision of proto-

planetary disks. In the meantime, the astrometric measurements of *Gaia* have mapped the 3D structure of our galaxy with a precision 200 times better than that of its predecessor *Hipparcos*, allowing us to calculate the distances of all the studied objects and nearby star forming regions with exquisite precision. Many questions are being answered, and many more arise: we are truly living in the Golden Age of observational planet formation!

This thesis will exploit the capabilities of these new instruments to study the gas and dust substructures observed in protoplanetary disks. The origin of these substructures can shed new light on the processes leading to the formation of planets, and help us understand what processes shape the observed exoplanetary systems.

1.1 Star and Planet formation

1.1.1 From clouds to stars

The path toward protoplanetary disks and, eventually, of planets, starts from molecular clouds, which are agglomerations of mainly molecular hydrogen gas and small sub-μm-sized dust grains, in a mass ratio of 100 to 1. Their typical masses are $10^2 - 10^5 \, M_\odot$, with sizes up to hundreds of parsecs, temperatures between ~ 10 to 100 K and densities of $10^2 - 10^4$ particles·cm^{-3}. At these temperatures and densities, thermal pressure is not enough to balance the gravitational force, and molecular clouds start collapsing undergoing the so-called Jeans instability, unless they are supported by some non-thermal pressure provided by turbulence, magnetic fields, or both. As they collapse, smaller and smaller regions become unstable, and the cloud fragments in a number of cores which ultimately lead to the creation of a cluster of individual protostars (e.g., Terebey et al., 1984; Shu et al., 1987; Galli and Shu, 1993).

If these cores possess even a small amount of angular momentum, their angular velocity increases during the collapse in order to conserve it. At some sufficiently small radius, the centrifugal force prevents the material in the collapsing clump from falling in a purely radial direction, giving rise to a flat, disk-shaped structure rotating around a newly formed protostar. Turbulence in the disks (Shakura and Sunyaev, 1973a), and possibly also self-gravity, winds and magnetic fields, cause a redistribution of angular momentum and a radial spread of the disk material (Armitage, 2011). In particular, some material loses angular momentum thus drifting inward accreting onto the star, whereas part moves outward to conserve angular momentum.

This evolutionary sequence is reflected in a classification of young stellar
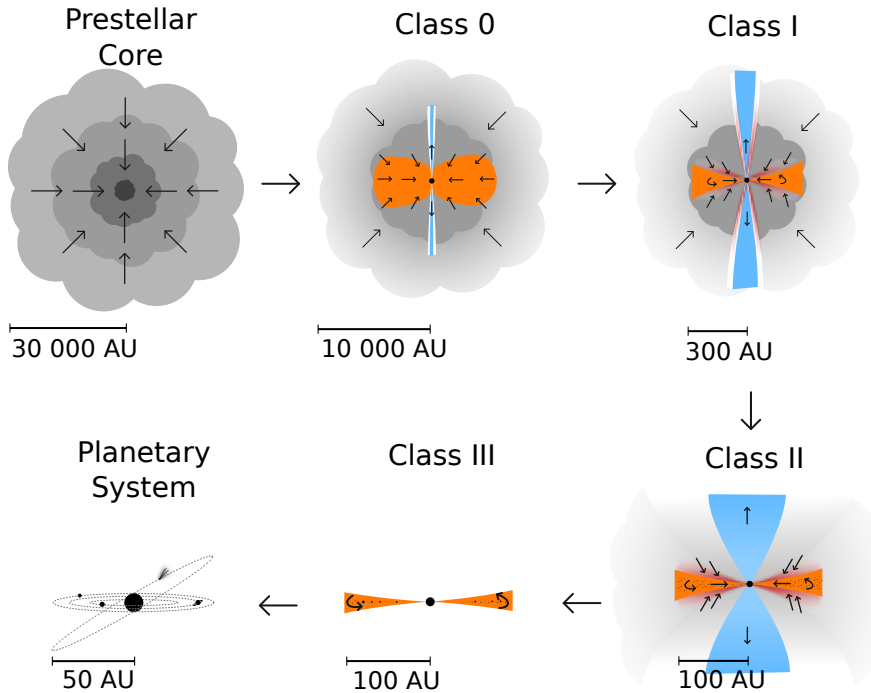
Figure 1.2: Representation of the evolution from prestellar core to planetary system, through the different classes of the protoplanetary disk phase. This thesis focuses on the Class II phase and on its transition to Class III. Figure by Magnus Persson.

objects (YSOs) based on the spectral slope of their spectral energy distribution typically in the $2.2\,\mu\text{m}-20\,\mu\text{m}$ wavelength range (Lada, 1987; Andre et al., 1993; Greene et al., 1994), and is represented in Fig. 1.2. Class 0 YSOs represent the earliest stages of the formation of a protostar, when it is still heavily embedded in its envelope which dominates the emission. As the envelope starts to be dissipated, emission from the central star as well as from the disk can be identified, and YSOs evolve into the Class I stage. When the Class II stage is reached, the envelope has completely dissipated; the central protostar is optically visible and surrounded by a protoplanetary disk which is optically thick in the infrared (IR) and mostly optically thin at mm wavelengths. Finally, Class III disks are even more evolved YSOs, where almost all the gas is dissipated and the star is surrounded by a planetary system and/or a "debris disk" made of asteroids and comet-sized objects, as well as smaller dust particles generated by the impact between the larger solid bodies.

This thesis will focus on the Class II evolutionary stage, where the capabilities of ALMA allow us to probe with unprecedented sensitivity and resolution the bulk of the dust content and the molecular emission from the gas (see Sec. 1.2.2). The transition from Class II to Class III stage will also be a topic of study.

1.1.2   From dust to planets

In the currently most widely accepted scenario, planets are formed in disks through the growth of microscopic dust grains that are found in the ISM. This growth process can be divided in different steps, depending on the physical mechanism driving this growth.

In the very first steps, tiny μm-sized dust grains grow in size by sticking after collision with other grains. Gravity is not important at these stages, and sticking can be explained by short-range van der Waals interaction. This can only happen for velocities $\lesssim 1 - 10\,\mathrm{m\,s^{-1}}$ (e.g., Dominik and Tielens, 1997; Blum, 2018); at higher velocities, sticking becomes less and less important, and the grains tend to fragment upon collision. At these small sizes, the dynamics of dust grains are still very well coupled to that of the gas, and their relative velocities depend on a number of factors such as turbulent mixing, Brownian motion, vertical settling and radial drift. Moreover, the stickiness of the dust grains also depends on other factors such as grain composition, ice mantles and fluffiness or shape. All of these factors should be considered when modelling dust growth (Brauer et al., 2008; Birnstiel et al., 2010).

The above processes produce the mm-sized particles that can be observed with ALMA, but larger cm-sized pebbles or even meter-sized bodies are also formed. At these radii and masses, however, the dynamical interaction between gas and dust begins to change, posing the first big problem along the path toward planet formation. Because of gas pressure that helps to counteract gravity, gas rotates around the central protostar at a slightly sub-Keplerian velocity. Tiny μm-sized grains are well coupled to the gas and feel this same pressure, but mm and meter-sized grains are more decoupled and are not supported by pressure. Consequently, they orbit at Keplerian velocity, i.e., slightly faster than the gas. This results in a headwind causing mm, cm and meter-sized grains to drift toward the central star on timescales as short as 100 years (Whipple, 1972; Weidenschilling, 1977), without having the time to grow to the size of planets. This barrier can be overcome because of the presence of regions where dust grains get trapped while drifting in the radial direction (Pinilla et al., 2012a,b, also see Sec. 1.3.1). In these "dust traps", grains have time to grow to larger sizes and to form the so-called planetesimals, with sizes of $1 - 100\,\mathrm{km}$.
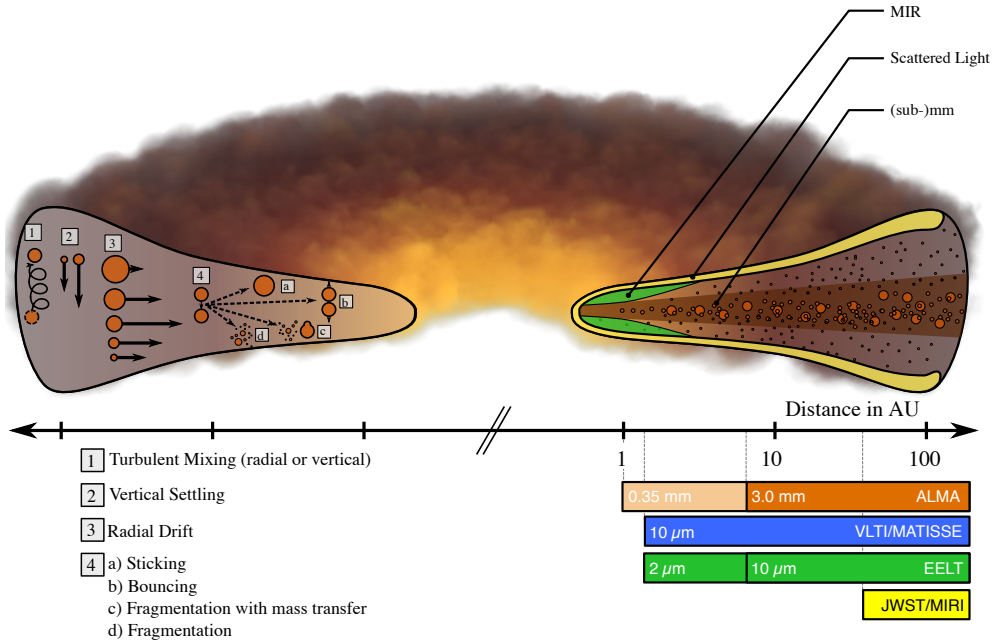
Figure 1.3: *Left-hand side:* Illustration of the relevant dust grain evolution processes leading to planet formation. *Right-hand side:* The left edge of the bars show the highest angular resolutions achievable with present and future observational facilities at different wavelengths and resolutions, assuming the typical distance of a nearby star-forming region (i.e., 150 pc). Figure from Testi et al. (2014)

These dust traps form ring-shaped structures in disks, as those observed from the very beginning with ALMA (see Fig. 1.1).

Once a population of planetesimals has been formed, gravity starts to dominate over sticking. At this stage rocky planets are formed, along with the cores of giant planets, which in turn form via gas capture.

1.2   Disk observations

Observational evidence of the presence of gas and dust around young stars exists for many years from a variety of different tracers, like optical emission spectra (Herbig, 1950), emission excess at IR wavelengths (Ney et al., 1973), and sub-mm continuum (e.g., Beckwith et al., 1990). However, it was not until the 1990s that the morphology of protoplanetary disks could really be determined. Optical high resolution observations with the *Hubble Space Telescope* (O'dell and Wen, 1994; O'dell and Wong, 1996), and in the mm with the IRAM Plateau

the Bure Interferometer (Dutrey et al., 1996), now called NOEMA, and later
with SMA (e.g. Andrews and Williams, 2007) and CARMA (e.g. Isella et al.,
2010) revealed flattened structures that were interpreted as disks projected
on the plane of the sky (also see Sargent and Beckwith, 1991; Beckwith and
Sargent, 1996). In some cases, observations of molecular lines, and especially
of the CO rotational transitions observed in the mm showed velocity gradients
along the major axis of disks, interpreted as evidence of material in Keplerian
rotation around the central young star (e.g., Koerner et al., 1993; Simon et al.,
2000). It is only in the last years, however, that we were able to really capture
the structure of protoplanetary disks, after the advent of the most powerful
mm-wavelength telescope ever.

1.2.1 ALMA

The Atacama Large Millemeter/submillimeter Array (ALMA) is an interferom-
eter located on the Chajnantor plateau, in the Chilean Andes, at an altitude
of about 5000 m above sea level, and its advent in 2011 marks one of the most
important milestones in the history of the study of star and planet formation.
ALMA is a partnership of ESO (representing its member states), NSF (USA)
and NINS (Japan), together with NRC (Canada) and NSC and ASIAA (Tai-
wan) and KASI (Republic of Korea), in cooperation with the Republic of Chile.

It is an array of 66 antennas operating in 10 different Bands at wavelengths
between 0.3 mm and 3.6 mm (see Tab. 1.1). Its main array has fifty 12 m
antennas. An additional compact array of four 12 m antennas, and twelve 7 m
antennas complement it. The antennas can be arranged in different configura-

Figure 1.4: Some of the 12 m antennas of the Atacama Large Milleme-
ter/submillimeter Array (ALMA). Picture from ESO/B. Tafreshi

tions, where the maximum distance between antennas, called a "baseline", can vary between 150 m and 16 km. ALMA is an interferometer: it samples the Fourier-transform of the sky emission on a range of scales corresponding to the baselines between antennas. These samples can be used to estimate the sky brightness with a resolution corresponding to the (approximately) the longest sampled baselines. In the case of ALMA, this translates into a resolution of the order of the milli-arcsec (mas). The diameter and number of antennas, finally, provide it with a collecting area of 6492 m^2, resulting in a level of sensitivity that allows to observe targets in a fraction of the integration time of previous generation interferometers.

These unique features allow us to carry out resolved observations of hundreds of disks, as well as to resolve substructures in them in both dust and gas. As a result, surveys of populations of protoplanetary disks in different star forming regions, encompassing different ages and environments, are now being performed, allowing for observational tests of evolutionary theories and theoretical predictions.

1.2.2   Dust observations

Mm and sub-mm wavelengths, i.e. ALMA's observation wavelengths, are particularly well suited for the observation of protoplanetary disks as they allow us to probe the bulk of the solid material that disks are made of. The reason for this is twofold.

Table 1.1: ALMA Bands and relative observing wavelength/frequency range

Band	Wavelength [mm]	Frequency [GHz]
1⋆	6-8.5	35-50
2⋆	3.3-4.5	65-90
3	2.6-3.6	84-116
4	1.8-2.4	125-163
5	1.4-1.8	163-211
6	1.1-1.4	211-275
7	0.8-1.1	275-373
8	0.6-0.8	385-500
9	0.4-0.5	602-720
10	0.3-0.4	787-950

⋆ Not installed at the time of writing

First, the thermal radiation emitted by cold (10-50 K) dust particles depends on the particle size. In particular, the emission at a wavelength λ_{obs} is dominated by the emission of grains with size comparable to λ_{obs} (Draine, 2006). Therefore, protoplanetary disks are expected to be the brightest at mm-wavelengths, since theoretically the dust population of Class II protoplanetary disks is mostly made of mm-sized grains, as explained in Sec. 1.1.2. Observationally, evidence for the presence of large grains in protoplanetary disks can be obtained by measuring the spectral index α_{mm}, which depends on the maximum grain size: values of α_{mm} lower than 3 in protoplanetary disks are regularly measured and are interpreted as a sign of the presence of large, mm/cm-sized grains (e.g., Ricci et al., 2010b,a; Testi et al., 2014).

The second reason that makes mm-wavelengths particularly interesting when observing protoplanetary disks, is the fact that at these wavelengths the emission is expected to be optically thin. This means that the total measured flux F_ν at a frequency ν is proportional to the dust mass through the relation

$$F_\nu = \frac{B_\nu(T)}{d^2} k_\nu M_{dust}, \qquad (1.1)$$

where B_ν is the Planck function at temperature T, d is the distance, k_ν is the dust opacity at frequency ν and M_{dust} is the dust mass of the disk. At mm-wavelength, k_ν scales with frequency as $k_\nu \propto \alpha$, and F_ν^β is well represented by the Rayleigh-Jeans approximation:

$$F_\nu \sim T k_\nu M_{dust} \nu^{\alpha_{mm}}, \qquad (1.2)$$

where $\alpha_{mm} = 2 + \beta$. This also means that the radiation emitted by grains located deep below the surface of the disk is not reabsorbed, and therefore that mm observations can probe dust grains close to the midplane, where planet formation occurs.

The shorter the observing wavelength, the more optically thick the radiation becomes. In ALMA Band 9 and 10, between 0.3 and 0.5 mm, the disk emission is mostly optically thick in the inner tens of au, and even more so at higher frequencies in the optical/near-IR. At these wavelengths, the radiation from the central star is efficiently scattered from the small, μm-sized dust grains. Optical images at high angular resolution can then be used to investigate the geometrical structure of the disk surface layers. VLT/SPHERE allows now for $<0.1''$ resolution observations, and have revealed in the last years a variety of substructures such as rings (Ginski et al., 2016; van Boekel et al., 2017) and spiral arms (Benisty et al., 2015, 2017; Stolker et al., 2016).

A combination of observations at short and long wavelengths has the potential to cast light on the distribution of dust grains of different sizes and

at different depth into the disks. This is critical to test our expectations and theoretical predictions about gas/dust interaction and to understand the mechanisms creating the dust substructures.

1.2.3   Gas observations

Part of the mm radiation coming from protoplanetary disks is not due to the dust, but rather to the rotational line emission of gaseous molecules. Albeit 100 times more abundant than dust, gas is much more elusive to observe. The main reason for this is the fact that the most abundant molecule, H_2, possesses no dipole moment. The second most abundant molecule is CO, which in the ISM is 10000 times less abundant than H_2, although some studies suggest that in disks it might actually be even less abundant (Bergin et al., 2013; Miotello et al., 2017).

The interpretation of gas emission is far less trivial than that of the dust. Molecular emission not only depends on the overall gas density, but also on the
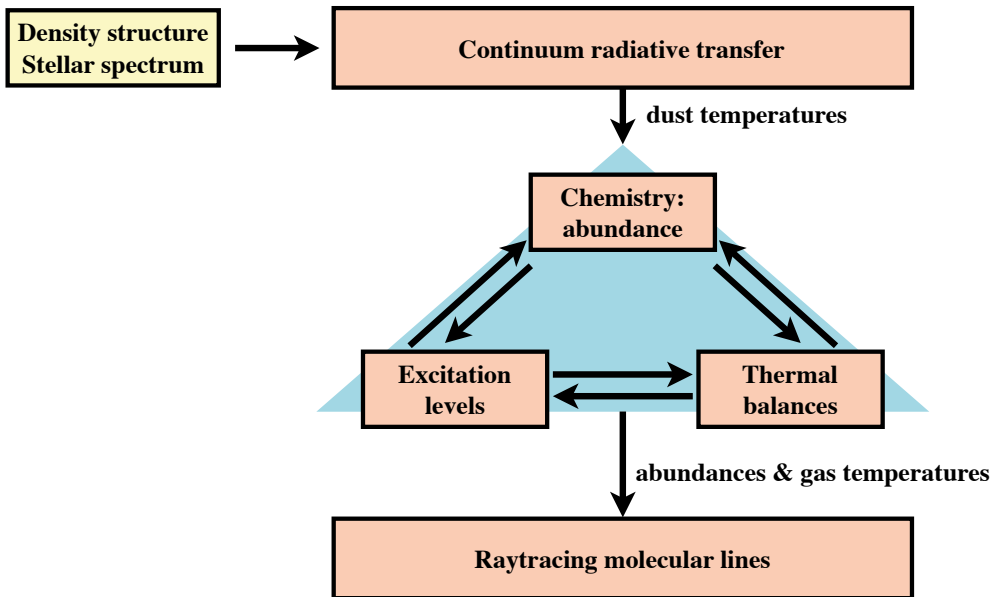

Figure 1.5: Diagram illustrating the DALI modelling procedure. After a density structure and a stellar spectrum are given as inputs, the dust temperature is estimated using continuum radiative transfer. The molecular abundances and gas temperature are then calculated self-consistently, and simulated observations are finally produced as outputs.

abundance of the molecule being observed with respect to the overall gas content. The abundance is regulated by a number of chemical reactions depending on many different physical properties of the disk. For example, the radiation field causes molecules to photo-dissociate and ionize, the dust temperature affects molecular freeze out, and the gas temperature and density affect the rate of the chemical reactions and the molecular excitation. In turn, the cooling rate of the gas, and therefore the gas temperature, depends on the molecular abundances and excitations. To make things even more complicated, in a protoplanetary disk all these physical parameters can vary with very steep gradients.

In order to take all of the above factors into consideration simultaneously, and therefore to be able to interpret gas observations in disks and to link them to the disks' physical properties, detailed physical-chemical modelling is required. The code used in this thesis is DALI (Dust And LInes, Bruderer et al., 2012; Bruderer, 2013). Assuming a given axisymmetric density structure and stellar radiation field the DALI modelling procedure is as follows (see Fig. 1.5):

1. The dust temperature is calculated through a Monte Carlo radiative transfer method.

2. Using an initial guess for the gas temperature, the chemical abundances for the different molecular species are calculated, along with the molecular excitations.

3. Based on the new abundances and excitations, the heating/cooling rates are updated.

4. The gas temperature is updated solving heating=cooling.

5. Steps 2 to 4 are repeated until convergence.

6. Based on the molecular excitations and abundances, a synthetic observation can be ray-traced,

The most relevant chemical reactions and rates used for the abundance and temperature calculations are included in a chemical network. In recent years, DALI has been used to model in great detail the emission of CO and of its isotopologs (^{13}CO and C^{18}O) in full and transitional disks[1] (Miotello et al., 2014; van der Marel et al., 2016a), as well as to study the dependence of other molecular line observations on disk's physical parameters (e.g., Bruderer et al., 2015; Kama et al., 2016; Trapman et al., 2017; Visser et al., 2018; van Terwisga

---

[1]Disks with an inner dust cavity
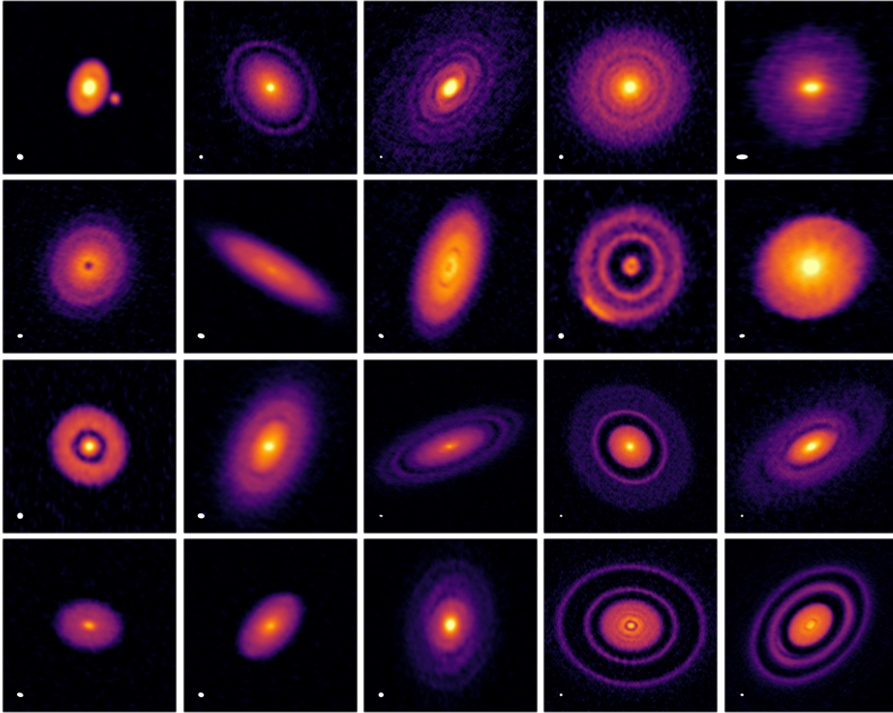
Figure 1.6: Overview of the high-resolution observations from the ALMA DSHARP large program (Andrews et al., 2018, and references therein). All of the observed disks clearly shows some substructures.

et al., 2019). In this thesis, DALI is used to model CN emission and morphology in protoplanetary disks. After CO, CN has often the brightest lines in disks, with intensities comparable to those of ^{13}CO but tracing layers higher up in the disk, being more sensitive to the UV photoprocesses.

1.3   Disk sub-structures

1.3.1   Structures in the dust

From the early observations of protoplanetary disks with ALMA, shown in Fig. 1.1, it has become clear that disks are not the smooth and axisymmetric structures imagined in the 90s and early 2000s. Each new high-resolution observation is rather showing us that almost every single disk hosts at least some kind of sub-structure, be them rings, vortices, cavities, or spiral arms.
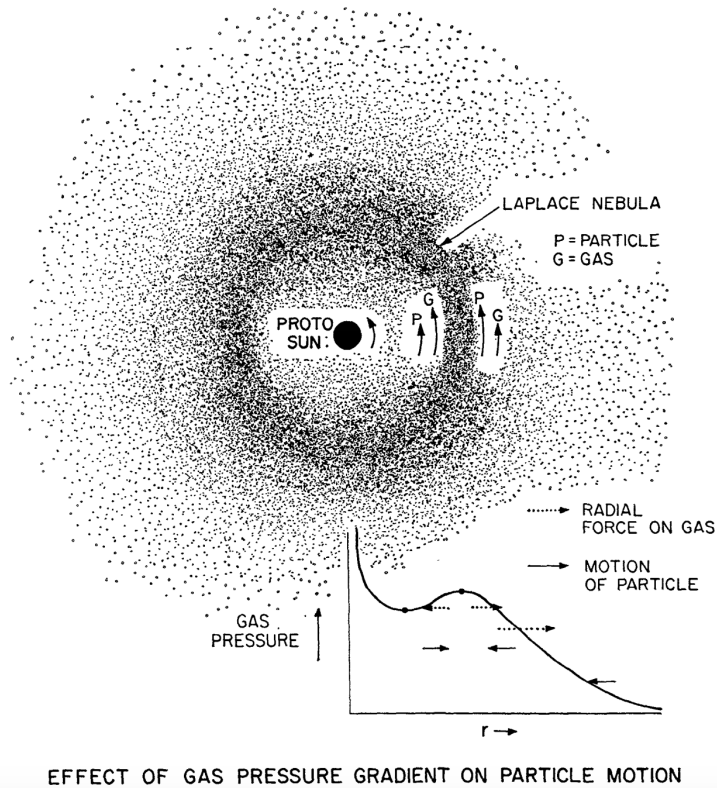
Figure 1.7: Radial pressure maxima in protoplanetary disks produce dust traps, that result in accumulations of mm-sized dust grains. When observed with ALMA, these can appear as rings. Figure from Whipple (1972).

This scenario has been strengthened by the first ALMA large program on protoplanetary disks (DSHARP Andrews et al., 2018, Fig. 1.6).

From the very beginning, planets have been invoked as the most natural explanation for these structures (e.g., Dipierro et al., 2015a). Assuming that a planet formed in a disk, the tidal forces would subtract angular momentum from the material orbiting inside the planet's orbit and redistribute it to the material at larger radii. This type of interaction would then carve a gap in the gaseous disk, accumulate material at the edges of the gap and produce local maxima in the gas pressure radial profile. As noted in Sec. 1.1.2 and as shown in Fig. 1.7, these pressure maxima act like dust-traps, preventing mm-sized dust grains from radially drifting into the star and instead accumulating them in ring-shaped structures such as those observed with ALMA. Moreover, when

the planet is very massive and orbiting at small radii or in the case of a binary, an entire cavity can be cleared and a hole in the inner region of the hosting disk can be created, thus originating a transitional disk (e.g., van der Marel et al., 2016a).

The interaction between a massive planet and a disk does not only create gaps and rings but can also result in spiral arms (e.g., Dong et al., 2015a; Stolker et al., 2016), or trigger the Rossby-Wave instability (Lovelace et al., 1999; Li et al., 2000, 2001) giving rise to high-pressure regions called vortices that can trap dust azimuthally and form crescent-shaped dust asymmetries such as those observed at mm-wavelengths (Lyra et al., 2009; Lin, 2012; van der Marel et al., 2013). While spiral arms are mostly observed in scattered light, crescent-shaped structures are almost exclusively seen at mm-wavelengths. One of the aims of this thesis is to understand the relation between these two types of structures, and how the different dynamical couplings of dust grains with the gas play a role in this.

On the one hand these dust traps provide the solution for the meter-sized barrier and are the ideal environment for dust to grow up to planetesimal size, but it is nevertheless clear that they cannot be at the origin of the formation of all planets, as first-generation planets are still required in order for dust traps to be triggered. To make this problem even worse is the fact that, despite all the efforts and instrumentation built specifically for the purpose of imaging planets embedded in disks (e.g. VLT/SPHERE and the Gemini Planet Imager, GPI), only one such planet has so far been imaged (PDS 70b Keppler et al., 2018). A handful additional planets have been proposed on the basis of indirect evidence in the gas kinematics (e.g., Pinte et al., 2018, 2019; Teague et al., 2018).

It is therefore becoming more and more clear that not all of these structures can be due to massive planets, and that some additional explanations are required in order to really answer the question about how planets form.

1.3.2   Structures in the gas

If the structures observed in the dust emission can be directly interpreted in terms of dust distribution, gas structures are harder to interpret because of the interplay between gas density, temperature, and chemistry regulating molecular abundances and their excitation, and ultimately regulating their gas emission (see Sec. 1.2.3). Because different molecular species form and emit under different conditions, when properly modelled the structures in the gas can provide unique information about the physical properties of the disks (see Fig. 1.8).

Rings have been observed in N_2H^+ (Qi et al., 2013): since this molecule can only be present in large abundance where CO is frozen-out onto the grains,
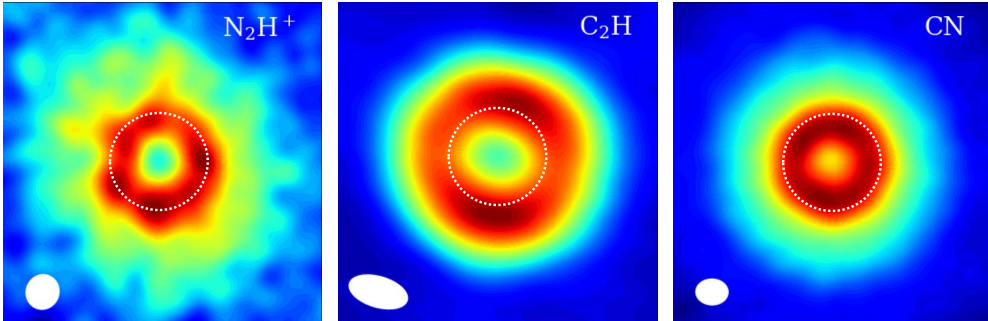
Figure 1.8: Emission detected in the TW Hya disk(d=60 pc) coming from 3 different molecular species. All three molecules show annulus-like structures, but the inner and outer radii of the annuli are different in each species. This illustrates how the emission from different species traces different physical and chemical conditions. The dotted circle has a radius of $1''$ (60 au). Data from Bergin et al. (2013), Qi et al. (2013), and Teague et al. (2016).

the location of the N_2H^+ ring is thought to trace the CO "snowline". At larger radii, the temperature is too cold for CO to survive in its gaseous state; at smaller radii, the warmer temperature allows CO to desorb from the dust grains. A double ring has been observed in DCO^+ (Öberg et al., 2015): the inner one can be explained by the same mechanism as above; the outer one, however, can only be explained by non-thermal desorption of CO from the dust grains. This happens because the column densities at these large radii are low enough to allow UV photons from the central star and the ISM to penetrate down to the disk midplane, hitting the grains and desorbing CO molecules. Alternatively, this second desorption front could be explained by an increasing dust temperature at large radii: this happens because the dust grains, on average smaller in size at large radii, are more easily stirred up by turbulence, thus intercepting more of the stellar radiation and finally heating-up (Facchini et al., 2017).

Lastly, hydrocarbon rings in C_2H and c-C_3H_2 have also been observed (Bergin et al., 2016). Such bright rings are due to a combination of high UV fluxes in the upper layers of the disks, and a combination of CO and H_2O freeze-out leaving the outer disk depleted in both C and O, but with an overall C/O$>$1 (Öberg et al., 2011). As a consequence, not all of the C will end up into CO, but some will be left free to form hydrocarbons.

Even more recently, CN rings have been observed in TW Hya (Teague et al., 2016), and in two disks in the Lupus star-forming region, namely Sz 71 and Sz 98 (van Terwisga et al., 2019). Proper modelling is required to understand under

which conditions CN emission can be ring-shaped, and which information CN rings can provide about the physical and chemical structures of protoplanetary disks.

1.4   SPH hydrodynamical models

In this thesis, hydrodynamical simulations were performed using the `PHANTOM` Smoothed Particle Hydrodynamics (SPH) code (Lodato and Price, 2010; Price and Federrath, 2010). The SPH method is a Lagrangian hydrodynamical scheme originally formulated by Lucy (1977) and Gingold and Monaghan (1977). A Lagrangian formulation of the fluid equations considers the evolution of the fluid properties for any given fluid element, whose position is in general not constant. This is different from the Eulerian approach, where the evolution of the fluid variables is followed in a given point in space. Eulerian numerical methods therefore use geometric grids, either fixed or adaptive, and are called grid-based codes. Lagrangian formulations such as SPH, rather than discretising space in cells, discretise the fluid quantities into particles of fixed mass, moving with the fluid velocity.

In SPH a continuous density distribution is then computed using the kernel weighted sum

$$\rho(\mathbf{r}) = \sum_{b=1}^{N_{\mathrm{part}}} m_b W(|\mathbf{r} - \mathbf{r}_b|, h), \qquad (1.3)$$

where W is a function called the "smoothing kernel", and should be positively defined, monotonically decreasing with distance and isotropic. The simplest example of W is a 3D Gaussian. h is called "smoothing length" and is in general $h = n(\mathbf{r})^{-1/3}$: this way, the smoothing length (and the resolution) follows the number density.

The density calculation is the key aspect of SPH and immediately shows some of its advantages. First the resolution of the method will follow the mass, since each particle carries a fixed mass and therefore density can only increase due to a higher concentration of particles. This is particularly well suited for astronomical problems involving gravitational collapse, since the dense regions will be better resolved. Second, since particles cannot lose, gain or diffuse mass, it will be an exactly conserved quantity.

Once the density distribution is calculated with Eq. 1.3, the Lagrangian (i.e., the difference between kinetic and potential energy) can be calculated. Combining the Lagrangian and the relative Euler-Lagrange equation with the first law of thermodynamics and the gradient of the density in Eq. 1.3, the

equations of motions can finally be derived self-consistently.

From this approach follow some other key features of SPH. The derivation of the equations of motion from the Lagrangian implies that the symmetries in the Lagrangian will reflect into conservation properties in the equations of motions. In particular, when the right smoothing kernel is chosen, linear and angular momentum, energy and entropy are exactly conserved, in addition to mass. This also means that the intrinsic dissipation in SPH is zero, i.e., that viscosity should be added manually when needed. This is sometimes necessary, e.g. to deal with shocks: ironically, this makes SPH codes intrinsically more dissipative than grid codes, and not well suited for the studies of disks in conditions of very low viscosity.

More details on the SPH code and on its advantages and disadvantages with respect to grid-based codes can be found in Price (2012).

1.5   This thesis and future outlook

ALMA and VLT/SPHERE have opened, since the beginning of this PhD work, a whole new branch within the field of planet-formation: the study and interpretation of substructures in protoplanetary (potentially planet-forming) disks. ALMA detected and spatially resolved substructures in both gas and mm-sized dust. SPHERE observed additional structures in μm-sized dust, linked to the gas. The fact that gas and solids of different sizes have different dynamics is now undisputed, but a clear connection between the structures observed with the different tracers is still missing. Are all substructures due to planets that have already formed in the disks? How many planets are needed to explain them? Or are they the signpost of ongoing planet formation? A comprehensive answer to these questions can only be provided by simultaneously explaining the substructures in the gas and dust at different wavelengths.

- In Chapter 2 the GG Tau (d=140 pc) circumbinary disk is studied in detail. Hydrodynamical simulations coupled to dust evolution models are carried out in order to model the system and reproduce archival observations in both gas and mm-sized dust simultaneously. The analysis allows to put strong constraints on the binary orbit. In particular, in order to reproduce the gas cavity size and the location of the dust ring observed at mm-wavelengths, the binary orbital plane and that of the protoplanetary disk must be misaligned with respect to each other.

- In Chapter 3, new ALMA Band 7 (0.8 mm) observations of the disk around HD 135344B (d=135 pc) are presented. Thanks to the new $0''.2$

(~ 30 au) resolution achieved, this disk, which in previous observations appeared as a single slightly asymmetric ring, is now resolved into an inner, symmetrical ring and an outer asymmetric structure. A fit of the image shows that the asymmetry is consistent with a vortex. The images at mm-wavelength have also been compared to the scattered light observations, showing "grand-design" (two-armed) spiral arms. A scenario explaining both the mm-dust structures and the μm-dust ones is proposed. In this scenario, the spiral arms are launched by the vortex itself, and a single planet is needed to explain all the structures, rather than 2 or 3 planets as in previous interpretations (e.g., Stolker et al., 2017).

- Chapter 4 presents new very high resolution ($0''.06$, ~ 10 au) ALMA Band 3 (3 mm) and Band 4 (2 mm) observations, requested in order to test the scenario proposed in Chapter 3. A multi-wavelength analysis is then performed by combining these observation with our Band 7 and archival Band 9 observations. With this analysis, different theoretical predictions of dust dynamics and evolution inside a vortex were tested, thus allowing to confirm the nature of the HD 135344B asymmetry as a dust-trapping vortex. Most notably, a shift in the peak of the emission of the vortex, due to different dust distributions of grains of different sizes, was measured for the first time. The mass of the vortex was also calculated, and was found to be high enough to launch spiral arms, as proposed in van der Marel et al., 2016b.

- In Chapter 5, CN emission in protoplanetary disks is modelled in detail using the thermo-chemical code DALI. The main result is that CN emission is always ring-shaped, independently of the underlying dust structure. The size of the rings and their brightness can provide information about the flaring of the disk, the UV flux from the central star, as well as the disk size.

- In Chapter 6, a survey of protoplanetary disks in the Corona Australis (CrA, d=154 pc) star forming region with ALMA Band 6 (1.3 mm) is presented. The disks in CrA appear very different from those in other regions of the same age previously surveyed. The measured fluxes are lower than expected, and the disks are smaller and do not show any substructure. Different possible explanation for are explored: it is possible that two different star formation events, a few Myrs apart, have occurred, with the older population already on its way to its Class III stage; alternatively, the initial conditions at the epoch of star formation may play a role in the properties we observe today.

The main conclusions of this thesis are the following:

1. The size of the dust ring around the GG Tau binary can only be explained if the orbital plane of the binary is misaligned with respect to the disk.

2. The spiral arms observed in scattered light may be triggered by massive vortices rather than by planets. This scenario can explain the structures observed in HD 135344B.

3. CN emission is ring-shaped even in full disks, with its location unrelated to that of any dust ring. The ring size and flux can provide information about the physical structure of the disk.

4. The mm-fluxes of the Class II disks in the CrA star forming region are lower than expected in a region of its age, and their dust radii are smaller. This could be due to the initial conditions of the star forming process, or to an old stellar population in the CrA region alongside the young one.

To date, it remains unclear whether the observed structures are due to already formed planets or to some other physical mechanism. So far only one planet has been imaged in a disk (Keppler et al., 2018), but future observations may directly image more embedded planets associated with these structures. In the meantime, new promising approaches to indirectly infer the presence of planets are becoming more and more common and will prove critical in the near future. The perturbations to the gas kinematics induced by planets, for example, has already been used in a few cases (e.g., Pinte et al., 2018; Teague et al., 2018), and the same technique can now be applied for more systems. Emission from circumplanetary disks associated to embedded protoplanets (Isella et al., 2019; Pérez et al., 2019) as well as the emission associated to their accretion onto the planets (Haffert et al., 2019) have also recently been detected with ALMA and MUSE, respectively. Such observations may be more common in the future.

In the meantime, additional multi-wavelength studies of protoplanetary disks such as that carried out for HD 135344B can shed light on the dust properties inside dust traps, including inside vortices. In particular, the connection between vortices in the mm and spiral arms in scattered light should be better investigated in more systems (e.g. V1247 Ori and MWC 758), also exploiting the sensitivity and spatial resolution of ALMA at the high frequencies available in Band 9 and Band 10.

These studies are critical to understand if substructures in disks are the birthplace of new planets. They will ultimately also tell whether and how the variety of structures observed at mm-wavelengths is linked to the diversity in the exoplanetary systems' properties.

2 | Testing dust trapping in the circumbinary disk around GG Tau A

Abstract

Context. The protoplanetary disk around GGTau A is so far the most studied circumbinary disk, and has been observed at many different wavelengths. Continuum mm/sub-mm observations detected a dust ring located between 200 AU and 300AU from the center of the system. Such a ring structure can be explained by the presence of a local maximum in the gas radial pressure profile which creates a "trap" for mm-sized dust grains, and likely induced by the dynamical interaction between the disk inner edge and the binary motion.

Aims. We want to investigate the origin of this ring structure, and test, consistently with the astrometric measurements, wether or not a the interaction between the binary and the gaseous disk can produce a pressure bump at the location of the observed ring.

Methods. We run a set of 3D hydrodynamical simulation for different orbits and for different values of viscosity. Using the obtained surface density and radial velocity profiles, we then apply a dust evolution model in post-processing in order to to retrieve the expected distribution of mm-sized grains.

Results. Comparing the results of our models with the observations, we show that if the binary orbit and the disk are coplanar, tidal truncation of the circumbinary disk occurs at a radius which is too small compared to the inner edge inferred by the dust observation, and that in this case the pressure bump and the dust ring are located at around 100-150AU. On the other hand, we also show that in order for dust trapping to occur at the observed radius, the disk and orbital plane must be misaligned of 27 degrees.

2.1   Introduction

Most stars form in multiple systems (e.g. Duquennoy and Mayor, 1991; Fischer and Marcy, 1992; Raghavan et al., 2010). It is also undisputed that the majority of stars in young star forming regions show direct or indirect evidence of the presence of a young circumstellar disk. Moreover, disks orbiting the whole multiple stellar system, called circumbinary in the case of binary systems, are sometimes observed (e.g. Simon and Prato, 1995). Planets originate from these disks, and so far ten circumbinary planets (sometimes called "Tatooine planets") have been discovered by Kepler orbiting around eight eclipsing binaries (Doyle et al., 2011; Welsh et al., 2012; Orosz et al., 2012b,a; Schwamb et al., 2013; Kostov et al., 2013, 2014; Welsh et al., 2014). Planets, therefore, are common in binary (or multiple) systems.

Disk-binary interaction plays a pivotal role in such systems. In binaries, part of the material of a disk around one or both stars is ripped away by tidal forces. The net result of the interaction between the gas disk and the binary is a net exchange of angular momentum via tidal torques. In particular, the angular momentum of the disk-binary system is transported outwards (Lin and Papaloizou, 1979a,b). This means that gas in the individual circumstellar disks loses angular momentum to the binary and moves toward inner orbits; the gas in circumbinary disks, on the other hand, acquires angular momentum from the binary and is repelled from the central stars. Disk viscosity tends to contrast the effect of tidal torques. At a certain radius, called the tidal truncation radius, viscous and tidal torques balance each other and an equilibrium configuration is reached (Lin and Papaloizou, 1986).

Theoretical studies have attempted to find a model capable of providing an estimate of the radius of each one of the three disks in a binary system (i.e., circumprimary, circumsecondary ,and circumbinary), given the key orbital parameters (semi-major axis a, eccentricity e, mass ratio q, and inclination i between disk and orbital plane) and some characterization of the disk viscosity (Papaloizou and Pringle, 1977; Paczynski, 1977; Artymowicz and Lubow, 1994; Pichardo et al., 2005; Miranda and Lai, 2015; Lubow et al., 2015). In one of the most comprehensive works so far Artymowicz and Lubow, 1994 estimated the truncation radius for binaries coplanar with the disks and for any value of q, e and viscosity. Miranda and Lai, 2015 recently generalized this study for misaligned systems.

Observations of young disks in multiple systems have the potential to test the predictions of tidal truncation theory (Harris et al., 2012). The best cases are offered by the systems in which the proper motion for the stellar components

are measured for a significant fraction of the stellar orbits. In this case, orbital solutions are obtained from the analysis of the proper motions, and models incorporating the tidal interaction between the multiple system and the disks can be used to predict the spatial distribution of gas and dust in the disks. High angular resolution observations of the disk emission can then be used to test the predictions of the models. In this work we use the results of recent observations for the GG Tau A circumbinary disk to test models of tidal truncation.

The young quadruple system GG Tau has been the subject of many different studies. It is composed of two low-mass binary systems, namely GG Tau A and GG Tau B. GG Tau Aa and GG Tau Ab, respectively of mass $0.78 \pm 0.09\,\mathrm{M_\odot}$ and $0.68 \pm 0.02\,\mathrm{M_\odot}$ (White et al., 1999) and with an angular separation of $0.25''$ (Leinert et al., 1993), are the two components of GG Tau A, one of the most studied and best known nearby ($\sim 140\,\mathrm{pc}$, Elias, 1978) young binary systems ($\sim 1\,\mathrm{Myr}$, White and Ghez, 2001)[1]. Its circumbinary disk has been observed in dust thermal emission (Dutrey et al., 1994; Guilloteau et al., 1999; Andrews et al., 2014), in scattered light emission (Roddier et al., 1996; Silber et al., 2000; Duchêne et al., 2004), and in CO gas emission (Dutrey et al., 2014), and has a total mass of $\sim 0.12\,M_\odot$ and an inclination $i = 37°$ with respect to the line of sight (Guilloteau et al., 1999) . The other binary system, GG Tau B, is located $10.1''$ south, is wider ($1.48''$), and is less massive (Leinert et al., 1993).

The disk around GG Tau A shows a peculiar ring-shaped dust distribution. Andrews et al., 2014 modeled the continuum dust emission measured at several millimeter wavelengths with a radial distribution for mm-sized grains as a Gaussian peaked at $235 \pm 5\,\mathrm{AU}$, and with a very narrow width, $FWHM \sim 60\,\mathrm{AU}$. Imaging in scattered light at near infrared wavelengths have shown that the inner radius of the disk in smaller, so that μm-sized particles lie between 180 and 190 AU (Duchêne et al., 2004). ALMA observations of the rotational transition $J = 3 - 2$ of ^{13}CO show an intensity radial profile with a peak around $175 - 180$ AU from the binary center (Tang et al., 2016). However the relatively poor spatial resolution of these observations (≈ 50 AU) does not allow the location of the inner radius in gas to be inferred with precision. Emission from both ^{12}CO$(J = 3 - 2)$ and ^{13}CO$(J = 3 - 2)$ is detected up to ~ 500 AU from the binary, clearly indicating that gas is also found at much larger radii than the mm-sized dust. Among all the components observed, only mm-sized dust grains are optically thin and can therefore provide information on the density profile

---

[1]VLTI/PIONIER and VLT/NACO observations suggest that GG Tau Ab is itself a close binary with two stars with very similar mass at a projected separation of ≈ 4 AU (Di Folco et al., 2014). Given the small separation relative to the distance to the circumbinary disk, which is the subject of our study, we will consider GG Tau Ab1 and GG Tau Ab2 as a single component GG Tau Ab.

Table 2.1: Parameters of the best orbital solutions. The first column is obtained by assuming the disk to be coplanar with the orbit, and therefore by fixing the value of i. The other values were obtained instead by fixing the value of a. The data in Cols. 1 and 2 are from Köhler, 2011, in Cols. 3 and 4 from Köhler (personal communication).

Orbital Element	Orbit coplanar with disk	$a = 60$ AU constraint	$a = 70$ AU constraint	$a = 80$ AU constraint
Date of periastron T_0 (Julian)	2477680^{+690}_{-270} (July 2071)	2463400^{+1470}_{-5420} (June 2032)	2462334^{+1436}_{-5222} (2029 Jul 16)	2461114^{+2013}_{*****} (2026 Mar 14)
Period P (years)	162^{+62}_{-15}	403^{+67}_{-32}	507^{+83}_{-41}	638^{+77}_{-68}
Semi-major axis a (mas)	243^{+38}_{-10}	429	500.0	571.4
Semi-major axis a (AU)	$34^{+5.9}_{-2.8}$	60	70.00	80.00
Eccentricity e	$0.28^{+0.05}_{-0.14}$	$0.44^{+0.02}_{-0.03}$	$0.510^{+0.017}_{-0.013}$	$0.565^{+0.004}_{-0.007}$
Argument of periastron ω (°)	91^{+4}_{-13}	19^{+9}_{-10}	-165^{+8}_{-13}	-169^{+10}_{-2}
P.A. of ascending node Ω (°)	$277^{+2.0}_{-2.0}$	131^{+13}_{-8}	133^{+11}_{-7}	135^{+11}_{-8}
Inclination i (°)	$143^{+1.3}_{-1.0}$	$132.5^{+1.0}_{-2.5}$	$131.1^{+0.9}_{-0.6}$	$131.4^{+0.9}_{-0.6}$
Angle between orbit and disk	0.02 ± 1.9	24.9 ± 1.7	26.9	28.1
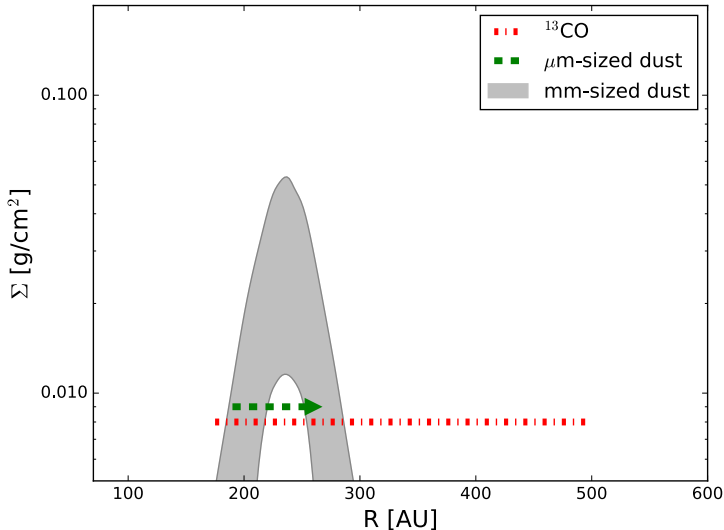
Figure 2.1: Observational constraints available to date for different sized grains and for CO distribution. The gray-shaded area shows the 2σ uncertainty on the mm-sized dust radial density profile as modeled in Andrews et al. (2014). The red dash-dotted and the green dashed lines show the radial extent of CO and micron-sized dust grains, respectively. It should be noted that these two tracers are optically thick and do not provide information about the density profile. The vertical location of the lines is therefore arbitrary.

of mm dust. For this reason, we will mainly focus our study on the dust ring observed at submillimeter wavelengths. A summary of the various constraints for the disk size in the various components is shown in Fig. 2.1.

In order to use this information on the spatial extent of the GG Tau A circumbinary disk to test the predictions of tidal truncation models, some constraints on the orbital parameters of the GG Tau A binary system are needed. For example, the classical calculations by Artymowicz and Lubow, 1994 predict disk truncation radii at 2 or 3 times the value of the binary semi-major axis a. A number of astrometric observations for the GG Tau A system are available, and span almost twenty years from 1990 to 2009. However, these measurements cover only a fraction of the orbital period of the binary and do not allow all the orbital parameters to be constrained at the same time. By fixing one of the orbital parameters, all the others can be obtained by fitting the proper motions (Köhler, 2011). Table 2.1 shows four different orbits consistent with the astro-

metric measurements: the first column is obtained by requiring that the disk and the binary orbit be coplanar (i.e., putting constraints on the inclination i of the orbit and on the position angle of its ascending node), while the other three are calculated by fixing the value of the semi-major axis of the orbit to 60, 70, and 80 AU.

If the inclination i and the position angle of the ascending node of the binary orbit are constrained by requiring the orbit to be coplanar with the disk, then $a \approx 34$ AU. In this case the dust inner ring is located much farther out than the predicted ~ 100 AU gas inner truncation radius. A possible explanation for this apparent discrepancy was proposed by Andrews et al., 2014: if the gas radial density profile at the inner edge of the disk were very shallow, then the pressure maximum where mm-size grains drift toward and accumulate would lie at a much larger radial position than the gaseous disk inner radius. Hydrodynamical simulations calculating the expected gas radial profile are needed to test this hypothesis.

Alternatively, if the hypothesis of coplanarity is relaxed, the astrometric measurements can be fit by orbits misaligned with respect to the disk plane and with higher values of a (as shown in Tab. 2.1). These misaligned configurations would allow the binary system to dynamically truncate the disk at a location closer to the observed dust ring. In this misaligned case, a steeper radial profile for the gas density would in principle also be able to produce a dust ring at radii even larger than 200 AU.

It should be noted that a coplanar disk-binary system with $a > 34$ AU is not entirely ruled out by the astrometric measurements, and that a coplanar orbit with a larger semi-major axis is still possible within a 5σ uncertainty. Owing to the much lower likelihood of this solution, however, we decide not to address it in this work. More astrometric measurements are needed for a more detailed analysis.

In this paper we run a set of hydrodynamical simulations that account for tidal interaction between the binary and the circumbinary disk to calculate the predicted distribution of gas density in the best-fit case of coplanar disk and binary system. We couple a dust evolution model (Lodato and Price, 2010) to the results of the hydrodynamical simulations for the gas to obtain predictions for the radial profile of the dust density. We compare these predictions with the main features observed for the dust in the disk in order to test the validity of the coplanar hypothesis. We also discuss whether the alternative hypothesis of a misaligned disk could be a likely explanation for the location of the dust observed in the GG Tau A circumbinary disk. For this study, we always consider orbital parameters that are consistent with the measured stellar proper motions.

In Section 2.2 we briefly present the setup of our simulations. In Sections 2.3 and 2.4 we show the results we obtained in our simulations and we discuss the effect that our results have on the search for an explanation for the observed narrow mm-dust ring.

2.2   Methods

2.2.1   Gas simulations

In our work we use the PHANTOM Smoothed Particle Hydrodynamics (SPH) code (Lodato and Price, 2010; Price and Federrath, 2010) in order to perform 3D hydrodynamical simulations for the gas alone. The code computes the viscous evolution of a gas distribution in a disk by solving the equations of hydrodynamics in the presence of a gravitational field generated by one or two central stars and/or a planetary mass companion. For our purposes, we use a circumbinary disk and we neglect its self-gravity. We want to study the resulting gas radial density and velocity profiles.

To mimic disk viscosity, we adopt the formulation by Flebbe et al. (1994), where the stress tensor in evaluated directly in the Navier-Stokes equations. We can express the shear viscosity using the Shakura and Sunyaev (1973b) prescription

$$\nu = \alpha \frac{c_{\mathrm{s}}^2(R)}{\Omega(R)}, \tag{2.1}$$

where α is the chosen value for the Shakura and Sunyaev (1973b) parameter, and $c_{\mathrm{s}}(R)$ and $\Omega(R)$ are the sound-speed and angular velocity radial profiles, respectively. The accuracy of this formulation has also been tested for physical phenomena strongly dependent on the chosen value of α, such as the dynamics of warps (Lodato and Price, 2010; Facchini et al., 2013).

Since the disk viscosity strongly affects both the location of the tidal truncation radius and the dust dynamics, we choose to run a set of different simulations using three different values of viscosity, corresponding to α of 0.01, 0.005 and 0.002.

A second source of viscosity is also present. SPH codes implement an artificial viscosity in order to be able to resolve discontinuities by spreading them over a few smoothing lengths and to prevent particle interpenetration. This artificial term can be understood as a numerical representation of second derivatives of the velocity (Artymowicz and Lubow, 1994; Murray, 1996; Lodato and Price,

2010); the resulting artificial viscosity parameter is given by

$$\alpha_{\text{art}} \approx \frac{1}{10} \alpha^{\text{AV}} \frac{\langle h \rangle}{H}, \qquad (2.2)$$

where $\langle h \rangle$ is the azimuthally averaged smoothing length (which is proportional to $n^{-1/3}$, n being the local density of SPH particles), H is the disk thickness, and α^{AV} is set to a minumum value $\alpha_{\text{min}}^{\text{AV}}$ and increases up to a value $\alpha_{\text{max}}^{\text{AV}}$ in the presence of shocks by means of a Morris and Monaghan, 1997 switch. We also note that we used the notation α_{art} to discriminate between the physical viscosity due to the artificial term and the directly implemented physical viscosity, for which we used α. The total viscosity in SPH is therefore given by $\alpha_{\text{tot}} \approx \alpha + \alpha_{\text{art}}$.

Since $\langle h \rangle \propto n^{-1/3}$, we can make the contribution of the artificial viscosity to the physical viscosity negligible by increasing the number of particles in the low-viscosity simulations (see Section 2.2.3), thus making $\alpha_{\text{tot}} \sim \alpha$.

In the simulations presented in this work, we set $\alpha_{\text{min}}^{\text{AV}} = 0.03$ and $\alpha_{\text{max}}^{\text{AV}} = 0.1$. The Von Neumann and Richtmyer, 1950 β^{AV} parameter was set equal to 2. We let each simulation evolve over 1000 binary orbital periods in order to reach steady state. We then compute the gas density and the gas radial velocity profile by averaging the quantities azimuthally. We also average them over a few orbital periods in order to smooth the profiles and to remove the fluctuations due to the discretization of the fluid operated by SPH.

2.2.2 Dust simulations

We use the gas density and radial velocity profiles obtained from our SPH simulations as a stationary "environment" where we let the dust evolve following the model from Lodato and Price (2010). We assume that the gas density in a binary system reaches a stationary state on timescales shorter than the dust evolution timescales, which for typical dust-to-gas ratios are on the order of hundreds of local orbits (e.g., Brauer et al., 2008), which at the position of the dust ring is long compared to the binary orbital timescale (~ 200 years). We use this stationary gas density distribution as input for a global model of dust evolution Birnstiel et al., 2012 to test how dust evolves under the physical conditions predicted by the SPH hydrodynamical simulations.

Our dust evolution model accounts for compact dust growth, cratering and fragmentation, radial drift, turbulent mixing, and gas drag. In order to calculate the relative velocity of the dust particles, Brownian motion, turbulence, vertical settling, and radial and azimuthal drift are taken into account. In these simulations, the initial size of all the particles is assumed to be $\sim 1\,\mu$m. At the

beginning of the growth process, when particles have still sizes of a few microns, the main contribution to their relative velocities comes from Brownian motion and settling. In these early stages, growth by coagulation is very efficient and is a result of van der Waal's interaction between small grains. As they grow to larger sizes, they start to decouple from the gas, and turbulence as well as radial drift become the main sources of their relative velocities.

As the grains grow, their relative velocities increase (Lodato and Price, 2010). When dust grains reach sizes with high enough velocities, collisions no longer produce coagulation only, but can also cause the dust grains to fragment. The threshold velocities above which fragmentation becomes dominant can be estimated through laboratory experiments and theoretical work of collisions for silicates and ices (e.g. Blum and Wurm, 2008; Schäfer et al., 2007; Wada et al., 2009). For the silica particles these threshold velocities are on the order of a m/s, and they increase with the presence of ices (Gundlach and Blum, 2015). We ran some test models with different values of fragmentation velocity v_{frag} and we found that the results were not significantly affected. In our models we adopted a standard value of $v_{\mathrm{frag}} = 10\,\mathrm{m/s}$.

The level of coupling between the dust and the gas is quantified with the dimensionless stopping time τ_{fric}, defined as the ratio between the stopping time of the particle due to friction with the gas and the orbital timescale Ω. Particles with $\tau_{\mathrm{fric}} \gg 1$ are decoupled from the gas; they are not affected by any drag force and therefore rotate around the star on their own Keplerian orbit. On the other hand, particles with $\tau_{\mathrm{fric}} \ll 1$ are strongly coupled with the gas and move along with it. Particles experiencing the biggest radial drift are those characterized by $\tau_{\mathrm{fric}} = 1$. In the case of the GG Tau A disk, in the vicinity of the observed dust ring we expect this to occur for grains with sizes of $\sim 1 - 10$ mm. Owing to the sub-Keplerian rotation velocity of the gas, these particles experience a gas headwind that leads them to lose angular momentum and to drift radially towards the disk inner regions (Whipple, 1972; Nakagawa et al., 1986; Brauer et al., 2007).

One of the biggest unknowns for dust evolution models is whether dust growth is compact or fractal. In our models we assume compact growth. However, fractal and compact growth models are not expected to produce significantly different results in terms of the sub-mm emission from the disk outer regions because these different modes of solid growth produce particles with similar τ_{fric} (even though they have different sizes and filling factors) and absorption/emission dust opacities are proportional to τ_{fric}. Therefore, we do not expect this intrinsic uncertainty of the models to play an important role on the results of the work presented here.

In section 2.3.3 we apply this dust model to simulate the behavior of dust particles in the coplanar case for the GG Tau A circumbinary disk. We use these results to compare the predictions of our models to the radial distribution of dust particles as constrained by the observations.

2.2.3   Initial conditions

We tune our initial conditions to reproduce the main characteristics of the GG Tau A system. First of all, the eccentricity e and the semi-major axis a of the orbit are set according to the best-fit orbits calculated by Köhler, 2011 to reproduce the measured stellar proper motions (Tab. 2.1). In this work we are interested in simulating in detail the case of coplanar disk and binary orbital plane (second column in Tab. 2.1), but we also discuss the hypothesis of a disk misaligned with the binary which allows for higher values of the semi-major axis than in the coplanar case (a few possible cases are listed in the Cols. 3, 4, and 5 in Tab. 2.1).

In the SPH simulations, the two stars are modeled as sink particles (Bate et al., 1995) with mass $0.78\,M_\odot$ and $0.68\,M_\odot$ (White et al., 1999). Each of the two sink particles has an associated accretion radius, i.e. a radius within which we can consider gas particles to be accreted onto the stars. Since for our purposes we do not need to know what happens to the gas in the vicinity of the stars, we can set the sink radii to fairly high values, thus speeding up the simulations. In particular, we use $R_{\rm sink} = 0.1\,a$.

We set the initial disk inner and outer radii at $t = 0$ to $R_{\rm in} = 2a$ and $R_{\rm out} = 800\,{\rm au}$, respectively. Between these two edges, the initial gas density profile we use is

$$\Sigma(R) = \Sigma_0 \frac{a}{R}\left(1 - \sqrt{\frac{R_{\rm in}}{R}}\right), \qquad (2.3)$$

where Σ_0 is a normalization factor. Its value is chosen in each simulations in order to give a total gas mass of around $\sim 0.12 M_\odot$ (the disk mass estimated by Guilloteau et al., 1999). We then set a Keplerian velocity profile for the gas, relative to a $1.46\,M_\odot$ central mass. It should be noted that our hydrodynamical results do not depend on the initial gas density profile since we let our system evolve until steady state is reached. We assume for the gas a locally isothermal equation of state, where the temperature along the z-axis at each radius is fixed. To describe the temperature radial profile we adopted the one inferred from the analysis of ^{13}CO measurements:

$$T(R) = 20\,{\rm K}\left(\frac{R}{300\,{\rm AU}}\right)^{-0.9}. \qquad (2.4)$$

In order to test the effect of this choice for the disk temperature on the results of our study, we also ran simulations with a less steep temperature radial profile ($T \propto R^{-0.5}$; see Appendix A).

The temperature profile is related to the disk thickness H by assuming vertical hydrostatic equilibrium

$$H(R) = \frac{c_{\mathrm{s}}(R)}{\Omega_{\mathrm{K}}} = \sqrt{\frac{k_{\mathrm{B}}T(R)}{\mu m_{\mathrm{p}}}} \frac{1}{\Omega_{\mathrm{K}}}, \qquad (2.5)$$

where $\mu = 2.3$ is the mean molecular weight and k_{B} is the Boltzmann constant. The particles are then distributed in the vertical direction to obtain a Gaussian density profile with thickness $H(R)$. Combining Eq. 2.4 and Eq. 2.5 we get $H/R \approx 0.12$ in our simulations.

Among all the factors that affect the evolution of gas and dust in the disk, viscosity plays an important role. For this reason we decided to run different simulations for different values of viscosity. When simulating disks with lower viscosities, we correspondingly increased the number of SPH particles to reduce the possible effects given by the artificial viscosity, as explained in section 2.2.1. In particular, we ran simulations with $\alpha = 0.01$ (using 10^6 particles), $\alpha = 0.005$ (using 3×10^6 particles), and $\alpha = 0.002$ (6×10^6 particles). We obtain $\alpha_{\mathrm{art}} \leq 0.002$ in the 10^6 particles simulation, $\alpha_{\mathrm{art}} \leq 0.0015$ in the 3×10^6 one, and $\alpha_{\mathrm{art}} \leq 0.001$ when using 6×10^6 particles.

2.3   Results

In this section we present the results obtained with our simulations with a binary orbiting on the same plane of the disk. In this case, the binary orbit has $a = 34\,\mathrm{au}$ and $e = 0.28$. We study how the initial gas density profile evolves with time, and how it is affected by the chosen values of viscosity. Particular focus is given to how time and viscosity affect the location and shape of the gas density maximum because marginally coupled dust particles will radially drift to this region. In these simulations, the binary orbit has semi-major axis and eccentricity of $a = 34\,\mathrm{au}$ and $e = 0.28$, respectively, corresponding to the best-fit orbit solutions of the measured stellar proper motions (Col. 2 in Tab. 2.1).

2.3.1   Time evolution of the gas density profile

We first verify that the evolution time in our simulations (1000 orbital periods) is sufficient for the gas density profile to reach a steady state configuration.
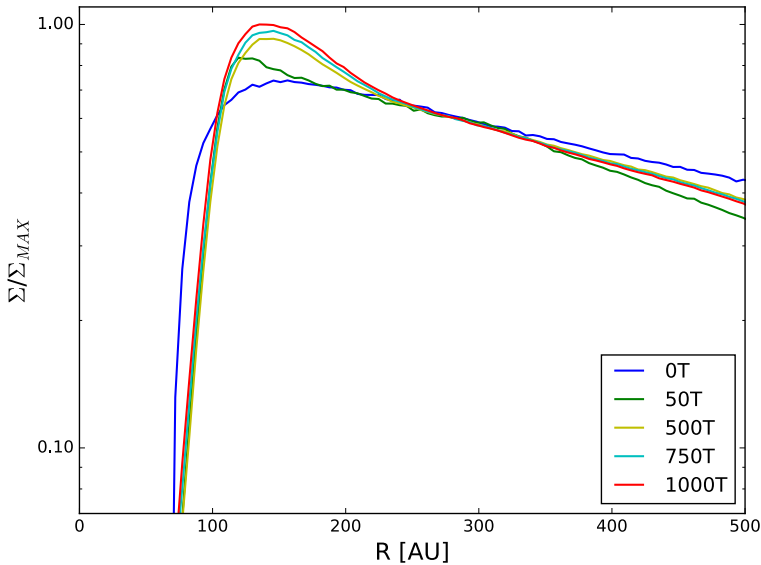
Figure 2.2: Azimuthally averaged gas density profile for the $\alpha = 0.002$ simulation at different evolutionary stages. After a few hundred binary orbits the density profile reaches a quasi-stationary configuration. All the density profiles are normalized to the maximum of the density profile at the end of the simulation.

Fig. 2.2 shows a comparison of the gas density profile at different times for the $\alpha = 0.002$ simulation, i.e. the one with the longest viscous timescale. Even for the lowest viscosity, the density profiles after 750 and 1000 orbital periods differ by at most $\sim 3\%$. We therefore assume that the disk has reached steady state after 1000 orbital periods.

2.3.2 Different viscosities

It is also important to test how the gas density profile is affected by different choices for the disk viscosity. Fig. 2.3 shows the three gas density profiles (azimuthally and temporally averaged over a few binary orbital periods in order to remove numerical noise) corresponding to the three values of viscosity tested in our simulations. These profiles are compared to the density profile modeled in Andrews et al. (2014), which was proposed to reproduce the necessary dust trapping at the location where the dust ring of $\sim$mm-sized grains was observed.

In all the three cases, our gas simulations produce very small tidal truncation radii ($< 100 \, \mathrm{au}$), and a gas density peak located at radii of $130 - 140 \, \mathrm{au}$, much
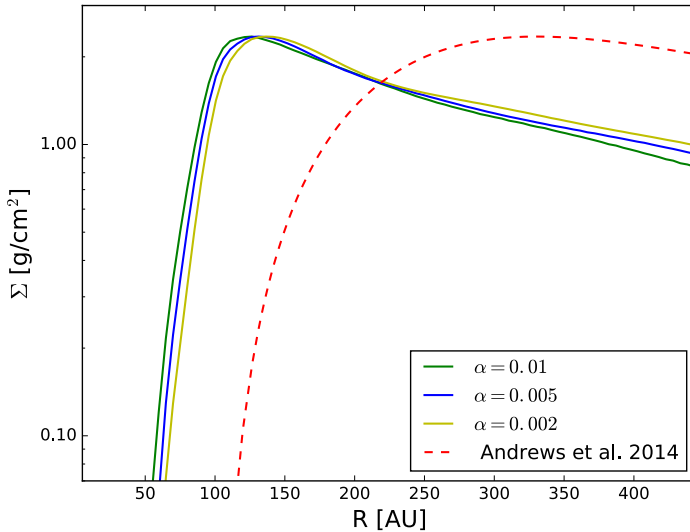
Figure 2.3: Gas density profiles obtained from our simulations (solid lines) in the coplanar case using $\alpha = 0.01, 0.005, 0.002$. The gas density profile invoked by Andrews et al. (2014) is also plotted (dashed line) for comparison.

smaller than in the profile proposed by Andrews et al. (2014). There is no strong dependence of the location of the gas density peak on the assumed value of α.

Fig. 2.4 shows the inner cavity in a snapshot of our simulation $\alpha = 0.002$ at 1000 binary orbits. The white dots mark the location of the two central stars, while the black dashed lines show the location of the maximum of the gas radial density profile.

2.3.3 Dust evolution

We use the dust evolution model from Lodato and Price (2010) to investigate the expected density distribution of dust in the disk. We apply these models to the outputs of the three *coplanar case* simulations, corresponding to the three values of viscosity.

We were able to obtain dust trapping for mm-sized grains only in the case of $\alpha = 0.002$. For higher α values, mm-sized dust particles tend to fragment to smaller sizes (e.g. Birnstiel et al., 2012) and their trapping efficiency decreases (see Lodato and Price, 2010) . As shown by the solid blue line in Fig. 2.5,
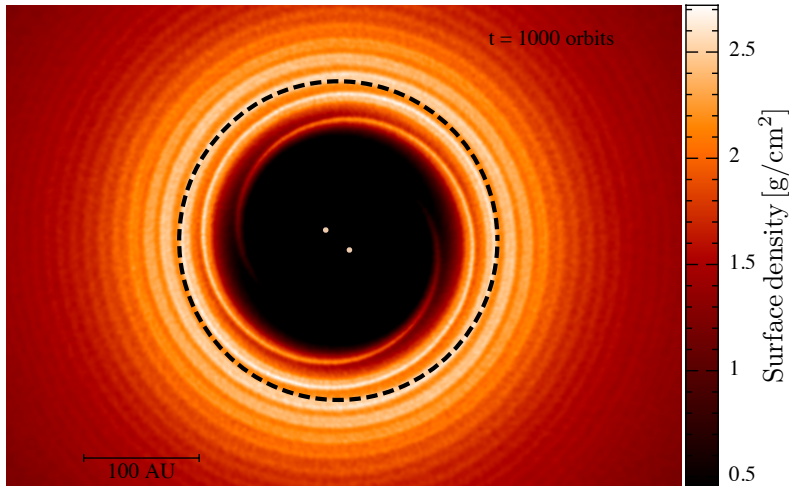
Figure 2.4: Snapshot of the inner cavity of the circumbinary disk at 1000 binary orbits in the $\alpha = 0.002$ case. The white dots indicate the location of the two central stars; the dashed lines show the location of the pressure maximum. The image was produced using `SPLASH` (Price, 2007).

at this low value of viscosity a large enough population of mm-sized grains is formed and it is efficiently trapped at $\sim 150\,\mathrm{AU}$, the location of the gas pressure maximum. However, the ring is too close to the central star and our results are inconsistent with the data, represented by the gray shaded area in Fig. 2.5.

This inconsistency cannot be solved by simply considering different values of viscosity or a different temperature profile. In fact, as shown in section 2.3.2 and Appendix A, the gas density profile obtained from our hydrodynamical simulations does not depend strongly on these properties of the disk. Since the dust ring in mm-sized particles around GGTau A is due to dust trapping at the location of the gas pressure maximum, we can therefore conclude that the orbit of the binary and the disk cannot be coplanar: the large radial location of the ring cannot be explained by such a configuration since the gas density maximum, and consequently the dust ring, would lie at a radius that is too small compared to the position of the ring of mm-sized dust. The inner radius of micron sized grains is also strongly underestimated with respect to the $180 - 190\,\mathrm{AU}$ observed by Duchêne et al. (2004) and shown in Fig. 2.1.
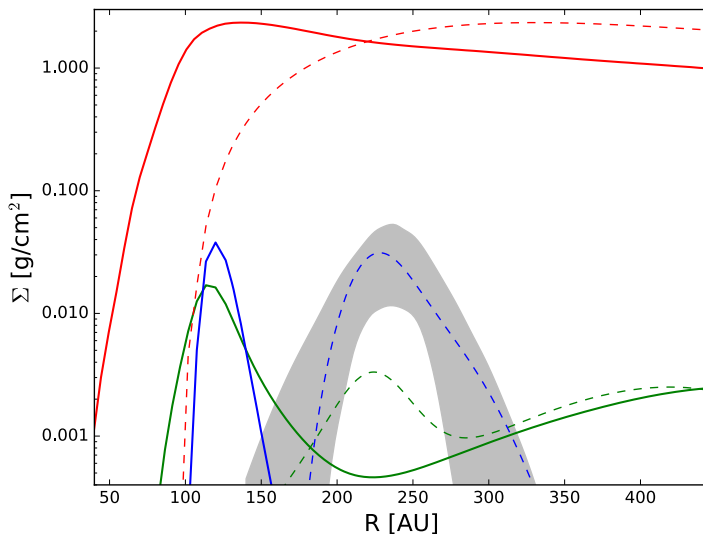
Figure 2.5: Density profiles for gas (solid red line) and dust (solid blue for mm-sized and solid green for micron-sized) obtained from our simulations in the coplanar case using $\alpha = 0.002$. The gas and dust density profiles from the model by Andrews et al. (2014) are also plotted (dashed lines) for comparison. It is clear that the solid blue line showing the mm-sized dust surface density profile is not consistent with the data (gray shaded area).

2.4 Discussion

We tested the hypothesis that the narrow dust ring around GG Tau A can be explained by dust trapping at the gas density maximum. We showed that this scenario cannot be explained consistently with astrometric measurements by a binary orbiting on the same plane of the circumbinary disk. Indeed, the best-fit orbit calculated by Köhler (2011) without fixing any parameter gives a misalignment between the disk and the orbital plane of $\sim 30°$ However, the uncertainties on the fitted orbital parameters in this case are much larger, given the poor sampling of the binary orbit.

   If, on the one hand, the resulting separation between the two stars in this coplanar case is too small to explain the location of the dust ring, on the other hand, a binary orbit with a larger semi-major axis could in principle create such a wide ring. As a increases, the truncation radius for the gas component of the disk moves farther out, and the gas pressure bump trapping the dust is located

at larger radii. The astrometric measurements for the proper motion of GG Tau A are consistent with wider binaries if the hypothesis of a disk coplanar with the binary motion is dropped and the binary and the disk are misaligned. Tab. 2.1 shows that orbits with $a = 60-80$ au are consistent with misalignments between 25° and 30°. In the latter scenario, we expect the disk to become eccentric and warped, and our approach, which assumes azimuthal symmetry, would not be suitable to test it; instead 3D hydrodynamical simulations including gas and dust would be required (Laibe and Price, 2014; Dipierro et al., 2015a, 2016).

Tidal truncation itself is influenced by the misalignment between orbital and disk plane. Recently Lubow et al. (2015) studied the dependence of the tidal torque on the misalignment angle at the 2:1 inner Lindblad resonance in the case of a nearly circular disk rotating around a circular-orbit binary. Furthermore, Miranda and Lai (2015) quantitatively computed how the tidal truncation radius changes in misaligned systems with respect to coplanar ones, adopting a truncation criterion determined by the balance between resonant torque (which they analytically calculated for a misaligned system) and viscous torque. The latter study also took eccentric binaries into consideration. The common conclusion is that in general the torques in misaligned systems are weaker, and that circumbinary disks in such systems tend to have smaller inner radii than in the aligned case. Therefore, in principle, a wide range of truncation radii could be expected for circumbinary disks, and not only the classical $2-3a$ prediction from Artymowicz and Lubow (1994). In practice, Miranda and Lai (2015) show that this happens only for very misaligned systems ($\Delta i \gtrsim 90°$); in these cases, the inner radius of a circumbinary disk can decrease to $1-1.5a$. We conclude that for $a = 60-80$ au and for the relative binary-disk misalignment, we should expect tidal torques to truncate the disk between 180 and 240 au.

Theoretical studies have shown that binaries and disks forming with different axes of rotation are not rare. For example, Bonnell et al. (1992) showed that in the case of an elongated cloud with a rotation axis is oriented arbitrarily with respect to the cloud axis, the disk plane (reflecting the angular momentum of the core) and the orbital plane (reflecting the symmetry of the initial core) can indeed be misaligned. Similarly, Bate et al. (2010) showed that during the star formation process, the variability of the angular momentum of the accreting material and dynamical interactions between stars can produce significant misalignment between the stellar rotation axis and the disk spin axis. However, tidal torques tend to realign the two planes. Foucart and Lai (2014) calculated this alignment torque, and concluded that we should expect circumbinary disks around close (sub-AU) binaries to be highly aligned, while disks and planets around wider binaries could still be misaligned. The latter is the case for GG

Tau A, where we expect $a \approx 70\,\text{AU}$.

Some observations of misaligned circumbinary disks already exist. Imaging of circumbinary debris disks shows that the disk plane and the orbital plane are misaligned for some systems, such as 99 Herculis, where the mutual inclination is $\Delta i \gtrsim 30°$ (Kennedy et al., 2012). Moreover, the pre-main sequence binary KH 15D is surrounded by a circumbinary disk inclined by $10° - 20°$ with respect to the orbital plane (e.g. Chiang and Murray-Clay, 2004; Lodato and Facchini, 2013), and the FS Tau circumbinary disk appears to be misaligned with the circumstellar disks (Hioki et al., 2011). Finally, evidence of some misalignment between the plane of the disk and the binary orbit has also been found for the HD142527 disk (Casassus et al., 2013).

Finally, another interesting point has recently been raised by Nelson and Marzari (2016): the inclination of the GG Tau A circumbinary disk has been calculated by assuming the disk to be circular. If this assumption is dropped, the disk inclination could be different from the commonly assumed $\sim 143°$.

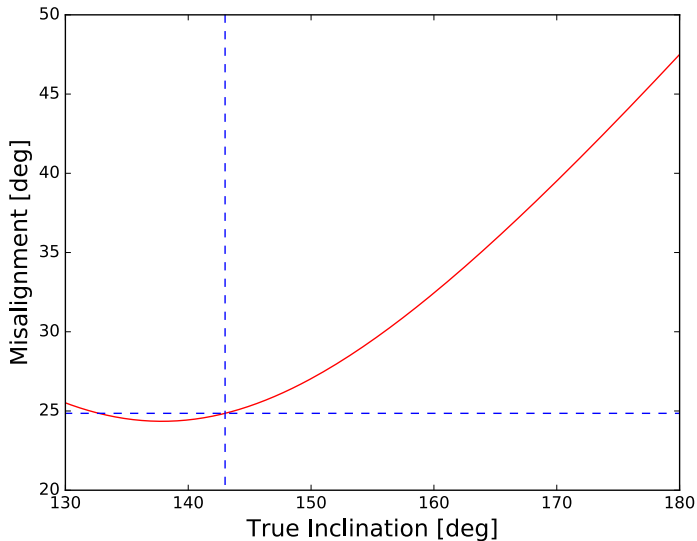**Figure 2.6:** Misalignment Δi between the disk and the binary orbit as a function of the disk inclination (red line) obtained from Eq. 2.6 for the case of GG Tau A by fixing $i_\text{o} = 132.5°$, $\Omega_\text{o} = 131°$ and $\Omega_\text{d} = 277°$. The dashed blue lines mark the values of inclination calculated by assuming the disk to be circular ($i_\text{d} = 143°$) and the relative misalignment ($\Delta i = 24.9°$).

Their conclusion is that it is possible to have an orbit with $a \approx 60\,\mathrm{AU}$ coplanar with the disk. However, it is important to underline that an incorrect estimate of the disk inclination is not enough to avoid misalignment between disk and binary orbit in the $a = 60 - 80\,\mathrm{AU}$ cases. In a 3D space, the angle Δi between orbit and disk depends on the inclinations i_d and i_o of the disk and the orbit with respect to the plane of the sky, and on the position angles of the ascending nodes Ω_d and Ω_o through the relation

$$\cos(\Delta i) = \cos(i_\mathrm{o})\cos(i_\mathrm{d}) + \sin(i_\mathrm{o})\sin(i_\mathrm{d})\cos(\Omega_\mathrm{o} - \Omega_\mathrm{d}). \qquad (2.6)$$

Here Ω_d is well constrained by the gas kinematics (e.g. Tang et al., 2016), is equal to $\sim 277°$ and does not depend on the disk eccentricity. i_o and Ω_o are set by the astrometric measurements and, in the case of $a = 60\,\mathrm{AU}$ in Tab. 2.1, we have $i_\mathrm{o} = 132.5°$ and $\Omega_\mathrm{o} = 131°$. By fixing these three parameters, the value Δi calculated from Eq. 2.6 is a function of the disk inclination alone. If the disk is eccentric, and not circular as usually assumed, then the actual disk inclination is higher than $143°$, and can be as high as $180°$. Fixing i_o, Ω_o, and Ω_d to the above values and varying the value of i_o between $143°$ and $180°$, we obtain the red curve in Fig. 2.6, which clearly shows how some misalignment is always present for all values of i_d and that it is always $> 20°$.

In the future, observations of the proper motion of young binary systems together with high-resolution observations will allow us to better study the dynamical state of these systems. In particular, we expect in the next years to have better constraints on the orbit of GG Tau A and to be able to verify the results of our work. We also expect warps to form as a consequence of the misalignment between binary and disk (e.g. Facchini et al., 2014): future gas emission observations with a high enough signal-to-noise ratio should be able to verify whether or not GG Tau A shows evidence of a warped disk. Some azimuthal asymmetry in GG Tau has already been detected in the gas emission by Dutrey et al., 2014 and Tang et al., 2016.

2.A   Dependence of the final gas density profile on the temperature profile

The temperature profile in Eq. 2.4 is very steep. We therefore also check how the assumed temperature profile affects the steady state gas density profile and the location of the dust trap. For the coplanar case, we compare the density profiles resulting from the hydrodynamical simulations assuming the temperature profile calculated by Guilloteau et al. (1999) ($T \propto R^{-0.9}$) and a less steep and more common $T \propto R^{-0.5}$ profile in the case of $\alpha = 0.01$. The
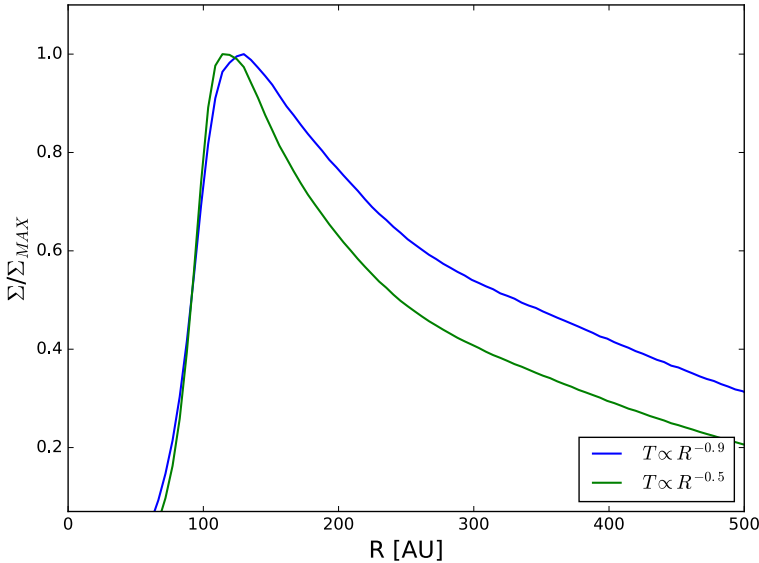
Figure 2.7: Azimuthally and temporally averaged gas radial density profiles, obtained using $\alpha = 0.01$ and two different temperature profiles. As expected, the density profile resulting from the $T \propto R^{-0.5}$ is steeper than the $T \propto R^{-0.9}$ profile, and the density maximum in the first case is even farther away from the observed dust location (~ 200 AU) than in the latter case. Both density profiles are normalized to their maximum values.

two profiles are shown in Fig. 2.7. In particular, we assume the temperature profile

$$T(R) = 20\,\mathrm{K} \left(\frac{\mathrm{R}}{300\,\mathrm{AU}} \right)^{-0.5}, \tag{2.7}$$

where the temperature at 300 AU is fixed to 20 K, as in Guilloteau et al. (1999).

The $T \propto R^{-0.5}$ profile leads to a steeper gas density profile, and the location of the density peak is located at smaller radii with respect to the $T \propto R^{-0.9}$ case. This shows that a less steep temperature profile does not cause an increase in the radius of the ring and that, even under the hypothesis that $T \propto R^{-0.5}$, a misalignment between the plane of the disk and that of the orbit is needed in order to explain the location of the mm-sized dust ring.

3 | Vortices and Spirals in the HD135344B Transition Disk

Abstract

In recent years spiral structures have been seen in scattered light observations and signs of vortices in millimeter images of protoplanetary disks, both probably linked with the presence of planets. We present ALMA Band 7 (335 GHz or 0.89 mm) continuum observations of the transition disk HD135344B at unprecedented spatial resolution of 0.16", using superuniform weighting. The data show that the asymmetric millimeter dust ring seen in previous work actually consists of an inner ring and an outer asymmetric structure. The outer feature is cospatial with the end of one of the spiral arms seen in scattered light, but the feature itself is not consistent with a spiral arm due to its coradiance. We propose a new possible scenario to explain the observed structures at both wavelengths. Hydrodynamical simulations show that a massive planet can generate a primary vortex (which dissipates at longer timescales, becoming an axisymmetric ring) and trigger the formation of a second generation vortex further out. Within this scenario the two spiral arms observed at scattered light originate from a planet at $\sim$30 AU and from the secondary vortex at $\sim$75 AU rather than a planet further out as previously reported.

3.1 Introduction

Protoplanetary disks are the cradles of young planets, where several dynamical processes are likely involved in the planet formation process (e.g. Armitage, 2011). Of particular interest are the transition disks, disks with inner millimeter-dust cavities. In the last decade, observations have revealed that some transition disks are far from axisymmetric: azimuthal asymmetries in the submillimeter continuum are thought to be dust traps, triggered by vortices acting as azimuthal pressure bumps (e.g. van der Marel et al., 2013; Lyra and Lin, 2013; Birnstiel et al., 2013a). On the other hand, near-infrared scattered light observations show large spirals (e.g. Muto et al., 2012; Garufi et al., 2013; Grady et al., 2013; Avenhaus et al., 2014). Both spirals and vortices may indicate the presence of recently formed massive planets: in the case of a vortex through Rossby wave instability (RWI) at the steep edges of the gap that is carved by the planet (Lovelace et al., 1999; de Val-Borro et al., 2007) and in the case of spirals through the trigger of density waves directly by the planet (e.g. Kley and Nelson, 2012).
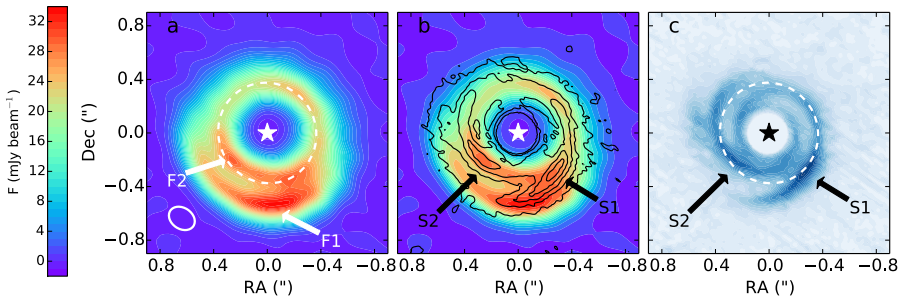
Figure 3.1: a. 335 GHz continuum emission of HD 135344B in superuniform weighting. **b.** Overlay of the PDI image of Garufi et al. (2013) (black contours) on top of the ALMA continuum emission. The spirals as identified by Muto et al. (2012) are labeled as S1 and S2. **c.** PDI image of Garufi et al. (2013) in blue colors. In a and c, the white dashed ellipse indicates the 45 AU radius.

Alternative explanations for spiral arms in disks include RWI at the edge of a dead zone (Lyra et al., 2015), accretion from an envelope (Lesur et al., 2015) and gravitational instability (Lodato and Rice, 2004; Lodato et al., 2005; Rice et al., 2004), although estimated disk masses generally appear to be too low for them to be self-gravitating (Williams and Cieza, 2011).

A natural question is whether there is any relation between the spiral arms

observed in near-infrared scattered light (from the disk surface) and the structures seen in submillimeter emission (from the midplane). Although spiral features in submillimeter emission have been seen in two transition disks (Piétu et al., 2005; Christiaens et al., 2014), they are not entirely consistent with their near infrared counterparts. Juhász et al. (2015), Pohl et al. (2015), and Dong et al. (2015a) demonstrated that spirals generated by planet-disk interaction more likely results from changes in the vertical structure rather than the density structure, which are hard to detect in millimeter emission. On the other hand, spirals that form through gravitational instability can trap dust (Lodato and Rice, 2004; Dipierro et al., 2015a; Dong et al., 2015b), resulting in millimeter continuum spirals.

In this Letter we present Atacama Large Millimeter/submillimeter Array (ALMA) submillimeter continuum observations at very high spatial resolution of HD 135344B [1] (F4 star, $d \sim$140 pc, $\sim$8 Myr (van Boekel et al., 2005; Grady et al., 2009)), a well-studied transition disk at both optical and millimeter wavelengths. The HD 135344B disk contains a $\sim$40 AU radius dust cavity (Brown et al., 2007, 2009; Andrews et al., 2011) with a minor azimuthal asymmetry along the dust ring (Pérez et al., 2014; Pinilla et al., 2015). CO observations and scattered light indicate that gas and small grains are present inside the cavity (Pontoppidan et al., 2008; Lyo et al., 2011; van der Marel et al., 2015b, 2016a; Garufi et al., 2013), consistent with a scenario where a massive planet at $\lesssim$30 AU has cleared its orbit and trapped the large dust further out (Pinilla et al., 2012a). Scattered light imaging reveal two major spiral arms (Muto et al., 2012; Garufi et al., 2013; Stolker et al., 2016), proposed to be linked to planet-disk interaction, with planets located at 55 and 126 AU.

The new images presented in this letter show substructure in the millimeter emission to an unprecedented level, revealing a double structure, which may be responsible for triggering the spiral arms seen in the scattered light. This new interpretation has consequences for the implied location of the putative planets.

3.2   Observations

HD 135344B was observed in ALMA Cycle 1 program 2012.1.00158.S (PI van Dishoeck) in Band 7 ($\sim$335 GHz or 896 μm) in the C32-5 configuration (20-800 m baselines), previously presented in van der Marel et al. (2016a) and Pinilla et al. (2015). The spectral settings and calibration are discussed in van der Marel et al. (2016a). For this work, the continuum emission is re-imaged using

---

[1]also known as SAO 206462

superuniform rather than briggs weighting of the observed visibilities, resulting in a smaller beam size of 0.20×0.16" (Figure 3.1a). In superuniform weighting, the weights of the grid cells in the u, v-plane are set inversely proportional to the sampling density function, minimizing the sidelobes over an arbitrary field size, whereas briggs weighting sets the weights also inversely proportional to the noise variance of each visibility. The peak S/N decreases from 210σ (briggs) to 120σ (superuniform) with σ the rms level (0.25 mJy beam^{-1}). We also make use of archival data of HD135344B obtained in Polarization Differential Imaging (PDI) in the K$_s$ band ($\sim$2.2 micron) (Garufi et al., 2013) with VLT/NACO. The data thus obtained trace the (polarized) scattered light from the disk surface and have angular resolution of 0.09".

Figure 3.1a reveals that the millimeter emission does not originate from a single dust ring with an azimuthal asymmetry, but an outer azimuthal asymmetric feature in the south (labeled F1) and an inner ring-like feature F2. With the current spatial resolution it remains unclear whether they are connected in the south-west. These features are located at 45 and 75 AU radius. The F1 feature is at least 4 times brighter than its opposite side in the north, while the F2 ring is almost azimuthally symmetric, with an azimuthal contrast of at most a factor 1.2. The peak brightness temperature is 20 K, implying that the emission is optically thick even at this wavelength (896 μm).

Figure 3.1b shows the overlay of the PDI image (multiplied by the squared distance to the central star) on top of the ALMA data. The ALMA features appear to follow the spiral structure: F1 is at the end of the spiral S1 (as defined in Muto et al. (2012)) while F2 appears to overlap with S2. The brightest part of the S1 spiral in the west is however not cospatial with the brightest ALMA data points, and as we will show below S1 and F1 are related in a different way.

In the modeling, we use the stellar position $15^h15^m48.^s42$ -37°09'16."36) as derived from the ^{13}CO emission, and for the deprojection a position angle of 62° and an inclination of 16° (van der Marel et al., 2016a).

3.3   Morphology

In order to understand the morphology of the disk, two different models are investigated. Model 1 follows the spiral description derived by Muto et al. (2012). Model 2 consists of an inner symmetric ring and outer azimuthal asymmetry, following the morphology of the image. This double structure has been seen in certain 2D hydrodynamical simulations of planet disk interaction, with a primary vortex at the outer edge of the planetary gap and subsequently, a second vortex external to the primary (Lobo Gomes et al., 2015).
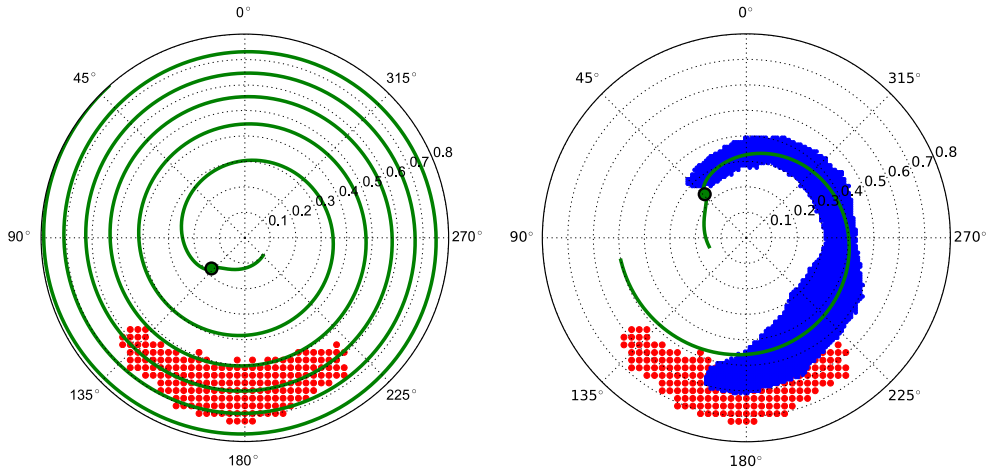
Figure 3.2: Left. Best fit of the ALMA continuum F1 feature (red dots) to the spiral model (green). This fit is unrealistic, as density waves are damped efficiently and the fourth winding would no longer be visible. **Right.** Overlay of the brightest data points of ALMA continuum (red dots) and the S1 feature in the scattered light data (blue dots, Garufi et al. (2013)), both deprojected. The green line shows our best-fit spiral to the blue data points, with $(r_c, \theta_0) = (0.24", 134°)$. This figure shows that F2 does not follow the spiral arm seen in scattered light.

3.3.1   The spiral model

We model the shape of a spiral density wave generated by a planet located at (r_c, θ_0) using the analytical shape derived by Rafikov, 2002. This analytical approach describes the propagation of the wave from a launching point and it is given by

$$
\begin{aligned}
\theta(r) = \theta_0 &- \frac{\mathrm{sgn}(r - r_c)}{h_c} \\
&\times \left[\left(\frac{r}{r_c}\right)^{1+\beta} \left\{ \frac{1}{1+\beta} - \frac{1}{1-\alpha+\beta}\left(\frac{r}{r_c}\right)^{-\alpha} \right\} \right. \\
&\left. - \left(\frac{1}{1+\beta} - \frac{1}{1-\alpha+\beta}\right) \right],
\end{aligned}
\tag{3.1}
$$

where h_c is the disk scale-height at $r = r_c$, disk angular velocity of $\Omega(r) \propto r^{-\alpha}$, and sound speed $c(r) \propto r^{-\beta}$. Equation 3.1 has been used to fit spiral arms observed in scattered light (Muto et al., 2012; Benisty et al., 2015), although

the approximations assumed to derive Eq. 3.1 may fail for massive planets
($\gtrsim 1~M_{\mathrm{Jup}}$, Zhu and Baruteau, 2016). This linear implementation results in 1
spiral for 1 planet, while in the non-linear case, one planet can generate one or
more spirals (Zhu and Baruteau, 2016; Dong et al., 2015a).

For Model 1, we fit Eq. 3.1 to the position of the maxima of F2. For this
purpose we select the pixels of the S1 arm, masking out the inner ring. We
also set $\alpha = 1.5$ (Keplerian rotation), $\beta = 0.45$ (from the temperature profile
in van der Marel et al., 2016a). The value of h_c is not well constrained by any
model of the system, and at the radii of interest it ranges between 0.08 and 0.16
(e.g. Andrews et al., 2011; Carmona et al., 2014; van der Marel et al., 2016a).
Therefore, we fix the scale-height value to the average $h_{\mathrm{c}} = 0.12$, so only two
free parameters remain for the fit: r_{c} and θ_0, which characterize the launching
position of the spiral.
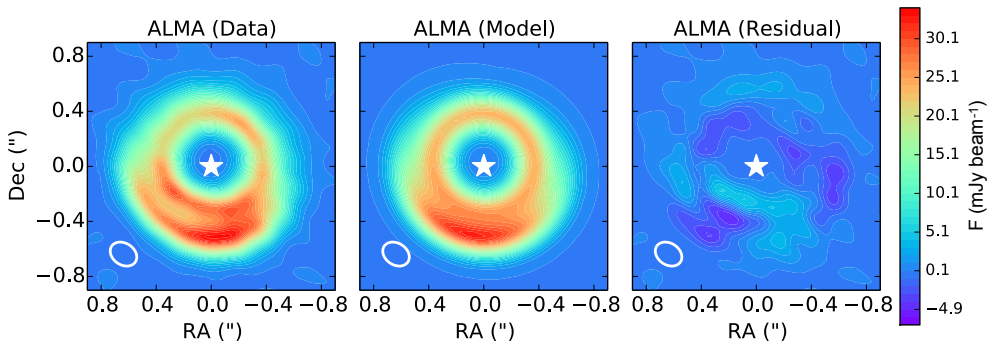
Figure 3.3: The best-fit model for a ring in combination with a vortex (2D Gaussian)
for the ALMA continuum data. Modeling has been performed in the uv plane.

We adopt an Orthogonal Distance Regression fitting procedure, that searches
for the curve that minimizes the sum of the distances to the data points orthog-
onally to the curve itself, thus assuming an observational error on both θ and
r in Equation 3.1. We assume the uncertainty on the positions of the maxima
to be equal to the FWHM of the beam. Finally, each data point is weighted
proportional to the corresponding pixel intensity.

BE The fit in Figure 3.2 (left) shows that the F1 structure is mostly coradial
and hence the spiral launching position has to be very close to the central
star ($r_{\mathrm{c}} < 0.2''$): the spiral pitch angle is close to $0°$. In such a scenario, F1
would be part of the 4th spiral winding. However, the density waves after the
first spiral winding are damped very efficiently due to the disk viscosity and
pressure torque (Baruteau et al., 2014) and therefore this scenario is unrealistic
to explain the observed azimuthal structure. Figure 3.2 (right) shows that the

ALMA continuum does not follow the best fit to the spiral arm in scattered light (blue dots).

3.3.2   The ring plus asymmetry model

Model 2 describes the structure as a combination of a ring (F2) with a azimuthal asymmetry (F1). This model assumes that the asymmetry may originate from a vortex, using the vortex prescription by Lyra and Lin (2013) of a Gaussian in the radial and azimuthal direction:

$$F(r,\theta) = F_{\mathrm{v}} e^{-(r-r_{\mathrm{v}})^2/2\sigma_{\mathrm{r,v}}^2} e^{-(\theta-\theta_{\mathrm{v}})^2/2\sigma_{\theta,\mathrm{v}}^2}, \qquad (3.2)$$

where F_{v} is the flux density at $(r_{\mathrm{v}}, \theta_{\mathrm{v}})$, r_{v} and θ_{v} (East of North) are the radial and azimuthal position of the asymmetry respectively, and $\sigma_{\mathrm{r,v}}$ and $\sigma_{\theta,\mathrm{v}}$ are the radial and azimuthal width of the asymmetry. F2, on the other hand, is modeled as a gaussian ring,

$$F(r,\theta) = F_{\mathrm{r}} e^{-(r-r_{\mathrm{r}})^2/2\sigma_{\mathrm{r,r}}^2}, \qquad (3.3)$$

where F_{r} is the flux density at r_{r}, and where r_{r} and $\sigma_{\mathrm{r,r}}$ are the radial position and width of the ring respectively.

Our model has therefore 8 free parameters (5 for the asymmetry and 3 for the ring model), and we fit it to the image using the MCMC python package `emcee`. The chains from the fit show good convergence for all the free parameters, and the best fit parameters are:

F_{v}	$1.44 \pm 1.6 \times 10^{-3}$ mJy/pixel
r_{v}	80.7 ± 0.005 AU ($0.58'' \pm 3.3'' \times 10^{-5}$)
$\sigma_{\mathrm{r,v}}$	6.3 ± 0.008 AU ($0.045'' \pm 5.7'' \times 10^{-5}$)
θ_{v}	$172° \pm 0.02°$
$\sigma_{\theta,\mathrm{v}}$	$57° \pm 0.02°$
F_{r}	$0.96 \pm 6.1 \times 10^{-4}$ mJy/pixel
r_{r}	51.3 ± 0.004 AU ($0.37'' \pm 2.8'' \times 10^{-5}$)
$\sigma_{\mathrm{r,r}}$	8.1 ± 0.007 AU ($0.058'' \pm 4.8'' \times 10^{-5}$)

The errors from the MCMC calculations are much smaller than the spatial uncertainty from the observations, which is typically $\sim 10\%$ of the beam size (i.e. 2-3 AU). Figure 3.3 shows the comparison between the convolved model and the observations. The best fit was simulated onto the observed visibilities, and no significant differences were found with the convolved image. Some residuals are still present, mostly due to the asymmetry in the inner ring, but
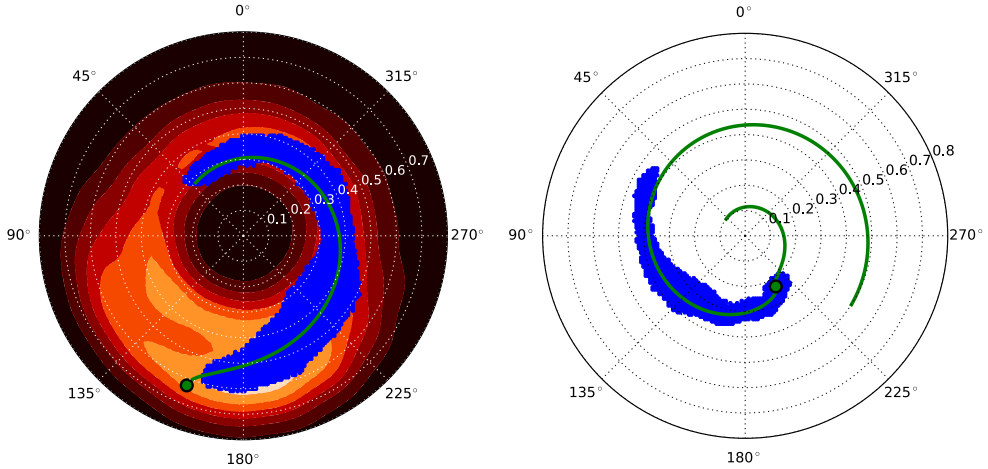
Figure 3.4: Left. Best fit for the S1 spiral in the scattered light data (deprojected), with a starting point inside the vortex. Overlaid on the ALMA image (colors), the blue dots indicate the data points of the PDI S1 feature with the central ring masked out, and the green line the best-fit spiral, with launching point $(r_c, \theta_0) = (0.62'', 170°)$ marked as a circle. **Right.** Best fit for the S2 spiral, with a starting point in the inner part of the disk. The blue dots are the brightest points of the PDI S2 feature and the green line the best-fit spiral, with launching point $(r_c, \theta_0) = (0.23'', 211°)$ marked as a circle.

at the 10% level of the original flux. The radius of the vortex is at a larger radius than found by earlier fitting of the millimeter data (Pérez et al., 2014; Pinilla et al., 2015), which could be due to their central position being 11 AU away from this study.

3.4   Discussion and conclusions

The F1 feature is not consistent with the spiral arm prescription, but it can be described as a ring (~ 50 AU) with an asymmetry at ~ 80 AU. Therefore we propose a new alternative scenario for this disk to explain the structure of both millimeter and scattered light data. The millimeter geometry is consistent with a model from Lobo Gomes et al., 2015, showing that a planet generates a pressure bump at 50 AU (F2), which triggers a second generation vortex at 80 AU (F1). The cavity radius of the gas and small grains (Garufi et al., 2013; van der Marel et al., 2016a) suggests the presence of a massive planet at 30 AU. A millimeter dust ring at 50 AU (F2) is consistent with this scenario, as the dust is trapped further out than the gas gap edge (Pinilla et al., 2012a).

1. A planet is formed at 30 AU

2a. Inner dust trap
due to planet gap

F2

S2

2b. Planet triggers spiral
arm outwards

F1   S1

4. Vortex triggers second
spiral arm inwards

3. Secondary vortex dust trap
triggered by inner ring
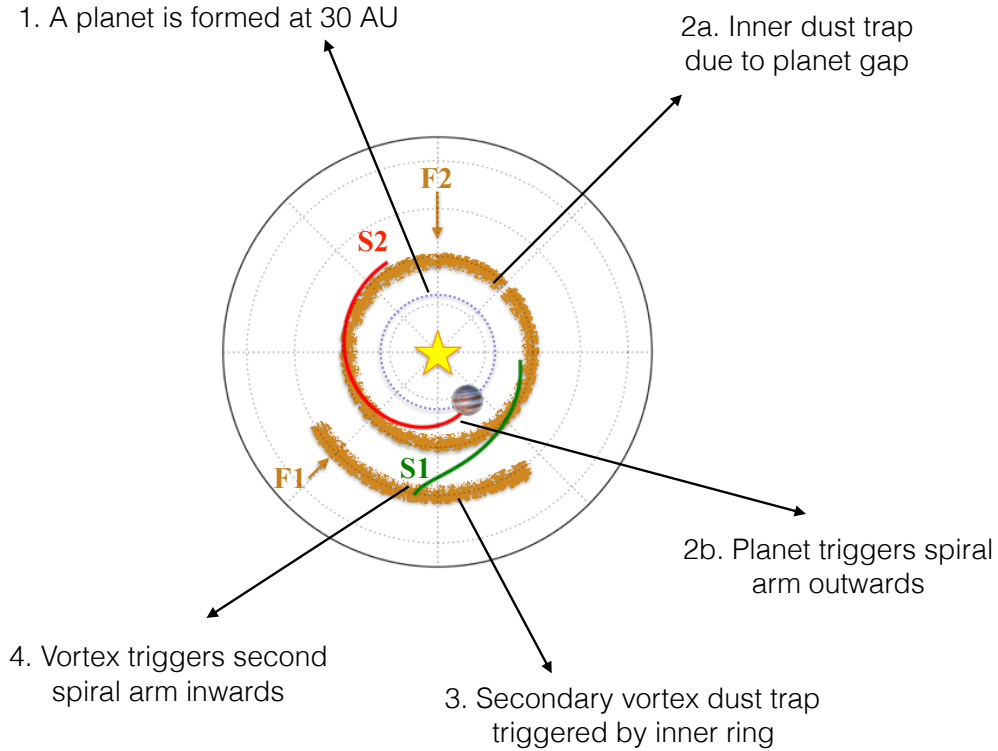
Figure 3.5: Cartoon explaining the proposed scenario.

The ALMA and PDI data trace different grain size populations and disk heights, possibly driven by different mechanisms. However, it is striking that F1 coincides with the edge of the S1 arm. We propose that the S1 is triggered by a vortex that has created the dust asymmetry F1, since vortices can be massive enough to launch their own density waves in a disk when self-gravity is included in hydrodynamical models (e.g. Baruteau and Zhu, 2016). Only a lower limit to the mass of the F1 feature can be set as the emission is partially optically thick: with a total flux of $\sim$200 mJy and a ISM gas-to-dust ratio of 100, the total mass is >16 M_{Jup} (using $M_{\mathrm{gas}} = 0.08 * F_\nu (d/140\mathrm{pc})^2$ M_{Jup} Cieza et al., 2008). The outer extent of S1 (outside the vortex) remains undetectable in the PDI image due to the lower brightness in the outer disk.

Muto et al. (2012) find a best-fit for the launching point of S1 at r_c=0.39" (55 AU) at θ_0=204°, but with a large confidence interval (see Figure 5 in Muto et al.). Fitting the S1 spiral with an initial guess close to the center of the vortex results in the fit in Figure 3.4a with $r_c, \theta_0 = 0.6'', 180°$ (84 AU) and

$h_c = 0.08$. This launching point does not coincide exactly with the center of F1, although there is a large uncertainty due to the unknown scale height at this location. Furthermore, ALMA continuum observations trace the mm-dust, whose center may not coincide with the gas vortex (Baruteau and Zhu, 2016), and the vortex can be a large scale structure where the center of mass may not be well represented by a single location, contrary to a planet.

On the other hand, the S2 spiral was best-fit by Muto et al. (2012) for $r_c, \theta_0 = 0.9"$ (126 AU), 353°, but we find that it can also be fit with a launching point in the inner part of the disk for $r_c, \theta_0 = 0.23"$ (32 AU), 211° (Figure 3.4b). The launching point of S2 would be a massive planet, just inside the gas cavity radius (van der Marel et al., 2016a). Stolker et al. (2016) finds a best fit for the S2 launching point to the VLT/SPHERE data slightly further in, at $r_c, \theta_0 = 0.15"$ (21 AU), 247°.

We propose that the combination of the scattered light and the millimeter observations is consistent with the following sequence of events (see Figure 3.5):

1. A massive planet is formed at ∼30 AU radius.

2. The planet triggers a spiral density wave outwards (PDI S2 feature).

3. The planet clears its orbit in the gas (CO observations) and creates a radial pressure bump at its edge where millimeter-dust gets trapped (ALMA continuum F2 feature).

4. The pressure bump creates an effective α viscosity that is large enough to induce accretion, depleting the gas and inducing a second pressure bump further out. The second pressure bump triggers RWI, forms a vortex and traps the millimeter-dust asymmetrically (ALMA continuum F1 feature).

5. The outer vortex triggers a spiral density wave inwards (PDI S1 feature).

This scenario can potentially explain both PDI and millimeter observations. Hydrodynamical models of gas and dust, including self-gravity, are required to check whether our proposed scenario can instead quantitatively explain the observed structures of HD135344B.

One of the major uncertainties in the scenario are the fits to the locations of the launching points. The reason is that the scattered light data are mainly sensitive to changes in the scale height and therefore, the observed scattered light is significantly affected by geometric parameters. The observed spirals form only the illuminated inner part of a surface change. Also, the inner disk region may shadow the outer part and thus alter the intrinsic disk scale height

distribution. In particular, the azimuthal angle of the continuum ALMA feature coincides with the brighter part of the closer-in S2 spiral and therefore, S2 may be casting a shadow on part of S1, affecting the fit of the launching points.

Another caveat is the symmetry of the two spiral arms at the time of observation, suggesting a common nature such as proposed by Dong et al. (2015a) who demonstrates the trigger of two symmetric spiral arms by a single planet at 100 AU. As this planet has remained undetected, this scenario cannot be confirmed. On the other hand, if there are instead two launching points (32 and 86 AU), the two spirals would have distinct angular velocities and their symmetric appearance is fortuitous, making the scenario less probable. The orbital period of the 32 AU point is only 143 years, implying a $2.5°$/year angular shift. Repeating the scattered light observations in 5 years should clearly reveal the motion of this arm. If the asymmetry is indeed related to a vortex, an azimuthal shift of $\sim 0.1"$ ($6°$) in the millimeter continuum (measurable at 0.2" resolution) is detectable after 10 years.

The scenario is an example of triggered planet formation, where the formation of a first planet can induce dust growth and potentially further planet formation in the outer disk.

4 | Evidence for a massive dust-trapping vortex connected to spirals. Multi-wavelength analysis of the HD 135344B protoplanetary disk

Abstract

Context. Spiral arms, rings and large scale asymmetries are structures observed in high resolution observations of protoplanetary disks, and it appears that some of the disks showing spiral arms in scattered light also show asymmetries in millimeter-sized dust. HD 135344B is one of these disks. Planets are invoked as the origin of these structures, but no planet has been observed so far and upper limits are becoming more stringent with time.

Aims. We want to investigate the nature of the asymmetric structure in the HD 135344B disk in order to understand the origin of the spirals and of the asymmetry seen in this disk. Ultimately, we aim at understanding whether or not one or more planets are needed to explain such structures.

Methods. We present new ALMA sub-0.1″ resolution observations at optically thin wavelengths ($\lambda = 2.8$ mm and 1.9 mm) of the HD 135344B disk. The high spatial resolution allows us to unambiguously characterize the mm-dust morphology of the disk. The low optical depth of continuum emission probes the bulk of the dust content of the vortex. Moreover, we combine the new observations with archival data at shorter wavelengths to perform a multi-wavelength analysis and to obtain information about the dust distribution and properties inside the observed asymmetry.

Results. We resolve the asymmetric disk into a symmetric ring + asymmetric crescent, and observe that: (1) the spectral index strongly decreases at the center of the vortex, consistent with the presence of large grains; (2) for the first time, an azimuthal shift of the peak of the vortex with wavelength is observed; (3) the azimuthal width of the vortex decreases at longer wavelengths, as expected for dust traps. These features allow to confirm the nature of the asymmetry as a vortex. Finally, under the assumption of optically thin emission, a lower limit to the total mass of the vortex is $0.3 M_{\mathrm{Jupiter}}$. Considering the uncertainties involved in this estimate, it is possible that the actual mass of the vortex is higher and possibly within the required values ($\sim 4\,\mathrm{M_{Jupiter}}$) to launch spiral arms similar to those observed in scattered light. If this is the case, no outer planet is needed to explain the morphology.

4.1 Introduction

In recent years, as higher angular resolution observations of protoplanetary disks are routinely performed, it is becoming apparent that almost every single disk hosts some structures. Rings (e.g. Andrews et al., 2016; Isella et al., 2016; Fedele et al., 2018), cavities and large-scale asymmetries (e.g. Casassus et al., 2013; van der Marel et al., 2013) and spirals (e.g. Benisty et al., 2015, 2017; Pérez et al., 2016; Follette et al., 2017; Stolker et al., 2016; Stolker et al., 2017; Dong et al., 2018) are being observed at mm-wavelength continuum emission with ALMA and in scattered light in the near-infrared (NIR) with VLT/SPHERE (Beuzit et al., 2008) and Gemini/GPI (Macintosh et al., 2008).

Rings and azimuthal asymmetries are often interpreted as dust traps, i.e. local pressure maxima where dust grains marginally coupled to the gas remain trapped (Weidenschilling, 1977). Such traps have critical implications in planet formation, since they allow dust particles to grow to large sizes and eventually to form planetesimals by preventing them from rapidly drifting into the central star (Klahr and Henning, 1997; Johansen et al., 2007; Pinilla et al., 2012b,a).

Planets are invoked as a potential origin for pressure bumps, and can also explain the observed spiral arms as these are the result of an exchange of angular momentum between the planet and the material in the disk (e.g. Dong et al., 2015a; Fung and Dong, 2015; Bae et al., 2016; Dong and Fung, 2017). Symmetric, ring-shaped dust traps are expected to form when a planet is massive enough (e.g. Dipierro et al., 2015b; Rosotti et al., 2016). The edges of these gaps can then become unstable against Rossby wave instability (RWI, Lovelace et al., 1999; Li et al., 2000, 2001) giving rise to vortices, i.e., high-pressure regions that can trap dust azimuthally and form crescent-shaped dust asymmetries such as those observed at mm-wavelength (e.g. Lyra et al., 2009; Lin, 2012) . The number of planets and their location are, however, degenerate, and the same system can often be explained by more than one scenario. Moreover, the lack of directly imaged planets and the increasingly strong upper limits on their mass (e.g. Maire et al., 2017, $M_{\mathrm{planet}} < 4\,\mathrm{M_{Jupiter}}$ at $r \geq 0.6''$ in HD 135344B) are challenging our understanding of the origin of such structures[1].

The wealth of information provided by observations at different wavelengths can now help us to break some of the degeneracies in the interpretation of the observed morphologies. In particular, to understand the role of planets in sculpting the disk morphology and vice versa, to understand the role of

---

[1]These upper limits are calculated assuming a hot start scenario; in the case of a cold start the upper limits could be substantially higher.

structures in the planet formation process, it is now timely to look for a common explanation for the different morphologies observed for grains of different sizes.

In this context, HD 135344B, also known as SAO 206462, is a particularly interesting object. Located at a distance of 135 ± 1.4 pc (Gaia Collaboration et al., 2016; Lindegren et al., 2018; Luri et al., 2018; Gaia Collaboration et al., 2018a), it is a transition disk with an inner mm-dust cavity of ~ 40 au (Brown et al., 2007, 2009; Andrews et al., 2011). In addition, the presence of a deep ^{13}CO and $C^{18}O$ gas cavity whose size is smaller than that of the dust (van der Marel et al., 2016a) suggests that the inner cavity observed in the dust could have been carved by a large inner planet at a radius $\lesssim 30$ au from the central star (as also suggested by e.g. Lyo et al., 2011).

At the same time, this system shows two bright, symmetric spiral arms in scattered light (Muto et al., 2012; Garufi et al., 2013; Stolker et al., 2016; Stolker et al., 2017) extending out to ~ 75 au, that can be explained either by two planets at 55 and 126 au (Stolker et al., 2016) or by a single, massive planet outside the dust cavity at ~ 100 au (Fung and Dong, 2015; Bae et al., 2016; Dong and Fung, 2017). However, no planet has yet been observed. Using $0.2''$ resolution data, van der Marel et al. (2016b) noted that the mm emission could be due to an inner symmetric ring and an outer vortex, rather than a single asymmetric ring. They proposed that the vortex may be triggering one of the observed spiral arms, while the massive inner planet, also carving the dust cavity, may be launching the second arm. No planet other than the inner one would therefore be required in this explanation.

Structures similar to those in HD 135344B, i.e. rings and asymmetries in the mm continuum and spirals arms in scattered light, have subsequently been observed in V1247 Ori (Kraus et al., 2017) and MWC 758 (Boehler et al., 2017; Dong et al., 2018), strengthening the idea of a connection between the asymmetries observed in the (sub-)mm continuum emission and spiral arms in scattered light.

The origin of the structures observed in HD 135344B is however still ambiguous, both because of the limited spatial resolution of the available data and because azimuthal asymmetries can in principle be due to mechanisms different than vortices (e.g. disk eccentricity, as in Ataiee et al., 2013; Ragusa et al., 2017) which cannot launch spiral density waves.

Spiral arms can also be explained by other mechanisms not involving an external perturber. Symmetrical spiral arms resembling the scattered light morphology of the HD 135344B disk can in principle arise from gravitational instability (GI, e.g. Dipierro et al., 2015b; Dong et al., 2015b), although for this specific system the total disk mass does not seem to be high enough for GI
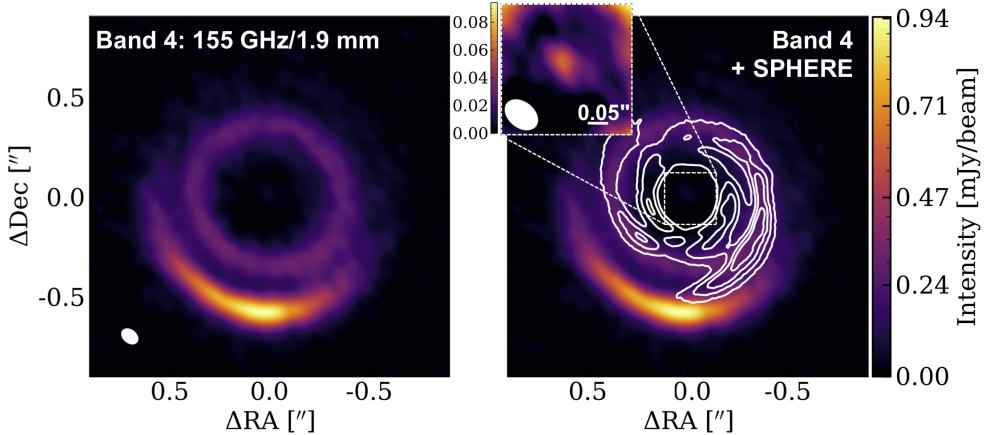
Figure 4.1: *Left*: ALMA Band 4 observations of HD 135344B at 1.9 mm. The panel in the upper right corner shows a zoom into the inner regions, with a colormap enhancing the emission from the central point-source. *Right*: same image with the contours of the spiral arms observed with SPHERE (Stolker et al., 2017) overlaid in white. Note that the spiral starts near the vortex position. The white ellipse in the bottom left corner of the left panel shows the beam size.

to arise. Shadows have also been proposed to trigger spiral arms (Montesinos et al., 2016), and have been observed in the disk around HD 135344B. Such shadows, however, change on a much faster time-scale than the spirals.

In this work, we present new high-resolution Cycle 4 and Cycle 5 ALMA observations of the HD 135344B disk at 1.9 mm and 2.8 mm, which allows us to test the different scenarios. We reach a much higher resolution of $0.08''$. The dust emission is expected to be optically thin at these long wavelengths, and the bulk of the dust mass inside the observed structures can be determined. These new observations, combined with archival observations at 0.87 mm and 0.43 mm for the same object, allow us to carry on a detailed multi-wavelength analysis.

In Sec. 6.3, the observations and the data reduction process are discussed. In Sec. 6.4, we present the observed morphology and the approach used to fit the data. In Sec. 4.4, we use the data to obtain information on the dust and gas content of the vortex and to test theoretical predictions on vortices. Finally, in Sec. 6.5, we use our new data and results to discuss the origin of the morphology observed in HD 135344B and its role in planet formation.
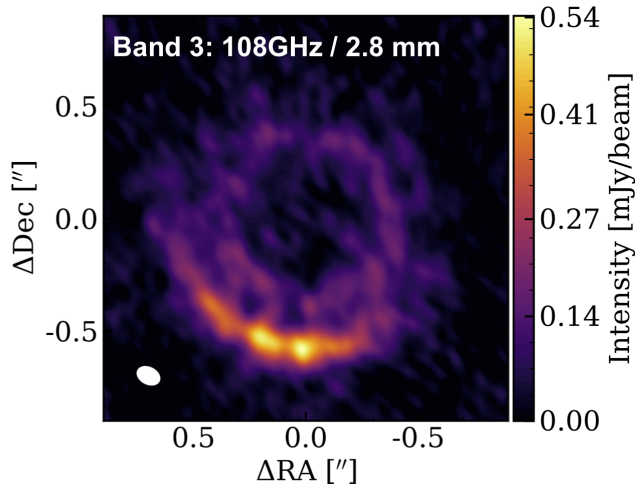
Figure 4.2: Band 3 observations of HD 135344B at 2.8 mm. The white ellipse in the bottom left corner shows the beam size.

4.2   Observations and data reduction

The new ALMA data of the disk around HD 135344B presented in this paper are part of three different projects. The Band 4 data have been observed in C40-8 configuration during ALMA Cycle 4 in two execution blocks on September 14th, 2017 and September 28th, 2017 as part of program 2016.1.00340.S (PI: Cazzoletti) for a total of ~ 45 min with 41 and 42 antennas. Additional Band 4 observations were carried out during Cycle 5 in C43-5 configuration, on January 17th, 2018 as part of the DDT program 2017.A.00025.S (PI: Cazzoletti) in order to recover the short uv-spacings, for a total of ~ 22 min on source and using 44 antennas. The Band 3 data were observed in Cycle 5 in the C43-8 configuration on November 11th, 2017 (2017.1.00884.S, PI: Pinilla) for ~ 24 min using 44 antennas, and in the C43-5 configuration on January 17th, 2018 (as part of the DDT proposal 2017.A.00025.S) for ~ 11 min on source and 46 antennas.

   The spectral setups of the Band 4 and 3 observations are as follows. In order to maximize continuum sensitivity, the Band 4 observations have 4 spectral windows each, with a bandwidth of 1875 MHz (channel width ~ 2 MHz, corresponding to $\sim 3.6\,\mathrm{km\,s^{-1}}$), with rest frequencies at 161.987722, 159.997750, 149.997890 and 147.997918 GHz. The spectral setup of the Band 3 observations also have 4 spectral windows in total. Two of them are centered on the ^{13}CO(1-0) and C^{18}O(1-0) transitions with rest frequencies at 110.201354 and 109.782176 GHz, and a bandwidth of 937.5 MHz (resolution of 488 kHz) and
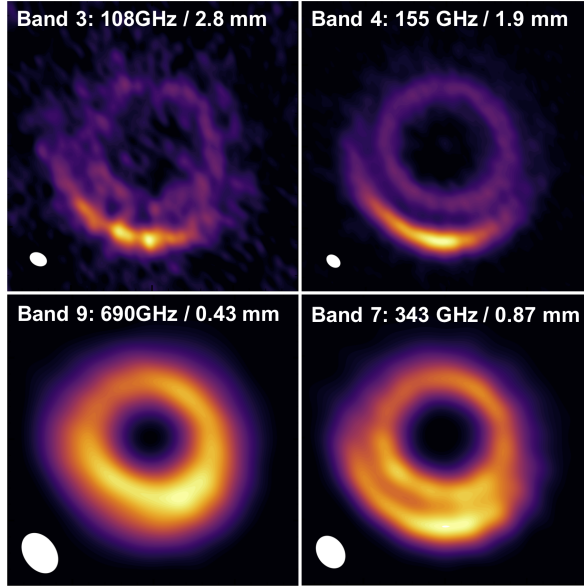
Figure 4.3: Observations of HD 135344B at different wavelengths. The white circle has a radius of 0.6″. The white ellipses show the beam size of each observation.

234.38 MHz (resolution of 122 kHz) respectively. The other two windows are dedicated to the continuum, and are both centered at 108 GHz. In one of them the correlator is set to Time Division Mode (128 channels, 31.25 MHz resolution and 1875 MHz total bandwidth), while in the other one it is set to Frequency Division Mode (3840 channels, 488 kHz resolution, 937.5 MHz total bandwidth). In all executions, J1427-4206 was used as bandpass, pointing and absolute flux calibrator, and J1457-3539 was used as phase calibrator.

The archival observations are from ALMA Cycle 0 program 2011.0.00724.S (P.I. Pérez) and Cycle 1 program 2012.1.00158.S (P.I. van Dishoeck), taken in Band 9 (690 GHz) and Band 7 (343 GHz), respectively. The details of the calibration are described in Pérez et al. (2014) and van der Marel et al. (2016a).

Data were then processed and calibrated through the ALMA calibration pipeline in the Common Astronomy Software Applications (CASA 5.1.1, McMullin et al., 2007). The high signal-to-noise allows self-calibration of the Band 4 data (both amplitude and phase) after standard phase referencing. The visibilities were then Fourier inverted and deconvolved using the `TCLEAN` task in `CASA`, and imaged using Briggs weighting with a Robust parameter of 0.5. The synthetized beam size achieved are $0.09″ \times 0.063″$ (Band 4 data) and $0.1″ \times 0.073″$ (Band 3 data). Note that the analysis carried out in this work was

performed in the uv-plane only, and is therefore not affected by the cleaning process. The achieved sensitivity in Band 3 and Band 4 is $25.3\,\mu$Jy beam^{-1} and $10.9\,\mu$Jy beam^{-1}, respectively. The corresponding peak signal-to-noise is 21 in the Band 3 data, and 86 in Band 4.

4.3   Results

4.3.1   ALMA images

The Band 3 (108 GHz, $\lambda = 2.8$ mm) and Band 4 (155 GHz, $\lambda = 1.9$ mm) observations of the HD 135344B disk, imaged as described above, are presented in Fig. 4.1 and 4.2. The dusty component of the HD 135344B disk consists of a symmetric inner ring and an outer azimuthally asymmetric, crescent-shaped structure, potentially due to a vortex. The ring and the crescent are separated by a gap. The Band 4 data also show a "bridge" at the west end of the crescent, connecting it to the inner ring. Interestingly, the bridge emission is located exactly where the spiral arm seen in scattered light crosses the gap between the ring and the crescent (see also Fig. 4.1), although it could also just be due to the synthesized beam elongation.
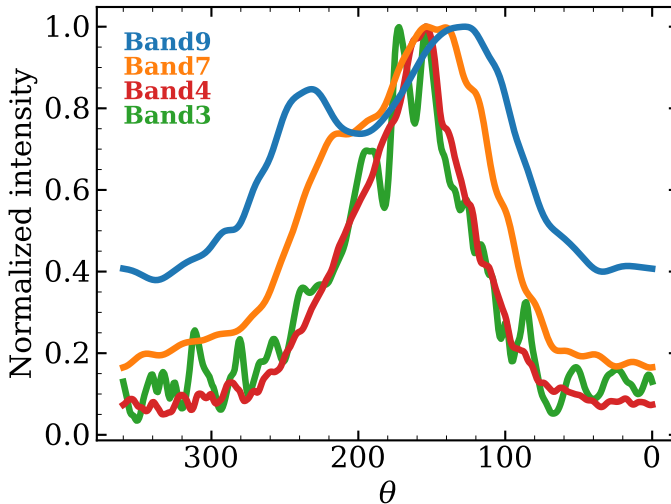
Figure 4.4: Normalized intensities at different wavelengths as a function of the azimuth, measured along the asymmetry (i.e. at radius $r = 0.6''$) after deprojecting the data. Note that the intensity peak shifts monotonically to smaller values of θ as the wavelength increases.
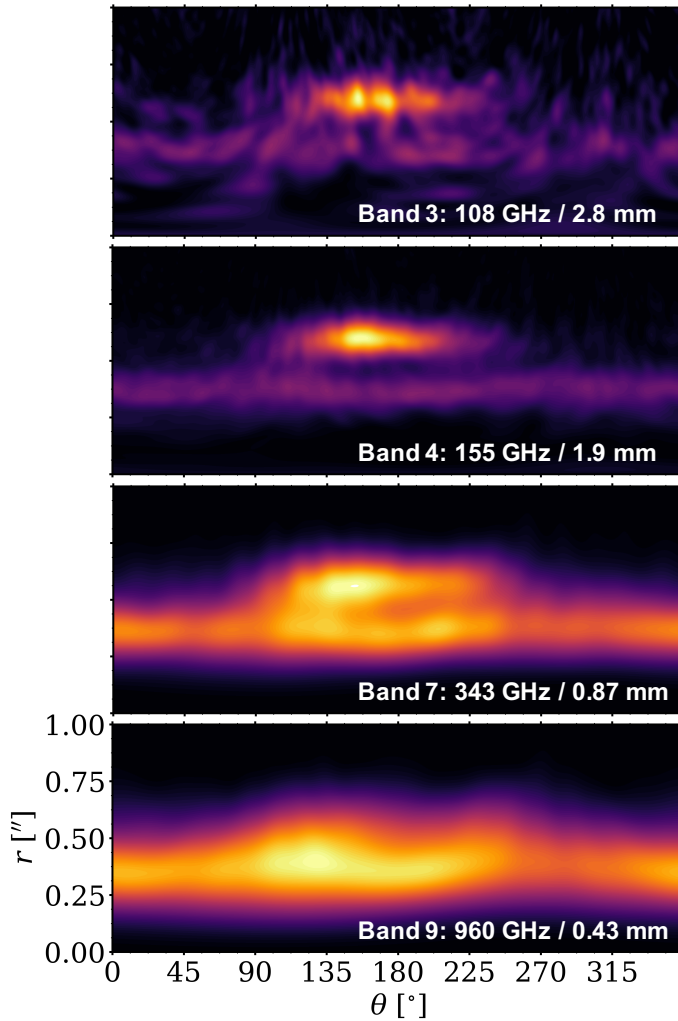
Figure 4.5: Observations of HD 135344B at different wavelengths in polar coordinates. The data have been deprojected using $PA = 62°$ and the inclinations in Table 4.1. Note the displacement of the peak of the vortex emission between the different wavelengths; also note that the ring has eccentricity very close to zero.

Although the images have different spatial resolution, a visual comparison between the Band 3 and Band 4 observations at $0.08''$ with the archival Band 7 and Band 9 at $0.2''$ shows some clear differences (Figs. 4.3 and 4.5). First, the relative contrast between the flux of the asymmetry and that of the ring increases with increasing wavelengths, showing that the two components have different spectral indices and perhaps even different dust populations. Second, the images suggest that the emission peak of the crescent is located at different azimuthal locations in the different data sets, and moves toward the east at longer wavelengths, as also highlighted by the azimuthal cuts in Fig. 4.4.

The high signal-to-noise Band 4 observations also allow for a $\sim 5\,\sigma$ detection of a central unresolved source, either due to a small inner circumstellar disk surrounding the star or to free–free/synchrotron emission from ionized gas in the proximity of the star (see right panel in Fig. 4.1), which appears to be at the center of the dust ring. The presence of a small inner disk is consistent with the large near infrared excess (Garufi et al., 2017) due to the presence of hot dust in the innermost regions, and with the shadows observed in scattered light by Stolker et al. (2017). No significant central emission is visible in the Band 3 observations because of the lower signal-to-noise, nor at shorter wavelengths due to the beam dilution (see end of Sec. 4.4.1).

4.3.2 Model fit in the uv-plane

To quantitatively constrain the large scale structures in the HD 135344B disk we fit the surface brightness in the uv-plane with a simple analytical model similar to that adopted by Pérez et al. (2014), Pinilla et al. (2015) and van der Marel et al. (2016b). The inner ring is fitted with an azimuthally symmetric Gaussian in the radial direction, centered at a radius r_R and with $\sigma = \sigma_\mathrm{R}$:

$$F_1(r, \theta) = F_\mathrm{R} e^{-(r - r_\mathrm{R})^2 / 2\sigma_\mathrm{R}^2}, \tag{4.1}$$

where F_R is the peak surface brightness. The outer asymmetric crescent is modelled as a double Gaussian in both the radial and azimuthal direction, based on the vortex prescription by Lyra and Lin (2013), radially centered at r_V, with a radial width $\sigma_{\mathrm{V},\mathrm{r}}$, and azimuthally peaking at θ_V. As for the azimuthal width, both preliminary tests and visual inspection of our Band 4 data show that the surface brightness of the system is better represented by an azimuthally asymmetric Gaussian rather than a symmetric one. We therefore allow our model to have two different widths $\sigma_{\mathrm{V},\theta 1}$ and $\sigma_{\mathrm{V},\theta 2}$ east and west of
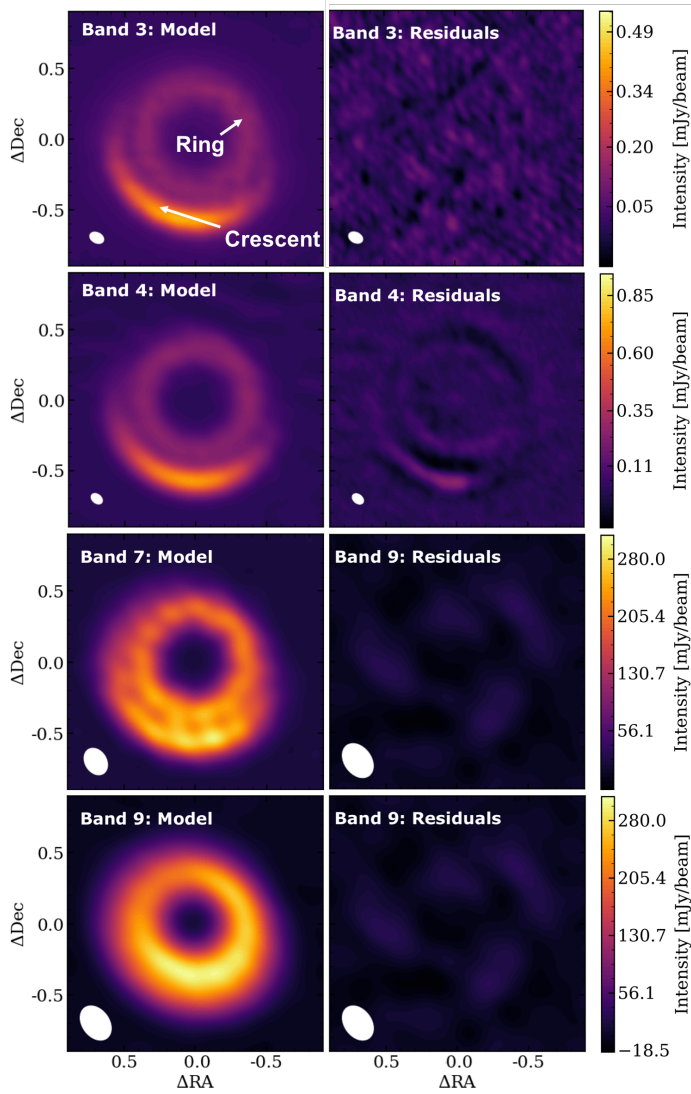
Figure 4.6: Models derived from the MCMC using the parameters in Tab. 4.1, and relative residuals for the four data sets available for HD 135344B. The color scale is the same for the models and the residuals. The white ellipses show the synthesized beam sizes.

Table 4.1: Parameters estimated from the marginalized likelihood distribution. The value is estimated as the median. The upper and lower uncertainty represent the extent to the 16th and 84th percentile, respectively.

		Band 3	Band 4	Band 7	Band 9
		108 GHz	155 GHz	343 GHz	690 GHz
Ring					
$\log F_{\rm R}$	[Jy/sr]	$8.71^{+0.03}_{-0.03}$	$9.229^{+0.004}_{-0.004}$	$10.621^{+0.002}_{-0.002}$	$11.464^{+0.005}_{-0.004}$
$r_{\rm R}$	["]	$0.381^{+0.006}_{-0.007}$	$0.3752^{+0.0009}_{-0.0009}$	$0.3686^{+0.0003}_{-0.0003}$	$0.354^{+0.001}_{-0.001}$
$\sigma_{\rm R}$	["]	$0.097^{+0.009}_{-0.008}$	$0.0858^{+0.0009}_{-0.0011}$	$0.0623^{+0.0004}_{-0.0004}$	$0.070^{+0.001}_{-0.001}$
Crescent					
$\log F_{\rm V}$	[Jy/sr]	$9.36^{+0.02}_{-0.02}$	$9.758^{+0.003}_{-0.003}$	$10.747^{+0.002}_{-0.002}$	$11.306^{+0.006}_{-0.007}$
$r_{\rm V}$	["]	$0.603^{+0.009}_{-0.009}$	$0.587^{+0.002}_{-0.001}$	$0.5783^{+0.0003}_{-0.0003}$	$0.544^{+0.002}_{-0.002}$
$\sigma_{\rm r,V}$	["]	$0.058^{+0.003}_{-0.003}$	$0.0545^{+0.0005}_{-0.0005}$	$0.0626^{+0.0004}_{-0.0004}$	$0.085^{+0.001}_{-0.001}$
$\theta_{\rm V}$	["]	$162.1^{+2.5}_{-2.3}$	$153.6^{+0.4}_{-0.4}$	$137.4^{+0.1}_{-0.1}$	$113.9^{+1.1}_{-1.0}$
$\sigma_{\theta 1,\rm V}$	["]	$34.9^{+2.2}_{-1.9}$	$33.8^{+0.4}_{-0.4}$	$34.6^{+0.2}_{-0.2}$	$41.7^{+0.9}_{-0.8}$
$\sigma_{\theta 2,\rm V}$	["]	$40.9^{+2.8}_{-2.6}$	$47.8^{+0.4}_{-0.4}$	$77.0^{+0.3}_{-0.2}$	$109.6^{+1.9}_{-1.8}$
i	[°]	$17.7^{+3.4}_{-4.7}$	$11.9^{+0.8}_{-0.7}$	$9.8^{+0.1}_{-0.1}$	$11.6^{+0.8}_{-0.8}$
x_c		$15{:}15{:}48.417^{+0.006}_{-0.006}{''}$	$15{:}15{:}48.417^{+0.001}_{-0.001}{''}$	$15{:}15{:}48.419^{+0.0003}_{-0.0003}{''}$	$15{:}15{:}48.423^{+0.0007}_{-0.0007}{''}$
y_c		$-37.09.16.433^{+0.007}_{-0.008}{''}$	$-37.09.16.453^{+0.001}_{-0.001}{''}$	$-37.09.16.346^{+0.0003}_{-0.0003}{''}$	$-37.09.16.333^{+0.0007}_{-0.0007}{''}$

the center of the asymmetry, respectively. Our adopted model is therefore:

$$F_2(r,\theta) = \begin{cases} F_{\mathrm{V}}e^{-(r-r_{\mathrm{V}})^2/2\sigma_{\mathrm{V,r}}^2}e^{-(\theta-\theta_{\mathrm{V}})^2/2\sigma_{\mathrm{V},\theta 1}^2} & \theta \le \theta_{\mathrm{V}} \\ F_{\mathrm{V}}e^{-(r-r_{\mathrm{V}})^2/2\sigma_{\mathrm{V,r}}^2}e^{-(\theta-\theta_{\mathrm{V}})^2/2\sigma_{\mathrm{V},\theta 2}^2} & \theta > \theta_{\mathrm{V}} \end{cases}$$

F_{V} is the peak surface brightness of the asymmetry at location $(r_{\mathrm{V}}, \theta_{\mathrm{V}})$. The final model $F(r,\theta) = F_1(r,\theta) + F_2(r,\theta)$ uses 9 parameters.

The parameters are then found by Fourier-transforming the analytical model, by sampling it at the same uv-locations as the observations using the code GALARIO (Tazzari et al., 2018), and by then fitting them to the observed visibilities with the Markov-chain-Monte Carlo (MCMC) code emcee (Foreman-Mackey et al., 2013). The center of the ring $(x_{\mathrm{c}}, y_{\mathrm{c}})$ and the inclination i are also left as 3 additional free parameters, while the position angle PA, defined east-of-north, is fixed to 62°, the value found by van der Marel et al. (2016a) from the CO isotopologues moment 1 maps. The Band 3 and Band 4 data, as well as the archival Band 7 and Band 9 data sets, are fitted independently with the model described above. In the MCMC, 120 walkers were used and the parameters were extracted using 24000 likelihoods.

The derived parameters at each wavelength are presented in Table 4.1. The model shows good agreement with the data at all wavelengths, with the inner ring located at 0.38″ (~ 50 au) radius and the crescent at 0.6″ (~ 80 au) from the central star.

Fig. 4.6 shows the synthesised images of the obtained models and relative residuals, derived with the same imaging parameters (mask, weighting and number of iterations) as the data. The data are generally very well fit, and residuals of at most 25% at the peak are found only in the Band 4 data set. These are due to the finest resolved structures that cannot be well represented by a simple double Gaussian as that used to model the crescent.

A comparison between the real and imaginary part of the visibilites of the data and the models are shown in Appendix 4.A.

4.4   Analysis

4.4.1   Dust mass

Under the assumption of optically thin emission it is possible to convert the observed flux into dust mass. In particular, the flux density measured in the crescent is 8.6 mJy at 108 GHz, and 20.2 mJy at 155 GHz. The dust mass is then calculated as

$$M_{\mathrm{dust}} = \frac{F_\nu d^2}{\kappa_\nu B_\nu(T_{\mathrm{dust}})}, \tag{4.2}$$

where the distance $d = 136\,\mathrm{pc}$, the dust temperature T_{dust} at the location of the asymmetry (i.e. ~ 80 au) is assumed to be 15 K, as modelled by van der Marel et al. (2016a) using radiative transfer to fit the spectral energy distribution, and the dust grain opacity κ_ν is taken as $10\,\mathrm{cm}^2\mathrm{g}^{-1}$ at 1000 GHz and scaled to the observed frequencies using an opacity power-law index $\beta = 1$ (Beckwith et al., 1990). The calculated dust masses are $44\,\mathrm{M}_\oplus$ and $52\,\mathrm{M}_\oplus$ in Band 4 and Band 3, respectively.

These numbers should be regarded as lower limits. First, mm-wavelength observations are insensitive to the emission from very large pebbles (cm-size and larger) which, if present, may be hiding part of the mass. Moreover, the dust densities reached at such high dust masses can make even mm-wavelength emission partially optically thick. An estimate of the optical thickness can be obtained from the brightness temperature T_{bright}. The calculated peak brightness temperatures are 7 K in Band 3 and 8 K in Band 4. The relation between brightness temperature and physical temperature T_{dust} is $T_{\mathrm{bright}} = T_{\mathrm{dust}}(1 - \exp(-\tau_\nu))$, which when inverted (using again $T_{\mathrm{dust}} = 15$ K) gives an optical thickness τ_ν of $\sim 0.5 - 0.6$ at 108 and 155 GHz. We conclude that the emission can only be considered marginally optically thin, and that the dust mass of the asymmetry is likely higher than $50\,\mathrm{M}_\oplus$. The crescent remains only marginally optically thin even assuming T_{dust} higher by a factor of 1.5, with $\tau_\nu \sim 0.4$.

The inferred dust surface density at the peak of the asymmetry, derived from the relation $\tau_\nu = \Sigma_{\mathrm{dust}}\kappa_\nu$ for $\tau_\nu = 0.6$, and using the same value of κ_ν as above, is of the order of $\sim 1\,\mathrm{g\,cm}^{-2}$.

The total flux densities in Band 3 and Band 4 are $\sim 20.0\,\mathrm{mJy}$ and $\sim 42.7\,\mathrm{mJy}$, respectively. The dust masses corresponding to these flux densities, calculated using Eq. 4.2 and assuming $T_{\mathrm{dust}} = 15\,\mathrm{K}$, are $\sim 90\,\mathrm{M}_\oplus$ in Band 4 and $\sim 120\,\mathrm{M}_\oplus$ in Band 3. About half of the dust is therefore concentrated inside the asymmetry.

The unresolved emission at the star location, seen in Band 4, has a flux density of $\sim 85\,\mu\mathrm{Jy}$, i.e., assuming it is due to a small inner disk, its dust mass is $\sim 0.1\,\mathrm{M}_\oplus$. The expected flux density in Band 7 can be calculated with $F_{343\,\mathrm{GHz}} = F_{155\,\mathrm{GHz}} \times (343/155)^2$ (assuming Rayleigh-Jeans, optically thick emission) which gives $F_{343\,\mathrm{GHz}} = 416\,\mu\mathrm{Jy}$, which is well below 3σ at the Band 7 rms level. The inner ring is therefore not observable in the current shorter wavelength observations.
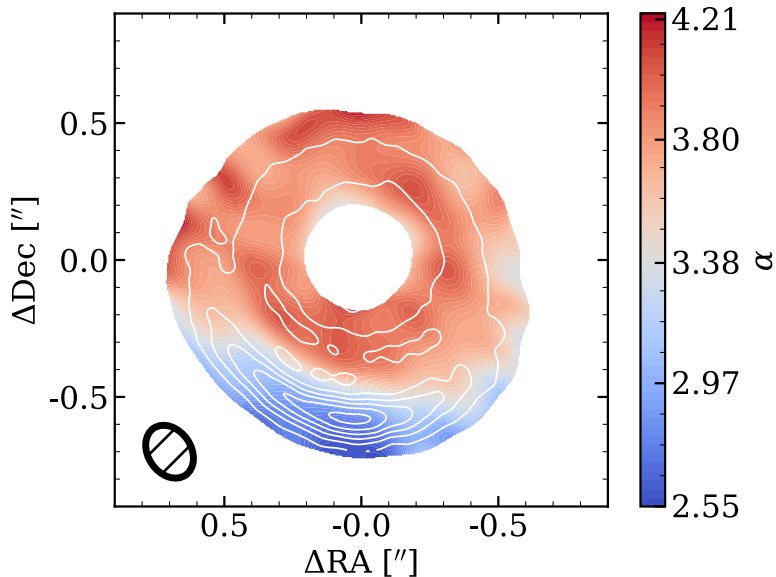
Figure 4.7: Map of the spectral index in HD 135344B, calculated between the Band 4 and the Band 7 data. A clear azimuthal variation in the value of α can be seen, consistent with the presence of large grains trapped inside a vortex. The typical uncertainty is ± 0.3. White contours show the Band 4 intensity profile at $0.08''$ resolution to highlight the location of the crescent. The ellipse shows the beam size of the Band 4 and Band 7 maps.

4.4.2 Spectral index distribution

In a particle trap, dust rapidly reaches larger sizes and grain growth can be measured through the spectral index of the dust opacity β. In the Rayleigh-Jeans regime, the spectral index α of the spectral energy distribution $F_\nu \propto \nu^\alpha$ at mm-wavelengths can be related to β, that can be interpreted in terms of grain size when the dust continuum emission is optically thin (e.g. Draine, 2006; Testi et al., 2014). Values of α with $2 < \alpha < 3$ hint at the presence of large, cm-sized grains and hence dust growth. In the case of an azimuthal trap, clear spatial variations of the inferred grain size along the azimuthal direction are expected, with the smallest values near the center of the vortex. Therefore, spatial variations of α should be detected. In this section we calculate the spatial distribution of α in the HD 135344B disk.

The spectral index is calculated between Band 4 and Band 7: the choice of these two wavelengths turned out to be the best trade-off between large enough wavelength leverage, high signal-to-noise, and enough spatial resolution to con-
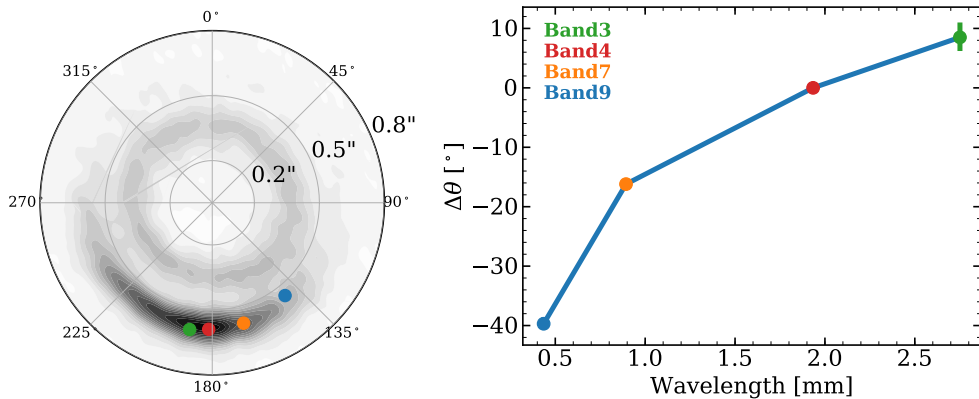
Figure 4.8: *Left*: Location of the peak of the emission at different wavelengths as obtained from the fit. The grey contours show the Band 4 data. *Right*: azimuthal shift of the emission peak at different wavelengths, calculated with respect to the position of the Band 4 emission peak. There is a shift of more than 30° between the Band 3 and Band 9 emission. The uncertainty on the peak location in Band 4, Band 7 and Band 9 is smaller than the size of the dot.

fidently calculate the value of α. uv-tapering is applied to the Band 4 data set, in order to obtain the same synthesized beam as that of Band 7. Finally, the spectral index α is calculated as $\alpha = \ln(F_{155\,\mathrm{GHz}}/F_{335\,\mathrm{GHz}})/\ln(155\,\mathrm{GHz}/335\,\mathrm{GHz})$, after re-centering the images on the best-fit center obtained in section 4.3.2. The value of α is calculated using only those pixels with a signal-to-noise greater than 20 in both bands. The uncertainty is therefore dominated by the $\pm 5\%$ and $\pm 10\%$ calibration uncertainties in Band 4 and Band 7 respectively, translating in a ± 0.15 uncertainty on the absolute value of α. The obtained map is shown in Fig. 4.7.

As expected, there is a clear azimuthal variation in the value of α, with α decreasing to values below 3 inside the crescent. This is consistent with the presence of large dust grains, and therefore with dust growth, but can also be due to high optical thickness, or to a combination of both effects. Interestingly, the symmetric ring appears to be both optically thin and devoid of large grains, with $\beta = 1.8 \pm 0.3$ consistent with interstellar medium (ISM) grains. The measured variation across the map is not affected by the absolute calibration uncertainty.

4.4.3   Peak shift

The fit of the brightness profile allows to quantitatively compare the morphology of the emission inside the crescent at different wavelengths. In particular, as shown in Fig. 4.8, we observe that at longer wavelengths the fitted peak of the crescent emission is azimuthally shifted towards the east, as already qualitatively seen in Fig. 4.4. Keplerian rotation can immediately be ruled-out as the cause of such a shift, as the gas-kinematics combined with the scattered light (which allows to identify the close and far sides of the disk) show that the rotation is in the opposite direction. Assuming that the emission at longer wavelengths is dominated by larger grains, and in particular that grain size $\sim 3 \times \lambda$ (Draine, 2006), we observe a shift of $\sim 50°$ between the 1.5 mm grains (traced in Band 9) and 9 mm grains (traced in Band 3).

A different distribution between small and large dust grains has been predicted by Mittal and Chiang (2015) and Baruteau and Zhu (2016) in vortices, and is an effect due to the vortex gas self-gravity. However, the direction of the shift is just the opposite in these models, which always predict a shift ahead of the vortex rather than behind as in the case of the HD 135344B disk. Baruteau and Zhu (2016), in particular, show that, whereas smaller grains are trapped close to the center of the gas vortex, larger grains can get trapped ahead of it. The amount of shift between the large and small grains depends on the coupling between the gas and the dust, parametrized with the Stokes number St defined as

$$\mathrm{St} = \frac{\pi}{2} \frac{s\rho_{\mathrm{pc}}}{\Sigma_{\mathrm{gas}}} \approx 0.015 \times \left(\frac{s}{1\,\mathrm{mm}} \right) \left(\frac{\rho_{\mathrm{pc}}}{1\,\mathrm{g\,cm^{-3}}} \right) \left(\frac{10\,\mathrm{g\,cm^{-2}}}{\Sigma_{\mathrm{gas}}} \right), \qquad (4.3)$$

where s is the radius of the dust grains, ρ_{pc} is their internal density, Σ_{gas} is the gas surface density. In practice, particles with $\mathrm{St} >> 1$ are decoupled from the gas, while those with $\mathrm{St} << 1$ are well coupled. Trapping usually occurs when $\mathrm{St} \lesssim 1$.

An azimuthal shift as large as that observed, between grains which are only a factor of a few different in size, means that the observed mm-sized grains are neither strongly coupled nor very decoupled from the gas, and that their Stokes number must be close to unity. Assuming a typical value of $\rho_{\mathrm{pc}} = 1\,\mathrm{g\,cm^{-3}}$, we can therefore invert Eq. 4.3 and obtain an estimate of the gas surface density at the vortex location of $\Sigma_{\mathrm{gas}} \approx 1\,\mathrm{g\,cm^{-2}}$. This gas surface density is consistent with that obtained by van der Marel et al. (2016a) by modelling the emission from $^{13}\mathrm{CO}$ and $\mathrm{C^{18}O}$. The absolute value of the displacement observed in our data is consistent also with the simulations by Baruteau and Zhu (2016) and indeed corresponds to grains with $\mathrm{St} \sim 1$. However, the fact that their models

cannot reproduce the direction of the shift observed in HD 135344B indicates that more simulations exploring a larger parameter space or studying different dynamical effects are still needed.

Even though the derivation of the local gas surface density has large uncertainties in both the Stokes number method and for the CO isotopologue one, it can be combined with the estimate of Σ_{dust} based on the optical thickness of our Band 4 data to get a qualitative estimate of the gas-to-dust ratio. We find that the gas-to-dust ratio inside the asymmetry is close to unity, i.e. significantly lower than 100, the value generally assumed for interstellar clouds. Given the large uncertainties involved in our calculations, our estimate is in line with the gas-to-dust ratio of 10 commonly found in simulations of dust traps (e.g. Miranda et al., 2017; Sierra et al., 2017). It should be noted that when the gas-to-dust ratio approaches 1, dust feedback becomes relevant and can even cause dynamical instabilities potentially destroying the vortex (Fu et al., 2014). The simulations by Baruteau and Zhu (2016) do not include dust feedback.

4.4.4   Azimuthal dust trapping

Simulations of dust dynamics and evolution in vortices also predict a different azimuthal concentration for differently sized grains (Birnstiel et al., 2013b). In particular, one of the key predictions in dust traps is that smaller grains with lower Stokes number, traced at shorter wavelengths, tend to be less concentrated than larger grains observed at longer wavelengths. This behaviour is expected only when dust-trapping is responsible for the observed crescent-shaped structure, while it is not present when the asymmetry is due to other mechanisms such as disk eccentricity. So far, this effect has been observed for the vortex in the Oph IRS 48 disk (van der Marel et al., 2015a), for the HD 142527 disk (Casassus et al., 2015), and the MWC 758 disk (Marino et al., 2015; Casassus et al., 2019).

We define the total width of the asymmetry as $\sigma_{\theta 1,\mathrm{V}} + \sigma_{\theta 2,\mathrm{V}}$. Using the values obtained for the models at all wavelengths (Tab. 4.1), the azimuthal width is found to monotonically decrease with wavelength, as shown in Fig. 4.9, consistent with the theoretical expectation for dust-trapping.

4.5   Discussion

In Section 4.4 different theoretical predictions for dust traps were tested, leading to the identification of the crescent-shaped structure in the HD 135344B disk as a vortex, trapping mm-sized dust grains. Dust-trapping vortices such as that observed in the HD 135344B disk can form at the edges of a gap carved by a
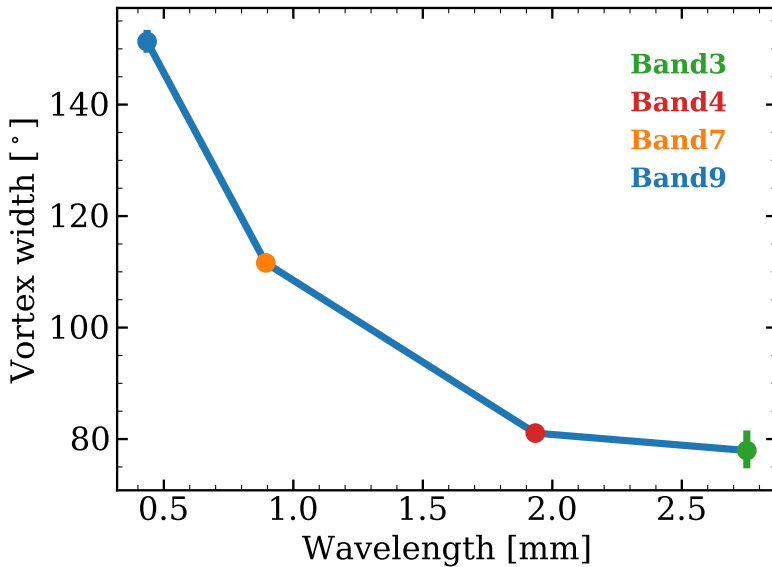
Figure 4.9: Azimuthal width of the crescent as a function of wavelength. Larger particles are more azimuthally concentrated than small particles, that are more coupled to the gas. The error bars in Band 4 and Band 7 are smaller than the size of the dots.

giant planet (Koller et al., 2003; de Val-Borro et al., 2007) or at the edges of dead zones (e.g. Inaba and Barge, 2006; Lyra and Mac Low, 2012; Flock et al., 2015). In the case of the HD 135344B disk, however, the vortex is not located at the edge of a cavity, but beyond a ring, and may be connected to the spiral arms seen in scattered light. Looking for a consistent explanation for all of the observed substructures can give important information about the number and location of planets potentially embedded in the disk. In particular, are planets needed to explain the observed structures, and which role do the ring and the vortex play in the formation of new planetesimals and planets? On the one hand, the distribution of gas and dust at radii between 0 and 40 au shows that the inner dust cavity is probably due to a planet (van der Marel et al., 2016a), but on the other hand the substructures beyond 40 au are more complex and require a more detailed discussion.

4.5.1 Spirals launched by a planet

The most common explanation for symmetrical spiral arms is an external, massive planet triggering density waves. Fung and Dong (2015) and Dong and Fung (2017) calculate that a $5 - 10\,M_{\rm J}$ at $r = 0.7''$ would indeed be able to excite spi-

ral pressure waves with the shape and the contrast similar to the scattered-light spirals observed in the HD 135344B disk. VLT/SPHERE observations, however, rule out planets with mass $> 4\,M_{\text{Jupiter}}$ at $r \geq 0.6''$ (Maire et al., 2017), making this scenario unlikely. These upper limits, though, become higher if cold start formation models are used instead of the hot start ones adopted by Maire et al. (2017). Moreover, the radial location of the planet is not well constrained by Fung and Dong (2015) and Dong and Fung (2017) and a planet with similar mass, but located at $r \approx 0.5''$ is still consistent with VLT/SPHERE upper limits even in the hot start scenario. A $5\,M_{\text{J}}$ planet located at $r \approx 0.5''$, i.e., in between the ring and the crescent, could at the same time launch the spiral arms, trigger the vortex asymmetry and carve the gap between the ring and the vortex, explaining all the features at once. In this context, Hammer et al. (2019) also show that a slowly accreting protoplanet can indeed trigger azimuthally asymmetric vortices, such as that observed here which appears to have two different azimuthal widths ($\sigma_{\theta 1,\text{V}}$ and $\sigma_{\theta 2,\text{V}}$ in our model).

However, this scenario presents some weaknesses. First, as shown in the right panel of Fig. 4.1, the western spiral arm extends further out than the orbit of the planet in this scenario, i.e. $r = 0.5''$. Assuming an external perturber, the launching point of the spiral would therefore not be consistent with the location of the planet. Second, since both the planet and the vortex rotate around the central star at their local Keplerian velocity, their azimuthal locations are not necessarily the same. The fact that the tip of the western spiral is so close to the vortex center seems therefore to favour a connection between the spirals and the vortex (see Sec. 4.5.2).

In addition, by using the relation between gap width and radial location described in Rosotti et al. (2016) and Facchini et al. (2018), it is possible to calculate the mass of the planet carving the observed gap. Assuming a gap with width of $\sim 20\,$au (i.e., $(r_{\text{V}} - r_{\text{R}})/2$, Tab 4.1), located at $\sim 68\,$au from the central star (i.e., $(r_{\text{V}} + r_{\text{R}})/2$, Tab 4.1), and a standard viscosity parameter $\alpha = 10^{-3}$ (Shakura and Sunyaev, 1973a), the derived mass for the gap-carving planet is only $\sim 0.2\,M_{\text{Jupiter}}$. This inferred mass is much lower than that required to launch the spiral arms, even though it should be noted that the relation by Rosotti et al. (2016) and Facchini et al. (2018) was derived for axisymmetric gaps, rather than gaps between a ring and a vortex as in our case.

4.5.2 Spirals launched by the vortex

A second possible explanation is that the vortex is massive enough to excite its own spiral density waves. This scenario is theoretically motivated(e.g. Paardekooper et al., 2010; Zhu and Baruteau, 2016), and Fig. 4.1 indeed shows

that the tip of the western, brightest spiral arm is consistent with a launching point close to the Band 4 vortex center. As opposed to planets that can be regarded as point-like, however, vortices are extended sources. No quantitative comparison between models where spirals are launched by vortices or planets has yet been made, and we will here assume that the mass of the spiral-driving-vortex is comparable to that calculated in the case of an external planet. Using $M_{\rm dust,vortex} \approx 50 M_{\oplus}$, as calculated in Section 4.4.1, and assuming the gas-to-dust ratio of 1 calculated in section 4.4.3, gives a total vortex mass of at least $0.3 M_{\rm Jupiter}$, which is much lower than that required to launch two symmetrical spiral arms as those observed.

Given the high uncertainties involved in the calculations of the gas surface density, it is possible to speculate that the gas-to-dust ratio is different than that estimated, and even higher by a factor of 10. Assuming a value of 10 (typical for dust-trapping vortices, e.g. Miranda et al., 2017; Sierra et al., 2017), the total mass for the vortex is $M_{\rm vortex} \approx 1.7 M_{\rm Jupiter}$. Although still a factor of 3 lower than the mass calculated by Fung and Dong (2015) and Dong and Fung (2017), one should note that the dust mass calculated in section 4.4.1 is only a lower limit (the dust emission in the vortex is only marginally optically thin, even at these long wavelengths), and that the uncertainties involved in the calculations of the dust mass (especially in the dust opacity κ_{ν}) can easily justify the additional missing factor of 3. Moreover, our results also show that dust is trapped and is possibly growing inside the vortex: if planetesimal formation is occurring, a large fraction of the dust mass of the vortex could already be hidden into larger bodies, not contributing to the observed millimeter emission.

If the vortex is not triggered by a planet, the dust morphology observed in the mm-continuum has to be explained by different scenarios. The ring could be what remains of a first generation vortex at the edge of the inner cavity, now decayed into a ring (e.g. Fuente et al., 2017; Pierens and Lin, 2018), that triggered Rossby wave instability developing in a second generation vortex at larger radii (Lobo Gomes et al., 2015), which is seen in the current observations. Only one planet carving the inner cavity and triggering the first generation vortex would then be required. This scenario is similar to was proposed by van der Marel et al. (2016b), with the difference that in the interpretation proposed here both spiral arms, and not only the western one, are due to the vortex.

Finally, Miranda et al. (2017) have shown that the presence of a ring alongside a vortex is typical when the vortex is generated at the edge of a dead-zone. They also show that dead-zone-generated vortices can overcome the effect of dust feedback, which would tend to destroy the vortex when the gas-to-dust ratio is low. However, in their results the ring is located outside of the vortex

(see their Fig. 6 and 7), in contrast with our observations.

4.6   Summary and conclusions

We present new observations of the HD 135344B transition disk at 155 GHz (ALMA Band 4, 1.9 mm) and 108 GHz (ALMA Band 3, 2.8 mm) and with beam sizes of $0.09'' \times 0.063''$ (12×9 au) and $0.1'' \times 0.073''$ (14×10 au), respectively. The high signal-to-noise millimeter continuum maps show a very symmetric inner ring and an asymmetric outer crescent-shaped structure, indicative of a vortex, separated by a narrow gap. This is consistent with the model proposed by van der Marel et al. (2016b) to explain 343 GHz (ALMA Band 7) observations of the same object. The higher signal-to-noise achieved in the Band 4 data also allows us to detect emission from a point source located at the center of the ring, either due to a small circumstellar disk or to free-free emission from hot ionized gas close to the central star.

The Band 3 and Band 4 data have been fitted in the *uv*-plane with a model consisting of an inner Gaussian ring in the radial direction, and an outer double Gaussian both in the radial and azimuthal direction. The same analysis was repeated for archival Band 7 and Band 9 data of the same system. This allows us to quantitatively study the variations in morphology at different wavelengths, and to interpret them in terms of the hydrodynamic response of different grain sizes. Our main conclusions are:

1. All the four data sets at different wavelengths are well represented by the same model, consisting of a symmetric ring+asymmetric, co-radial crescent.

2. A clear azimuthal variation of the spectal index α (Fig. 4.7) is found, with the lowest values approaching $\alpha = 2$ inside the crescent. This could be due to the fact that the crescent is only marginally optically thin, but is consistent with the presence of large, cm-sized grains (Testi et al., 2014). Future optically thin observations will be needed to disentangle the two effects.

3. A monotonic azimuthal shift in the peak of the emission at different wavelengths is observed for the first time (Fig. 4.8), which cannot be due to Keplerian rotation (opposite direction). Assuming that the emission at longer wavelengths is dominated by larger grains, this shift could mean that the crescent is due to a vortex, and that grains of different size are trapped at different distances from the center of the vortex. A shift of

the same magnitude between large and small grains in vortices was indeed predicted by Baruteau and Zhu (2016), although in the opposite direction. This indicates that some additional dynamical effect still needs to be studied or that relevant regions of parameter space have yet to be explored.

4. The emission at longer wavelengths, tracing larger grains, is more azimuthally concentrated than the emission at shorter wavelengths, tracing smaller grains that are more coupled to the gas. This is a key prediction of dust trapping models and simulations (Birnstiel et al., 2013b).

5. The results summarized above are strong evidence for identifying the crescent-shaped structure of HD 135344B as a vortex. Massive enough vortices can act like planets and trigger spiral density waves. We propose that the vortex is the origin of the spiral density waves observed in scattered light.

6. A planet of $5\,\mathrm{M_{Jupiter}}$ located outside the crescent can produce spiral arms with the shape and contrast of those seen in the HD 135344B disk (Fung and Dong, 2015; Dong et al., 2015a). The mass of the vortex, inferred from the dust emission and assuming a gas-to-dust ratio of 10 is $M_{\mathrm{Vortex}} = 1.7\,\mathrm{M_{Jupiter}}$. This value could however be even higher, since the dust emission is only marginally optically thin. A low gas-to-dust ratio 10 or less is consistent with our estimates and with hydrodynamical simulations of gas and dust in vortices (Sierra et al., 2017; Miranda et al., 2017).

7. Our calculations estimate that about half of the dust mass of HD 135344B is trapped in the vortex. Hence, the vortex is a very favourable spot for planetesimal formation. Planetesimals may already have formed inside the vortex, and could be contributing to its dust mass without showing any emission at mm wavelengths.

Future high resolution observations at shorter wavelengths and optically thin observations at longer ones, together with hydrodynamical modelling to study the proposed scenarios will be crucial to strengthen our interpretation, to confirm the nature of the HD 135344B system and to understand the connection between vortices in the mm and spiral arms in scattered light. Gas observations at higher spatial and spectral resolution will also be critical to constrain the gas content and its kinematics inside the vortex.

4.A   Fit results

Here we report the results of the fits for the four different data sets. For each data set we show a triangle plot, showing the MCMC results and the marginalized posteriors for each parameter and the deprojected real and imaginary part of the models (red lines) obtained with the parameters in Tab. 4.1 compared to the data (black dots). For Band 3 and Band 4, only the inner $1000 \, k\lambda$ are shown.

Figure 4.10: Fit results for the Band 3 data set.

Figure 4.11: Fit results for the Band 4 data set.

Figure 4.12: Fit results for the Band 7 data set.

Figure 4.13: Fit results for the Band 9 data set.

5 | CN rings in full protoplanetary disks around young stars as probes of disk structure

Abstract

Context. Bright ring-like structure emission of the CN molecule has been observed in protoplanetary disks. We investigate whether such structures are due to the morphology of the disk itself or if they are instead an intrinsic feature of CN emission. With the intention of using CN as a diagnostic, we also address to which physical and chemical parameters CN is most sensitive.

Aims. A set of disk models were run for different stellar spectra, masses, and physical structures via the 2D thermochemical code DALI. An updated chemical network that accounts for the most relevant CN reactions was adopted.

Methods. Ring-shaped emission is found to be a common feature of all adopted models; the highest abundance is found in the upper outer regions of the disk, and the column density peaks at 30-100 AU for T Tauri stars with standard accretion rates. Higher mass disks generally show brighter CN. Higher UV fields, such as those appropriate for T Tauri stars with high accretion rates or for Herbig Ae stars or for higher disk flaring, generally result in brighter and larger rings. These trends are due to the main formation paths of CN, which all start with vibrationally excited H_2^* molecules, that are produced through far ultraviolet (FUV) pumping of H_2. The model results compare well with observed disk-integrated CN fluxes and the observed location of the CN ring for the TW Hya disk.

Results. CN rings are produced naturally in protoplanetary disks and do not require a specific underlying disk structure such as a dust cavity or gap. The strong link between FUV flux and CN emission can provide critical information regarding the vertical structure of the disk and the distribution of dust grains which affects the UV penetration, and could help to break some degeneracies in the SED fitting. In contrast with C_2H or c-C_3H_2, the CN flux is not very sensitive to carbon and oxygen depletion.

5.1 Introduction

Rotating disks of dust and gas around young stars are the cradles of planets, but detailed studies of these objects have only been possible in the last few years since the advent of the Atacama Large Millimeter/submillimeter Array (ALMA). The resolution and sensitivity of the data in the pre-ALMA era only allowed a handful of disks to be characterized, most of the time only in dust (Williams and Cieza, 2011; Andrews, 2015). The ALMA radio telescope now opens up the possibility to survey hundreds of disks and spatially resolve these disks in gas and dust (Ansdell et al., 2016, 2017; Barenfeld et al., 2016; Pascucci et al., 2016).

One particularly intriguing feature of the new images are the ring-like structures observed in dust (Muto et al., 2012; Andrews et al., 2016; Isella et al., 2016) and gas (Bruderer et al., 2014; Kastner et al., 2015; Öberg et al., 2015; Bergin et al., 2016). In some cases, such as the so-called transitional disks (TDs) with inner cavities, a depletion of material in the central regions of the disk can lead to ring-shaped structures for both solids and gaseous molecules (e.g., van der Marel et al., 2016a). However, it is apparent that gas and dust can have different distributions and that molecular rings can be due to peculiar physical and chemical conditions rather than to the morphological structure of the disk. In this sense, the morphological structure of the disk and intensity of molecular line emission can provide a wealth of information that cannot be obtained by dust emission alone.

In this scenario, CN is a particularly interesting molecule. One of the brightest molecules after ^{12}CO, with fluxes comparable to those of ^{13}CO, CN has been observed and studied in disks both with single-dish observations (e.g. Thi et al., 2004; Kastner et al., 2008; Salter et al., 2011; Kastner et al., 2014) and interferometric data (e.g., Dutrey et al., 1997; Muto et al., 2012; Öberg et al., 2011; Chapillon et al., 2012; Guilloteau et al., 2014; Teague et al., 2016; van Terwisga et al., 2019). Although none of the pre-ALMA era data had enough spatial resolution to give information about the morphology of CN emission, CN has been used as a dynamical mass tracer (Guilloteau et al., 2014).

CN emission is expected to be sensitive to UV radiation, since its formation relies on the existence of atomic C and N or can result from photodissociation of HCN. Modelling of CN in photodissociation regions (PDRs) (e.g. Jansen et al., 1995; Sternberg and Dalgarno, 1995; Walsh et al., 2010) and disks (e.g. van Zadelhoff et al., 2003) has been performed and confirms this expectation, placing CN in the upper warm molecular layers. For these reasons, CN is also referred to as a PDR tracer and could thus be a sensitive probe of disk structure.

With ALMA, more information about this molecule is rapidly gathered.
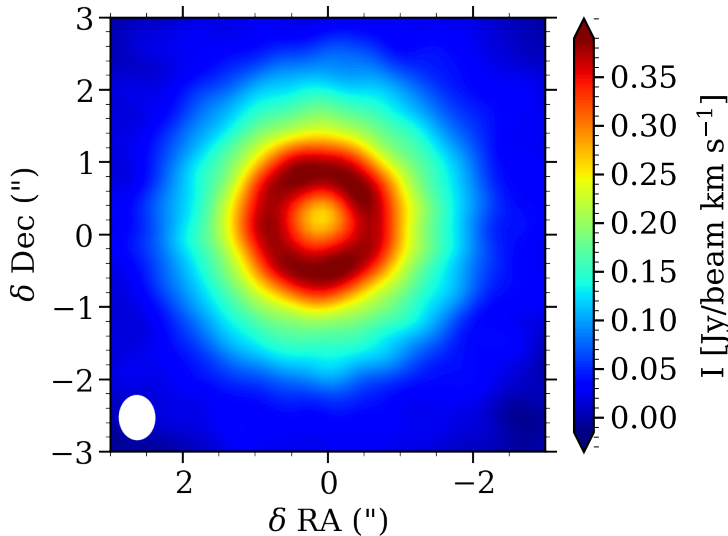
Figure 5.1: CN ($N = 2 - 1$) ring observed at 0.9" (47 AU) in TW Hya with ALMA (data from Teague et al., 2016). The white ellipse at the bottom-left corner shows the synthesized beam size.

The CN ($N = 2 - 1$) and CN ($N = 3 - 2$) transitions are observable with Band 6 and Band 7 respectively, and the emission can now be spatially resolved. Observations at both wavelengths have provided new information, in particular about the morphology. Teague et al. (2016) used CN ($N =$2-1) hyperfine transitions data to measure the velocity dispersion in the TW Hya disk. At the same time, the beam size of $0.5'' \times 0.42''$ allowed Teague et al. (2016) to clearly resolve and distinguish a ring-like structure in their data (Fig. 5.1). CN was also detected in many disks the ALMA Lupus disk survey (Ansdell et al., 2016). Two of these disks, namely Sz 98 and Sz 71, were large and bright enough to show resolved ring structures, as presented in van Terwisga et al. (2019).

Ring-shaped emission has also been observed for other PDR tracers, such as C_2H. Bergin et al. (2016) concluded that in order to have ring-shaped C_2H emission in full (i.e., non-transitional) disks, a [C]/[O]>1 ratio is required, which at the same time also explains the high observed fluxes (Kama et al., 2016). In this work, we investigate whether ring-shaped emission is an intrinsic feature of CN in all protoplanetary disks or whether it is due to the specific underlying morphology of some particular disks, such as transitional disks. By modelling CN chemistry we also want to gain further insight into what kind of physical

and chemical information about the disk structure can be inferred from resolved CN observations, i.e. to which parameters the CN flux and ring size are most sensitive.

Section 5.2 describes the code, adopted model, physical structure, and chemical network. In Section 6.4 the results of our models are presented: the main observed trends and the most important reactions responsible for the ring-shaped CN emission. Finally, in Section 6.5 our results are compared with the data available to date, and the main information that can be obtained from CN is highlighted.

5.2   Model

In this work, we modelled the disks and CN emission using the 2D thermo-chemical code DALI, which combines radiative transfer, chemistry, thermal balance and ray-tracing calculations. This code has been described in detail and extensively tested with benchmark problems (Bruderer et al., 2012; Bruderer, 2013) and its results have been compared to observations in a series of other papers (Bruderer et al., 2012; Fedele et al., 2013; Bruderer et al., 2014; Miotello et al., 2016; Facchini et al., 2017). Given an input gas and dust density structure, the dust radiative transfer problem is solved via a 2D Monte Carlo method to obtain the dust temperature structure T_{dust} and the mean continuum intensities at wavelengths ranging from the UV to mm. Using an initial guess for the gas temperature, the abundances of the molecular and main atomic species are then calculated with either a time-dependent or steady-state chemical network simulation, and their excitation is computed through non-LTE calculations. Finally, the gas temperature structure T_{gas} can be obtained from the balance between the cooling and heating processes: the new T_{gas} is then used to re-calculate the chemistry, and the last two steps are iterated until a self-consistent solution is obtained. Both continuum emission and spectral image cubes are finally created using a ray tracer.

5.2.1   Adopted physical model

For our disk models we assumed a simple parametrized surface density distribution as in Andrews et al. (2011), following an exponentially tapered power law:

$$\Sigma_{\mathrm{gas}}(R) = \Sigma_{\mathrm{c}} \left(\frac{R}{R_{\mathrm{c}}} \right)^{-\gamma} \exp\left[-\left(\frac{R}{R_{\mathrm{c}}} \right)^{2-\gamma} \right], \qquad (5.1)$$

where R_c is a characteristic radial scale for the surface density profile and Σ_c sets the normalization of the density profile. This surface density profile corresponds to the so-called self-similar solution to the viscous accretion disk model (Lynden-Bell and Pringle, 1974; Hartmann et al., 1998), where the shear viscosity parameter is assumed to depend on the radius via $\nu \propto R^{-\gamma}$ and not to change in time.

The vertical gas density distribution follows a Gaussian, with an aspect ratio that depends on the radius as

$$h(R) = h_c \left(\frac{R}{R_c} \right)^{\psi}. \tag{5.2}$$

In order to mimic dust settling, two populations of grains are considered following the approach of D'Alessio et al. (2006): a small-grains population $(0.005 - 1\,\mu\text{m})$ and a large-grains population $(1 - 1000\,\mu\text{m})$. The small-grains population has a scale height of h, while the scale height of the more settled large-grains population is reduced to χh, where $0 < \chi < 1$. The fraction of dust surface density distributed in the two populations is controlled by the f_{large} parameter via the relations $\Sigma_{\text{dust,large}} = f_{\text{large}}\Sigma_{\text{dust}}$ and $\Sigma_{\text{dust,small}} = (1 - f_{\text{large}})\Sigma_{\text{dust}}$. We assumed that most of the dust mass in concentrated into the more settled dust grains (e.g., Testi et al., 2003; Rodmann et al., 2006; Lommen et al., 2009; Ricci et al., 2010a). After some preliminary testing, we concluded that varying the f_{large} settling parameter between 0.9 and 0.99 does not produce any significant difference in CN emission. Consequently, we kept f_{large} fixed in our grid and assumed $f_{\text{large}} = 0.99$ in all of our models. Also, negligible variation was observed in both the abundance and emission profiles when the settling parameter χ is varied between 0.1 and 0.4. In this work, $\chi = 0.2$ was used.

Other important parameters that affect the chemistry in the models are the stellar and interstellar radiation fields, and the cosmic-ray ionization rate. For the chemistry of CN, the FUV part of the spectrum $(6 - 13.6\,\text{eV})$ becomes particularly important, since photons in this energy range can be responsible for both the formation of CN (through HCN photodissociation) and for its destruction (e.g., Jansen et al., 1995; Sternberg and Dalgarno, 1995; Visser et al., 2018; Heays et al., 2017). We modelled different stellar spectra to study the effect of different UV fluxes by assuming the stars to emit as a black body at a given effective temperature T_{eff} with an excess UV due to accretion. The stellar X-ray spectrum was modelled as a black body at $7 \times 10^7\,\text{K}$ between 1 and 100 keV. The interstellar radiation field and the cosmic microwave background were also accounted for and considered to be isotropic. We set the cosmic-ray ionization rate per H_2 to $5 \times 10^{-17}\,\text{s}^{-1}$.

The computation was carried out on a spatial grid of 265 cells in the radial direction and 120 in the vertical direction. In the radial direction, 35 cells were logarithmically spaced in the first 20 AU and 230 are linearly spaced at ~ 2.5 AU resolution in the outer disk. The cells in the vertical direction were linearly spaced and their size scales with the aspect ratio h at a given radius. A spectral grid was also used for the radiative transfer, consisting of 58 wavelength bins extending from 912 Å to 3 mm. The abundance for CN and the other chemical species were then derived by assuming steady-state chemistry for the chemical calculations. Such an approach is justified by the fact that the chemistry in the upper layers is fast, therefore making the relevant timescales much shorter than the average age of a Class II disk.

5.2.2   Grid of models

The goal of our work is to investigate whether or not the ring-like CN emission observed in spatially resolved disks is a common feature in all protoplanetary disks, or if it is due to the specific global morphology of some particular disks such as TDs. The origin of such rings is also investigated. In addition, it is also clear observationally that CN emission can be very bright and it is important to understand which disk and stellar properties most strongly affect the CN line emission intensity. We ran a small grid of models varying some of the parameters describing the physical structure of the disk, dust distribution, and the stellar spectrum. A summary of the parameters used in the models can be found in Table 5.1.

5.2.3   Chemical network

Our models use the chemical network from Bruderer et al. (2012), expanded and updated by Visser et al. (2018) to produce accurate abundances for HCN, HNC and CN. In particular, this network includes all reactions from the cyanide chemistry review by Loison et al. (2014) and the updated CN photodissociation rate from Heays et al. (2017). Isotopes are not considered.

The network contains standard gas-phase reactions, photoionization and photodissociation, reactions induced by X-rays and cosmic rays. some reactions with PAHs, and a limited grain-surface chemistry. Full details can be found in Appendix A.3.1 from Bruderer et al. (2012) and Visser et al. (2018). Gas-grain interactions include freeze-out, sublimation, and photodesorption. The binding energy of CN is set to 1600 K, as recommended by the Kinetic Database for Astrochemistry (KIDA; Wakelam et al., 2012).

In the surface layers and outer disk, the UV radiation field is strong enough

Table 5.1: Parameters of the disk models in the main grid.

Parameter	Range
Chemistry	
[C]/[H]	1×10^{-4}
[O]/[H]	3.5×10^{-4}
[N]/[H]	1.6×10^{-5}
[PAH]	10^{-3} ISM abundance
Physical structure	
γ	1
ψ	0.1, 0.2, 0.3
h_{c}	0.1, 0.2 rad
R_{c}	60 AU
M_{gas}	$10^{-5}, 10^{-4}, 10^{-3}, 10^{-2}, 10^{-1} M_{\odot}$
f_{large}	0.99
χ	0.2
Stellar spectrum	
T_{eff}	4000 K + UV ($\dot{M} = 10^{-8}\,\mathrm{M_{\odot}/year}$),
	10000 K
L_{bol}	1, 10 $L_{\odot}$
L_{X}	$10^{30}\,\mathrm{erg\,s^{-1}}$
Dust properties	
Dust	0.005-1 μm (small)
	1-1000 μm (large)
Other parameters	
Cosmic-ray ionization	
rate per H_2	$5 \times 10^{-17}\mathrm{s^{-1}}$
External UV flux	G_0

to pump H_2 into vibrationally excited states, denoted as H_2^*. This vibrational energy can enable neutral-neutral reactions that would otherwise have insurmountable activation barriers (London, 1978; Tielens and Hollenbach, 1985; Sternberg and Dalgarno, 1995; Bruderer et al., 2012). Of particular importance to our models is the reaction of atomic N with H_2^* to form NH, which in turn reacts with C or C^+ to form CN or CN^+ (see below). The initial step has an activation energy of 12 650 K (Davidson et al., 1990) and would normally

only proceed at gas temperatures above $\sim$1200 K. However, the UV pumping of H_2 in the surface layers allows the $N + H_2^*$ reaction to proceed regardless of temperature. As such, it is a crucial first step in the formation of CN. The H_2 pumping rate is taken to be eight times its photodissociation rate (Sternberg et al., 2014).

The chemistry is run in steady-state mode, assuming initial molecular abundances as in Cleeves et al. (2015) but with [C]/[H] increased to 10^{-4} from 10^{-6} unless specified otherwise. Because the surface layer dominates the CN abundance, its chemistry and emission are not found to be sensitive to the specific period over which the chemistry is run and results are similar in steady state.

5.3 Results

5.3.1 CN abundance

CN is often referred to as a PDR tracer, and many studies have shown that in protoplanetary disks this molecule forms and survives mostly in the surface layers exposed to intense UV radiation. The same feature is found in our models, with the highest CN abundance region close to the surface and outer edge of the disks.

Fig. 5.2a shows the CN abundance (with respect to the total gas density) for a typical T Tauri disk. Highest CN abundances are located high up in the disk between 10 and 100 AU and extend down to the midplane at the disk edge at large radii where the external UV also plays a role. Such an abundance distribution in turn translates into a ring of high column densities (Fig. 5.2b), which is consistent with a ring-shaped emission intensity profile (see Sec. 5.3.2). In contrast, the HCN abundance and column density peak at small radii (see Fig. 5.2b).

Fig. 5.3. shows a vertical cut of the abundances of the main species at the radial location of the CN abundance maximum (green dot in Fig. 5.2a). Again, the CN molecule is located near the surface of the disk and between the hydrogen atomic and molecular hydrogen layer, with HCN located deeper into the disk.

It is worth investigating whether the increase in CN column density towards the outer disk is due to decreasing UV, decreasing temperature, or some combination of parameters. The strongest dependence on temperature is found in the back-reaction

$$CN + H_2 \rightarrow HCN + H, \tag{5.3}$$

which has an activation temperature of 900 K (Baulch et al., 2005). However,
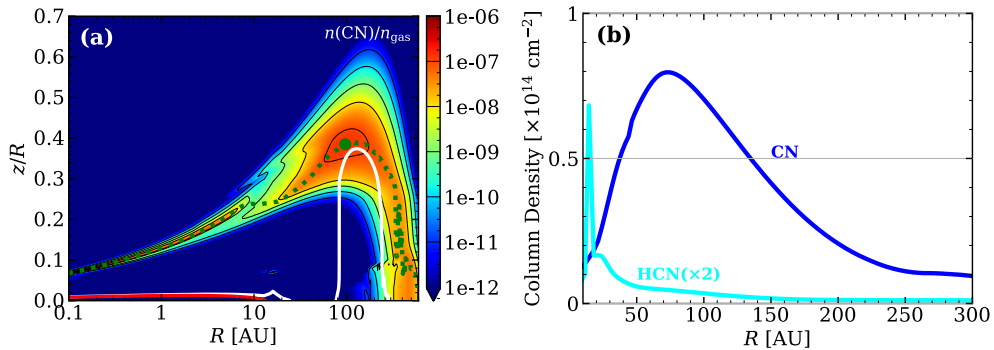
Figure 5.2: (a) Abundance of CN in a $10^{-2}\,\mathrm{M_\odot}$, $\psi = 0.3$, $h_\mathrm{c} = 0.1$ disk surrounding a T Tauri star. The location of the peak value is indicated with the green dot. The shape of the distribution of the outer high-CN-abundance region is representative for all the other models. The white line shows the $\tau = 0.5$ contour of the CN ($N = 3 - 2$) emission line. The red line shows the dust $\tau = 1$ layer at the same wavelength. The green dotted line indicates the location of the vertical CN abundance maximum for each radius. (b) CN (solid blue line) and HCN (cyan line) column densities calculated for the same model, plotted on a linear rather than logarithmic scale. The HCN column density was multiplied by 2 and is more radially concentrated than CN.

while this reaction is important in increasing HCN in the inner disk, it does not play a role in setting the CN abundance since the newly formed HCN is readily photodissociated back to CN.

The main reactions that dominate the formation of CN are instead

$$N + H_2^* \rightarrow \quad NH + H \tag{5.4}$$

$$C^+ + NH \rightarrow \quad CN^+ + H. \tag{5.5}$$

CN^+ proceeds then to CN through a charge transfer reaction with H or through the intermediates HCN^+ and $HCNH^+$ followed by dissociative recombination. Alternatively, NH can react with neutral C directly to form CN. Another less important route to cyanides starts from reactions of N with CH_2 and C_2H. Alternatively, reactions of N^+ with H_2 lead to NH_4^+, through a series of ion-molecule reactions, which then reacts with C to form $HCNH^+$.

CN is primarily destroyed by photodissociation and by reactions with atomic O. The rate coefficient of the CN + O reaction is taken to have no temperature dependence, as discussed in Visser et al. (2018) and consistent with the KIDA recommendations. The normalized abundances of the most relevant species are shown in Fig. 5.4a along the dotted green line shown in Fig. 5.2a. The peak
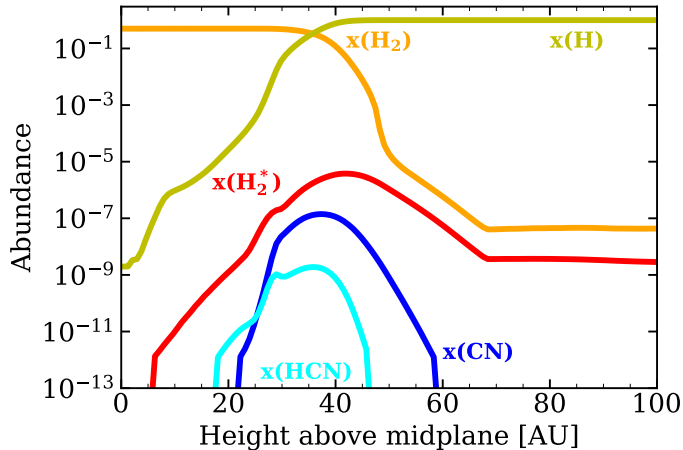
Figure 5.3: Vertical cut at the radial location of the CN peak abundance. The CN peak is located between the molecular hydrogen (H_2) region and the atomic layer.

of the CN abundance corresponds to that of NH. In turn, H_2^* is required in order for NH to exist. NH also shows a second inner peak at 20 AU. This, however, does not translate into a second CN peak because of the lack of C^+ in this region, which is required for reaction (5.5) to happen. The net result is that outside 30 AU the normalized abundance profiles of H_2^*, NH, and CN are qualitatively similar.

The H_2^* abundance is controlled by the molecular hydrogen excitation and de-excitation rates shown in Fig. 5.4b . Moving inward from the CN abundance peak, the de-excitation of H_2^* increases faster than the excitation due to FUV pumping; this leads to a decrease in $x(H_2^*)$, and consequently also in $x(NH)$ and $x(CN)$. At larger radii the FUV radiation field is attenuated by the dust, de-excitation turns from collisional to spontaneous emission and starts to dominate again, leading to a decrease in $x(H_2^*)$ and x(CN). Their ratio (solid red line in Fig. 5.4b) thus has its maximum right at the location of the CN abundance maximum.

In general, the dependence of CN abundance on the balance between H_2 excitation (via FUV pumping) and de-excitation (via collisions) can be summarized with the local ratio between FUV flux G_0 and gas density n_{gas}. In fact, FUV pumping is proportional to $G_0 \times n_{gas}$, while collisional de-excitation scales as n_{gas}^2. We observe that the value of G_0/n_{gas} at the CN abundance peak is constant for all of our models; this is consistent with the UV controlling the abundance of CN. When G_0/n_{gas} is too low, collisional de-excitation dominates over FUV pumping, thus hindering the formation of H_2^*. On the
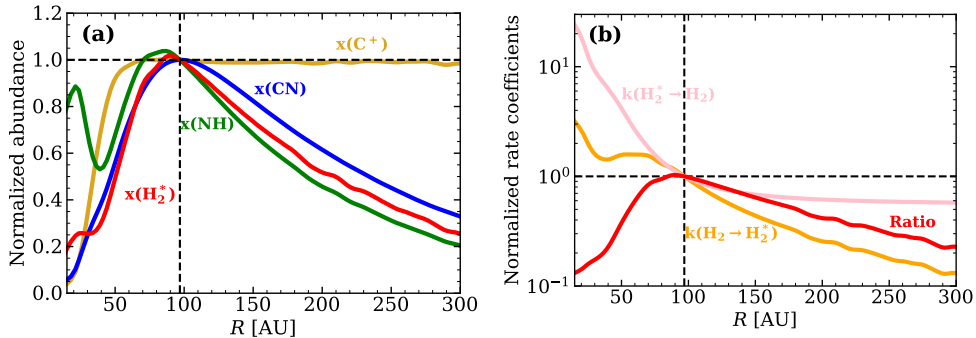
Figure 5.4: (a) Radial abundances for the most important reactants in the formation of CN (see reactions 5.4 and 5.5), along the dotted green line in Fig. 5.2a. Each curve is normalized to 1 at the location of the CN maximum. (b) H_2 excitation rate, H_2^* de-excitation rate and their ratio along the dotted green line in Fig. 5.2a. All quantities are normalized to their value at the CN peak abundance (green dot in Fig. 5.2a) and refer to the model shown in Fig. 5.2a. The dashed vertical line indicates the location of the CN peak abundance.

other hand, when G_0 is high enough, H_2 gets photodissociated. Photodissociation scales with $G_0 \times n_{\mathrm{gas}}$ and formation with n_{gas}^2. If G_0/n_{gas} is too high, photodissociation dominates over formation, thus removing molecular hydrogen and preventing the formation of H_2^*. The H_2^* layer is located between the molecular and atomic hydrogen layers, and therefore the maximum of H_2^* and consequently of CN is located where the correct ratio between G_0 and n_{gas} is met (see Fig. 5.16 in the Appendix).

Finally, previous astrochemical models have shown that X-rays can play an important role in the chemistry of CN (Lepp and Dalgarno, 1996). However, Stäuber et al. (2005, 2007) find that the effect of X-rays in negligible in environments where a high FUV flux is present. Our results indeed do not show significant differences when the L_X parameter is varied between 10^{27} and $10^{31}\,\mathrm{erg\,s^{-1}}$.

5.3.2   Emission

From the temperature structure and chemical abundances obtained for each model it is possible to ray-trace CN emission. In the CN molecule, each rotational energy level (labelled with the quantum number N) is split into a doublet by the spin-rotation interaction (quantum number J), thus leading to three fine structure transitions. Each of the two sub-levels is in turn split into
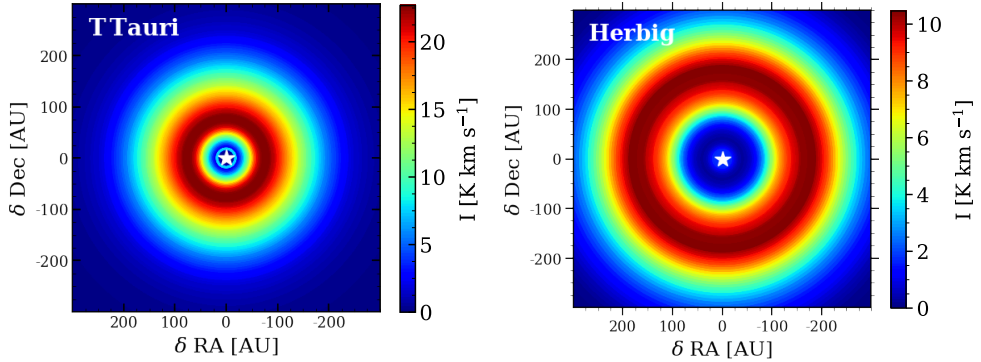
Figure 5.5: Ray-traced images of the CN emission rings in models with $10^{-2}\,M_\odot$, $\psi = 0.3$, $h_c = 0.1$ disks around a T Tauri and a Herbig star. The ring in the Herbig disk is clearly more extended than that around the T Tauri star. The images are not convolved with any beam, and the resolution is set by the size of the cells in the spatial gridding of the disk ($\sim 2.5\,\mathrm{AU}$). For the ray-tracing, the disks are assumed to be at a distance of 150 pc.
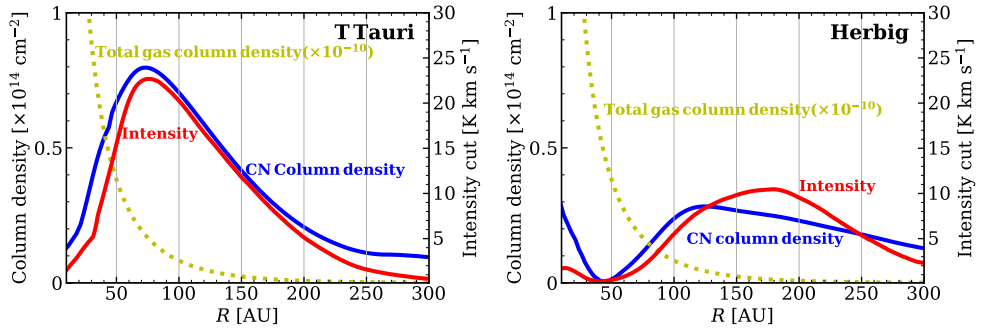
Figure 5.6: Comparison between the radial CN column density profile (blue) and intensity profile (red) for the two disks shown in Fig. 5.5. The total gas column density multiplied times 10^{-10} is also plotted in yellow as a reference.
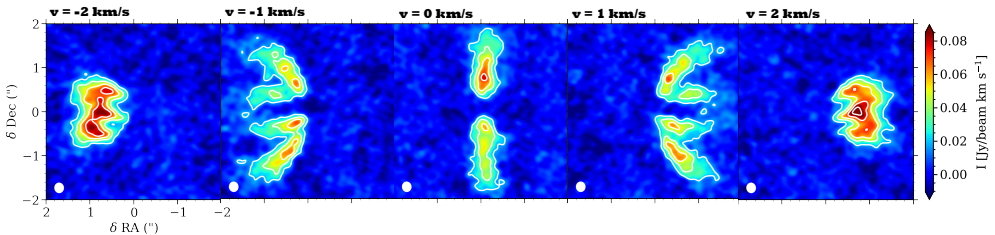
Figure 5.7: Simulated observations of a $M_{\mathrm{disk}} = 10^{-2}\,M_\odot$, $h_c = 0.1$, $\psi = 0.2$ disk around a Herbig star, inclined of $60°$. The image was simulated using the tasks `simobserve` and `simanalyze` in the CASA software.

a triplet by nuclear magnetic interactions (quantum number F), giving rise to hyperfine transitions. In this work we ignored the latter transitions, and discuss only the fine structure transitions. In particular, if not otherwise specified, on the brightest of the three, namely the CN (N, J)=(3-2,7/2-5/2) transition at 340.25 GHz. Fig. 5.5 shows the ray-traced images for two disks from our grid that have the same physical structure but rotate around a T Tauri and a Herbig star, respectively. In the ray tracing, the disks are set to be face-on to allow the CN emission to be clearly distinguishable. The distance of the disks is assumed to be 150 pc.

As shown in Fig. 5.2a, CN is optically thin. Accordingly, for T Tauri stars the radial intensity profile is consistent with the radial column density profiles, and the peak of the column density is located at the same radius as that of the emission peak (Fig. 5.6). In the disks around Herbig stars, CN forms at larger radii than in T Tauri stars. In addition, in some Herbig models, such as that shown in Figs. 5.5 and 5.6, emission can peak at even larger radii than the column density peak. This is because the peak in overall CN column density does not correspond to the peak in column density of the CN molecules in the upper state of the transition we are studying (N=3, J=7/2), which is located further out. A detailed explanation of this excitation mechanism can be found in Appendix 5.C.

All other models in our study show similar ring-like structures, thus confirming that ring-like emission is an intrinsic feature of CN emission in full disks. In every case, such a structure is due to the higher abundance of CN at larger radii and is not caused by ring-shaped features in the global disk morphology such as those characteristic in transitional disks.

We also concluded that it is not due to sub-thermal excitation effects, which in previous studies have been shown to potentially play an important role for high dipole moment molecules such as CN (e.g., van Zadelhoff et al., 2003), confirming the conclusions of Hily-Blant et al. (2017) for the TW Hya disk. Nevertheless we find that the high critical density of CN does play a role in enhancing the size of CN rings, especially in Herbig stars.

Finally, given the fact that CN in our models is mostly abundant in the uppermost layers of the disk, CN can be used as a probe for the vertical structure of disks. Fig. 5.7 shows a simulated ALMA observation of CN in an inclined disk around a Herbig star, for five representative channels 0.25 km/s wide: even with a modest resolution of 0.22" and with 30 minutes of on-source integration, the two layers are clearly distingushable.

5.3.3   Dependence on mass and flaring

We investigated how CN emission is affected by some of the key parameters of our models. First, we studied the dependence of the integrated flux and the location of the ring on the total gas mass of the disks.

Fig. 5.8 shows that both for Herbig and T Tauri stars the CN integrated flux increases as the total disk mass increases. The measured fluxes range from $200 \, \mathrm{mJy \, km \, s^{-1}}$ and $9 \, \mathrm{Jy \, km \, s^{-1}}$, which is consistent with observed values (e.g. Guilloteau et al., 2013). The dependence of the flux on the mass is steeper at low masses for T Tauri stars and flattens for $M_{\mathrm{disk}} > 10^{-3} \, \mathrm{M_{\odot}}$. For the Herbig stars, the flux generally increases less steeply with mass. For both stellar spectra, more flared disks always show higher intensities.

Fig. 5.9, on the other hand, shows the size of the ring as a function of M_{disk}. More massive disks have larger rings. The difference between T Tauri and Herbig stars is much more evident here than for the flux, hinting at a strong dependence of the CN abundance on the FUV spectrum. In particular, disks surrounding T Tauri stars show rings with sizes ranging between $30 \, \mathrm{AU}$ and $100 \, \mathrm{AU}$ while Herbig disks show rings extending to more than $200 \, \mathrm{AU}$. The disk scale height, parametrized through h_{c}, does not play a strong role, as the scatter due to the variation of h_{c} is small compared to the ranges of the fluxes and of the ring sizes, which from now on we define as the radial location of the emission peak.

Finally, disks with a larger flaring angle, exposed to stronger FUV fluxes, show systematically larger rings for both Herbig and T Tauri stars. Changing the flaring angle of the disks in our models has an impact on the CN abundance and consequently on its emission intensity. Fig. 5.10 shows a model with $M_{\mathrm{disk}} = 10^{-2} \, \mathrm{M_{\odot}}$ and $h_{\mathrm{c}} = 0.1$ rotating around a T Tauri star as an example. The radial intensity cuts are shown for the three different values of ψ used in our grid. As ψ increases, the emission increases in the ring, which moves outward. This confirms our earlier conclusion that UV flux plays an important role in regulating the CN abundance. For each model, the vertical location of the CN peak is determined by the UV field relative to the gas density (Fig. 5.16): when the flaring angle is larger the optimal ratio between UV flux and gas density is found at lower altitudes where the gas density is higher.

The same qualitative trends are observed in our models for the $(N, J) = (3-2, 5/2-5/2)$ and $(N, J) = (3-2, 5/2-3/2)$ fine transitions and for the brightest of the $N = 2-1$ transitions, namely the $J = 5/3 - 3/2$ one at 226.88 GHz. Finally, the ratio between the integrated flux of the $(N, J) = (3-2, 7/2-5/2)$ transition and that of the $(N, J) = (2-1, 5/2-3/2)$ one lies between 0.5 and 3 in all our models.
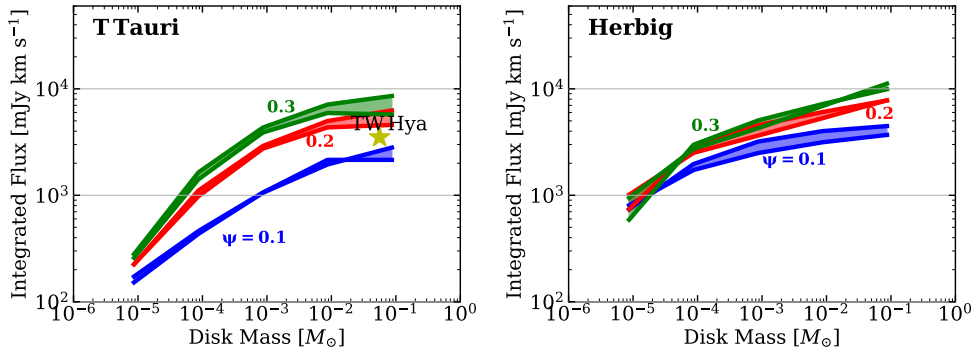
Figure 5.8: Dependence of the CN integrated flux on the total disk mass for disks around T Tauri (upper panel) and Herbig (lower panel) stars. For each value of ψ, the range highlighted by the shaded area is due to the variation of h_c. The fluxes are measured by assuming the disks are at a distance of 150 pc. The value measured for TW Hya and rescaled for the distance of the models is also shown.
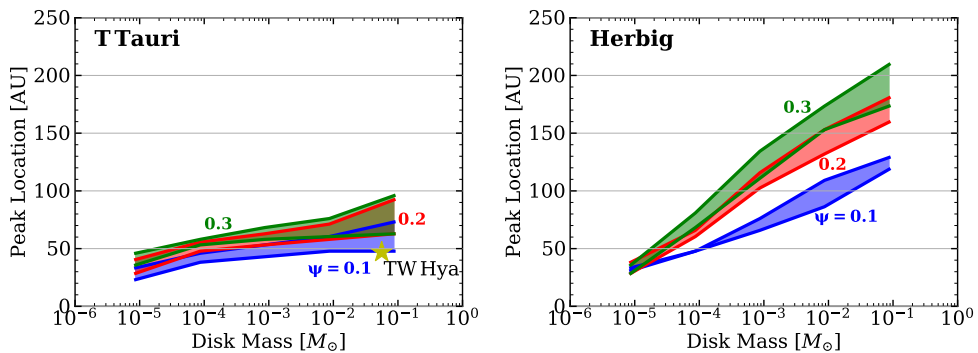
Figure 5.9: Dependence of the CN ring location on the total disk mass in the models.

Finally the dependence of the CN emission pattern on the settling and degree of growth of the dust grains was studied. For this purpose, two additional models were run of a $10^{-2}\,\mathrm{M}_\odot$, $\psi = 0.2$, $h_c = 0.1$ disk surrounding a T Tauri star assuming $f_{\mathrm{large}} = 0.1$ and 0.8. In these models, the higher amount of small grains in the disk atmosphere lowers the intensity of the FUV field. Accordingly, the high CN-abundance region is moved to even higher altitudes in the disks in which G_0/n_{gas} is similar. As a consequence, the CN column density and integrated flux decreases by a factor of ~ 3 for the $f_{\mathrm{large}} = 0.8$ model, and the rings are only a few AUs smaller than in the $f_{\mathrm{large}} = 0.99$ case. In the
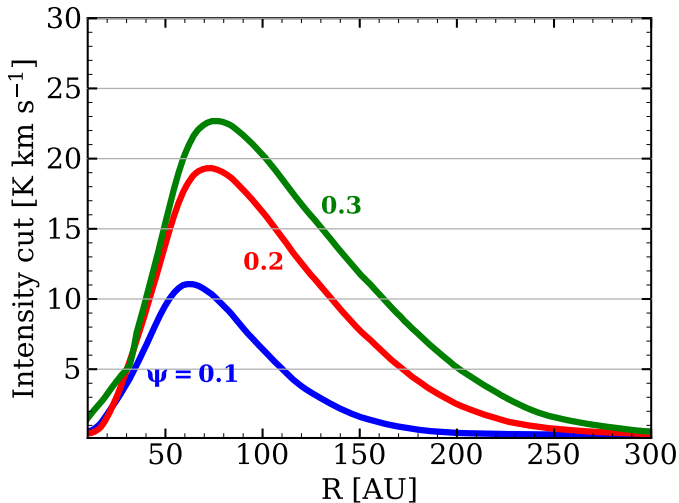
Figure 5.10: Different intensity radial profiles for $\psi = 0.1, 0.2$ and 0.3 in a disk with $M_{\mathrm{disk}} = 10^{-2} \, M_\odot$ and $h_{\mathrm{c}} = 0.1$ rotating around a T Tauri star. The intensity of the CN emission increases in more flared disks and moves to slightly larger radii.

extreme $f_{\mathrm{large}} = 0.1$ model, however, the column density and intensity decrease by almost an order of magnitude.

5.3.4 Excess UV from accretion

In order to further test the impact of the UV field on the CN flux and distribution, we ran an additional set of models by varying the excess UV due to accretion onto a T Tauri star. So far, the T Tauri stellar spectrum was modelled as a 4000 K black-body spectrum with a UV excess for an accretion rate of $10^{-8} \, M_\odot \mathrm{year}^{-1}$. The excess accretion UV was modelled as a 10000 K black body on a $1.65 \, R_\odot$ radius star (Kama et al., 2016). The additional accretion rates considered are 10^{-7}, 10^{-9}, $10^{-10} \, M_\odot \mathrm{year}^{-1}$ and a non-accreting blackbody spectrum, and we investigated the effects of the different UV excess on a disk with $M_{\mathrm{gas}} = 10^{-2} \, M_\odot$, $\psi = 0.2$ and $h_{\mathrm{c}} = 0.1$.

The integrated flux and ring size as functions of accretion rate are plotted in Fig. 5.11. The observed trends presented in Fig. 5.11 confirm the main differences seen between T Tauri and Herbig stars. Higher accretion rates corresponding to higher UV fluxes show higher CN integrated emission. Moreover, the radius of the CN rings increases in size as the UV field becomes stronger. Of course, for a given accretion rate, a spread in the flux and ring size is expected due to the other parameters as explained above.

Figure 5.11: (a) Integrated flux of the CN (N, J)=(3-2,7/2-5/2) emission in a T Tauri disk with $M_{\text{gas}} = 10^{-2}\,M_\odot$, $\psi = 0.2$ and $h_c = 0.1$ as a function of the accretion rate on the central star. For each accretion rate, the UV luminosity between 91.2 and 110 nm is also shown at the top of the figure. The standard model ($\dot{M} = 10^{-8}\,M_\odot\,\text{year}^{-1}$) is marked with a blue square. (b) Same as (a), for the CN ring radius.

5.3.5   Varying the disk size

As a last test, we investigated the effect of different values of R_c on CN morphology, which ultimately reflects on the disk size. As a base model, we used the $M_{\text{gas}} = 10^{-2}\,M_\odot$, $\psi = 0.2$, $h_c = 0.1$ T Tauri disk, and then varied R_c keeping the inner surface density profile equal in all the models (see Fig. 5.18 in the appendix). In particular, we tested models with $R_c = 15, 30, 60$ and 120 AU. Fig. 5.13a shows that the inner part of the CN column density profiles remains constant in all models: this is consistent with the fact that CN abundance is regulated by the balance between stellar FUV and gas density. The CN column density then starts to decrease following the overall gas density profile. Consequently, the CN column density peak is reached at larger radii for higher values of R_c. The same occurs for the radial intensity profile: the ring radius moves increasingly outward as R_c increases from 15 to 60 AU, and becomes almost constant for larger disk radii (Fig. 5.13b and 5.12b). Since a high percentage of the intensity comes from the outer disk, the integrated fluxes increase with R_c (Fig. 5.12a), and the smallest disk shows an order of magnitude lower intensity than the largest. It should be noted that there is a difference in mass between the R_c=120 AU disk and for the 15 AU of about a factor of ten. However such a difference alone would only provide a variation of a few in flux (Fig. 5.8a).
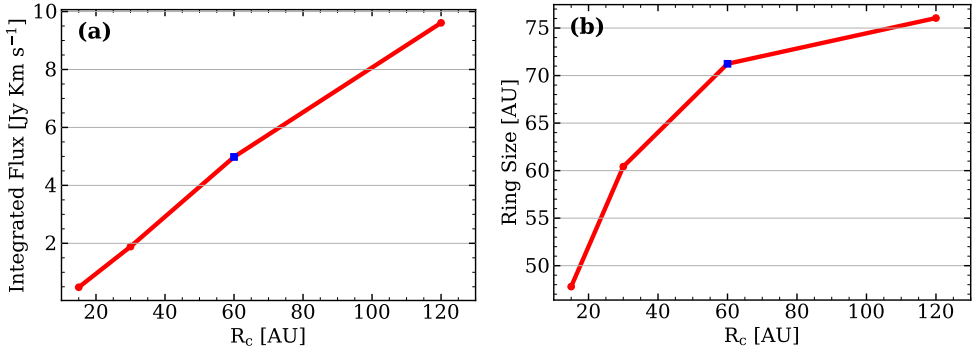
Figure 5.12: Dependence of (a) integrated fluxes and (b) ring size in models with different R_c values. The standard model ($R_c = 60\,\mathrm{AU}$) is marked with a blue square.
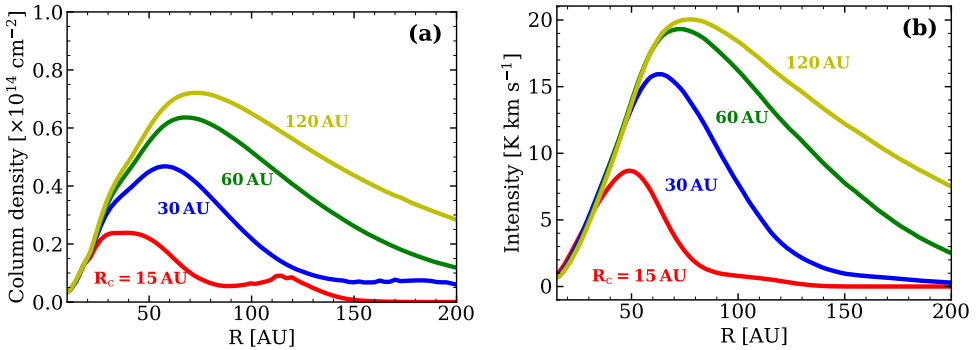
Figure 5.13: Comparison between (a) column density radial profiles and (b) radial intensity cuts in models with different R_c values.

5.3.6   Varying the carbon abundance

Recent observations of protoplanetary disks have shown that lines from CO and its isotopologues, the molecules usually adopted to measure the disk mass, are much weaker than expected in many disks (e.g., Favre et al., 2013; McClure et al., 2016; Miotello et al., 2016; Pascucci et al., 2016; Long et al., 2017; Trapman et al., 2017). This depletion of CO is inferred after photodissociation and freeze-out have been accounted for. One interpretation is that CO is transformed to other less volatile molecules, which is mimicked in our models with an overall volatile C depletion. The gas-phase carbon abundance therefore has recently become one of the largest uncertainties in protoplanetary disks. To account for
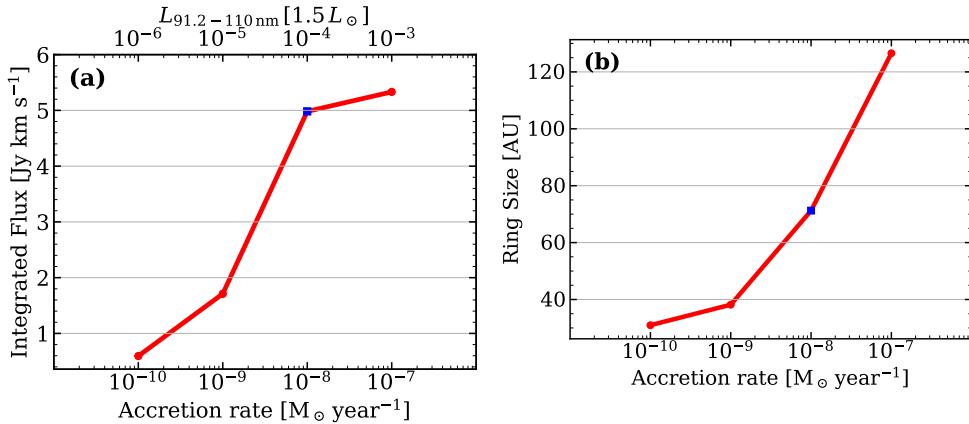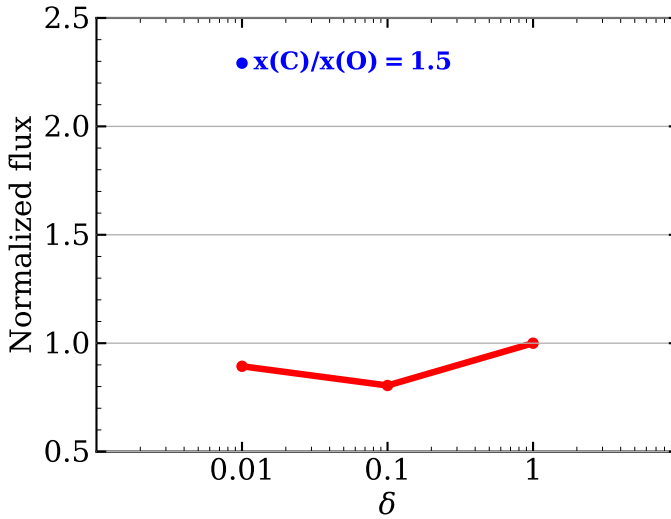
Figure 5.14: Integrated flux of the CN (N, J)=(3-2,7/2-5/2) emission in a disk with $M_{\text{gas}} = 10^{-2}\,M_\odot$, $\psi = 0.2$ and $h_{\text{c}} = 0.1$ as a function of the C and O depletion. The blue dot refers to the model where a higher gas-phase carbon abundance than oxygen is assumed. All the fluxes are normalized to the non-carbon-depleted $\delta = 1$ case. The fluxes vary by less than a factor of 2.

this effect, we ran three additional models of the $M_{\text{gas}} = 10^{-2}\,M_\odot$, $\psi = 0.2$ and $h_{\text{c}} = 0.1$ T Tauri disk. In the first two, the initial overall abundances of carbon, oxygen, sulphur and nitrogen are depleted by a factor of 10 and 100. In the third model, carbon, nitrogen and sulphur are again depleted by a factor of 100, while oxygen is even more depleted in order to get [C]/[O] = 1.5. This assumption is motivated by Kama et al. (2016) and Bergin et al. (2016), where a ratio [C]/[O] > 1 has been used to fit the C$_2$H flux in TW Hya. As shown in Fig. 5.14, the CN flux only varies by a factor of less than 2.5 in the four models in spite of two order of magnitude C and O abundance variations, thus showing a weak dependence of CN flux on the level of C and O abundance.

This happens because as the CN abundance in the surface layers decreases, this abundance increases deeper in the disk, because of the lower amount of O, which is the species that CN is mainly destroyed by. For this reason, CN is not a good tracer of C and O depletion in protoplanetary disks.

5.4   Discussion

The integrated fluxes in our models are consistent with single-dish and interferometric observations. Guilloteau et al. (2013) measured fluxes ranging from a few hundred mJy km s^{-1} up to ~ 10 Jy km s^{-1}, which is exactly the range of values observed in the models. The same holds for the SMA interferometric observations in Muto et al. (2012) and Öberg et al. (2011). Öberg et al. (2011) stated that the radial profiles show different extents for CN and HCN in different disks. In particular, CN appears more radially extended than HCN in V4046 Sgr and LkCa 15. Using more recent ALMA observations, Guzmán et al. (2015) also concluded that CN is ~ 2 times more extended than HCN in the disk surrounding the Herbig star MWC 480. This feature is well reproduced in our models (see Fig. 5.2a).

Finally, TW Hya is so far the only disk in which the CN emission has been observed and spatially resolved. CN shows a ring located close to 47 AU radius. With a mass of $0.056\,M_\odot$ (Bergin et al., 2013) and a flaring index $\psi = 0.3$ (Kama et al., 2016), both the measured integrated flux for the CN $(N, J)=(3-2, 7/2-5/2)$ transition of 27.1 Jy km s^{-1} (Kastner et al., 2014) and the the ring size is only slightly lower/smaller than the $\psi = 0.3$ models we show in Fig. 5.8a. Still, those values are perfectly consistent with the fact that TW Hya is a low accretor, with $\dot{M} \sim 10^{-9}\,M_\odot$ year^{-1} (Debes et al., 2013). For our models we assumed instead $\dot{M} = 10^{-8}\,M_\odot$ year^{-1}, and, as shown in Fig. 5.11a, smaller rings and lower fluxes are expected for lower accretion rates.

Recently, Bergin et al. (2016) have shown that in TW Hya other PDR tracers such as C_2H and $c-C_3H_2$ also present ring-like structures in their emission morphology. In order to reproduce such emission, Bergin et al. (2016) concluded that a strong UV field combined with [C]/[O]>1 in the upper disk are needed. These conditions are not required for CN, and its ring shape is a natural consequence of the CN formation mechanism and therefore is expected to be a common feature observable in many full disks. The ring and brightness of the CN rings can however be enhanced by a higher UV flux impinging on the disk.

CN emission is therefore a good diagnostic for those parameters affecting UV flux. Among all, flaring is a particularly interesting case. The flaring index is usually derived by fitting the mid-IR range of the SED emitted by the inner few AU of the disk and this value is then assumed to be uniform out to the outer disk. For the first time, information about flaring at much larger radii can be gathered by studying the CN ring radius and flux when some constraints about the spectral type of the central star are available.

CN flux is however not a good tracer for the mass of the disk and CO
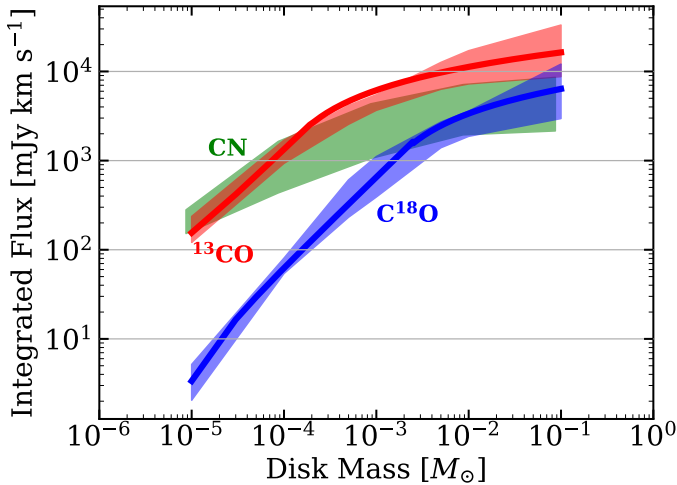
Figure 5.15: Comparison between CN, ^{13}CO and C^{18}O integrated flux dependence on the total disk mass. The ^{13}CO and C^{18}O fluxes are taken from Miotello et al. (2016). The solid lines represent the fit functions of the median for ^{13}CO (red) and C^{18}O (blue).

isotopologues still provide a more sensitive diagnostic (see Fig. 5.15). This is because in our models CN is most abundant in the upper layers of the disk, and no emission originates from the midplane where the bulk of the gas mass is. Our model results therefore do not support the results of Chapillon et al. (2012), who suggested the existence of large quantities of gas-phase CN close to the disk midplane, based on the low measured values of the excitation temperature with pre-ALMA data.

5.5 Conclusions

We modelled the CN abundance and emission in full protoplanetary disks around Herbig and T Tauri stars with the 2D thermochemical code DALI to self-consistently solve for the gas temperature structure and molecular abundance. The mass of the disks was varied between 10^{-5} and 10^{-1} M$_\odot$. We also varied other physical parameters, such as the flaring of the disk, and tested the effect of disk size, UV excess due to accretion onto the central star, and level of depletion of volatile C and O. The modelling shows the following results:

1. CN shows ring-shaped emission even in full protoplanetary disks. This is due to the formation route of CN, which is triggered by the excitation

of H_2 to H_2^* that is mostly abundant in a ring-shaped region close to the surface layer of the disk. H_2 is excited to H_2^* mostly through UV pumping. For this reason CN emission is very sensitive to UV flux.

2. Flaring plays an important role: disks with larger ψ show systematically higher fluxes and larger rings. On the other hand, the UV intensity of the central stellar spectrum is critical itself. Herbig stars generally have stronger UV fields, and are thus expected to present larger disks and higher integrated fluxes than T Tauri stars. As for T Tauri stars, UV excess can in first approximation be quantified through the accretion rate (e.g., Kama et al., 2016), with higher accretion rates producing higher UV excess fluxes and consequently brighter and larger CN rings.

3. The integrated fluxes of the models increase as the total disk mass increases but CN is still less sensitive than the CO isotopologues to the total gas mass. On the other hand, ring size is a much easier parameter to measure and, especially for Herbig stars, it is strongly dependent on the total gas disk mass, therefore providing a useful additional parameter to put constraints on the mass of disks around Herbig stars.

4. The disk critical radius R_c only plays a role in the CN morphology when smaller than 60 AU: in this case, smaller disks also show smaller CN rings and lower integrated fluxes. However, disks with R_c larger than 60 AU do not show any qualitative difference from disks with $R_c = 60\,\mathrm{AU}$. The disk scale height does not strongly affect the CN emission.

The dependence of CN flux and ring size on the above disk parameters make it a sensitive probe of the disk structure. In particular, when the spectral type of the central star is known CN can be combined with the SED to obtain information about parameters that are usually poorly constrained, such as the flaring of the disk at large radii, and to get an independent estimate of the UV flux.

5.A   Constant G_0/n_{gas}

In all of our models, the value of G_0/n_{gas} is constant to within a factor of a few. Fig. 5.16 shows this value for our T Tauri models and the same holds for Herbigs. In Fig. 5.17 not only the abundance peak, but at each radius the CN abundance maximum (dotted green line) follows the constant G_0/n_{gas} profile (white line). The model represents a $10^{-2}\,\mathrm{M_\odot}$, $\psi = 0.3$, $h_{\mathrm{c}} = 0.1$ around a T Tauri star.
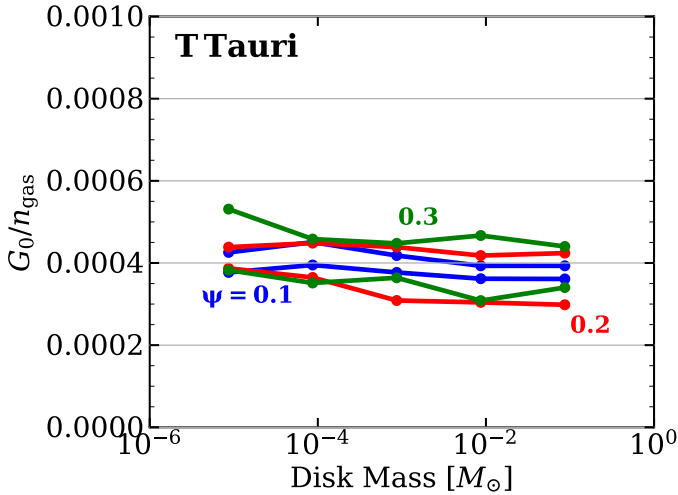
Figure 5.16: Value for G_0/n_{gas} where the CN abundance peaks for all the T Tauri models. The different lines for each colour refer to models with different h_{c} .

5.B   Density profiles for different values of R_{c}

When testing the effect of the disk size on CN emission, we varied the values of R_c keeping the density profiles at the small radii equal for all the models, as shown in Fig. 5.18. This keeps the conditions in the inner disk equal for all the models.

5.C   Level excitation and ring location

As shown in Fig. 5.6, and as observed also in other disk models around Herbig stars, the CN (N=3-2) emission peaks at radii which are larger than that of the column density peak. This is an excitation effect that originates from the high
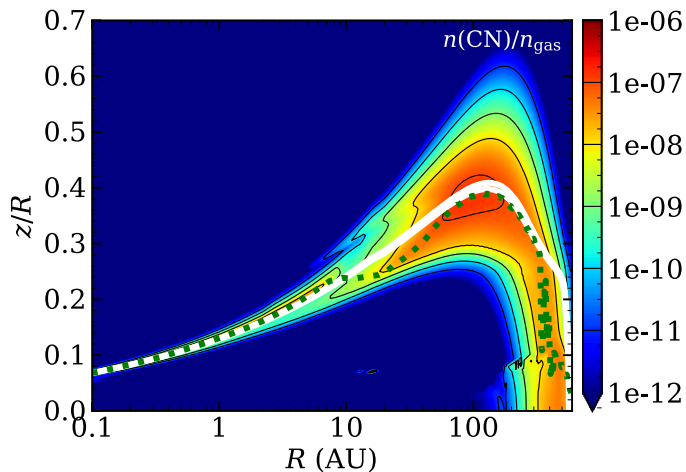
Figure 5.17: Overlay of the CN abundance structure in a $10^{-2}\,\mathrm{M_\odot}$, $\psi = 0.3$, $h_\mathrm{c} = 0.1$ disk surrounding a T Tauri star with a green dotted line indicating the location of the vertical CN abundance maximum for each radius. The white line highlights a surface of constant G_0/n_gas. The two lines follow each other very closely.
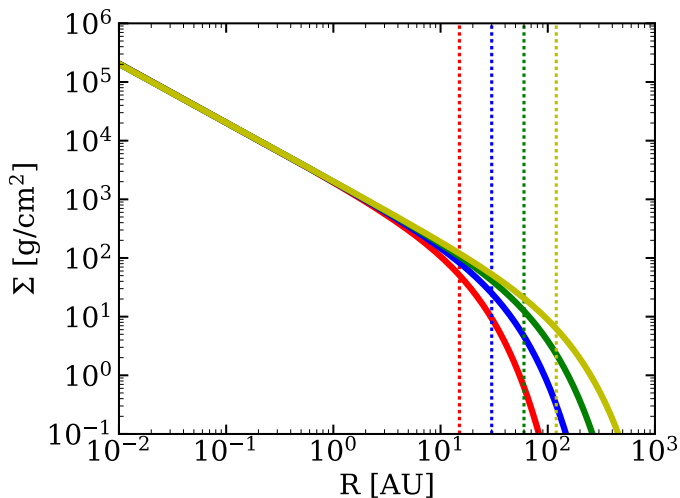
Figure 5.18: Comparison between the radial surface density profiles used when comparing models with different R_c parameters. The dotted line indicates, for each profile, the location of R_c.

critical densities of the CN transitions, combined with the low energies of the transitions.

Two main effects play a role:

1. The CN column density decreases more slowly toward the outer radii for the Herbig disks than for the T Tauri ones (see Fig. 5.6).

2. The gas density along the CN high-abundance layer decreases with radius (Fig. 5.19a). Gas temperature also decreases, but remains always above the energy of the N=3-2 transitions ($\sim$ 30K) and also of the N=4-3 one ($\sim$ 50K).

What happens is then the following:

- In the inner region of the disk, the gas density and temperature are high enough for the lines to be thermalized: as the column density increases, the intensity increases accordingly.

- Moving outward along the CN layer, even though the gas temperature remains high, the gas density decreases: as the peak of the CN column density is reached ($\sim$ 120 AU in this models) the gas density has fallen below the critical density of the higher level transitions ($n_{\mathrm{crit}} = 9.12 \times 10^6 \, \mathrm{cm}^{-3}$ at 50 K for the N=4-3, J=9/2-7/2 transition). Consequently, higher levels get depopulated and the population of the lower levels grows at larger radii t and at lower gas densities (see Fig. 5.19c).

- Since CN is optically thin, the emission intensity only depends on the population of the upper layers of the transition. The emission thus follows the increase/decrease of populations (Fig. 5.19b).

- Moving even further out, at some radius the critical density of the N=3-2 transition ($n_{\mathrm{crit}} = 3.84 \times 10^6 \, \mathrm{cm}^{-3}$ at 50 K for the N=3-2, J=7/2-5/2 transition) is also reached: as explained above level 3 gets unpopulated, the column density of CN in level N=3 decreases, 3-2 intensity starts decreasing and the population of levels 2 and 1 increases.

This effect is not evident for the T Tauri stars: as mentioned above, for their disks the CN column density profile decreases more steeply, and dominates over the increase in population of the lower levels.
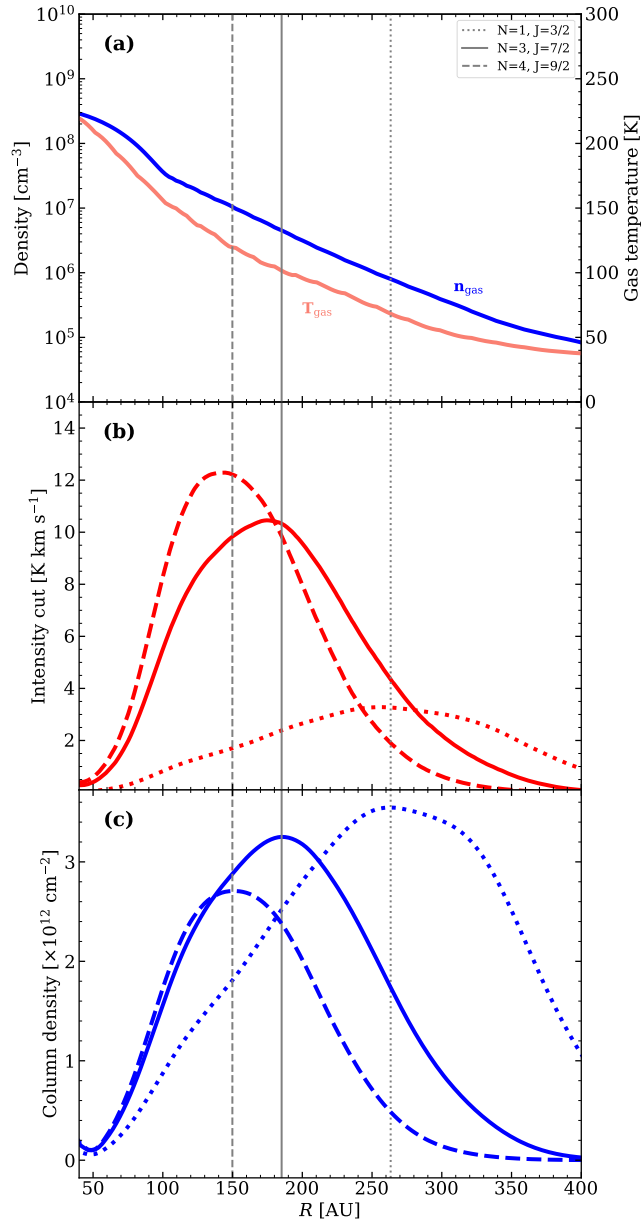
Figure 5.19: (a) Gas density and temperature along the CN high abundance layer (dotted-green line in Fig. 5.2a). (c) Column densities of CN molecules in the (N=1, J=3/2) (dotted), (N=3, J=7/2) (solid) and (N=5, J=11/2) (dashed) levels. (b) Intensities of the N=4-3, N=3-2 and N=1-0 transitions, for comparison with panel (c). The vertical lines mark the location of the column density peaks of CN molecules in the three levels.

6 | ALMA survey of Class II protoplanetary disks in Corona Australis: a young region with low disk masses

Cazzoletti, P., Manara, C. F., Hauyu, B. L., van Dishoeck, E. F., Facchini, S., Alcalà, J. M., Ansdell, M., Testi, L., Williams, J. P., Carrasco-González, C., Dong, R., Forbrich, J., Fukagawa, M., Galván-Madrid, R., Hirano, N., Hogerheijde, M., Hasegawa, Y., Muto, T., Pinilla, P., Takami, M., Tamura, M., Tazzari, M., and Wisniewski, J. P., 2019, Astronomy and Astrophysics, 626, A11

Abstract

Context. In recent years, the disk populations in a number of young star-forming regions have been surveyed with the Atacama Large Millimeter/submillimeter Array (ALMA). Understanding the disk properties and their correlation with the properties of the central star is critical to understand planet formation. In particular, a decrease of the average measured disk dust mass with the age of the region has been observed, consistent with grain growth and disk dissipation.

Aims. We want to compare the general properties of disks and their host stars in the nearby ($d = 160\,\mathrm{pc}$) Corona Australis (CrA) star forming region to those of the disks and stars in other regions.

Methods. We conducted high-sensitivity continuum ALMA observations of 43 Class II young stellar objects in CrA at 1.3 mm (230 GHz). The typical spatial resolution is $\sim 0.3''$. The continuum fluxes are used to estimate the dust masses of the disks, and a survival analysis is performed to estimate the average dust mass. We also obtained new VLT/X-Shooter spectra for 12 of the objects in our sample for which spectral type information was missing.

Results. 24 disks are detected, and stringent limits have been put on the average dust mass of the non-detections. Taking into account the upper limits, the average disk mass in CrA is $6 \pm 3\,\mathrm{M}_\oplus$. This value is significantly lower than that of disks in other young (1-3 Myr) star forming regions (Lupus, Taurus, Chamaeleon I, and Ophiuchus) and appears to be consistent with the average disk mass of the 5-10 Myr old Upper Sco. The position of the stars in our sample on the Herzsprung-Russel diagram, however, seems to confirm that that CrA has age similar to Lupus. Neither external photoevaporation nor a lower than usual stellar mass distribution can explain the low disk masses. On the other hand, a low-mass disk population could be explained if the disks are small, which could happen if the parent cloud has a low temperature or intrinsic angular momentum, or if the the angular momentum of the cloud is removed by some physical mechanism such as magnetic braking. Even in detected disks, none show clear substructures or cavities.

Results. We conducted high-sensitivity continuum ALMA observations of 43 Class II young stellar objects in CrA at 1.3 mm (230 GHz). The typical spatial resolution is $\sim 0.3''$. The continuum fluxes are used to estimate the dust masses of the disks, and a survival analysis is performed to estimate the average dust mass. We also obtained new VLT/X-Shooter spectra for 12 of the objects in our sample for which spectral type information was missing.

6.1   Introduction

Planets form in protoplanetary disks around young stars, and the way these disks evolve also impacts what kind of planetary system will be formed (Morbidelli and Raymond, 2016). The evolution of the disk mass with time is one of the key ingredients of planetary synthesis models (Benz et al., 2014). For a long time infrared telescopes (e.g., *Spitzer*) have shown how the inner regions of disks dissipate on a timescale of $\sim$3-5 Myr (Haisch et al., 2001; Hernández et al., 2007; Fedele et al., 2010; Bell et al., 2013).

Only recently, however, we have been able to measure the bulk disk mass for statistically significant samples of disks, thanks to the high sensitivity of the Atacama Large Millimeter/submillimeter Array (ALMA). Pre-ALMA surveys of disk masses were restricted to the northern hemisphere Taurus, Ophiuchus and Orion Nebula Cluster regions (Andrews and Williams, 2005; Andrews et al., 2009, 2013; Eisner et al., 2008; Mann and Williams, 2010). In the first years of operations of ALMA this has changed dramatically: hundreds of disks have been surveyed to determine the disk population in the $\sim$1-3 Myr old Lupus, Chamaeleon I, Orion Nebula Cluster, Ophiuchus, IC348 and Taurus regions (Ansdell et al., 2016; Pascucci et al., 2016; Eisner et al., 2018; Cieza et al., 2019; Ruíz-Rodríguez et al., 2018; Long et al., 2018), in the $\sim$3-5 Myr old σ-Orionis region (Ansdell et al., 2017), and in the older $\sim$5-10 Myr Upper Scorpius association (Barenfeld et al., 2016). These surveys have shown that the typical mass of protoplanetary disks decreases with the age of the region, in line with the observations that the inner regions of disks are dissipated within $\sim$ 3-5 Myr, similar to the dissipation time scale measured in the infrared. A positive correlation between disk and stellar mass was also found, and a steepening of its slope with time was identified (Ansdell et al., 2016, 2017; Pascucci et al., 2016). This is consistent with the result that massive planets form and are found preferentially around more massive stars e.g. Bonfils et al., 2013; Alibert et al., 2011. Finally, the steepening of the relation with time is explained with more efficient radial drift around low mass stars (Pascucci et al., 2016), and it suggests that a significant portion of the planet formation process, especially around low mass stars, must happen in the first $\sim$1-2 Myr, when enough material to form planets is still available in disks (Testi et al., 2016; Manara et al., 2018). Studying the evolution of the $M_{disk} - M_\star$ relation in as many different environments as possible is therefore critical for understanding how the planet formation process is affected by the mass of the central stars.

We present here a survey of the Class II disks in the Corona Australis star forming region (CrA). Located at an average distance of about 154 pc (Gaia Collaboration et al., 2018b; Dzib et al., 2018), the CrA molecular cloud
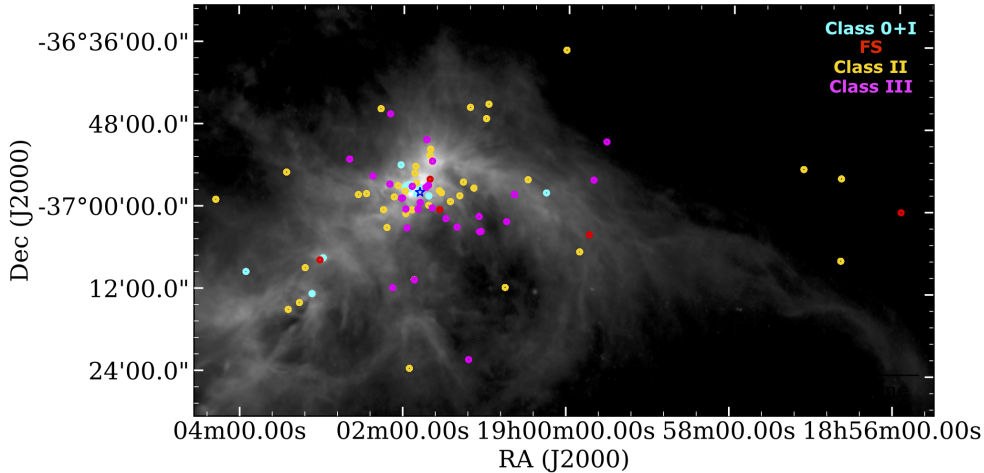
Figure 6.1: Spatial distribution of the CrA sources from the Peterson et al. (2011) catalogue on top of the *Herschel* 250 μm map of the Corona Australis molecular Cloud. The different colours represent the classification of the YSOs. The blue star indicates the position of R CrA

complex is one of the nearest star-forming regions (see review in Neuhäuser and Forbrich, 2008). It has been the target of many infrared surveys, the most recent being the Gould Belt (GB) *Spitzer* Legacy program presented in Peterson et al. (2011). At the center of the CrA region is located the *Coronet* cluster, which is a region of young embedded objects in the vicinity of R CrA (Herbig Ae star, Neuhäuser et al., 2000), on which many of the previous studies have focused. All studies agree in assigning to the *Coronet* an age < 3 Myr (e.g. Meyer and Wilking, 2009; Sicilia-Aguilar et al., 2011). However, there are also some indications of a more evolved population (e.g. Neuhäuser et al., 2000; Peterson et al., 2011; Sicilia-Aguilar et al., 2011). A deep, sub-mm wavelength survey of the disk population in the region can help to further understand the formation and evolutionary history of CrA.

We therefore use ALMA to conduct a high-sensitivity millimeter wavelength survey of all the known Class II sources in CrA and compare the results with other regions surveyed to-date. In Sec. 6.2 the sample is described, while

the ALMA observations are detailed in Sec. 6.3. We also describe there new VLT/X-Shooter observations to determine the stellar charachteristics. The continuum millimeter measurements, their conversion to dust masses and a comparison with other star-forming regions is presented in Sec. 6.4. Our findings are interpreted in the context of disk evolution in Sec. 6.5. Finally, the work is summarized in Sec. 6.6.

Table 6.1: Stellar properties of the central sources of the disks in the sample. The RA and DEC in J2000 are from the *Spitzer* data presented in Peterson et al. (2011)

2MASS ID	Name	RA	DEC	SpT	Ref.
J18563974-3707205	CrA-1	18:56:39.76	-37:07:20.8	M6	1
J18595094-3706313	CrA-4	18:59:50.95	-37:06:31.6	M8	2
J19002906-3656036	CrA-6	19:00:29.07	-36:56:03.8	M4	3
J19004530-3711480	CrA-8	19:00:45.31	-37:11:48.2	M8.5	4
J19005804-3645048	CrA-9	19:00:58.05	-36:45:05.0	M1	3
J19005974-3647109	CrA-10	19:00:59.75	-36:47:11.2	M4	5
J19011629-3656282	CrA-12	19:01:16.29	-36:56:28.3	M5	6
J19011893-3658282	CrA-13	19:01:18.95	-36:58:28.4	M2	7
J19013232-3658030	CrA-15	19:01:32.31	-36:58:03.0	M3.5	7
J19013385-3657448	CrA-16	19:01:33.85	-36:57:44.9	M2.5	7
J19014041-3651422	CrA-18	19:01:40.41	-36:51:42.3	M1.5	7
J19015112-3654122	CrA-21	19:01:51.12	-36:54:12.4	M2	8
J19015180-3710478	CrA-22	19:01:51.86	-37:10:44.7	M4.5	1
J19015374-3700339	CrA-23	19:01:53.75	-37:00:33.9	M7.5	7
J19020682-3658411	CrA-26	19:02:06.80	-36:58:41.0	M7	1
J19021201-3703093	CrA-28	19:02:12.00	-37:03:09.4	M4.5	5
J19021464-3700328	CrA-29	19:02:14.63	-37:00:32.9	...	...
J19022708-3658132	CrA-30	19:02:27.07	-36:58:13.1	M0.5	5
J19023308-3658212	CrA-31	19:02:33.07	-36:58:21.2	M3.5	1
J19031185-3709020	CrA-35	19:03:11.84	-37:09:02.1	M5	3
J19032429-3715076	CrA-36	19:03:24.29	-37:15:07.7	M5	1
J19012576-3659191	CrA-40	19:01:25.75	-36:59:19.1	M4.5	1
J19014164-3659528	CrA-41	19:01:41.62	-36:59:52.7	M2	9
J19015037-3656390	CrA-42	19:01:50.48	-36:56:38.4	...	...
J19031609-3714080	CrA-45 E	19:03:16.09	-37:14:08.2	M3.5	1
J19031609-3714080	CrA-45 W	19:03:16.09	-37:14:08.2	M3.5	1
J18564024-3655203	CrA-47	18:56:40.28	-36:55:20.8	M6	1
J18570785-3654041	CrA-48	18:57:07.86	-36:54:04.4	M5	1

Table 6.1: Continues from previous page

2MASS ID	Name	RA	DEC	SpT	Ref.
J19000157-3637054	CrA-52	19:00:01.58	-36:37:06.2	M1	10
J19011149-3645337	CrA-53	19:01:11.49	-36:45:33.8	M5	1
J19013912-3653292	CrA-54	19:01:39.15	-36:53:29.4	K7	9
J19015523-3723407	CrA-55	19:01:55.23	-37:23:41.0	K5	11
J19021667-3645493	CrA-56	19:02:16.66	-36:45:49.4	M4	4
J19032547-3655051	CrA-57	19:03:25.48	-36:55:05.3	M4.5	1
J19010860-3657200	SCrA N	19:01:08.62	-36:57:20	K3	6
J19010860-3657200	SCrA S	19:01:08.62	-36:57:20	M0	6
J19015878-3657498	TCrA	19:01:58.78	-36:57:49	F0	6
J19014081-3652337	TYCrA	19:01:40.83	-36:52:33.88	B9	6
J19041725-3659030	Halpha15	19:04:17.25	-36:59:03.0	M4	12
J19025464-3646191	ISO-CrA-177	19:02:54.65	-36:46:19.1	M4.5	4
...	G09-CrA-9	19:01:58.34	-37:01:06.0	...	...
J19015173-3655143	Haas17	19:01:51.74	-36:55:14.2	...	...
J19020410-3657013	IRS10	19:02:04.09	-36:57:01.2	...	...

References. (1) This work, (2) Bouy et al. (2004), (3) Romero et al. (2012), (4) López Martí et al. (2005), (5) Sicilia-Aguilar et al. (2011), (6) Forbrich and Preibisch (2007), (7) Sicilia-Aguilar et al. (2008), (8) Currie and Sicilia-Aguilar (2011), (9) Meyer and Wilking (2009), (10) Walter et al. (1997), (11) Herczeg and Hillenbrand (2014), (12) Patten (1998)

6.2   Sample selection

Peterson et al. (2011) present in their work a comprehensive catalogue of known Young Stellar Objects (YSOs) in the CrA star forming region selected based on *Spitzer*, 2MASS, *ROSAT*, and *Chandra* data. In addition to the these, they also added more YSOs from the literature. Their final catalogue includes a total of 116 YSOs, 14 of which are classified as Class I, 5 as Flat Spectrum (FS), 43 as Class II and 54 as Class III. The Infrared Class was determined by calculating the spectral slope α over the widest possible range of IR wavelengths as follows:

$$\alpha = \frac{\Delta \log (\lambda F_\lambda)}{\Delta \log \lambda}, \tag{6.1}$$

where λ is the wavelength and F_λ the flux at λ. Sources with $\alpha \geq 0.3$ are classified as Class I; FS have $-0.3 \leq \alpha < 0.3$; Class II have $-1.6 \leq \alpha < -0.3$;
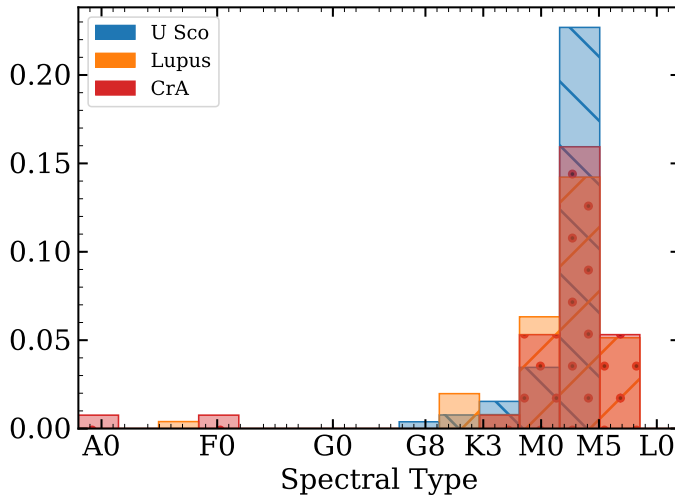
Figure 6.2: Distribution of the spectral types of the stars in CrA (Red) compared to that of Lupus (Orange) and Upper Sco (Blue).

sources with $\alpha < -1.6$ are Class III (Evans et al., 2009; Peterson et al., 2011). Fig. 6.1 shows the spatial distribution of the sources and their classification on top of the *Herschel* $250\,\mu$m map of the molecular Cloud.

Our sample includes all the Class II sources from the Peterson et al. (2011) catalogue. Two of them (CrA-49 and CrA-51) were later identified as background, evolved stars based on parallax measurements with Gaia (Gaia Collaboration et al., 2016; Lindegren et al., 2018; Luri et al., 2018; Gaia Collaboration et al., 2018b) and on our VLT/X-Shooter spectra (see Sec. 6.3.2). We then checked our sample against the more recently published survey by Dunham et al. (2015) in which the *Spitzer* data are re-analysed and the spectral slopes re-calculated. We find broad agreement between the classification in Peterson et al. (2011) and Dunham et al. (2015), except for a few very marginal cases at the boundaries of classes.

Our final sample contains 41 targets, two of which are clearly resolved binaries (S CrA and CrA-45). Of the 43 targeted disks, 24 are detected with ALMA. The spectral type (SpT) was known for only 26 of the stars from the literature. We obtained VLT/X-Shooter spectra for 11 of the remaining targets, and derived their properties as explained in Sec. 6.4.1.

The basic stellar properties for the CrA sample are given in Table 6.1, the distribution of SpTs is shown in Fig. 6.2, while the millimeter observations, flux densities, and calculated disk masses are presented in Table 6.3.

6.3 Observations

6.3.1 ALMA observations

We have carried out three executions of observations at 1.3 mm towards 43 Class II YSOs in the Corona Australis molecular cloud, using ALMA (2015.1.01058.S, PI: H. B. Liu).. Each one of the 43 target sources were integrated for approximately 1 minute in each epoch. The spectral setup consists of six spectral windows, of which the (central frequency [GHz], total bandwidth [MHz], and frequency channel width [kHz]) are (216.797, 1875, 488), (219.552, 59, 61), (219.941, 59, 61), (220.390, 117, 61), (230.531, 117, 31), (231.484, 1875, 488), respectively. Additional observational details are summarized in Table 6.2. ^{12}CO (2-1), ^{13}CO (2-1) and C^{18}O (2-1) transitions were also targeted with our spectral setup, but no clear detection was found because of strong foreground contamination. SO (6-5) and SiO (5-4) lines were also covered and not detected.

The data were manually calibrated using the CASA v5.1.1 software package (McMullin et al., 2007) . The gain calibrator for the first epoch of observations was faint. To yield reasonably high signal-to-noise (S/N) ratios when deriving the gain phase solutions, the phase offsets among spectral windows were first solved using the passband calibration scan. After applying the phase offsets solution, the gain phase solution was then derived by combining all spectral windows. The calibration of the other two epochs of observations followed the standard procedure of ALMA quality assurance (i.e., QA2). The bootstrapped flux values of the calibrator quasar J1924-2914 were consistent with the SMA Calibrator list[1] (Gurwell et al., 2007) to ∼10%. After calibration, we fit the continuum baseline and subtract it from the spectral line data, using the CASA task `uvcontsub`.

The continuum data imaging was performed with multi-frequency synthesis (MFS) imaging of the continuum data using the CASA-`clean` task, and correcting for the primary beam. By jointly imaging all three epochs of data, for each target source field, the achieved continuum root-mean-square (RMS) noise level is ∼0.15 mJy beam^{-1}, and the synthesized beam is $\theta_{\mathrm{maj}} \times \theta_{\mathrm{min}}$=0.$''$33×0.$''$31 (P.A.=67°), corresponding to a spatial resolution of ∼ 50 au at $d = 154$ pc. The imaged detections are presented in Fig. 6.3.

It is important to note that because of an error when setting the observation coordinates, the decimal places of the target RAs have been trimmed: this results in an offset of the sources of up to 15$''$ east of the phase center: as a consequence, our images had to be primary beam corrected. The images in

---

[1]http://sma1.sma.hawaii.edu/callist/callist.html
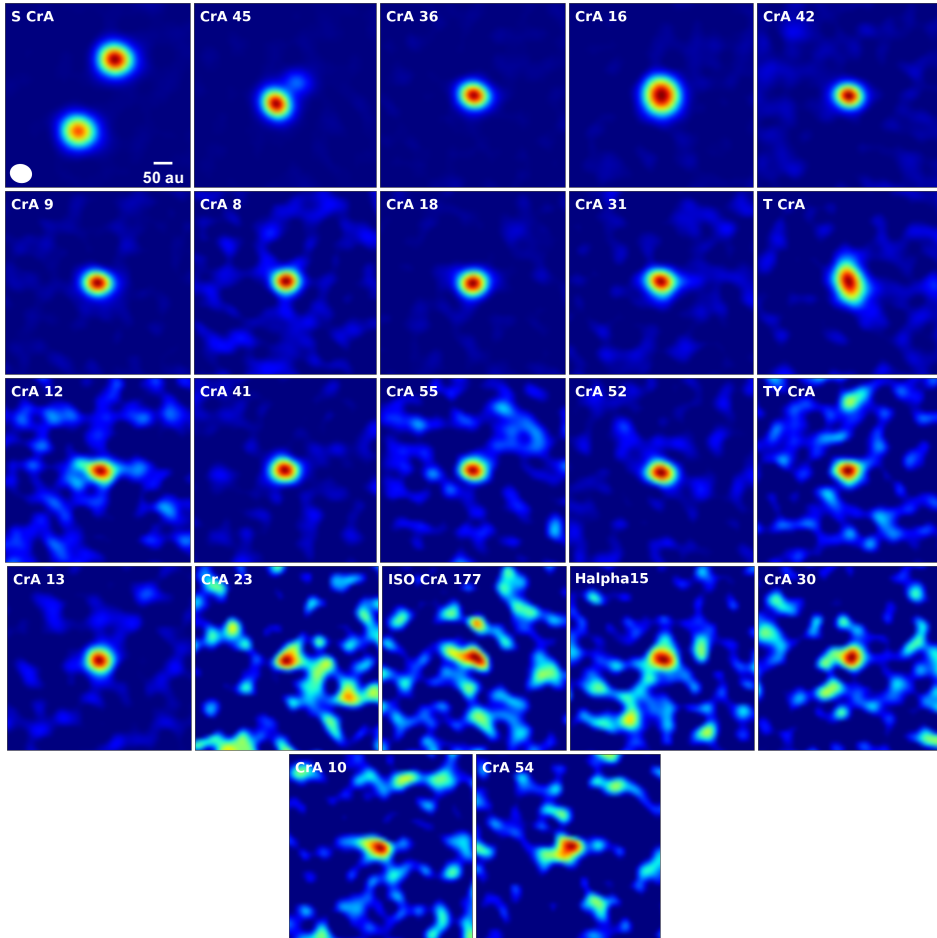
Figure 6.3: ALMA Band 6 1.3 mm continuum images of the 24 detections in Corona Australis. The size of the images is $3'' \times 3''$. The size of the beam is indicated at the bottom-left corner of the first panel ($0''.31 \times 0''.33$). The north of each image is upwards. The presented images have not been primary beam corrected.

Table 6.2: ALMA observations towards Class II objects in the CrA molecular cloud

Epoch	1	2	3
Time (UTC; 2016)	(Aug.01) 03:32-04:54	(Aug.01) 05:01-06:23	(Aug.02) 03:18-04:40
Project baseline lengths (min-max) [m]	14-1108	15-1075	15-1110
Absolute flux calibrator	Pallas	Pallas	Pallas
Gain calibrator	J1937-3958	J1924-2914	J1924-2914
Bootstrapped gain calibrator flux [Jy]	0.26	3.9	4.1
Passband calibration	J1924-2914	J1924-2914	J1924-2914
Bootstrapped passband calibrator flux [Jy]	4.1	3.9	4.1

Fig. 6.3 have therefore been re-centered using the best-fit positions in Tab. 6.3.

6.3.2   VLT/X-Shooter observations

The spectroscopic follow-up observations for the 13 targets with missing spectral type information were carried out in Pr.Id. 299.C-5048 (PI Manara) and Pr.Id. 0101.C-0893 (PI Cazzoletti) with the VLT/X-Shooter spectrograph (Vernet et al., 2011). This instrument covers the wavelength range from ∼300 nm to ∼2500 nm simultaneously, dividing the spectrum in three arms, the UVB ($\lambda\lambda \sim$ 300-550 nm), the VIS ($\lambda\lambda \sim$ 500-1050 nm), and the NIR ($\lambda\lambda \sim$ 1000-2500 nm). All targets were observed both with a narrow slit - $1.0''$ in the UVB, $0.9''$ in the VIS and NIR arms - leading to R∼9000 and ∼10000, respectively, and a wide slit of $5.0''$ used to obtain an accurate flux calibration of the spectra. The log of the observations is reported in Table 6.7. The spectra of all the observed targets are detected in the NIR arm, while only 5 targets are bright enough and not extincted too much to be detected also in the UVB arm.

The reduction of the data was performed using the ESO X-Shooter pipeline 2.9.3 (Modigliani et al., 2010). The pipeline performs the typical reduction steps, such as flat fielding, bias subtraction, order extraction and combination, rectification, wavelength calibration, flux calibration using standard stars observed in the same night. We extracted the 1D spectra from the 2D images produced by the pipeline using IRAF and then removed telluric absorption lines in the VIS and NIR arms using telluric standard stars observed close in time and airmass (see e.g., Alcalá et al. 2014). The S/N of the spectra at different wavelengths is reported in Table 6.7.

6.4   Results and analysis

6.4.1   Stellar properties

The spectral type for the targets were obtained from the literature (see Tab. 6.1) or from the VLT/X-Shooter spectra. The procedure used for the analysis of the X-Shooter spectra was as follows. First, we corrected the spectra for extinction using the values from the literature (Dunham et al., 2015; Sicilia-Aguilar et al., 2008, 2011) and the reddening law by Cardelli et al. (1989) with R_V=3.1, as suggested by Sicilia-Aguilar et al. (2008). Then, we calculated the values of a number of spectral indices both at wavelengths in the VIS and the NIR arms, taken by those calibrated by Riddick et al. (2007), Jeffries et al. (2007), and Herczeg and Hillenbrand (2014), as in Manara et al. (2017), and by Testi et al. (2001), as in Manara et al. (2013). The spectral types derived from these

Table 6.3: 1.3 mm continuum properties of the sources targeted in our sample.

Name	$\Delta\alpha$ ['']	$\Delta\delta$ ['']	$F_{1.3\,\mathrm{mm}}$ [mJy]	RMS [mJy beam^{-1}]	a_{maj} ['']	a_{min} ['']	PA [°]	M_{dust} [$M_\oplus$]
CrA-1	...	...	...	0.10	...	...	...	...
CrA-4	...	...	...	0.14	...	...	...	...
CrA-6	...	...	...	0.08	...	...	...	...
CrA-8	-0.14	0.39	2.06 ± 0.17	0.16	0.365 ± 0.018	0.31 ± 0.014	81.90 ± 13.3	1.50 ± 0.12
CrA-9	-0.01	0.35	5.07 ± 0.16	0.33	0.389 ± 0.008	0.31 ± 0.005	81.07 ± 3.4	3.70 ± 0.12
CrA-10	0.07	0.34	0.65 ± 0.11	0.22	0.481 ± 0.119	0.25 ± 0.034	73.11 ± 7.9	0.48 ± 0.15
CrA-12	-0.05	0.42	1.37 ± 0.24	0.10	0.661 ± 0.100	0.32 ± 0.030	90.67 ± 4.8	1.00 ± 0.17
CrA-13	0.06	0.27	2.77 ± 0.26	0.21	0.367 ± 0.021	0.35 ± 0.019	126.02 ± 60.2	2.02 ± 0.19
CrA-15	...	...	...	0.08	...	...	...	...
CrA-16	-0.23	0.45	20.34 ± 0.53	1.00	0.478 ± 0.008	0.44 ± 0.007	13.42 ± 11.5	14.84 ± 0.39
CrA-18	-0.20	0.52	5.36 ± 0.19	0.35	0.380 ± 0.008	0.32 ± 0.006	93.93 ± 5.3	3.92 ± 0.14
CrA-21	...	...	...	0.08	...	...	...	...
CrA-22	...	...	...	0.12	...	...	...	...
CrA-23	-0.26	0.76	0.35 ± 0.15	0.12	0.401 ± 0.120	0.28 ± 0.061	108.44 ± 24.8	0.26 ± 0.11
CrA-26	...	...	...	0.11	...	...	...	...
CrA-28	...	...	...	0.09	...	...	...	...
CrA-29	...	...	...	0.11	...	...	...	...
CrA-30	-0.36	0.61	0.51 ± 0.18	0.09	0.504 ± 0.139	0.27 ± 0.046	96.59 ± 10.6	0.37 ± 0.13
CrA-31	-0.28	0.60	2.82 ± 0.19	0.19	0.416 ± 0.019	0.33 ± 0.013	80.58 ± 7.3	2.05 ± 0.14
CrA-35	...	...	...	0.11	...	...	...	...
CrA-36	-0.14	0.38	12.9 ± 0.21	0.82	0.384 ± 0.004	0.32 ± 0.002	74.97 ± 2.1	9.41 ± 0.15
CrA-40	...	...	...	0.11	...	...	...	...
CrA-41	-0.34	0.62	2.80 ± 0.19	0.21	0.384 ± 0.017	0.30 ± 0.011	85.01 ± 6.7	2.04 ± 0.14
CrA-42	-1.00	0.34	4.87 ± 0.21	0.34	0.377 ± 0.010	0.31 ± 0.007	81.88 ± 4.9	3.55 ± 0.16
CrA-45 E	-0.36	0.63	29.82 ± 0.35	1.92	0.400 ± 0.003	0.34 ± 0.002	46.21 ± 1.7	21.76 ± 0.26

Table 6.3: Continues from previous page

Name	$\Delta\alpha$ ["]	$\Delta\delta$ ["]	$F_{1.3\,\mathrm{mm}}$ [mJy]	RMS [mJy beam^{-1}]	a_{maj} ["]	a_{min} ["]	PA [°]	M_{dust} [$M_\oplus$]
CrA-45 W	0.05	0.28	6.36 ± 0.34	1.92	0.393 ± 0.013	0.33 ± 0.009	87.43 ± 7.0	4.64 ± 0.25
CrA-47	...	...	...	0.09	...	...	...	...
CrA-48	...	...	...	0.12	...	...	...	...
CrA-52	0.05	-0.27	1.95 ± 0.17	0.16	0.404 ± 0.023	0.29 ± 0.012	70.00 ± 5.4	1.43 ± 0.12
CrA-53	...	...	...	0.10	...	...	...	...
CrA-54	0.61	-0.14	0.48 ± 0.19	0.09	0.577 ± 0.189	0.26 ± 0.044	105.67 ± 7.8	0.35 ± 0.14
CrA-55	-0.26	0.24	0.81 ± 0.14	0.10	0.354 ± 0.037	0.29 ± 0.025	96.62 ± 19.4	0.59 ± 0.10
CrA-56	...	...	...	0.10	...	...	...	...
CrA-57	...	...	...	0.10	...	...	...	...
S CrA S	-0.36	1.34	129.53 ± 2.09	10.4	0.451 ± 0.005	0.40 ± 0.004	75.03 ± 4.3	94.51 ± 1.52
S CrA N	0.23	0.13	140.30 ± 2.00	10.4	0.439 ± 0.004	0.39 ± 0.003	80.73 ± 3.7	102.36 ± 1.46
T CrA	-0.06	1.34	4.99 ± 0.37	0.28	0.568 ± 0.033	0.37 ± 0.016	20.25 ± 4.3	3.64 ± 0.27
TY CrA	0.01	0.46	0.91 ± 0.18	0.13	0.362 ± 0.044	0.28 ± 0.026	90.13 ± 14.6	0.66 ± 0.13
IRS10	...	...	...	0.08	...	...	...	...
Halpha15	-0.07	0.54	0.69 ± 0.22	0.08	0.529 ± 0.128	0.39 ± 0.078	142.60 ± 27.2	0.50 ± 0.16
ISO-CrA-177	-0.01	0.49	0.52 ± 0.17	0.11	0.535 ± 0.146	0.25 ± 0.037	71.91 ± 7.3	0.38 ± 0.13
Haas17	...	...	...	0.11	...	...	...	...
G09-CrA-9	...	...	...	0.09	...	...	...	...

Notes. † Offset with respect to coordinates listed in Tab. 6.1.

indices are presented in Tab. 6.6 in Appendix 6.B. The spectral indices in the VIS arms are more reliable, and we select the spectral type from these indices when available. The observed spectra along with a template of the relative Spectral Types are presented in Fig. 6.8.

The spectral types are converted in effective temperatures ($T_{\rm eff}$) using the relation by Herczeg and Hillenbrand (2014). Stellar luminosity ($L_\star$) is obtained from the reddening-corrected J-band magnitudes and using the bolometric correction from Herczeg and Hillenbrand (2014), assuming for all the target the average distance of 154 pc calculated by Dzib et al. (2018). With this information, we have been able to plot our data on the HR diagram (Fig. 6.6) and to estimate the stellar masses ($M_\star$) for all the targets using the evolutionary tracks by Baraffe et al. (2015) for $M_\star < 1.4 M_\odot$ and Siess et al. (2000) for higher $M_\star$ and ages younger than 1 Myr . The stellar parameters for the targets are reported in Tab. 6.5.

6.4.2   mm continuum emission

Among the 41 targets, 20 of them show a clear ($\geq 4\sigma$) detection within a $1''$ radius from the nominal *Spitzer* location from Peterson et al. (2011). In addition, CrA-42 and T CrA show a $\sim 36\sigma$ and a $\sim 22\sigma$ detection respectively at a slightly larger distance from their nominal *Spitzer* positions ($1''.05$ for CrA-42 and $1''.34$ T CrA), and are also regarded as detections. S CrA is a known binary (Reipurth and Zinnecker, 1993; Ghez et al., 1997; Takami et al., 2003), and we detected millimeter emission associated with both binary components. CrA-45 is also identified as a binary. The total number of detections is therefore 24 out of the 43 targeted disks, so the detection rate is $\sim 56\%$.

None of the disks show clear substructures, no transition disk with cavities with radius $> 25\,\mathrm{au}$ are found and all of them appear to be unresolved or marginally resolved: a Gaussian is therefore fitted to the detected sources (two Gaussians for the binaries) in the image plane using the `imfit` task in `CASA`. The task returns the total flux-density $F_{1.3\,\mathrm{mm}}$ of the source along with the statistical uncertainty, the FWHM along the semi-major ($a_{\rm maj}$) and semi-minor ($a_{\rm min}$) axis and the position angle (PA). The results of the fit are shown in Table 6.3[2] The right ascension offset ($\Delta\alpha$) and the declination offset ($\Delta\delta$) with respect to the *Spitzer* coordinates is also shown. The rms noise for the non-detections was calculated using the `imstat` task within a $1''$ radius centered at the *Spitzer* coordinates; for the detection, it was calculated in an annular region centered on the source and with inner and outer radii equal to $2''$ and $4''$, respectively.

---

[2]Note that the $F_{1.3\,\mathrm{mm}}$ uncertainty only includes the statistical uncertainty from the fit, and not the 10% absolute flux calibration uncertainty.

In order to constrain the average flux density of individually undetected sources, a stacking analysis was also performed. The images were centered at their *Spitzer* coordinates (Table 6.1) and then stacked. Even after the stacking, no detection was found and an average rms noise is $0.017\,\mathrm{mJy\,beam^{-1}}$, corresponding to a 3σ upper limit of $0.051\,\mathrm{mJy}$ is found assuming unresolved disks. However, it should be noted that the average offset between the disks and the *Spitzer* positions, measured on the detections, are $<\Delta\alpha> = -0.13''$ and $<\Delta\delta> = 0.47''$: it is therefore possible that the undetected sources did not overlap during the stacking, and that the upper limit is actually higher than that quoted.

6.4.3   Dust masses

Assuming that the observed sub-millimeter emission is optically thin and isothermal, the relation between the emitting dust mass (M_dust) and the observed continuum flux at frequency ν (F_ν) is as follows (Hildebrand, 1983):

$$M_\mathrm{dust} = \frac{F_\nu\, d^2}{\kappa_\nu\, B_\nu(T_\mathrm{dust})} \approx 2.19 \times 10^{-6} \left(\frac{d}{160}\right)^2 F_{1.3\,\mathrm{mm}}\,[\mathrm{M_\odot}], \qquad (6.2)$$

where d is the distance of the object, F_ν is measured the flux-density, $B_\nu(T_\mathrm{dust})$ is the Planck function for a given dust temperature T_dust and κ_ν is the dust opacity at frequency ν. To make the comparison with previous surveys easier, for the dust opacity κ_ν we follow the same approach of Ansdell et al. (2016), assuming $\kappa_\nu = 10\,\mathrm{cm^2\,g^{-1}}$ at 1000 GHz (Beckwith et al., 1990) and scaling it to our frequency using $\beta = 1$. The adopted value is therefore $\kappa_\nu = 2.3\,\mathrm{cm^2\,g^{-1}}$ at $\nu = 230\,\mathrm{GHz}$ (1.3 mm). In the right-hand side of Eq. 6.2, the distance d is measured in pc and the flux density $F_{1.3\,\mathrm{mm}}$ is in mJy. For each object, the average distance of the cluster $d = 154$ pc was used. For the dust temperature, we use a constant $T_\mathrm{dust} = 20\,\mathrm{K}$ (Andrews and Williams, 2005), rather than the $T_\mathrm{dust} = 25\,\mathrm{K} \times (L_*/L_\odot)^{0.25}$ relation based on two-dimensional continuum radiative transfer by Andrews et al. (2013) and used in other works (e.g. Law et al., 2017). We adopt this simplified approach with a single grain opacity and temperature for all the disks in the sample following the approach of Ansdell et al. (2016) and to facilitate the comparison with other star-forming regions (see Sec. 6.4.4). Moreover, it should be noted that no dependence of the average dust temperature on the stellar parameters was found with the more detailed modelling by Tazzari et al. (2017) for the Lupus disks.

The dust masses of the disks in our sample are presented in Tab. 6.3, along with the relative uncertainty calculated from the flux uncertainty. Only
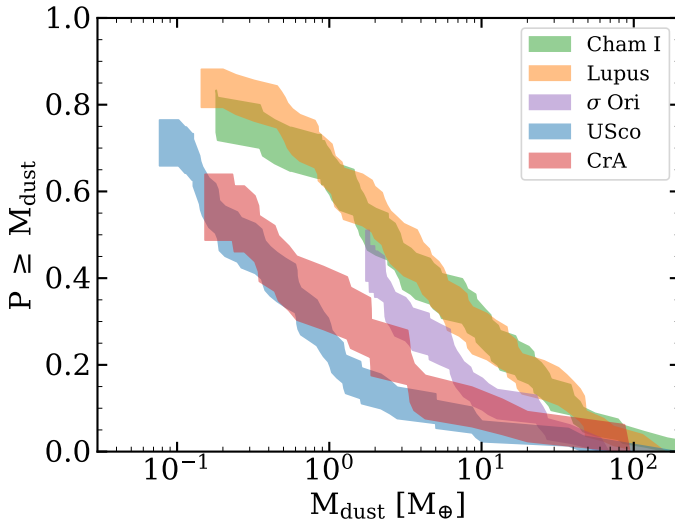
Figure 6.4: Comparison of the cumulative dust mass distributions of Lupus, CrA, Cham I, σ Ori and Upper Sco, derived using a survival analysis accounting for the upper limits.

3 disks out of 24 detections have a dust content $\geq 10\,M_\oplus$[3] and large enough to form the cores of giant planets in the future. However, it is still possible that a similar amount of dust mass is hidden at the inner few region due to very high optical depth (e.g. Zhu et al., 2010; Liu et al., 2017; Vorobyov et al., 2018). Also note that very recent high angular resolution ALMA and VLA observations of disks are revealing that an important amount of dust is located in dense regions such as rings (e.g. Andrews et al., 2018), which are optically thick at wavelengths around 1 mm (Dullemond et al., 2018). When optically thin emission is detected, higher masses are estimated (Carrasco-González et al., 2016).

The stacking of the non-detections gives an average 3σ upper limit corresponding to $0.036\,M_\oplus$, about 3 Lunar masses.

6.4.4   Comparison with other regions

The surveys of nearby star forming regions over the last years have shown growing evidence of a decrease in the mass of the disks with age, reflecting dust growth and disk dispersal. Ansdell et al. (2016, 2017) found consistent results, calculating the highest average mass in the youngest regions (1-3 Myrs),

---

[3]5 sources in total have a dust content $\geq 10\,M_\oplus$ if we also consider CrA-16 and CrA-36, which have dust masses only marginally below $10\,M_\oplus$.

Table 6.4: Global properties of the star forming regions surveyed with ALMA in order of age.

Name	Distance [pc]	Age [Myr]	Average dust mass $[M_\oplus]$
Taurus	129.5^1	1-3	13 ± 2
Lupus	$160^{1,\star}$	1-3	14 ± 3
CrA	$154\ ^1$	1-3	6 ± 3
Chameleon I	192^1	2-3	24 ± 9
IC 348	321^1	2-3	4 ± 1
σ Ori	388^1	3-5	7 ± 1
Upper Sco	144^3	5-10	5 ± 3

References. (1) Dzib et al. (2018) (2) Comerón (2008) (3) de Zeeuw et al. (1999) ⋆ The average distance of the 4 Lupus clouds was used.

and the lowest for the the oldest Upper Sco association (5-10 Myrs). The 2-3 Myrs old IC348 is the only exception, showing an average dust mass of only $4 \pm 1\,M_\oplus$ (between the average σ Orionis and that of Upper Sco) despite its young age. This can be explained by the low-mass stellar population in the region (Ruíz-Rodríguez et al., 2018) (also see Tab. 6.4).

The same analysis was done here for CrA. The dust masses are uniformly calculated following the approach used by Ansdell et al. (2016), namely using Eq. 6.2 with the continuum fluxes (or the $3\,\sigma$ upper limits) from our ALMA data or from the literature, assuming a uniform $T = 20\,\mathrm{K}$, and inputting the frequency of the observation for each specific dataset. The distances assumed for each region are listed in Tab. 6.4. For the Upper Sco region, only the disks classified as "full", "evolved" and "transitional" from the Barenfeld et al. (2016) sample are included, while the "debris" and Class III YSOs, which likely represent a separate evolutionary stage, are excluded. Finally, in order to facilitate the comparison with the other samples, in this analysis we only include the disks around stars with masses above the brown-dwarf limit ($M_\star \geq 0.1\,M_\odot$). The Kaplan-Meier estimator from the `lifelines`[4] and `ASURV` (Lavalley et al., 1992) packages were then used to estimate the cumulative mass distribution and to calculate the average dust mass and its uncertainty while properly accounting for the upper limits by using well-established techniques for left-censored data sets.

Fig. 6.4 presents the results accounting for the upper limits given by the
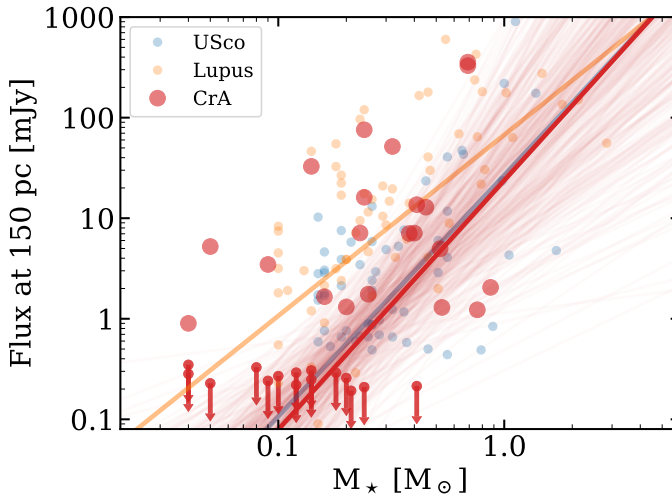
---

[4]10.5281/zenodo.1495175

Figure 6.5: Correlation between dust disk flux scaled at 330 GHz (assuming $\alpha = 2.25$, as in Ansdell et al., 2018) and at a distance of 150 pc with stellar mass for the objects in CrA. The slopes of Lupus and Upper Sco are also plotted for comparison. We show the results of the Bayesian fitting procedure by Kelly (2007). The solid line represents the best fit model, while the light lines show a subsample of models from the chains, giving an idea of the uncertainties.

non-detections. With an average dust mass of $6 \pm 3\,M_\oplus$, the distribution of the CrA disks appear closer to that of the old Upper Sco region rather than to those of the younger systems.

6.4.5 $M_{\mathrm{disk}} - M_\star$ relation

A clear correlation between the dust mass of disks and the mass of the central star has been identified across all protoplanetary disk populations surveyed (Pascucci et al., 2016; Ansdell et al., 2017). This finding highlights how the disk properties are affected by the central star, and is consistent with the correlation between frequency of giant planets and mass of the host star, both from the observational and theoretical points of view (Alibert et al., 2011; Bonfils et al., 2013). Moreover, the slope of this relation has been observed to steepen with time, with the young Taurus, Lupus and Chemeleon I regions ($\sim 1 - 3\,\mathrm{Myr}$) having slopes similar to each other and shallower than that found for the disks in the Upper Sco association ($5 - 10\,\mathrm{Myr}$).

Studying the $M_{\mathrm{dust}} - M_\star$ relation for the disks in the CrA sample contributes to gain insight on the origin of the overall low mass of the disk population found in Sec. 6.4.4. We derive the $M_{\mathrm{dust}} - M_\star$ relation using the same

linear-regression Bayesian approach followed by Ansdell et al. (2017) and presented by Kelly (2007)[5]. Unlike other linear regression methods, this approach is capable of simultaneously accounting for the uncertainties in both the measurements of M_{dust} and $M_\star$, of the intrinsic scatter of the data and of the disk non detections, which result in upper-limits on the disk masses. Note that the SpT, and therefore the stellar mass, is missing for 5 of our targets: for these objects the stellar mass is randomly drawn from the stellar mass distribution of the entire sample. In particular, 4 of the objects with unknown SpT are also not detected with ALMA, while the other one (CrA-42) shows a clear detection of a disk at mm-wavelengths. For the 4 non detections, the stellar mass is therefore randomly drawn among the masses of the stars with non-detected disks, while the mass of CrA-42 is drawn from those showing a detection with ALMA. This uncertainty is also taken into account in the Bayesian approach we adopt by performing 100 different draws. In our fit, a standard uncertainty of 20% of $M_\star$ on the stellar mass is assumed (Alcalá et al., 2017; Manara et al., 2017), while the uncertainties shown in Tab. 6.3 were used for the M_{dust} values. Finally, it should be noted that only 1 out of 89 sources in Lupus was a Herbig Ae/Be star, while Upper Sco did not include any Herbig. We therefore decided not to include T CrA and TY CrA in the fit , for which the $M_{dust} - M_\star$ relation might not hold.

The best fit relation we find is then plotted in Fig. 6.5 in dark red, along with a subsample of all the models in the chains to show the uncertainty. As in the other surveys, we also find a correlation, where the best-fit model has a slope $\beta = 2.32 \pm 0.77$ and intercept $\alpha = 1.29 \pm 0.60$. This regression intercept is lower that that of other regions, as a consequence of the low disk masses found in the region. The uncertainties of the best-fit parameters reflect the large scatter in the data and the low number statistics.

In order to test that no strong bias was introduced by our procedure, we also run the fit described above without any random draw, finding consistent results.

6.5   Discussion

6.5.1   Is CrA old?

The observed low disk dust masses suggest that the CrA objects targeted in our survey may have an age comparable to that of the Upper Sco association, rather than to the young Lupus region. Unlike CrA, however, Upper Sco shows

---

[5]https://github.com/jmeyers314/linmix

no presence of Class 0 or Class I sources, as expected for a $5 - 10$ Myr region (Dunham et al., 2015). Moreover, most studies agree in assigning Corona Australis an age < 3 Myr (e.g. Meyer and Wilking, 2009; Nisini et al., 2005; Sicilia-Aguilar et al., 2008, 2011).

On the other hand, most of these studies focused only on the *Coronet* cluster, a small region extending ~ 1 pc around the R CrA YSO, and where most of the young embedded Class 0 and Class I sources are located (see Fig. 6.1). The hypothesis that the large scale YSO population of the whole CrA cloud also includes a population of older objects therefore cannot be entirely ruled out. Some evidence of an additional older population has already been presented in previous studies. Neuhäuser et al. (2000) for example identify two classical T Tauri stars located outside the main cloud with an age of ~ 10 Myr using ROSAT data. In addition, Peterson et al. (2011) perform a clustering analysis of the 116 YSOs in their sample, identifying a single core (corresponding to the *Coronet*) and a more extended population of PMS stars showing an age gradient west of the *Coronet*. They also observe that in the central core, the ratio Class II/ Class I=1.8, while the same ratio is Class II/ Class I=2.3 when all the objects in the sample are considered, again hinting toward a younger
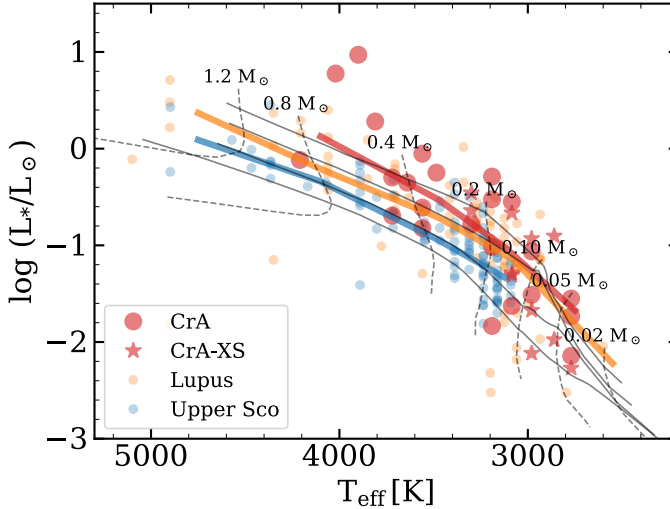
Figure 6.6: HR diagram showing the sources in our CrA sample (red), in the Lupus sample from Ansdell et al. (2016) (orange) and in the Upper Sco sample (blue) from Barenfeld et al. (2016). The evolutionary tracks for different stellar masses and the relative isochrones from Baraffe et al. (2015) are also plotted for reference. The isochrones refer (from top to bottom) to the 1 Myr, 2Myr, 5 Myr and 10 Myr isochrone. The coloured solid lines show the approximate median value of the luminosity at each temperature.

population inside the *Coronet*. Finally, Sicilia-Aguilar et al. (2011) point out that the relatively low disk fraction observed in the *Coronet* ($\sim 50\%$ López Martí et al., 2010, based on near IR photometry) is in strong contrast with the young age of the system: this inconsistency could be solved if an older population were also present. The large scatter in the $M_{\mathrm{dust}} - M_\star$ relation could also be a consequence of two stellar populations of different ages.

In order to further test if the Class II population in our sample indeed includes an older population, we have placed them on the HR diagram, by using the spectral types listed in Tab. 6.1 and by deriving effective temperatures and bolometric corrections using the relationships in Herczeg and Hillenbrand (2014) and tables in Herczeg and Hillenbrand (2015), respectively. The obtained diagram is presented in Fig. 6.6. For comparison, the Upper Sco and Lupus objects are also plotted. In contrast with what Fig. 6.4 suggests, the HR diagram supports the scenario of a young CrA cluster with an age more consistent to that of Lupus than to Upper Sco.

In order to make this conclusion evident, the median values of the bolometric luminosities for each temperature are also shown (solid coloured lines in Fig. 6.6). The indicative age of the cluster is the isochrone closer to those median values: these lines also suggest that CrA is younger than Upper Sco. However, a more extended spectral classification for a larger number of objects in CrA would be needed to fully test this older-population scenario.

6.5.2   Is CrA young?

If the whole CrA is coeval with an age of $1 - 3\,\mathrm{Myr}$, some other mechanism has to be invoked to explain the low observed mm fluxes. For example, these fluxes could be due to low metallicity. However, James et al. (2006) determined metallicities for three T Tauri stars in CrA, finding them to be only slightly sub-solar, and not low enough to explain our obesrvations.

External photo-evaporation is also known to play an important role in the disk mass evolution (Facchini et al., 2016; Winter et al., 2018b), and evidence of it occurring has been found in σ Ori (Maucó et al., 2016; Ansdell et al., 2017), where a clear correlation between disk mass and distance from the central Herbig O9V star has been observed and in the Orion Nebula Cluster (Mann and Williams, 2010; Eisner et al., 2018). However, in CrA no correlation between the mass of the disks (or the disk detection rate) and the distance from the brightest star (R CrA) is found. Moreover, in σ Ori external photo-evaporation has been shown to affect disks up to 2 pc away from the Herbig star, where the geometrically diluted far-ultraviolet (FUV) flux reached a value of $\sim 2000\,G_0$. The spectral type of R CrA is still uncertain, ranging from F5 (e.g. Garcia

Lopez et al., 2006) to B8 (e.g. Hamaguchi et al., 2005). Even in the latter case, assuming a typical FUV luminosity for a B8 star of $L_{\mathrm{FUV}} \sim 10\,\mathrm{L}_\odot$ (Antonellini et al., 2015) and accounting for geometric dilution, we find that the FUV flux would drop to $\sim 1\,G_0$ in the first inner pc from R CrA, thus ruling-out external photo-evaporation as an explanation. Also, this calculation neglects dust absorption, which is probably very effective in the Coronet cluster around R CrA.

Because of the $\mathrm{M}_{\mathrm{disk}} - \mathrm{M}_\star$ relation presented in Sec. 6.4.5, it is also possible that a system dominated by low-mass stars shows a low-mass disk population, regardless of its age, as in the case of IC348 (Ruíz-Rodríguez et al., 2018). It is therefore important, when comparing disk dust masses from different regions, to verify that they have the same stellar mass distribution. In order to do this, we employ a Monte Carlo (MC) approach similar to that used by Andrews et al. (2013). We first normalize the stellar populations by defining stellar mass bins and randomly drawing the same number of sources in each bin from the reference sample (CrA) and from a comparison sample (Lupus, Chamaeleon I or Upper Sco). We then perform a two-sample logrank test for censored datasets between the disk dust masses of the two samples, to test the probability (p_ϕ value) that the two samples are randomly drawn from the same parent population. A low p_ϕ value indicates that the difference in disk masses cannot only be ascribed to different stellar populations and that some other factor, such as disk evolution and the age of the system, must play a role. This process is repeated 10^4 times, and the results are used to create the cumulative distributions shown in Fig. 6.7. When using Upper Sco as a comparison sample, we find a median p_ϕ value of 0.53, while the median p_ϕ for Lupus is only 0.004. The conclusion is that even when accounting for the $\mathrm{M}_{\mathrm{dust}} - \mathrm{M}_\star$ relation, the disk dust mass distribution of CrA appears to be statistically different from that of Lupus, while it is significantly more similar to that from that of Upper Sco. Therefore, the comparably low masses of the protoplanetary disks in CrA cannot be explained in terms of the low stellar masses.

Another way a disk can lose part of its mass is via tidal interaction with other stars (e.g. Clarke and Pringle, 1993; Pfalzner et al., 2005). This mechanism is, however, only effective in much denser environments than CrA (e.g. Winter et al., 2018a). In principle, it is possible to imagine that at very early stages most of the stars were located in a dense region (e.g. the *Coronet*) where they interacted violently before being ejected. However, the very low velocity dispersion of the stars in the cluster makes this scenario very unlikely (Neuhäuser et al., 2000). Tidal interaction can be effective in removing dust mass from a disk even in later stages when the disk is in a binary system (e.g.
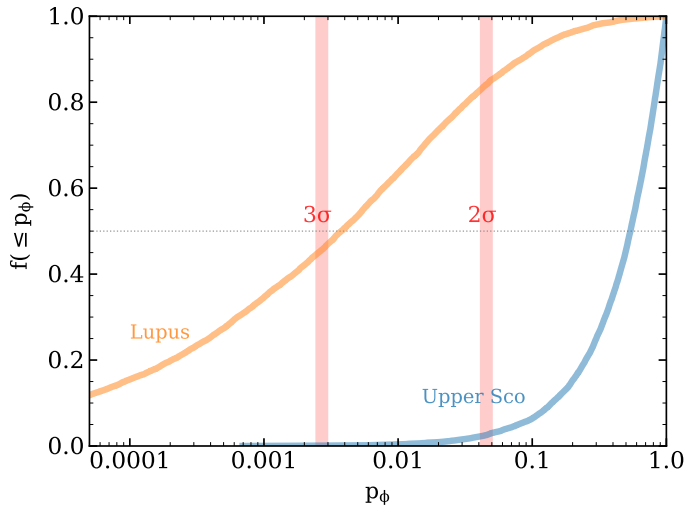
Figure 6.7: Comparison of the mass distributions of Lupus and USco to that of CrA, following the MC analysis proposed by Andrews et al. (2013). p_ϕ is the probability that the synthetic population drawn from the comparison sample (Lupus and Upper Sco) and the reference sample come from the same parent population. $f(< p_\phi)$ is the cumulative distribution for p_ϕ resulting from the logrank two-sample test for censored datasets after 10^4 MC iterations.

Artymowicz and Lubow, 1994), as proposed to explain the low mm flux of some objects in Taurus by Long et al. (2018). A higher than usual binary fraction could therefore explain the low disk masses observed in CrA. However, Ghez et al. (1997) show that the binary fraction of CrA is indistinguishable from those of Lupus and Chameleon I.

Finally it is possible that the low mass distribution observed today is a consequence of a population of disks that has formed with a low mass from the very beginning. For example, the disk formation efficiency in a cloud with mass M_0 depends on the sound speed c_s and on the solid body rotation rate Ω_0, where we have defined the disk formation efficiency as the fraction of M_0 that is in the disk at the end of the collapse stage, or as the ratio between $M_{\rm disk}/M_\star$ at that time (Cassen and Moosman, 1981; Terebey et al., 1984). In particular, clouds with higher c_s and Ω_0 (i.e. warmer or more turbulent) will form more massive disks (also see Appendix A in Visser et al., 2009). Therefore, a cold parent cloud or one with low intrinsic angular momentum Ω_0, will form disks with a lower mass, and with a lower $M_{\rm disk}/M_\star$ as observed in CrA. Consistently, observations of dense cloud cores in the CrA cloud show line-widths lower than in other regions (Tachihara et al., 2002). Moreover, because of the smaller

circularization radius, the formed disks would also be smaller (e.g. Dullemond et al., 2006) and potentially mostly optically thick, thus hiding an even larger fraction of the mass . Alternatively, small and optically thick disks could result from magnetic braking of the disks by means of the magnetic field threading the disk and the surrounding molecular cloud at the formation stage (e.g. Mellon and Li, 2008; Herczeg and Hillenbrand, 2014; Krumholz et al., 2013). The same scenario was proposed by Maury et al. (2019) to explain the low occurrence of large ($> 60\,$AU) Class 0 disks in the CALYPSO sample.

Such scenarios, although not testable with the present dataset, are consistent with the low disk mass distribution and with the low intercept of the $M_{disk} - M_\star$ in CrA and are not in contradiction with the young age of the stellar popultion. If the parent cloud initial conditions are indeed responsible for the low masses observed, this would be an additional critical aspect to be considered when studying planet formation and evolution. Since the conditions at the epoch of disk formation can be different in each star-forming region, proper modelling is required to assert to which extent they can affect the initial disk mass distribution, the subsequent disk evolution, planet formation and planetary populations.

Observationally, this could be tested by observing the mass of disks around Class 0 and Class I objects in CrA: if the disks are born with a low-mass, the disk mass distribution even at these younger stages should be significantly lower than in other regions.

6.6 Conclusion

We presented the first ALMA survey of 43 Class II protoplanetary disks in the Corona Australis nearby ($d = 160\,$pc) star forming region, in order to measure their dust content and understand how it scales with the stellar properties. The ultimate goal was to test if the relations between disk properties, age of the stellar population found in other surveys also hold for this region.

1. The average mm fluxes from the disks in CrA is low. This in turn converts into a low disk mass distribution. Even though our observations are able to constrain dust masses down to $\sim 0.2\,M_\oplus$, the detection rate is only 56%. Moreover, we find that only 3 disks in our sample have a dust mass $\geq 10\,M_\oplus$ and thus sufficient mass to form giant planet cores.

2. We obtained VLT/X-Shooter spectra for 8 objects with previously unknown spectral type, and derived their stellar physical properties.

3. Despite the apparent young age of the CrA stellar population, we find that the dust mass distribution of the disks in CrA is much lower than that of the Lupus young star forming region which shares a similar age, while it appears to be consistent with that in the 5-10 Myr old Upper Sco association. The correlation between disk dust mass M_{dust} and stellar mass $M_\star$ previously identified in all other surveyed star forming regions is confirmed. However, because of the low mass of the disks in our sample we find a much lower intercept. The large scatter of the data points does not allow the slope of the relation to be well constrained for CrA.

4. Since most of the age estimates of the CrA regions are based on the population of the compact *Coronet* cluster, a possible explanation for the low disk masses might be in principle that CrA also hosts an old population of disks, consistently with previous observations. The position of the objects of our sample on the HR diagram, however, seems to support the idea of a mostly coeval, young population.

5. Low disk masses in a young star forming region can be explained by external photo-evaporation (as in the case of σ Ori) or by a low stellar mass population (as in IC348). With our analysis, we can rule out both these scenarios for CrA. Tidal interaction between different members of CrA, stripping material from the disks, as well as close binaries can also be ruled out.

6. We suggest that initial conditions may play a crucial role in setting the initial disk mass distribution and its subsequent evolution. Small disks with low mass can originate from a cloud with very low turbulence or sound speed, or can alternatively result from disk magnetic braking. It is therefore important to better study the impact of initial conditions on the disk properties, especially if planet formation occurs even before 1 Myr age, as the recent results from Tychoniec et al. (2018) and Manara et al. (2018) suggest.

Future surveys including younger Class 0 and I objects in CrA and other star forming regions will help testing wether or not initial conditions play a critical role in shaping the physical properties of circumstellar disks.

6.A   Additional stellar properties

Tab. 6.5 shows a compilation of the most relevant stellar parameters used in our analysis. The J magnitude is taken from the 2MASS survey (Cutri et al., 2003).

The extinctions are either derived from our VLT/X-Shooter spectra or from the references in Column 4. Note that the extinctions from Dunham et al. (2015) were not derived from the stellar spectra but from extinction maps and might therefore systematically overestimate the real extinction towards the star by 1-2 mag (see Sec. 4.1 in Peterson et al., 2011). In order to make sure that the extinction values from Dunham et al. (2015) were accurate, we compared them to those derived from the spectra by Sicilia-Aguilar et al. (2011) for 8 targets common to the two samples. We found that the extinctions derived with the two methods are consistent within the uncertainties. The effective temperatures and bolometric luminosities have finally been derived as explained in Sec. 6.5.1 and then used to determine the stellar masses as explained in Sec. 6.4.1.

Table 6.5: Compilation of the most relevant stellar properties used in our analysis. Only the stars with known Spectral Type were included.

Source	J [mag]	A_{v} [mag]	Ref.	T_{eff} [K]	$\log L_\star/L_\odot$	$M_\star$ [$M_\odot$]
CrA-1	10.99	0.0	1	2860	-0.90	0.10[s]
CrA-4	13.98	3.3	2	2770	-1.73	0.04[b]
CrA-6	10.77	2.2	2	3190	-0.52	0.21[b]
CrA-8	12.92	1.2	2	2770	-1.55	0.05[b]
CrA-9	10.38	2.1	2	3720	-0.29	0.45[b]
CrA-10	14.19	2.7	3	3190	-1.83	0.16[b]
CrA-12	12.95	1.4	2	2980	-1.51	0.09[b]
CrA-13	12.83	8.1	3	3560	-0.61	0.38[b]
CrA-15	14.85	14.0	3	3300	-0.78	0.24[b]
CrA-16	14.45	17.0	3	3485	-0.24	0.32[b]
CrA-18	13.90	14.0	3	3640	-0.35	0.41[b]
CrA-21	14.91	13.5	3	3560	-0.82	0.41[b]
CrA-22	12.33	1.1	1	3085	-1.28	0.14[b]
CrA-23	14.08	0.08	3	2770	-2.14	0.04[b]
CrA-26	15.58	4.2	1	2770	-2.26	0.04[b]
CrA-28	13.41	1.9	3	3085	-1.62	0.12[b]
CrA-30	9.31	3.3	2	3810	0.28	0.53[s]
CrA-31	10.59	2.0	1	3300	-0.45	0.23[b]
CrA-35	12.03	2.1	2	2980	-1.06	0.12[b]
CrA-36	14.57	12.1	1	2980	-0.93	0.14[b]
CrA-40	11.61	4.0	1	3085	-0.66	0.18[b]
CrA-41	10.46	4.7	3	3560	-0.05	0.40[b]

Table 6.5: Continues from previous page

Source	J [mag]	A_{v} [mag]	Ref.	T_{eff} [K]	$\log L_\star/L_\odot$	$M_\star$ [$M_\odot$]
CrA-45	11.91	5.0	1	3300	-0.63	0.24[b]
CrA-47	13.67	0.0	1	2860	-1.97	0.05[b]
CrA-48	14.06	0.0	1	2980	-2.11	0.08[b]
CrA-52	10.82	0.2	3	3720	-0.69	0.52[b]
CrA-53	13.38	1.5	1	2980	-1.67	0.09[b]
CrA-54	7.60	1.4	3	4020	0.77	0.76[s]
CrA-55	9.78	1.0	3	4210	-0.11	0.87[b]
CrA-56	12	2.2	3	3190	-1.01	0.20[b]
CrA-57	12.31	0.8	1	3085	-1.31	0.14[b]
SCrA N	8.49*	7.9	2	3900	0.97	0.69[s]
SCrA S	8.49*	7.9	2	3900	0.97	0.69[s]
TCrA	8.93	7.9	2	7200	1.46	2.25[s]
TYCrA	7.49	7.9	2	10500	2.47	4.10[s]
Halpha15	11.82	0.8	4	3190	-0.28	0.25[s]
ISO-CrA-177	12.44	0.5	5	3085	-0.54	0.20[s]

A_{v} references. (1) This work (2) Dunham et al. (2015) (3) Sicilia-Aguilar et al. (2011) (4) Patten (1998) (5) López Martí et al. (2005)
Evolutionary Tracks. (s) Siess et al. (2000) (b) Baraffe et al. (2015)

6.B   VLT/X-Shooter Spectra

In this section we present the VLT/X-Shooter spectra obtained (Fig. 6.8). The Spectral Types derived from the different spectral indices calibrated are presented in Tab. 6.6. In particular, SpT VIS was obtained from the average values from Riddick et al. (2007), as in Manara et al. (2013, 2017); SpT TiO was obtained with the index by Jeffries et al. (2007); SpT NIR was obtained with the indices by Testi et al. (2001), as in Manara et al. (2013); the uncertainties represent the spread between the different indices in the VIS and NIR arms. The adopted spectral types, reported in the last column of Tab. 6.6, are taken from the indices calculated in the VIS arm of the spectrum. In addition, the log of the our X-Shooter observations is presented in Tab. 6.7 along with the Signal to Noise ratio achieved at different wavelengths.

Table 6.6: Spectral types derived from different spectral indices

Source	SpT VIS	SpT TiO	SpT NIR	SpT
CrA-1	M6.05±1.3	M5.46	M7.70±1.3	M6
CrA-22	M3.74±2.1	M4.48	M5.54±2.1	M4.5
CrA-26	M6.68±1.7	M0.64	L1 ±1.7	M7*
CrA-31	M3.66±3.0	M3.61	M7.96±3.0	M3.5
CrA-36	M4.86±2.3	M2.84	L1 ±2.3	M5*
CrA-40	M3.07±1.6	...	M6.42±1.6	M4.5*
CrA-42	M4.44±3.5	...	L2 ±3.5	...
CrA-45	M3.56±1.3	M2.22	M5.37±1.3	M3.5
CrA-47	M5.74±2.0	M5.87	L0.92±2.0	M6
CrA-48	M3.17±2.1	...	M5.22±2.1	M5*
CrA-53	M5.02±1.1	M5.13	M7.90±1.1	M5
CrA-57	M4.05±1.8	M4.57	M5.89±1.8	M4.5
IRS10	...	...	L1.87±5.4	...

$\star$ Uncertain estimate of SpT due to the low S/N of the spectra.

Table 6.7: Night log and basic information on the spectra. In Column 1 is the name of the source, in Column 2 the date and time of the observations, in Column 3-5 the exposure times, in Column 6-8 the slit widths, in Column 9-11 the S/N measured at the indicated wavelengths, in Column 12-13 we show whether or not the H_α and Li lines have been detected.

| Source	Date of observation [UT]	Exp. Time [$N_{exp} \times$ s]			Slit width ["]			S/N @ λ [nm]			H_α	Li
		UVB	VIS	NIR	UVB	VIS	NIR	400	700	1000		
		Pr.Id. 299.C-5048 (PI Manara)										
CrA-31	2017-09-01T03:30:30.048	4x215	4x135	4x3x75	1.0	0.9	0.9	8	20	21	Y	Y
CrA-36	2017-09-17T02:22:50.221	4x600	4x690	4x3x250	1.0	0.9	0.9	0	0	23	Y	N
CrA-42	2017-09-09T02:14:39.978	4x630	4x700	4x3x250	1.0	0.9	0.9	0	0	1	N	N
CrA-45	2017-09-06T00:37:53.044	4x440	4x340	4x3x150	1.0	0.9	0.9	0	24	1110	Y	Y
		Pr.Id. 0101.C-0893 (PI Cazzoletti)										
CrA-1	2018-05-28T04:25:20.708	4x90	4x150	4x150	1.0	0.9	0.9	24	14	35	Y	Y
CrA-22	2018-06-14T06:36:52.359	4x190	4x250	4x250	1.0	0.9	0.9	3	20	58	Y	...
CrA-26	2018-06-12T05:54:41.945	4x190	4x250	4x250	1.0	0.9	0.9	0	2	13	Y	N
CrA-40	2018-05-26T08:08:42.457	4x190	4x250	4x250	1.0	0.9	0.9	1	56	69	Y	Y
CrA-47	2018-06-15T04:01:23.919	4x190	4x250	4x250	1.0	0.9	0.9	1	13	309	Y	Y
CrA-48	2018-05-26T05:05:48.019	4x190	4x250	4x250	1.0	0.9	0.9	11	21	20	Y	N
CrA-53	2018-05-26T06:41:48.012	4x190	4x250	4x250	1.0	0.9	0.9	1	14	52	Y	Y
CrA-57	2018-05-27T05:18:45.651	4x90	4x150	4x150	1.0	0.9	0.9	3	17	83	Y	Y
IRS10	2018-06-11T06:08:20.787	4x190	4x250	4x250	1.0	0.9	0.9	0	0	2	N	N
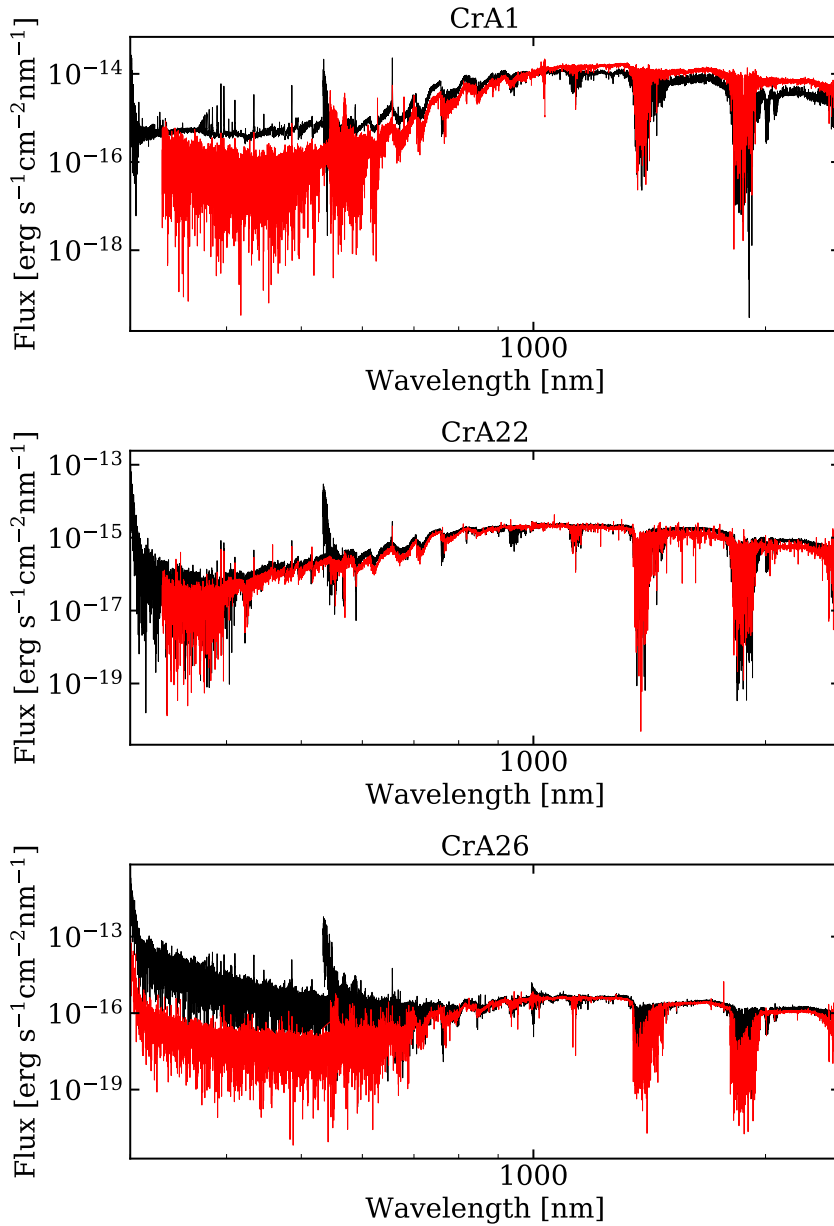
Figure 6.8: Spectra observed in our X-Shooter programs (black) along with a template with the same Spectral Type (red). The name of the sources is in the title of each subfigure. The absolute flux of each template was normalized to the flux of the observation at $\lambda = 1\mu m$.

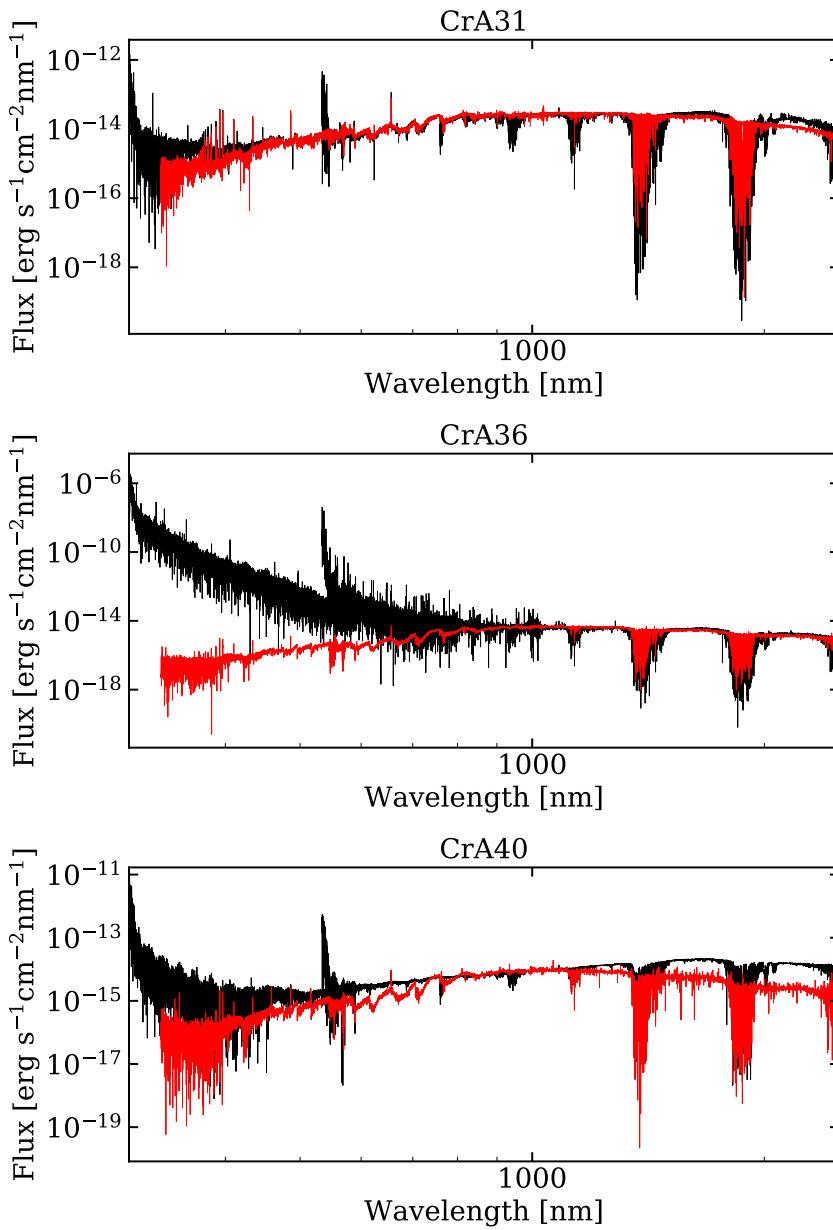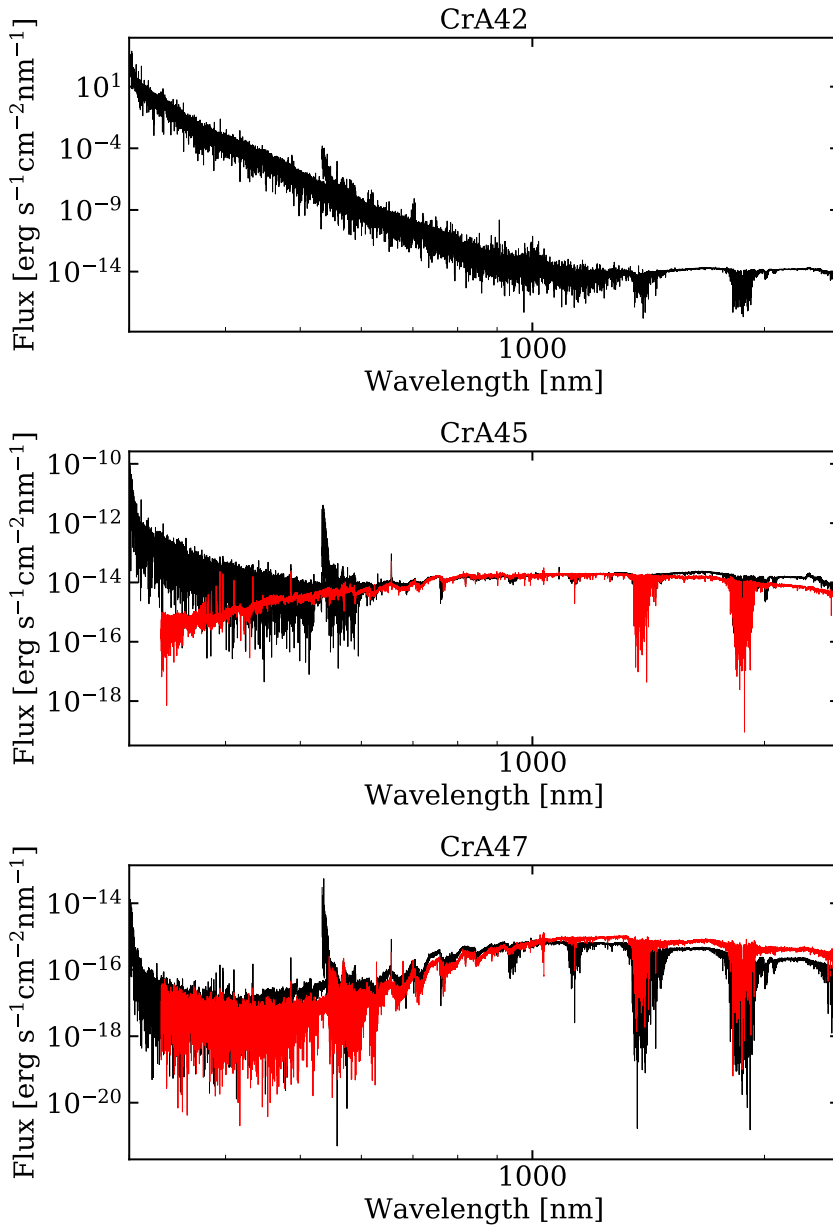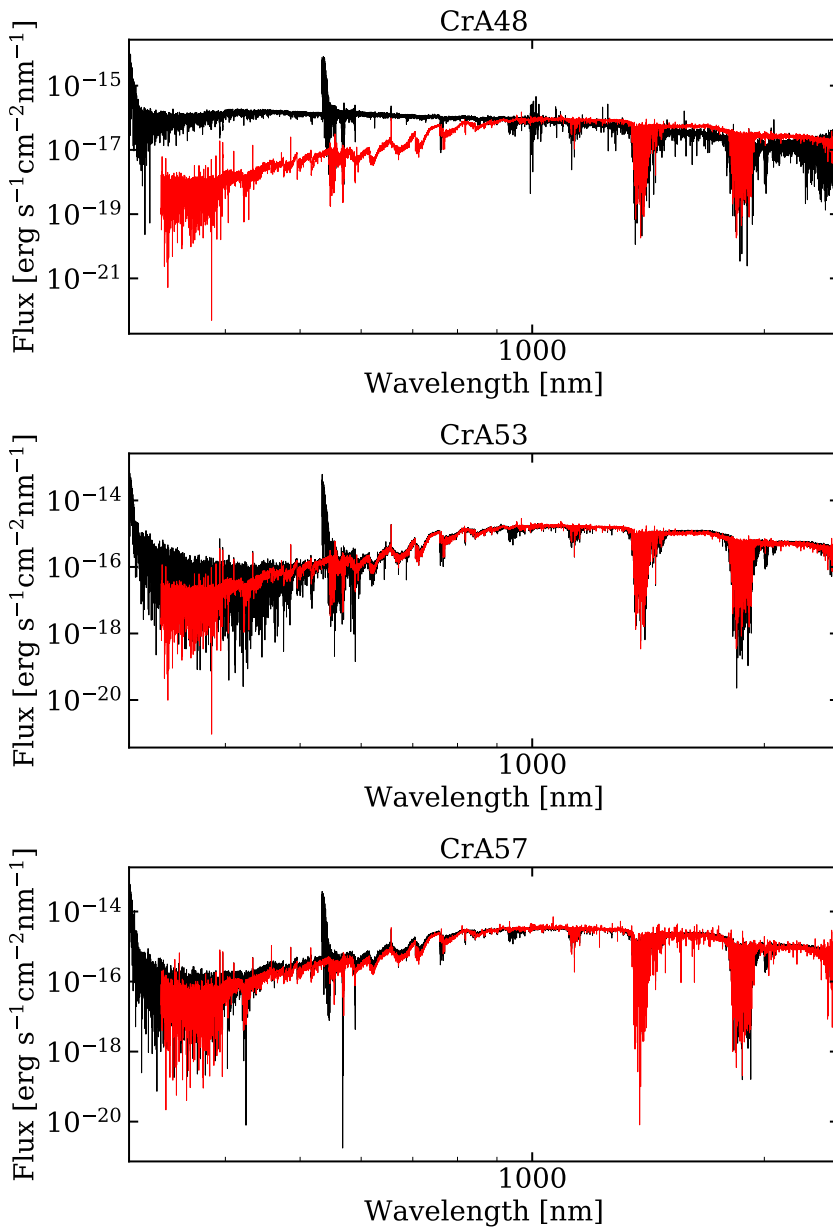**Figure 6.8:** Continued
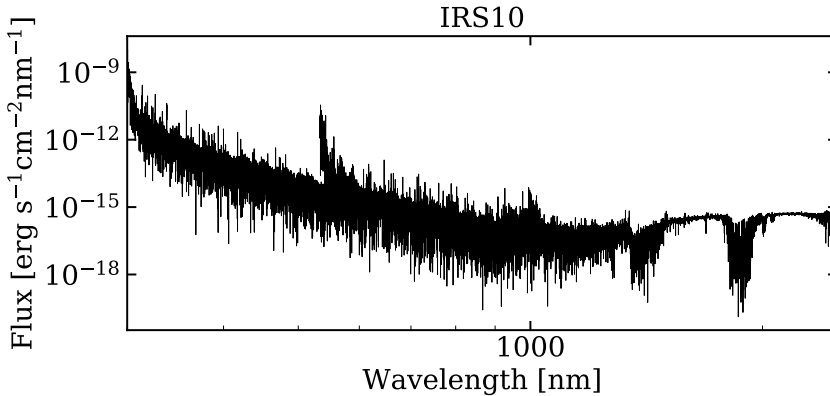
Figure 6.8: Continued

Figure 6.8: Continued

Figure 6.8: Continued

NINS (Japan), together with NRC (Canada) and NSC and ASIAA (Taiwan), in cooperation with the Republic of Chile. The Joint ALMA Observatory is operated by ESO, AUI/NRAO and NAOJ. All the figures were generated with the `python`-based package `matplotlib` (Hunter, 2007).

Bibliography

Alcalá, J. M., A. Natta, C. F. Manara, et al. 2014. *Astronomy and Astrophysics* 561, A2, A2.

Alcalá, J. M., C. F. Manara, A. Natta, et al. 2017. *Astronomy and Astrophysics* 600, A20, A20.

Alibert, Y., C. Mordasini, and W. Benz. 2011. *Astronomy and Astrophysics* 526, A63, A63.

ALMA Partnership, C. L. Brogan, L. M. Pérez, et al. 2015. *Astrophysical Journal, Letters to the Editor* 808.1, L3, p. L3.

Andre, P., D. Ward-Thompson, and M. Barsony. 1993. *Astrophysical Journal* 406, pp. 122–141.

Andrews, S. M. and J. P. Williams. 2007. *Astrophysical Journal* 671, pp. 1800–1812.

Andrews, S. M., C. J. Chandler, A. Isella, et al. 2014. *Astrophysical Journal* 787, 148, p. 148.

Andrews, S. M., J. Huang, L. M. Pérez, et al. 2018. *Astrophysical Journal, Letters to the Editor* 869, L41, p. L41.

Andrews, S. M. 2015. *Publications of the Astronomical Society of the Pacific* 127.956, p. 961.

Andrews, S. M. and J. P. Williams. 2005. *Astrophysical Journal* 631.2, pp. 1134–1160.

Andrews, S. M., D. J. Wilner, A. M. Hughes, et al. 2009. *Astrophysical Journal* 700.2, pp. 1502–1523.

Andrews, S. M., D. J. Wilner, C. Espaillat, et al. 2011. *Astrophysical Journal* 732.1, 42, p. 42.

Andrews, S. M., K. A. Rosenfeld, A. L. Kraus, et al. 2013. *Astrophysical Journal* 771.2, 129, p. 129.

Andrews, S. M., D. J. Wilner, Z. Zhu, et al. 2016. *Astrophysical Journal, Letters to the Editor* 820.2, L40, p. L40.

Ansdell, M., J. P. Williams, N. van der Marel, et al. 2016. *Astrophysical Journal* 828.1, 46, p. 46.

Ansdell, M., J. P. Williams, C. F. Manara, et al. 2017. *Astronomical Journal* 153.5, 240, p. 240.

Ansdell, M., J. P. Williams, L. Trapman, et al. 2018. *Astrophysical Journal* 859.1, 21, p. 21.

Antonellini, S., I. Kamp, P. Riviere-Marichalar, et al. 2015. *Astronomy and Astrophysics* 582, A105, A105.

Armitage, P. J. 2011. *Annual Review of Astronomy and Astrophysics* 49.1, pp. 195–236.

Artymowicz, P. and S. H. Lubow. 1994. *Astrophysical Journal* 421, pp. 651–667.

Ataiee, S., P. Pinilla, A. Zsom, et al. 2013. *Astronomy and Astrophysics* 553, L3, p. L3.

Avenhaus, H., S. P. Quanz, M. R. Meyer, et al. 2014. *Astrophysical Journal* 790.1, 56, p. 56.

Bae, J., Z. Zhu, and L. Hartmann. 2016. *Astrophysical Journal* 819.2, 134, p. 134.

Baraffe, I., D. Homeier, F. Allard, et al. 2015. *Astronomy and Astrophysics* 577, A42, A42.

Barenfeld, S. A., J. M. Carpenter, L. Ricci, et al. 2016. *Astrophysical Journal* 827.2, 142, p. 142.

Baruteau, C., A. Crida, S. J. Paardekooper, et al. 2014. *Protostars and Planets VI*. Ed. by H. Beuther, R. S. Klessen, C. P. Dullemond, et al., p. 667.

Baruteau, C. and Z. Zhu. 2016. *Monthly Notices of the RAS* 458.4, pp. 3927–3941.

Bate, M. R., I. A. Bonnell, and N. M. Price. 1995. *Monthly Notices of the RAS* 277, pp. 362–376.

Bate, M. R., G. Lodato, and J. E. Pringle. 2010. *Monthly Notices of the RAS* 401, pp. 1505–1513.

Baulch, D. L., C. T. Bowman, C. J. Cobos, et al. 2005. *Journal of Physical and Chemical Reference Data* 34.3, pp. 757–1397.

Beckwith, S. V. W. and A. I. Sargent. 1996. *Nature* 383.6596, pp. 139–144.

Beckwith, S. V. W., A. I. Sargent, R. S. Chini, et al. 1990. *Astronomical Journal* 99, p. 924.

Bell, C. P. M., T. Naylor, N. J. Mayne, et al. 2013. *Monthly Notices of the RAS* 434.1, pp. 806–831.

Benisty, M., A. Juhasz, A. Boccaletti, et al. 2015. *Astronomy and Astrophysics* 578, L6, p. L6.

Benisty, M., T. Stolker, A. Pohl, et al. 2017. *Astronomy and Astrophysics* 597, A42, A42.

Benz, W., S. Ida, Y. Alibert, et al. 2014. *Protostars and Planets VI*. Ed. by H. Beuther, R. S. Klessen, C. P. Dullemond, et al., p. 691.

Bergin, E. A., L. I. Cleeves, U. Gorti, et al. 2013. *Nature* 493.7434, pp. 644–646.

Bergin, E. A., F. Du, L. I. Cleeves, et al. 2016. *Astrophysical Journal* 831.1, 101, p. 101.

Beuzit, J.-L., M. Feldt, K. Dohlen, et al. 2008. *SPIE Proceedings*. Vol. 7014. Society of Photo-Optical Instrumentation Engineers (SPIE) Conference Series, p. 701418.

Birnstiel, T., C. P. Dullemond, and F. Brauer. 2010. *Astronomy and Astrophysics* 513, A79, A79.

Birnstiel, T., H. Klahr, and B. Ercolano. 2012. *Astronomy and Astrophysics* 539, A148, A148.

Birnstiel, T., C. P. Dullemond, and P. Pinilla. 2013a. *Astronomy and Astrophysics* 550, L8, p. L8.

— 2013b. *Astronomy and Astrophysics* 550, L8, p. L8.

Blum, J. and G. Wurm. 2008. *Annual Review of Astronomy and Astrophysics* 46, pp. 21–56.

Blum, J. 2018. *Space Science Review* 214.2, 52, p. 52.

Boehler, Y., E. Weaver, A. Isella, et al. 2017. *Astrophysical Journal* 840.1, 60, p. 60.

Bonfils, X., X. Delfosse, S. Udry, et al. 2013. *Astronomy and Astrophysics* 549, A109, A109.

Bonnell, I., J.-P. Arcoragi, H. Martel, et al. 1992. *Astrophysical Journal* 400, pp. 579–594.

Borucki, W. J., D. G. Koch, G. Basri, et al. 2011a. *Astrophysical Journal* 728.2, 117, p. 117.

Borucki, W. J., D. G. Koch, G. Basri, et al. 2011b. *Astrophysical Journal* 736.1, 19, p. 19.

Bouy, H., W. Brandner, E. L. Martín, et al. 2004. *Astronomy and Astrophysics* 424, pp. 213–226.

Brauer, F., C. P. Dullemond, A. Johansen, et al. 2007. *Astronomy and Astrophysics* 469, pp. 1169–1182.

Brauer, F., C. P. Dullemond, and T. Henning. 2008. *Astronomy and Astrophysics* 480, pp. 859–877.

Brown, J. M., G. A. Blake, C. P. Dullemond, et al. 2007. *Astrophysical Journal, Letters to the Editor* 664.2, pp. L107–L110.

Brown, J. M., G. A. Blake, C. Qi, et al. 2009. *Astrophysical Journal* 704.1, pp. 496–502.

Bruderer, S., E. F. van Dishoeck, S. D. Doty, et al. 2012. *Astronomy and Astrophysics* 541, A91, A91.

Bruderer, S. 2013. *Astronomy and Astrophysics* 559, A46, A46.

Bruderer, S., N. van der Marel, E. F. van Dishoeck, et al. 2014. *Astronomy and Astrophysics* 562, A26, A26.

Bruderer, S., D. Harsono, and E. F. van Dishoeck. 2015. *Astronomy and Astrophysics* 575, A94, A94.

Cardelli, J. A., G. C. Clayton, and J. S. Mathis. 1989. *Astrophysical Journal* 345, p. 245.

Carmona, A., C. Pinte, W. F. Thi, et al. 2014. *Astronomy and Astrophysics* 567, A51, A51.

Carrasco-González, C., T. Henning, C. J. Chand ler, et al. 2016. *Astrophysical Journal, Letters to the Editor* 821.1, L16, p. L16.

Casassus, S., G. van der Plas, S. P. M, et al. 2013. *Nature* 493, pp. 191–194.

Casassus, S., C. M. Wright, S. Marino, et al. 2015. *Astrophysical Journal* 812.2, 126, p. 126.

Casassus, S., S. Marino, W. Lyra, et al. 2019. *Monthly Notices of the RAS* 483.3, pp. 3278–3287.

Cassen, P. and A. Moosman. 1981. *Icarus* 48.3, pp. 353–376.

Chapillon, E., S. Guilloteau, A. Dutrey, et al. 2012. *Astronomy and Astrophysics* 537, A60, A60.

Chiang, E. I. and R. A. Murray-Clay. 2004. *Astrophysical Journal* 607, pp. 913–920.

Christiaens, V., S. Casassus, S. Perez, et al. 2014. *Astrophysical Journal, Letters to the Editor* 785.1, L12, p. L12.

Cieza, L. A., J. J. Swift, G. S. Mathews, et al. 2008. *Astrophysical Journal, Letters to the Editor* 686.2, p. L115.

Cieza, L. A., D. Ruíz-Rodríguez, A. Hales, et al. 2019. *Monthly Notices of the RAS* 482.1, pp. 698–714.

Clarke, C. J. and J. E. Pringle. 1993. *Monthly Notices of the RAS* 261.1, pp. 190–202.

Cleeves, L. I., E. A. Bergin, C. Qi, et al. 2015. *Astrophysical Journal* 799.2, 204, p. 204.

Comerón, F. 2008. *Handbook of Star Forming Regions, Volume II: The Southern Sky ASP Monograph Publications, Vol. 5. Edited by Bo Reipurth, p.295.* Ed. by B. Reipurth. Vol. 5, p. 295.

Currie, T. and A. Sicilia-Aguilar. 2011. *Astrophysical Journal* 732.1, 24, p. 24.

Cutri, R. M., M. F. Skrutskie, S. van Dyk, et al. 2003.

D'Alessio, P., N. Calvet, L. Hartmann, et al. 2006. *Astrophysical Journal* 638.1, pp. 314–335.

Davidson, D. F., D. C. Snell, and R. K. Hanson. 1990. *American Institute of Physics Conference Series.* Vol. 208, pp. 525–530.

de Val-Borro, M., P. Artymowicz, G. D'Angelo, et al. 2007. *Astronomy and Astrophysics* 471.3, pp. 1043–1055.

de Zeeuw, P. T., R. Hoogerwerf, J. H. J. de Bruijne, et al. 1999. *Astronomical Journal* 117.1, pp. 354–399.

Debes, J. H., H. Jang-Condell, A. J. Weinberger, et al. 2013. *Astrophysical Journal* 771.1, 45, p. 45.

Di Folco, E., A. Dutrey, J.-B. Le Bouquin, et al. 2014. *Astronomy and Astrophysics* 565, L2, p. L2.

Dipierro, G., D. Price, G. Laibe, et al. 2015a. *Monthly Notices of the RAS* 453, pp. L73–L77.

Dipierro, G., G. Laibe, D. J. Price, et al. 2016. *Monthly Notices of the RAS* 459, pp. L1–L5.

Dipierro, G., P. Pinilla, G. Lodato, et al. 2015b. *Monthly Notices of the RAS* 451.1, pp. 974–986.

Dominik, C. and A. G. G. M. Tielens. 1997. *Astrophysical Journal* 480.2, pp. 647–673.

Dong, R. and J. Fung. 2017. *Astrophysical Journal* 835.1, 38, p. 38.

Dong, R., Z. Zhu, R. R. Rafikov, et al. 2015a. *Astrophysical Journal, Letters to the Editor* 809.1, L5, p. L5.

Dong, R., C. Hall, K. Rice, et al. 2015b. *Astrophysical Journal, Letters to the Editor* 812.2, L32, p. L32.

Dong, R., S.-y. Liu, J. Eisner, et al. 2018. *Astrophysical Journal* 860.2, 124, p. 124.

Doyle, L. R., J. A. Carter, D. C. Fabrycky, et al. 2011. *Science* 333, pp. 1602–.

Draine, B. T. 2006. *Astrophysical Journal* 636, pp. 1114–1120.

Duchêne, G., C. McCabe, A. M. Ghez, et al. 2004. *Astrophysical Journal* 606, pp. 969–982.

Dullemond, C. P., A. Natta, and L. Testi. 2006. *Astrophysical Journal, Letters to the Editor* 645.1, pp. L69–L72.

Dullemond, C. P., T. Birnstiel, J. Huang, et al. 2018. *Astrophysical Journal, Letters to the Editor* 869.2, L46, p. L46.

Dunham, M. M., L. E. Allen, I. Evans Neal J., et al. 2015. *Astrophysical Journal, Supplement* 220.1, 11, p. 11.

Duquennoy, A. and M. Mayor. 1991. *Astronomy and Astrophysics* 248, pp. 485–524.

Dutrey, A., S. Guilloteau, and M. Simon. 1994. *Astronomy and Astrophysics* 286, pp. 149–159.

Dutrey, A., S. Guilloteau, G. Duvert, et al. 1996. *Astronomy and Astrophysics* 309, pp. 493–504.

Dutrey, A., S. Guilloteau, and M. Guelin. 1997. *Astronomy and Astrophysics* 317, pp. L55–L58.

Dutrey, A., D. Semenov, E. Chapillon, et al. 2014. *Protostars and Planets VI*, pp. 317–338.

Dzib, S. A., L. Loinard, G. N. Ortiz-León, et al. 2018. *Astrophysical Journal* 867.2, 151, p. 151.

Eisner, J. A., R. L. Plambeck, J. M. Carpenter, et al. 2008. *Astrophysical Journal* 683.1, pp. 304–320.

Eisner, J. A., H. G. Arce, N. P. Ballering, et al. 2018. *Astrophysical Journal* 860.1, 77, p. 77.

Elias, J. H. 1978. *Astrophysical Journal* 224, pp. 857–872.

Evans Neal J., I., M. M. Dunham, J. K. Jørgensen, et al. 2009. *Astrophysical Journal, Supplement* 181.2, pp. 321–350.

Facchini, S., G. Lodato, and D. J. Price. 2013. *Monthly Notices of the RAS* 433, pp. 2142–2156.

Facchini, S., L. Ricci, and G. Lodato. 2014. *Monthly Notices of the RAS* 442, pp. 3700–3710.

Facchini, S., T. Birnstiel, S. Bruderer, et al. 2017. *Astronomy and Astrophysics* 605, A16, A16.

Facchini, S., P. Pinilla, E. F. van Dishoeck, et al. 2018. *Astronomy and Astrophysics* 612, A104, A104.

Facchini, S., C. J. Clarke, and T. G. Bisbas. 2016. *Monthly Notices of the RAS* 457.4, pp. 3593–3610.

Favre, C., L. I. Cleeves, E. A. Bergin, et al. 2013. *Astrophysical Journal, Letters to the Editor* 776.2, L38, p. L38.

Fedele, D., M. E. van den Ancker, T. Henning, et al. 2010. *Astronomy and Astrophysics* 510, A72, A72.

Fedele, D., S. Bruderer, E. F. van Dishoeck, et al. 2013. *Astrophysical Journal, Letters to the Editor* 776.1, L3, p. L3.

Fedele, D., M. Carney, M. R. Hogerheijde, et al. 2017. *Astronomy and Astrophysics* 600, A72, A72.

Fedele, D., M. Tazzari, R. Booth, et al. 2018. *Astronomy and Astrophysics* 610, A24, A24.

Fischer, D. A. and G. W. Marcy. 1992. *Astrophysical Journal* 396, pp. 178–194.

Flebbe, O., S. Muenzel, H. Herold, et al. 1994. *Astrophysical Journal* 431, pp. 754–760.

Flock, M., J. P. Ruge, N. Dzyurkevich, et al. 2015. *Astronomy and Astrophysics* 574, A68, A68.

Follette, K. B., J. Rameau, R. Dong, et al. 2017. *Astronomical Journal* 153.6, 264, p. 264.

Forbrich, J. and T. Preibisch. 2007. *Astronomy and Astrophysics* 475.3, pp. 959–972.

Foreman-Mackey, D., D. W. Hogg, D. Lang, et al. 2013. *Publications of the Astronomical Society of the Pacific* 125.925, p. 306.

Foucart, F. and D. Lai. 2014. *Monthly Notices of the RAS* 445, pp. 1731–1744.

Fu, W., H. Li, S. Lubow, et al. 2014. *Astrophysical Journal, Letters to the Editor* 795.2, L39, p. L39.

Fuente, A., C. Baruteau, R. Neri, et al. 2017. *Astrophysical Journal, Letters to the Editor* 846.1, L3, p. L3.

Fung, J. and R. Dong. 2015. *Astrophysical Journal, Letters to the Editor* 815.2, L21, p. L21.

Gaia Collaboration, T. Prusti, J. H. J. de Bruijne, et al. 2016. *Astronomy and Astrophysics* 595, A1, A1.

Gaia Collaboration, C. Babusiaux, F. van Leeuwen, et al. 2018a. *Astronomy and Astrophysics* 616, A10, A10.

Gaia Collaboration, A. G. A. Brown, A. Vallenari, et al. 2018b. *Astronomy and Astrophysics* 616, A1, A1.

Galli, D. and F. H. Shu. 1993. *Astrophysical Journal* 417, p. 220.

Garcia Lopez, R., A. Natta, L. Testi, et al. 2006. *Astronomy and Astrophysics* 459.3, pp. 837–842.

Garufi, A., S. P. Quanz, H. Avenhaus, et al. 2013. *Astronomy and Astrophysics* 560, A105, A105.

Garufi, A., G. Meeus, M. Benisty, et al. 2017. *Astronomy and Astrophysics* 603, A21, A21.

Ghez, A. M., D. W. McCarthy, J. L. Patience, et al. 1997. *Astrophysical Journal* 481.1, pp. 378–385.

Gingold, R. A. and J. J. Monaghan. 1977. *Monthly Notices of the RAS* 181, pp. 375–389.

Ginski, C., T. Stolker, P. Pinilla, et al. 2016. *Astronomy and Astrophysics* 595, A112, A112.

Grady, C. A., G. Schneider, M. L. Sitko, et al. 2009. *Astrophysical Journal* 699.2, pp. 1822–1842.

Grady, C. A., T. Muto, J. Hashimoto, et al. 2013. *Astrophysical Journal* 762.1, 48, p. 48.

Greene, T. P., B. A. Wilking, P. Andre, et al. 1994. *Astrophysical Journal* 434, p. 614.

Guilloteau, S., A. Dutrey, and M. Simon. 1999. *Astronomy and Astrophysics* 348, pp. 570–578.

Guilloteau, S., E. Di Folco, A. Dutrey, et al. 2013. *Astronomy and Astrophysics* 549, A92, A92.

Guilloteau, S., M. Simon, V. Piétu, et al. 2014. *Astronomy and Astrophysics* 567, A117, A117.

Gundlach, B. and J. Blum. 2015. *Astrophysical Journal* 798, 34, p. 34.

Gurwell, M. A., A. B. Peck, S. R. Hostler, et al. 2007. *From Z-Machines to ALMA: (Sub)Millimeter Spectroscopy of Galaxies.* Ed. by A. J. Baker, J. Glenn, A. I. Harris, et al. Vol. 375. Astronomical Society of the Pacific Conference Series, p. 234.

Guzmán, V. V., K. I. Öberg, R. Loomis, et al. 2015. *Astrophysical Journal* 814.1, 53, p. 53.

Haffert, S. Y., A. J. Bohn, J. de Boer, et al. 2019. *Nature Astronomy* 3, pp. 749–754.

Haisch Karl E., J., E. A. Lada, and C. J. Lada. 2001. *Astrophysical Journal, Letters to the Editor* 553.2, pp. L153–L156.

Hamaguchi, K., S. Yamauchi, and K. Koyama. 2005. *Astrophysical Journal* 618.1, pp. 360–384.

Hammer, M., P. Pinilla, K. M. Kratter, et al. 2019. *Monthly Notices of the RAS* 482.3, pp. 3609–3621.

Harris, R. J., S. M. Andrews, D. J. Wilner, et al. 2012. *Astrophysical Journal* 751, 115, p. 115.

Hartmann, L., N. Calvet, E. Gullbring, et al. 1998. *Astrophysical Journal* 495, pp. 385–400.

Heays, A. N., A. D. Bosman, and E. F. van Dishoeck. 2017. *Astronomy and Astrophysics* 602, A105, A105.

Herbig, G. H. 1950. *Astrophysical Journal* 111, p. 11.

Herczeg, G. J. and L. A. Hillenbrand. 2014. *Astrophysical Journal* 786.2, 97, p. 97.

— 2015. *Astrophysical Journal* 808.1, 23, p. 23.

Hernández, J., L. Hartmann, T. Megeath, et al. 2007. *Astrophysical Journal* 662.2, pp. 1067–1081.

Hildebrand, R. H. 1983. *Quarterly Journal of the Royal Astronomical Society* 24, pp. 267–282.

Hily-Blant, P., V. Magalhaes, J. Kastner, et al. 2017. *Astronomy and Astrophysics* 603, L6, p. L6.

Hioki, T., Y. Itoh, Y. Oasa, et al. 2011. *Publications of the Astronomical Society of Japan* 63, pp. 543–.

Hunter, J. D. 2007. *Computing in Science and Engineering* 9.3, pp. 90–95.

Inaba, S. and P. Barge. 2006. *Astrophysical Journal* 649.1, pp. 415–427.

Isella, A., J. M. Carpenter, and A. I. Sargent. 2010. *Astrophysical Journal* 714.2, pp. 1746–1761.

Isella, A., G. Guidi, L. Testi, et al. 2016. *Physical Review Letters* 117.25, 251101, p. 251101.

Isella, A., M. Benisty, R. Teague, et al. 2019. *Astrophysical Journal, Letters to the Editor* 879.2, L25, p. L25.

James, D. J., C. Melo, N. C. Santos, et al. 2006. *Astronomy and Astrophysics* 446.3, pp. 971–983.

Jansen, D. J., M. Spaans, M. R. Hogerheijde, et al. 1995. *Astronomy and Astrophysics* 303, p. 541.

Jeffries, R. D., J. M. Oliveira, T. Naylor, et al. 2007. *Monthly Notices of the RAS* 376.2, pp. 580–598.

Johansen, A., J. S. Oishi, M.-M. Mac Low, et al. 2007. *Nature* 448.7157, pp. 1022–1025.

Juhász, A., M. Benisty, A. Pohl, et al. 2015. *Monthly Notices of the RAS* 451.2, pp. 1147–1157.

Kama, M., S. Bruderer, E. F. van Dishoeck, et al. 2016. *Astronomy and Astrophysics* 592, A83, A83.

Kastner, J. H., B. Zuckerman, P. Hily-Blant, et al. 2008. *Astronomy and Astrophysics* 492.2, pp. 469–473.

Kastner, J. H., P. Hily-Blant, D. R. Rodriguez, et al. 2014. *Astrophysical Journal* 793.1, 55, p. 55.

Kastner, J. H., C. Qi, U. Gorti, et al. 2015. *Astrophysical Journal* 806.1, 75, p. 75.

Kelly, B. C. 2007. *Astrophysical Journal* 665.2, pp. 1489–1506.

Kennedy, G. M., M. C. Wyatt, B. Sibthorpe, et al. 2012. *Monthly Notices of the RAS* 421, pp. 2264–2276.

Keppler, M., M. Benisty, A. Müller, et al. 2018. *Astronomy and Astrophysics* 617, A44, A44.

Klahr, H. H. and T. Henning. 1997. *Icarus* 128.1, pp. 213–229.

Kley, W. and R. P. Nelson. 2012. *Annual Review of Astronomy and Astrophysics* 50, pp. 211–249.

Koerner, D. W., A. I. Sargent, and S. V. W. Beckwith. 1993. *Icarus* 106.1, pp. 2–10.

Köhler, R. 2011. *Astronomy and Astrophysics* 530, A126, A126.

Koller, J., H. Li, and D. N. C. Lin. 2003. *Astrophysical Journal, Letters to the Editor* 596.1, pp. L91–L94.

Kostov, V. B., P. R. McCullough, T. C. Hinse, et al. 2013. *Astrophysical Journal* 770, 52, p. 52.

Kostov, V. B., P. R. McCullough, J. A. Carter, et al. 2014. *Astrophysical Journal* 784, 14, p. 14.

Kraus, S., A. Kreplin, M. Fukugawa, et al. 2017. *Astrophysical Journal, Letters to the Editor* 848.1, L11, p. L11.

Krumholz, M. R., R. M. Crutcher, and C. L. H. Hull. 2013. *Astrophysical Journal, Letters to the Editor* 767.1, L11, p. L11.

Lada, C. J. 1987. *Star Forming Regions*. Ed. by M. Peimbert and J. Jugaku. Vol. 115. IAU Symposium, p. 1.

Laibe, G. and D. J. Price. 2014. *Monthly Notices of the RAS* 440, pp. 2136–2146.

Lavalley, M., T. Isobe, and E. Feigelson. 1992. *Astronomical Data Analysis Software and Systems I*. Ed. by D. M. Worrall, C. Biemesderfer, and J. Barnes. Vol. 25. Astronomical Society of the Pacific Conference Series, p. 245.

Law, C. J., L. Ricci, S. M. Andrews, et al. 2017. *Astronomical Journal* 154.6, 255, p. 255.

Leinert, C., H. Zinnecker, N. Weitzel, et al. 1993. *Astronomy and Astrophysics* 278, pp. 129–149.

Lepp, S. and A. Dalgarno. 1996. *Astronomy and Astrophysics* 306, pp. L21–L24.

Lesur, G., P. Hennebelle, and S. Fromang. 2015. *Astronomy and Astrophysics* 582, L9, p. L9.

Li, H., J. M. Finn, R. V. E. Lovelace, et al. 2000. *Astrophysical Journal* 533.2, pp. 1023–1034.

Li, H., S. A. Colgate, B. Wendroff, et al. 2001. *Astrophysical Journal* 551.2, pp. 874–896.

Lin, D. N. C. and J. Papaloizou. 1979b. *Monthly Notices of the RAS* 186, pp. 799–812.

— 1979a. *Monthly Notices of the RAS* 188, pp. 191–201.

— 1986. *Astrophysical Journal* 309, pp. 846–857.

Lin, M.-K. 2012. *Monthly Notices of the RAS* 426.4, pp. 3211–3224.

Lindegren, L., J. Hernández, A. Bombrun, et al. 2018. *Astronomy and Astrophysics* 616, A2, A2.

Liu, H. B., E. I. Vorobyov, R. Dong, et al. 2017. *Astronomy and Astrophysics* 602, A19, A19.

Lobo Gomes, A., H. Klahr, A. L. Uribe, et al. 2015. *Astrophysical Journal* 810.2, 94, p. 94.

Lodato, G. and S. Facchini. 2013. *Monthly Notices of the RAS* 433, pp. 2157–2164.

Lodato, G. and W. K. M. Rice. 2004. *Monthly Notices of the RAS* 351, pp. 630–642.

Lodato, G., E. Delgado-Donate, and C. J. Clarke. 2005. *Monthly Notices of the RAS* 364, pp. L91–L95.

Lodato, G. and D. J. Price. 2010. *Monthly Notices of the Royal Astronomical Society* 405.2, pp. 1212–1226.

Loison, J.-C., V. Wakelam, and K. M. Hickson. 2014. *Monthly Notices of the RAS* 443.1, pp. 398–410.

Lommen, D., S. T. Maddison, C. M. Wright, et al. 2009. *Astronomy and Astrophysics* 495.3, pp. 869–879.

London, R. 1978. *Astrophysical Journal* 225, pp. 405–416.

Long, F., G. J. Herczeg, I. Pascucci, et al. 2017. *Astrophysical Journal* 844.2, 99, p. 99.

Long, F., P. Pinilla, G. J. Herczeg, et al. 2018. *Astrophysical Journal* 869.1, 17, p. 17.

López Martí, B., J. Eislöffel, and R. Mundt. 2005. *Astronomy and Astrophysics* 444.1, pp. 175–186.

López Martí, B., L. Spezzi, B. Merín, et al. 2010. *Astronomy and Astrophysics* 515, A31, A31.

Lovelace, R. V. E., H. Li, S. A. Colgate, et al. 1999. *Astrophysical Journal* 513.2, pp. 805–810.

Lubow, S. H., R. G. Martin, and C. Nixon. 2015. *Astrophysical Journal* 800, 96, p. 96.

Lucy, L. B. 1977. *Astronomical Journal* 82, pp. 1013–1024.

Luri, X., A. G. A. Brown, L. M. Sarro, et al. 2018. *Astronomy and Astrophysics* 616, A9, A9.

Lynden-Bell, D. and J. E. Pringle. 1974. *Monthly Notices of the RAS* 168, pp. 603–637.

Lyo, A. R., N. Ohashi, C. Qi, et al. 2011. *Astronomical Journal* 142.5, 151, p. 151.

Lyra, W., A. Johansen, H. Klahr, et al. 2009. *Astronomy and Astrophysics* 493.3, pp. 1125–1139.

Lyra, W., N. J. Turner, and C. P. McNally. 2015. *Astronomy and Astrophysics* 574, A10, A10.

Lyra, W. and M.-K. Lin. 2013. *Astrophysical Journal* 775.1, 17, p. 17.

Lyra, W. and M.-M. Mac Low. 2012. *Astrophysical Journal* 756.1, 62, p. 62.

Macintosh, B. A., J. R. Graham, D. W. Palmer, et al. 2008. *SPIE Proceedings*. Vol. 7015. Society of Photo-Optical Instrumentation Engineers (SPIE) Conference Series, p. 701518.

Maire, A. L., T. Stolker, S. Messina, et al. 2017. *Astronomy and Astrophysics* 601, A134, A134.

Manara, C. F., L. Testi, E. Rigliaco, et al. 2013. *Astronomy and Astrophysics* 551, A107, A107.

Manara, C. F., L. Testi, G. J. Herczeg, et al. 2017. *Astronomy and Astrophysics* 604, A127, A127.

Manara, C. F., A. Morbidelli, and T. Guillot. 2018. *Astronomy and Astrophysics* 618, L3, p. L3.

Mann, R. K. and J. P. Williams. 2010. *Astrophysical Journal* 725.1, pp. 430–442.

Marino, S., S. Casassus, S. Perez, et al. 2015. *Astrophysical Journal* 813.1, 76, p. 76.

Maucó, K., J. Hernández, N. Calvet, et al. 2016. *Astrophysical Journal* 829.1, 38, p. 38.

Maury, A. J., P. André, L. Testi, et al. 2019. *Astronomy and Astrophysics* 621, A76, A76.

Mayor, M. and D. Queloz. 1995. *Nature* 378, pp. 355–359.

McClure, M. K., E. A. Bergin, L. I. Cleeves, et al. 2016. *Astrophysical Journal* 831.2, 167, p. 167.

McMullin, J. P., B. Waters, D. Schiebel, et al. 2007. *Astronomical Data Analysis Software and Systems XVI*. Ed. by R. A. Shaw, F. Hill, and D. J. Bell. Vol. 376. Astronomical Society of the Pacific Conference Series, p. 127.

Mellon, R. R. and Z.-Y. Li. 2008. *Astrophysical Journal* 681.2, pp. 1356–1376.

Meyer, M. R. and B. A. Wilking. 2009. *Publications of the Astronomical Society of the Pacific* 121.878, p. 350.

Miotello, A., S. Bruderer, and E. F. van Dishoeck. 2014. *Astronomy and Astrophysics* 572, A96, A96.

Miotello, A., E. F. van Dishoeck, M. Kama, et al. 2016. *Astronomy and Astrophysics* 594, A85, A85.

Miotello, A., E. F. van Dishoeck, J. P. Williams, et al. 2017. *Astronomy and Astrophysics* 599, A113, A113.

Miranda, R. and D. Lai. 2015. *Monthly Notices of the RAS* 452, pp. 2396–2409.

Miranda, R., H. Li, S. Li, et al. 2017. *Astrophysical Journal* 835.2, 118, p. 118.

Mittal, T. and E. Chiang. 2015. *Astrophysical Journal, Letters to the Editor* 798.1, L25, p. L25.

Modigliani, A., P. Goldoni, F. Royer, et al. 2010. *SPIE Proceedings.* Vol. 7737. Society of Photo-Optical Instrumentation Engineers (SPIE) Conference Series, p. 773728.

Montesinos, M., S. Perez, S. Casassus, et al. 2016. *Astrophysical Journal, Letters to the Editor* 823.1, L8, p. L8.

Morbidelli, A. and S. N. Raymond. 2016. *Journal of Geophysical Research (Planets)* 121.10, pp. 1962–1980.

Morris, J. P. and J. J. Monaghan. 1997. *Journal of Computational Physics* 136, pp. 41–50.

Murray, J. R. 1996. *Monthly Notices of the RAS* 279, pp. 402–414.

Muto, T., C. A. Grady, J. Hashimoto, et al. 2012. *Astrophysical Journal, Letters to the Editor* 748.2, L22, p. L22.

Nakagawa, Y., M. Sekiya, and C. Hayashi. 1986. *Icarus* 67, pp. 375–390.

Nelson, A. F. and F. Marzari. 2016. *ArXiv e-prints.*

Neuhäuser, R. and J. Forbrich. 2008. *Handbook of Star Forming Regions, Volume II: The Southern Sky ASP Monograph Publications, Vol. 5. Edited by Bo Reipurth, p.735.* Ed. by B. Reipurth. Vol. 5, p. 735.

Neuhäuser, R., F. M. Walter, E. Covino, et al. 2000. *Astronomy and Astrophysics Supplement* 146, pp. 323–347.

Ney, E. P., D. W. Strecker, and R. D. Gehrz. 1973. *Astrophysical Journal* 180, pp. 809–816.

Nisini, B., S. Antoniucci, T. Giannini, et al. 2005. *Astronomy and Astrophysics* 429, pp. 543–557.

Öberg, K. I., R. Murray-Clay, and E. A. Bergin. 2011. *Astrophysical Journal, Letters to the Editor* 743.1, L16, p. L16.

Öberg, K. I., K. Furuya, R. Loomis, et al. 2015. *Astrophysical Journal* 810.2, 112, p. 112.

O'dell, C. R. and Z. Wen. 1994. *Astrophysical Journal* 436, p. 194.

O'dell, C. R. and K. Wong. 1996. *Astronomical Journal* 111, p. 846.

Orosz, J. A., W. F. Welsh, J. A. Carter, et al. 2012a. *Science* 337, pp. 1511–.

Orosz, J. A., W. F. Welsh, J. A. Carter, et al. 2012b. *Astrophysical Journal* 758, 87, p. 87.

Paardekooper, S.-J., G. Lesur, and J. C. B. Papaloizou. 2010. *Astrophysical Journal* 725.1, pp. 146–158.

Paczynski, B. 1977. *Astrophysical Journal* 216, pp. 822–826.

Papaloizou, J. and J. E. Pringle. 1977. *Monthly Notices of the RAS* 181, pp. 441–454.

Pascucci, I., L. Testi, G. J. Herczeg, et al. 2016. *Astrophysical Journal* 831.2, 125, p. 125.

Patten, B. M. 1998. *Cool Stars, Stellar Systems, and the Sun*. Ed. by R. A. Donahue and J. A. Bookbinder. Vol. 154. Astronomical Society of the Pacific Conference Series, p. 1755.

Pérez, L. M., A. Isella, J. M. Carpenter, et al. 2014. *Astrophysical Journal, Letters to the Editor* 783.1, L13, p. L13.

Pérez, L. M., J. M. Carpenter, S. M. Andrews, et al. 2016. *Science* 353.6307, pp. 1519–1521.

Pérez, S., S. Casassus, A. Hales, et al. 2019. *arXiv e-prints*, arXiv:1906.06305, arXiv:1906.06305.

Peterson, D. E., A. Caratti o Garatti, T. L. Bourke, et al. 2011. *Astrophysical Journal, Supplement* 194.2, 43, p. 43.

Pfalzner, S., P. Vogel, J. Scharwächter, et al. 2005. *Astronomy and Astrophysics* 437.3, pp. 967–976.

Pichardo, B., L. S. Sparke, and L. A. Aguilar. 2005. *Monthly Notices of the RAS* 359, pp. 521–530.

Pierens, A. and M.-K. Lin. 2018. *Monthly Notices of the RAS* 479.4, pp. 4878–4890.

Piétu, V., S. Guilloteau, and A. Dutrey. 2005. *Astronomy and Astrophysics* 443.3, pp. 945–954.

Pinilla, P., T. Birnstiel, L. Ricci, et al. 2012b. *Astronomy and Astrophysics* 538, A114, A114.

Pinilla, P., M. Benisty, and T. Birnstiel. 2012a. *Astronomy and Astrophysics* 545, A81, A81.

Pinilla, P., N. van der Marel, L. M. Pérez, et al. 2015. *Astronomy and Astrophysics* 584, A16, A16.

Pinilla, P., L. M. Pérez, S. Andrews, et al. 2017. *Astrophysical Journal* 839.2, 99, p. 99.

Pinte, C., D. J. Price, F. Ménard, et al. 2018. *Astrophysical Journal, Letters to the Editor* 860.1, L13, p. L13.

Pinte, C., G. van der Plas, F. Ménard, et al. 2019. *Nature Astronomy*, p. 419.

Pohl, A., P. Pinilla, M. Benisty, et al. 2015. *Monthly Notices of the RAS* 453.2, pp. 1768–1778.

Pontoppidan, K. M., G. A. Blake, E. F. van Dishoeck, et al. 2008. *Astrophysical Journal* 684.2, pp. 1323–1329.

Price, D. J. 2007. *Publications of the Astronomical Society of Australia* 24, pp. 159–173.

— 2012. *Advances in Computational Astrophysics: Methods, Tools, and Outcome.* Ed. by R. Capuzzo-Dolcetta, M. Limongi, and A. Tornambè. Vol. 453. Astronomical Society of the Pacific Conference Series, p. 249.

Price, D. J. and C. Federrath. 2010. *Monthly Notices of the RAS* 406, pp. 1659–1674.

Qi, C., K. I. Öberg, D. J. Wilner, et al. 2013. *Science* 341.6146, pp. 630–632.

Rafikov, R. R. 2002. *Astrophysical Journal* 572.1, pp. 566–579.

Raghavan, D., H. A. McAlister, T. J. Henry, et al. 2010. *Astrophysical Journal, Supplement* 190, pp. 1–42.

Ragusa, E., G. Dipierro, G. Lodato, et al. 2017. *Monthly Notices of the RAS* 464.2, pp. 1449–1455.

Reipurth, B. and H. Zinnecker. 1993. *Astronomy and Astrophysics* 278, pp. 81–108.

Ricci, L., L. Testi, A. Natta, et al. 2010b. *Astronomy and Astrophysics* 512, A15, A15.

Ricci, L., L. Testi, A. Natta, et al. 2010a. *Astronomy and Astrophysics* 521, A66, A66.

Rice, W. K. M., G. Lodato, J. E. Pringle, et al. 2004. *Monthly Notices of the RAS* 355.2, pp. 543–552.

Riddick, F. C., P. F. Roche, and P. W. Lucas. 2007. *Monthly Notices of the RAS* 381.3, pp. 1067–1076.

Roddier, C., F. Roddier, M. J. Northcott, et al. 1996. *Astrophysical Journal* 463, p. 326.

Rodmann, J., T. Henning, C. J. Chandler, et al. 2006. *Astronomy and Astrophysics* 446.1, pp. 211–221.

Romero, G. A., M. R. Schreiber, L. A. Cieza, et al. 2012. *Astrophysical Journal* 749.1, 79, p. 79.

Rosotti, G. P., A. Juhasz, R. A. Booth, et al. 2016. *Monthly Notices of the RAS* 459.3, pp. 2790–2805.

Ruíz-Rodríguez, D., L. A. Cieza, J. P. Williams, et al. 2018. *Monthly Notices of the RAS* 478.3, pp. 3674–3692.

Salter, D. M., M. R. Hogerheijde, R. F. J. van der Burg, et al. 2011. *Astronomy and Astrophysics* 536, A80, A80.

Sargent, A. I. and S. V. W. Beckwith. 1991. *Astrophysical Journal, Letters to the Editor* 382, p. L31.

Schäfer, C., R. Speith, and W. Kley. 2007. *Astronomy and Astrophysics* 470, pp. 733–739.

Schwamb, M. E., J. A. Orosz, J. A. Carter, et al. 2013. *Astrophysical Journal* 768, 127, p. 127.

Shakura, N. I. and R. A. Sunyaev. 1973b. *Astronomy and Astrophysics* 24, pp. 337–355.

— 1973a. *Astronomy and Astrophysics* 500, pp. 33–51.

Shu, F. H., F. C. Adams, and S. Lizano. 1987. *Annual Review of Astronomy and Astrophysics* 25, pp. 23–81.

Sicilia-Aguilar, A., T. Henning, A. Juhász, et al. 2008. *Astrophysical Journal* 687.2, pp. 1145–1167.

Sicilia-Aguilar, A., T. Henning, J. Kainulainen, et al. 2011. *Astrophysical Journal* 736.2, 137, p. 137.

Sierra, A., S. Lizano, and P. Barge. 2017. *Astrophysical Journal* 850.2, 115, p. 115.

Siess, L., E. Dufour, and M. Forestini. 2000. *Astronomy and Astrophysics* 358, pp. 593–599.

Silber, J., T. Gledhill, G. Duchêne, et al. 2000. *Astrophysical Journal, Letters to the Editor* 536, pp. L89–L92.

Simon, M. and L. Prato. 1995. *Astrophysical Journal* 450, p. 824.

Simon, M., A. Dutrey, and S. Guilloteau. 2000. *Astrophysical Journal* 545, pp. 1034–1043.

Stäuber, P., S. D. Doty, E. F. van Dishoeck, et al. 2005. *Astronomy and Astrophysics* 440.3, pp. 949–966.

Stäuber, P., A. O. Benz, J. K. Jørgensen, et al. 2007. *Astronomy and Astrophysics* 466.3, pp. 977–988.

Sternberg, A. and A. Dalgarno. 1995. *Astrophysical Journal, Supplement* 99, p. 565.

Sternberg, A., F. Le Petit, E. Roueff, et al. 2014. *Astrophysical Journal* 790.1, 10, p. 10.

Stolker, T., C. Dominik, H. Avenhaus, et al. 2016. *Astronomy and Astrophysics* 595, A113, A113.

Stolker, T., M. Sitko, B. Lazareff, et al. 2017. *Astrophysical Journal* 849.2, 143, p. 143.

Tachihara, K., T. Onishi, A. Mizuno, et al. 2002. *Astronomy and Astrophysics* 385, pp. 909–920.

Takami, M., J. Bailey, and A. Chrysostomou. 2003. *Astronomy and Astrophysics* 397, pp. 675–691.

Tang, Y.-W., A. Dutrey, S. Guilloteau, et al. 2016. *Astrophysical Journal* 820, 19, p. 19.

Tazzari, M., L. Testi, A. Natta, et al. 2017. *Astronomy and Astrophysics* 606, A88, A88.

Tazzari, M., F. Beaujean, and L. Testi. 2018. *Monthly Notices of the RAS* 476.4, pp. 4527–4542.

Teague, R., S. Guilloteau, D. Semenov, et al. 2016. *Astronomy and Astrophysics* 592, A49, A49.

Teague, R., J. Bae, E. A. Bergin, et al. 2018. *Astrophysical Journal, Letters to the Editor* 860.1, L12, p. L12.

Terebey, S., F. H. Shu, and P. Cassen. 1984. *Astrophysical Journal* 286, pp. 529–551.

Testi, L., F. D'Antona, F. Ghinassi, et al. 2001. *Astrophysical Journal, Letters to the Editor* 552.2, pp. L147–L150.

Testi, L., A. Natta, D. S. Shepherd, et al. 2003. *Astronomy and Astrophysics* 403, pp. 323–328.

Testi, L., T. Birnstiel, L. Ricci, et al. 2014. *Protostars and Planets VI*. Ed. by H. Beuther, R. S. Klessen, C. P. Dullemond, et al., p. 339.

Testi, L., A. Natta, A. Scholz, et al. 2016. *Astronomy and Astrophysics* 593, A111, A111.

Thi, W. F., G. J. van Zadelhoff, and E. F. van Dishoeck. 2004. *Astronomy and Astrophysics* 425, pp. 955–972.

Tielens, A. G. G. M. and D. Hollenbach. 1985. *Astrophysical Journal* 291, pp. 747–754.

Trapman, L., A. Miotello, M. Kama, et al. 2017. *Astronomy and Astrophysics* 605, A69, A69.

Tychoniec, Ł., J. J. Tobin, A. Karska, et al. 2018. *Astrophysical Journal, Supplement* 238.2, 19, p. 19.

van Boekel, R., M. Min, L. B. F. M. Waters, et al. 2005. *Astronomy and Astrophysics* 437.1, pp. 189–208.

van Boekel, R., T. Henning, J. Menu, et al. 2017. *Astrophysical Journal* 837.2, 132, p. 132.

van der Marel, N., E. F. van Dishoeck, S. Bruderer, et al. 2015b. *Astronomy and Astrophysics* 579, A106, A106.

van der Marel, N., P. Pinilla, J. Tobin, et al. 2015a. *Astrophysical Journal, Letters to the Editor* 810.1, L7, p. L7.

van der Marel, N., E. F. van Dishoeck, S. Bruderer, et al. 2016a. *Astronomy and Astrophysics* 585, A58, A58.

van der Marel, N., P. Cazzoletti, P. Pinilla, et al. 2016b. *Astrophysical Journal* 832.2, 178, p. 178.

van der Marel, N., E. F. van Dishoeck, S. Bruderer, et al. 2013. *Science* 340.6137, pp. 1199–1202.

van Terwisga, S. E., E. F. van Dishoeck, P. Cazzoletti, et al. 2019. *Astronomy and Astrophysics* 623, A150, A150.

van Zadelhoff, G. J., Y. Aikawa, M. R. Hogerheijde, et al. 2003. *Astronomy and Astrophysics* 397, pp. 789–802.

Vernet, J., H. Dekker, S. D'Odorico, et al. 2011. *Astronomy and Astrophysics* 536, A105, A105.

Visser, R., E. F. van Dishoeck, S. D. Doty, et al. 2009. *Astronomy and Astrophysics* 495.3, pp. 881–897.

Visser, R., S. Bruderer, P. Cazzoletti, et al. 2018. *Astronomy and Astrophysics* 615, A75, A75.

Von Neumann, J. and R. D. Richtmyer. 1950. *Journal of Applied Physics* 21, pp. 232–237.

Vorobyov, E. I., V. Akimkin, O. Stoyanovskaya, et al. 2018. *Astronomy and Astrophysics* 614, A98, A98.

Wada, K., H. Tanaka, T. Suyama, et al. 2009. *Astrophysical Journal* 702, pp. 1490–1501.

Wakelam, V., E. Herbst, J. C. Loison, et al. 2012. *Astrophysical Journal, Supplement* 199.1, 21, p. 21.

Walsh, C., T. J. Millar, and H. Nomura. 2010. *Astrophysical Journal* 722.2, pp. 1607–1623.

Walter, F. M., F. J. Vrba, S. J. Wolk, et al. 1997. *Astronomical Journal* 114, p. 1544.

Weidenschilling, S. J. 1977. *Monthly Notices of the RAS* 180, pp. 57–70.

Welsh, W. F., J. A. Orosz, J. A. Carter, et al. 2012. *Nature* 481, pp. 475–479.

Welsh, W. F., J. A. Orosz, J. A. Carter, et al. 2014. *IAU Symposium.* Ed. by N. Haghighipour. Vol. 293. IAU Symposium, pp. 125–132.

Whipple, F. L. 1972. *From Plasma to Planet.* Ed. by A. Elvius, p. 211.

White, R. J. and A. M. Ghez. 2001. *Astrophysical Journal* 556, pp. 265–295.

White, R. J., A. M. Ghez, I. N. Reid, et al. 1999. *Astrophysical Journal* 520, pp. 811–821.

Williams, J. P. and L. A. Cieza. 2011. *Annual Review of Astronomy and Astrophysics* 49.1, pp. 67–117.

Winn, J. N. and D. C. Fabrycky. 2015. *Annual Review of Astronomy and Astrophysics* 53, pp. 409–447.

Winter, A. J., C. J. Clarke, G. Rosotti, et al. 2018a. *Monthly Notices of the RAS* 475.2, pp. 2314–2325.

Winter, A. J., C. J. Clarke, G. Rosotti, et al. 2018b. *Monthly Notices of the RAS* 478.2, pp. 2700–2722.

Wolszczan, A. and D. A. Frail. 1992. *Nature* 355, pp. 145–147.

Zhu, Z. and C. Baruteau. 2016. *Monthly Notices of the RAS* 458.4, pp. 3918–3926.

Zhu, Z., L. Hartmann, and C. Gammie. 2010. *Astrophysical Journal* 713.2, pp. 1143–1158.

Nederlandse samenvatting

Sinds het ontstaan van de mensheid was men nieuwsgierig naar zijn oorsprong en plaats in het universum. Sterren en sterrenbeelden waren de oorsprong van ontelbare legendes en mythes, welke nog steeds terug te vinden zijn in namen van sterren en sterrenbeelden. Tegenwoordig gelooft niemand meer dat deze verhalen echt gebeurd zijn, maar ze onthullen duidelijk de intuïtie van de mensheid dat het antwoord op de vragen over zijn oorsprong en plaats in het universum alleen te vinden zijn door het observeren van de hemel. Gedurende de vooruitgang in de wetenschap is het laatste punt blijven gelden. Constant worden er telescopen gebouwd en de ruimte in gelanceerd, met als doel om naar de hemel te kijken en dezelfde vragen te beantwoorden; en in het bijzonder de vraag: hoe is het leven ontstaan?

In het heelal is er slechts één plek waar we zeker zijn dat leven is ontstaan: de Aarde. Tot ongeveer 25 jaar geleden kende we nog geen enkele planeet buiten ons eigen zonnestelsel. In 1995 werd echter de eerste *exoplaneet* ontdekt en sindsdien zijn er meer dan 4000 nieuwe exoplaneten gevonden. Deze toename aan ontdekkingen heeft een nieuwe weg geopend naar de oorsprong van het leven. Vooral het begrijpen van de vorming van deze planeten uit zowel fysisch als chemisch oogpunt is een belangrijk vakgebied.

De weg van een grote interstellaire wolk, zoals die in Fig. 6.15, naar planeten is complex en omvat veel verschillende fysische processen op verschillende schalen (zie Fig. 1.2). Veel aspecten van deze weg begrijpt men daarom nog steeds niet goed. Wel is het duidelijk dat sterren en planeten vormen in grote interstellaire wolken. 99% van de materie in deze wolken bestaat uit moleculair gas, de overige 1% bestaat uit stof. Sommige wolken zijn instabiel onder hun eigen zwaartekracht, wat betekent dat hun massa te hoog is om ondersteund te worden door de druk van het gas waar ze van gemaakt zijn. Als gevolg hiervan beginnen deze wolken onder hun eigen zwaartekracht ineen te storten. Tijdens deze instorting beginnen ze harder en harder te roteren door het behoud van impulsmoment, totdat op een gegeven moment de centrifugale kracht de ineen-

Figure 6.9: Opname van de donkere wolken in het Corona Australis stervormingsgebied. De dichtere wolken blokkeren effectief het licht van verre achtergrondsterren in de Melkweg door de grote hoeveelheden stof. Auteursrechten figuur: Fabian Neyer.

storting kan tegenwerken en een schijfachtige structuur word gevormd. Deze structuren worden *protoplanetaire schijven* genoemd en zijn de geboorteplaats van planeten.

Stof in protoplanetaire schijven kan dan groeien van de grootte van kleine zandkorrels tot kleine steentjes, keien en planetoïden, welke de bouwstenen zijn van rotsachtige planeten en de kernen van gasreuzen. Wanneer deze gevormd zijn, zullen planeten gaten en ringen creëren in het resterende materiaal van de schijf.

Tot ongeveer 10 jaar geleden kon men deze structuren nog niet waarnemen vanaf de Aarde omdat de ruimtelijke resolutie van de telescopen in die tijd niet genoeg was. Het was alsof je van een verre afstand naar een schilderij keek: de grote structuren kan je zien maar de details zijn onzichtbaar. Evenzo leken schijven glad en symmetrisch. Echter, als je dichter bij het schilderij komt worden meer details zichtbaar en als je maar dichtbij genoeg komt kan je zelfs enkele penseelstreken van elkaar onderscheiden (zie bijv. Fig. 6.16). Wat het voor ons mogelijk heeft gemaakt om "dichter bij" protoplanetaire schijven te komen zijn de weergaloze mogelijkheden van een nieuwe krachtige telescoop: de Atacama Large Millimeter/submillimeter Array (ALMA). Wanneer er naar schijven wordt gekeken met de volledige mogelijkheden van ALMA, dan zijn deze schijven niet meer glad en symmetrisch maar zijn er vele structuren en morfologieën te zien; zelfs meer dan wat men van tevoren had verwacht.

Naast ALMA zijn er andere telescopen en instrumenten, zoals VLT/SPHERE en Gemini/GPI, ontwikkeld om te zoeken naar planeten die verborgen liggen in protoplanetaire schijven. Interessant en tegen alle verwachtingen in is dat
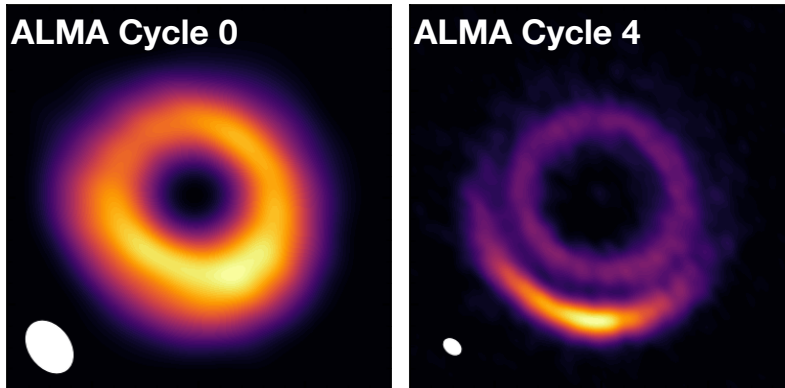
Figure 6.10: Afbeeldingen van de protoplanetaire schijf rond HD 135344B met twee verschillende resoluties. Aan de linkerzijde, de allereerste ALMA afbeelding met $0.''25$ (~ 30 au) resolutie die een licht asymmetrische ring lijkt te hebben. Aan de rechterkant, een meer recente ALMA afbeelding van hetzelfde object, maar nu met een hogere resolutie van $0.''06$ (~ 8 au): met deze resolutie kunnen meerdere substructuren worden onderscheiden, zoals een binnenste symmetrische ring en een buitenste azimuthale asymmetrie.

slechts een handvol planeten in schijven zijn ontdekt.

De alom geobserveerde substructuren gecombineerd met het gebrek aan gedetecteerde planeten in schijven maken het moeilijker om substructuren te verklaren door de interactie tussen schijf en planeten. De vragen die dit proefschrift met name zal proberen te beantwoorden zijn:

- Kunnen substructuren in protoplanetaire schijven ontstaan door andere fenomenen dan planeet-schijf interacties?

- Welke informatie kunnen substructuren in protoplanetaire schijven geven over de fysische structuur van de schijf?

- Zijn substructuren in het gas gerelateerd aan die in het stof, of leveren deze onafhankelijke informatie?

- Met welke mate zijn eigenschappen van de schijf afhankelijk van evolutie in plaats van de begincondities?

Dit proefschrift en vooruitzicht

Hoofdstuk 1 van dit proefschrift geeft een algemene inleiding over de theorie van ster- en planeetvorming. De fases die leiden van de moleculaire wolk naar

een schijf worden uitgelegd samen met het fysische mechanisme dat een rol speelt in de groei en evolutie van stofdeeltjes. Tevens worden de telescopen en numerieke methodes die gebruikt zijn in de analyse geïntroduceerd.

Hoofdstuk 2 presenteert een onderzoek naar de structuren in de schijf rond GG Tau A. De eigenaardigheid van deze protoplanetaire schijf is dat deze niet rond een enkele ster draait, maar rond een dubbelster. De schijf rond de dubbelster GG Tau A vertoont een zeer smalle ring op ongeveer 200 AU van de dubbelster. De regio tussen de dubbelster en de ring is compleet stofvrij en bijna helemaal gasvrij aangezien al het materiaal hier naar buiten is gedrukt door de interactie met de zwaartekracht van de dubbelster. De interactie tussen de tweede ster en de schijf is vergelijkbaar met wat er zou gebeuren als er in plaats van de tweede ster een zware planeet aanwezig was. Afhankelijk van de massa van de tweede ster voorspellen theoretische berekeningen echter een andere locatie voor de ring. De positie van de ring is ook afhankelijk van de baan van de tweede ster. Na het draaien van hydrodynamische simulaties en het vergelijken van de resultaten hiervan met de waarnemingen van de schijf en de beweging van de sterren, concluderen we dat de baan van de ster die het beste past bij de observaties een baan is die in een ander vlak ligt dan het vlak waar de schijf in ligt.

Hoofdstuk 3 en 4 richten zich op een ander specifiek object, namelijk HD 135344B (zie Fig. 6.16). Al vanaf de allereerste ALMA observaties leek de schijf rond HD 135344B interessant met een grote ~ 50 AU holte aan de binnenkant en een stof ring vergelijkbaar met GG Tau A, maar net iets kleiner, zoals we zouden verwachten wanneer deze is ontstaan door een planeet. Een ander verschil met GG Tau A is het feit dat de HD 135344B schijf niet symmetrisch is, maar helderder is in het zuiden. Daarnaast laten waarnemingen van verstrooid zichtbaar licht, wat afkomstig is van kleine stofdeeltjes in de bovenste laag van de schijf, spiraalarmen zien die typisch verklaard worden door twee extra planeten. Hoofdstuk 3 presenteert hogere resolutie ALMA waarnemingen van deze schijf. Wat in eerdere observaties een duidelijke asymmetrische ring leek, is met de hogere resolutie onder te verdelen in een symmetrische ring aan de binnenkant en een gescheiden banaanvormige asymmetrie die geïnterpreteerd kan worden als een werveling. Het lanceerpunt van de spiraalarmen ligt dichtbij het centrum van de asymmetrie (middelste paneel in Fig. 3.1). Wij stellen daarom voor dat deze spiraalarmen ontstaan zijn door de werveling in plaats van door extra planeten. Slecht één planeet, die de binnenste holte creëert, is nodig in deze verklaring. Dit komt overeen met het feit dat ondanks de nodige moeite nog steeds geen enkele planeet geïdentificeerd is in de buitenste regionen van HD 135344B.
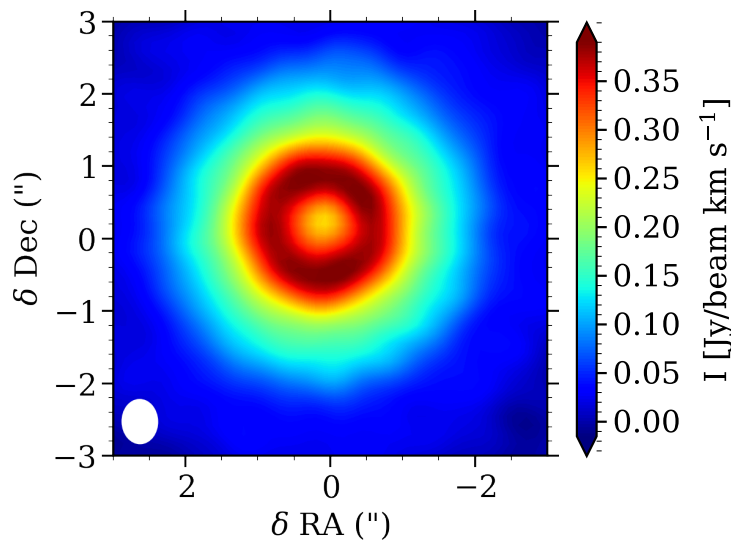
Figure 6.11: De ringvormige CN emissie die gedetecteerd is in de schrijf rond TW Hya.

Hoofdstuk 4 presenteert waarnemingen van de schijf rond HD 135344B met een nog hogere resolutie en op een andere golflengte. Deze keer zijn de binnenste ring en de buitenste asymmetrie duidelijk van elkaar te onderscheiden. Bovendien wordt, door het combineren van de nieuwe met de vorige waarnemingen, een onderzoek naar de werveling uitgevoerd op meerdere golflengtes. Hierdoor kunnen vele eigenschappen van de stofdeeltjes in deze werveling worden bepaald. Het is bijvoorbeeld duidelijk dat de stofdeeltjes in de werveling groter zijn dan in de rest van de schijf en dus dat het stof hier tot grotere deeltjes groeit, allicht zelfs tot grootte van planetoïden. De massa van de werveling is ook gemeten; deze is binnen de onzekerheden consistent met de lancering van spiraalarmen vanuit de werveling.

De eerste drie hoofdstukken leggen vooral de focus bij stofstructuren. Hoofdstuk 5 richt zich in plaats daarvan op gas en in het bijzonder op de emissie van CN. Als één van de helderste spectraallijnen in schijven is CN een interessant molecuul om te bestuderen. Wat het nog interessanter maakt is dat ruimtelijk opgeloste waarnemingen van protoplanetaire schijven altijd ringachtige structuren laten zien (zie Fig. 6.17). Komen deze ringen ook door een planeet? Zijn ze gecorreleerd aan stofringen? Om deze vragen te beantwoorden is de CN emissie voor een grid aan modellen van protoplanetaire schijven gesimuleerd

met de DALI code. De conclusie is dat CN altijd ringen vertoont, ook als er geen structuren in de schijf aanwezig zijn. De oorsprong van deze ringen is chemisch. De reactie die leidt tot deze eigenaardige emissie is echter sterk afhankelijk van een aantal eigenschappen van de schijf zoals de dikte, straal, massa en ver-ultraviolet straling van de centrale ster. Als men dus CN waarneemt in protoplanetaire schijven, kunnen de grootte en helderheid van de ring gebruikt worden om deze eigenschappen te bepalen.

Hoofdstuk 6, tenslotte, richt zich op ALMA waarnemingen van stof en gas in niet een enkele schijf, maar in vele schijven in een enkel stervormingsgebied: Corona Australis (CrA), afgebeeld in Fig. 6.15. Men denkt dat CrA een jong stervormingsgebied is en dus werd verwacht dat het relatief grote en heldere schijven zou vertonen vergelijkbaar met andere stervormingsgebieden met dezelfde leeftijd zoals Lupus. Geen enkele schijf is echter gedetecteerd in het gas en de stofschijven lijken minder helder en klein, meer vergelijkbaar met een stervormingsgebied dat 10 keer ouder is dan Lupus, zoals Upper Sco. Nieuwe VLT/X-shooter van de waargenomen objecten lijken hun jonge leeftijd echter te bevestigen. De vraag naar de oorsprong van de lage helderheid blijft onbeantwoord, maar de twee hoofdopties zijn mogelijk: ofwel twee verschillende stervormingsgebeurtenissen met een paar miljoen jaar verschil hebben zich voorgedaan in CrA, ofwel de helderheid en grootte van de schijven zijn sterk beïnvloed door de condities (zoals de rotatie van de wolk) in het vroegste begin van het stervormingsproces. In het bijzonder, als schijven rond de jongste objecten in dit gebied worden geobserveerd en gevonden word dat deze minder helder zijn, dan zou het duidelijk zijn dat begincondities een belangrijke rol spelen door al vanaf het begin de schijven kleiner en minder zwaar te maken.

Tot op heden blijft het onduidelijk of de waargenomen structuren komen door reeds gevormde planeten of door een ander fysisch mechanisme. Tot nu toe is er slechts één planeet waargenomen in een schijf, maar toekomstige waarnemingen kunnen mogelijk andere planeten in schijven detecteren die geassocieerd zijn met substructuren. In de tussentijd worden nieuwe veelbelovende methoden om indirect planeten waar te nemen steeds gebruikelijker. Deze zullen essentieel zijn in de nabije toekomst. De verschillen in de beweging van het gas die ontstaan door planeten zijn bijvoorbeeld al in een aantal gevallen waargenomen en kunnen ook voor meer objecten gebruikt worden. Emissie van schijven rond dubbelsterren die geassocieerd wordt met een protoplaneet is ook al waargenomen met ALMA en tevens is recent de inval van materiaal op een protoplaneet zelfs direct waargenomen met MUSE. Dit soort waarnemingen zullen in de toekomst gebruikelijker worden.

In de tussentijd zullen meer waarnemingen van protoplanetaire schijven op

verschillende golflengtes, zoals hier zijn uitgevoerd voor HD 135344B, informatie geven over de eigenschappen van het stof in stofvallen, met inbegrip van wervelingen. In het bijzonder zou de connectie tussen wervelingen en spiraalarmen in observaties van verstrooid zichtbaar licht beter onderzocht moeten worden in meerdere bronnen, waar we gebruik kunnen maken van de gevoeligheid en ruimtelijke resolutie van ALMA op hogere frequenties.

Dit soort onderzoeken zijn cruciaal om vast te stellen of substructuren in schijven de geboorteplaats zijn van nieuwe planeten. Op den duur zal dit ook duidelijkheid geven over hoe variëteit van substructuren in sub-mm waarnemingen gelieerd is aan de diversiteit in systemen van exoplaneten en uiteindelijk aan onze oorsprong.

English summary

Since the beginning of Human existence, mankind has wondered about its origin and place in the universe. Stars and constellations were the origin of countless legends and myths, and the names of some of them still carry the trace of them. Nobody today would think that those stories have actually happened, but they clearly highlight the intuition of people of all times that the answers to the questions about our origin and place in the universe can only come from the observation and study of the skies. As science progresses, the latter statement is still true. Telescopes are continuously being built around the world and sent to space, with the goal to be able to look better at those same skies and to answer those same questions. In particular, how did life begin?

In the greatness of the universe, there is only one place where we know for sure that life has originated: planet Earth. Until about 25 years ago, no planet was known outside of the solar system. In 1995, however, the first *exoplanet* was discovered, and since then more than 4000 new planets have been confirmed. This boost of discoveries opens a promising new path toward the understanding of the origin of life. In particular, understanding how planets form from the chemical and physical point of view is a critical field of study.

The path that leads from giant interstellar clouds, as the ones in Fig. 6.15, to planets is complicated and involves many different physical and processes at different scales (see Fig. 1.2). Many aspects of this path are therefore still not well understood. It is clear, however, that star and planet formation starts from giant molecular clouds. 99% of such clouds is made of molecular gas, while 1% is made of solid dust. Some clouds are gravitationally unstable: this means that their mass is too high to be supported by the pressure of the gas they are made of. Consequently, they start collapsing under the effect of their own gravity. During the collapse, they start rotating faster and faster due to conservation of angular momentum, until at some point the centrifugal force can actually prevent the material from further collapse and a disk-like structure is formed. These structures are called *protoplanetary disks*, as they are the cradle of planet

Figure 6.12: View of the dust component of the clouds in the Corona Australis star forming region. The denser clouds effectively block light from more distant background stars in the Milky Way. Image Credit & Copyright: Fabian Neyer.

formation.

Dust in protoplanetary disks can then grow from the size of tiny, sand grains to pebbles, boulders, and planetesimals, the building block of rocky planets and of the cores of giant gaseous planets. Once formed, planets interact with the rest of the material in the disks by carving gaps and cavities, creating rings and exciting waves.

Until abut 10 years ago such structures could not be observed from Earth, due to the spatial resolution of former-generation telescopes. It was like looking at a painting from far away: the large shapes can be seen, but the details are hidden and cannot be seen. Similarly, disks appeared smooth and symmetric. Moving closer to a painting, however, more details become clear, and when one is close enough even the single paintbrush strokes can be distinguished (e.g., see Fig. 6.16). What allowed us to "move closer" to protoplanetary disks are the unprecedented capabilities of a new powerful telescope: the Atacama Large Millimeter/submillimeter Array (ALMA). When observed with ALMA's full capabilities, disks are not smooth and symmetric anymore, but show many structures and a variety of morphologies, and even more than we would have expected.

Alongside ALMA, other telescopes and instruments, such as VLT/SPHERE and Gemini/GPI, have been built to look for planets embedded in protoplanetary disks. Interestingly and against expectations, only a handful have been detected to date.

The ubiquity of substructures combined with the lack of planet detections in protoplanetary disks are challenging the interpretation of substructures as
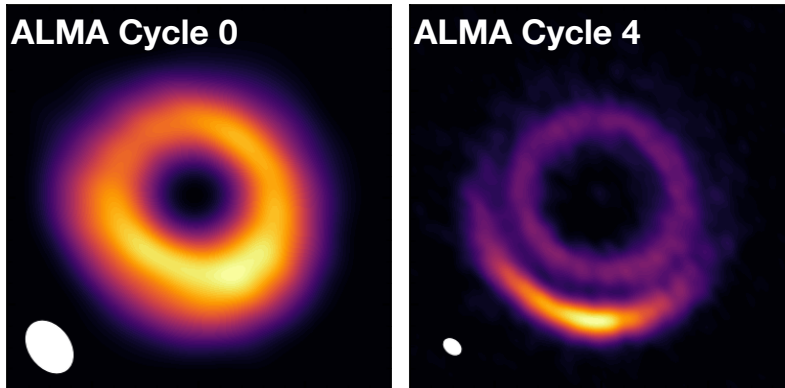
Figure 6.13: Images of the protoplanetary disk around HD 135344B taken at different resolutions. On the left, the very first ALMA observations at $0.''25$ (~ 30 au) resolution, apparently showing a slightly asymmetric ring. On the right, the more recent ALMA observations of the same object, reaching a spatial resolution of $0.''06$ (~ 8 au): at this resolution, more substructures can be distinguished, i. e. an inner, symmetric ring and an outer azimuthal asymmetry.

originating by the interaction between disk and planets. In particular, the questions that this Thesis will try to answer are the following:

- Can substructures in protoplanetary disks originate from other phenomena than planet-disk interaction?

- Which kind of information can substructures in protoplanetary disk provide about the physical properties of the disk?

- Are substructures in the gas related to those in the dust, or do they provide indipendent information?

- To what extent are disk properties due to evolution, rather than initial condition?

This thesis and future outlook

Chapter 1 of this thesis gives an overall introduction of the star and planet formation theory. The phases that lead from cloud to disk phase are explained, as well as the physical mechanism playing a role in dust growth and evolution. The telescopes and numerical tools employed in the analysis are also presented.

Chapter 2 presents a study of the structures in the disk surrounding GG Tau A. The peculiarity of this protoplanetary disk is that it is not rotating around a

single star, but around a binary (it is therefore called *circumbinary* disk). The GG Tau A circumbinary disk shows a very narrow ring located at ~ 200 au from the central stars. The region between the stars and the ring is completely devoid of dust and of most of the dust, as the material has been pushed out by the gravitational interaction with the stars. The interaction between the stellar companion and the disk is very similar to what would happen if a massive planet was present instead. Depending on the mass of the companion, however, the theoretical calculations predict a different ring locations. The position of the ring also depends on the orbit of the star. Running a set of hydrodynamical simulations and comparing the results with the observations of the disk and the stellar motion, we conclude that the stellar orbit that better fits into the observational constraints is an orbit misaligned with respect to the plane of the disk.

Chapter 3 and 4 focus on another specific object, namely HD 135344B (see Fig. 6.16). From the very first ALMA observations, the disk around HD 135344B appeared to be very interesting, with a large ~ 50 au inner cavity and a dust ring similar to that of GG Tau A, but smaller, as expected if it was carved by a planet. Another difference with GG Tau A is the fact that the HD 135344B disk is not symmetric, but is brighter in the south. In addition, scattered light observation of the same disk, probing small grains, located in the surface layer of the disk, show bright, symmetric spiral arms, usually explained with two additional planets. Chapter 3 presents higher resolution ALMA observations of the disk, highlighted that what seemed to be an asymmetrical ring in earlier ALMA observations, rather appeared at higher resolution like a symmetric, inner ring and a separated outer banana-shaped asymmetry, which could be interpreted as a vortex. The tip of the spiral arms is very close to the center of the asymmetry (central panel if Fig. 3.1): we therefore propose that the spiral arms are being triggered by the vortex, rather than by additional planets. Only one planet, carving the inner ring, is required in this explanation. This is consistent with the fact that despite the efforts no planet has been yet identified in the outer regions of HD 135344B.

Chapter 4 presents observations of the disk around HD 135344B at even higher resolution and at a different wavelength: this time, the inner ring and the outer asymmetry are clearly distinguishable. Moreover, combining the new observations with the previous one, a multi-wavelength study of the vortex is carried out. This allows to constrain many properties of the dust grains inside the vortex. For example it is clear that grains are larger in the vortex than in the rest of the disk: it is therefore likely that the dust is growing there to larger sizes, possibly originating a population of planetesimals. The mass of the
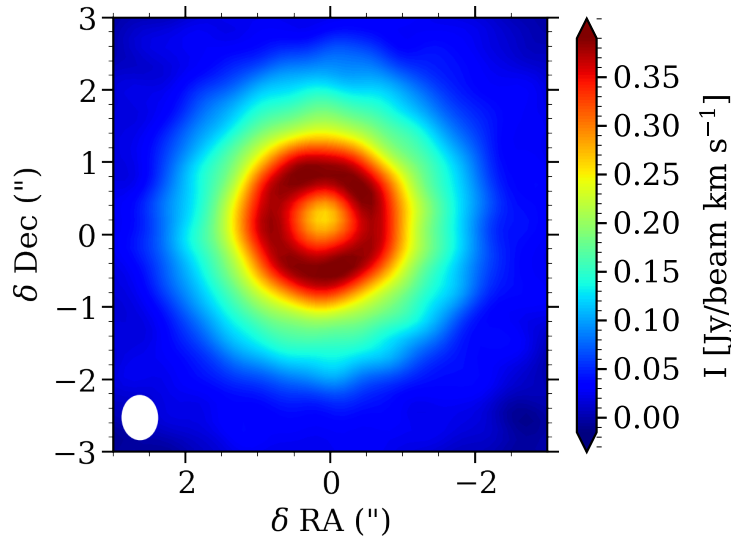
Figure 6.14: The ring shaped CN emission detected in the disk around TW Hya.

vortex is also measured, and found, within the uncertainties, to be consistent with the scenario of a spiral-launching vortex.

The first three chapters focus mostly on dust structures. Chapter 5 focuses on gas instead, and in particoualr on CN emission. Being one of the brightest lines in disks, CN is an interesting molecule to study. What makes it even more interesting is the fact that resolved observations of protoplanetary disks always show ring-like structures (see Fig. 6.17). Are these rings also due to a planet? Are they correlated with dust rings? In order to answer these questions, CN emission from a grid of models of protoplanetary disks was simulated using the DALI code. The conclusion is that CN always shows rings, even in structureless full disks. The origin of those rings is in fact chemical. The reaction leading to this peculiar emission, however, strongly depends on some properties of the disk, such as its flaring, radius, mass and the far Ultraviolet emission from the central star. When observing CN in protoplanetary disks, therefore, the ring size and brightness can potentially be used to constrain these properties.

Chapter 6, finally, focuses on the ALMA observations of dust and gas not only in single disks, but in many disks in a single star-forming region, Corona Australis (CrA), shown in Fig. 6.15. CrA is thought to be a young star-forming region, and as such is expected to show relatively large and bright disks as other regions of the same age such as Lupus. No disk is however detected in the gas,

and the dust disks appears to be faint and small, comparable to those of a region 10 times older than Lupus, i.e. Upper Sco. New VLT/X-Shooter spectra of the targeted objects, however, seem to confirm their young age. The question about the origin of the low fluxes remains open, but two main options are possible: either two different star formation events occured in CrA, a few Myrs apart, or the disk brightness and size observed today are strongly affected by the initial conditions (such as the rotation of the core) in the very early phases of the star formation process. More observations are needed to distinguish the scenarios. In particular, if disks around the youngest objects in the region are observed and found to be fainter than usual, it would be clear that initial conditions play an important role by making the disks small and less massive from the very beginning.

To date, it remains unclear whether the observed structures are due to already formed planets or to some other physical mechanism. So far only one planet has been imaged in a disk, but future observations may directly image more embedded planets associated with these structures. In the meantime, new promising approaches to indirectly infer the presence of planets are becoming more and more common and will prove critical in the near future. The perturbations to the gas motions induced by planets, for example, has already been used in a few cases, and the same technique can now be applied to more systems. Emission from circumplanetary disks associated to embedded protoplanets as well as the emission associated with their accretion onto the planets have also recently been detected with ALMA and MUSE, respectively. Such observations may be more common in the future.

In the meantime, additional multi-wavelength studies of protoplanetary disks such as that carried out for HD 135344B can shed light on the dust properties inside dust traps, including inside vortices. In particular, the connection between vortices and spiral arms in scattered light should be better investigated in more systems, also exploiting the sensitivity and spatial resolution of ALMA at the higher frequencies.

These studies are critical to understand if substructures in disks are the birthplace of new planets. They will ultimately also tell whether and how the variety of structures observed at mm-wavelengths is linked to the diversity in the exoplanetary systems' properties, and ultimately, our origins.

Riassunto

Fin dal principio della sua esistenza, l'umanità si è sempre interrogata sulla propria origine e posto nell'universo. Le stelle e le costellazioni hanno dato origine ad innumerevoli leggende e miti, che in molti casi hanno lasciato traccia nei nomi che stelle e costellazioni ancora portano. Nessuno oggi penserebbe che quelle storie siano realmente accadute, ma evidenziano chiaramente l'intuizione dei popoli di ogni epoca che le risposte alle domande sulla nostra origine e sul nostro posto nell'universo siano da ricercare nell'osservazione e nello studio dei cieli. Con il progredire della scienza, quest'ultima affermazione è rimasta vera. Telescopi sono continuamente costruiti in tutto il mondo e lanciati nello spazio con l'obiettivo di poter osservare meglio quegli stessi cieli e rispondere a quelle stesse domande. In particolare, come è iniziata la vita?

Nell'immensità dell'universo, vi è un unico luogo in cui sappiamo per certo che la vita abbia avuto origine: il pianeta Terra. Fino a circa 25 anni fa, nessun pianeta era conosciuto al di fuori del sistema solare. Nel 1995, tuttavia, il primo *esopianeta* è stato scoperto, e da allora è stata confermata l'esistenza di più di 4000 nuovi esopianeti. Questa esplosione di scoperte spalanca a nuove e promettenti possibilità verso la comprensione dell'origine della vita. In particolare risulta critico comprendere come i pianeti si formino dal punto di vista fisico e chimico .

Il percorso che conduce dalle nubi molecolari, come quella mostrata in Fig. 6.15, ai pianeti è complicato e richiede numerosi processi fisici e chimici a diverse scale (vedi Fig. 1.2). Per questo motivo, molti aspetti di questo percorso non sono ancora ben compresi. È tuttavia chiaro che la formazione di stelle e pianeti comincia dalle nubi molecolari. Il 99% di queste nubi è composto di gas molecolare e l'1% di polvere. Alcune nubili sono gravitazionalmente instabili: questo significa che la loro massa è troppo grande perché possa essere supportata dalla pressione del gas di cui sono composte. Di conseguenza, queste nubi collassano sotto l'effetto della loro stessa gravità. Durante il collasso, esse iniziano a ruotare sempre più velocemente per effetto della conservazione del

Figure 6.15: Vista della componente di polvere delle nubi nella regione di formazione stellare Corona Australis. Le nubi più dense sono in grado di bloccare efficacemente la luce proveniente dalle stelle più lontane. Credito & Copyright: Fabian Neyer.

momento angolare, fino a quando, ad un certo punto, la forza centrifuga è in grado di impedire l'ulteriore collasso del materiale. Viene dunque a formarsi una struttura a disco. Queste strutture sono chiamate *dischi protoplanetari*, e sono la culla della formazione dei pianeti.

A questo punto, la polvere nei dischi protoplanetari può crescere dalle dimensioni di minuscoli granelli di sabbia a ciottoli, massi e pianetesimi, ovvero il componente fondamentale dei pianeti rocciosi e dei nuclei dei pianeti gassosi. Una volta formati, i pianeti interagiscono con il resto del materiale dei dischi scavando solchi e cavità, creando anelli ed eccitando onde.

Fino a circa 10 anni fa tali strutture non potevano essere osservate dalla Terra, a causa della limitata risoluzione spaziale dei telescopi di vecchia generazione. Era come guardare un dipinto da lontano: le grandi forme sono visibili, ma i dettagli sono nascosti e non distinguibili. Allo stesso modo, i dischi apparivano uniformi e simmetrici. Avvicinandosi al dipinto, tuttavia, più dettagli diventano chiari, e quando si è abbastanza vicini si possono distinguere anche i singoli tratti di pennello (per esempio, vedi Fig. 6.16). Ciò che ci ha permesso di "avvicinarci" ai dischi protoplanetari sono state le capacità senza precedenti di un nuovo potente telescopio: l'Atacama Large Millimeter/submillimeter Array (ALMA). Se osservati con le piene capacità di ALMA, i dischi non sono più uniformi e simmetrici, ma presentano diverse strutture e una varietà di morfologie, anche più di quanto ci saremmo aspettati.

Oltre ad ALMA, altri telescopi e strumenti, come VLT/SPHERE e Gemini/GPI, sono stati costruiti per cercare pianeti ancora immersi nei dischi protoplanetari. È interessante notare che, contro le aspettative, solo una manciata
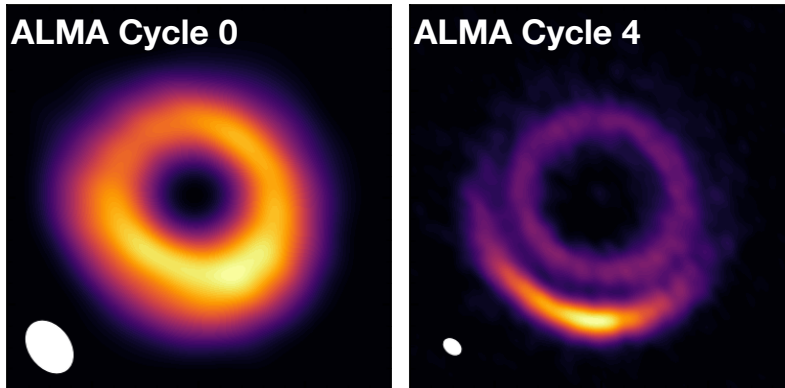
Figure 6.16: Immagini del disco protoplanetario attorno a HD 135344B, a diverse risoluzioni. A sinistra, la primissima osservazione ALMA con una risoluzione di $0.''25$ (~ 30 au) resolution, apparentemente di un singolo anello leggermente asimmetrico. A destra, le più recenti osservazioni ALMA dello stesso oggetto, con una risoluzione spaziale di $0.''06$ (~ 8 au): a questa risoluzione, è possibile distinguere più sottostrutture, e cioè un anello interno e simmetrico ed una struttura esterna azimutalmente asimmetrica.

di pianeti è stata fino ad ora rilevata.

L'ubiquità delle sottostrutture nei dischi protoplanetari, combinata alla mancanza di pianeti osservati sfidando l'interpretazione delle sottostrutture come originate dall'interazione tra disco e pianeti. In particolare, le domande alle quali questa tesi cercherà di rispondere sono le seguenti:

- Possono le sottostrutture nei dischi protoplanetari essere originate da fenomeni che non siano l'interazione tra dischi e pianeti?

- Che tipo di informazioni possono darci le sottostrutture nei dischi protoplanetari riguardo alle proprietà fisiche dei dischi?

- C'è qualche legame tra le sottostrutture nel gas e quelle nella polvere, o ci forniscono informazioni indipendenti?

- Fino a che punto sono le proprietà dei dischi dovute all'evoluzione, rispetto che alle condizioni iniziali?

Questa tesi e le prospettive future

Il Capitolo 1 di questa tesi fornisce una introduzione generale della teoria della formazione di stelle e pianeti. Vengono spiegate le fasi che portano dalle nubi ai

dischi, e i meccanismi fisici che giocano un ruolo nella crescita ed evoluzione dei grani di polvere. Vengono anche presentati i telescopi e gli strumenti numerici utilizzati per l'analisi dei dati.

Il Capitolo 2 presenta uno studio delle strutture del disco attorno a GG Tau A. La particolarità di questo disco protoplanetario è che esso non ruota intorno ad una singola stella, ma intorno ad una binaria (viene per questo chiamato *circumbinario*). Il disco circumbinario GG Tau A mostra un anello molto sottile situato a ∼ 200 au dalle stelle centrali. La regione tra le stelle e l'anello è completamente priva di polvere e della maggior parte del gas, poiché il materiale è stato spinto fuori dall'interazione gravitazionale con le stelle. L'interazione tra la compagna stellare ed il disco è molto simile a ciò che accadrebbe se, invece di una stella, fosse presente un pianeta massiccio. A seconda della massa del compagno, tuttavia, i calcoli teorici prevedono una diversa posizione dell'anello. La posizione dell'anello dipende anche dall'orbita della stella. Eseguendo una serie di simulazioni idrodinamiche e confrontando i risultati con le osservazioni del disco ed il moto stellare, si conclude che l'orbita stellare che meglio si adatta ai vincoli osservativi è un'orbita disallineata rispetto al piano del disco.

I Capitoli 3 e 4 si concentrano su un altro oggetto specifico, HD 135344B (vedi Fig. 6.16). Fin dalle primissime osservazioni con ALMA, il disco attorno a HD 135344B è apparso molto interessante, con una grande cavità interna di ∼ 50 au ed un anello di polvere simile a quello di GG Tau A, ma più piccolo, come ci si aspetterebbe se fosse scolpito da un pianeta. Un'altra differenza rispetto a GG Tau A è il fatto che il disco HD 135344B non è simmetrico, ma è più luminoso nella regione sud. Inoltre, osservando la luce proveniente dalla stella centrale e diffusa dal disco, è possibile osservare due braccia a spirale molto luminose, che sono state generalmente spiegate con la presenza di due ulteriori pianeti. Il Capitolo 3 presenta osservazioni del disco effettuate ad alta risoluzione con ALMA. Esse evidenziano che quello che nelle precedenti osservazioni sembrava essere un anello asimmetrico, appare invece ad alta risoluzione come 2 strutture: un anello interno simmetrico ed una asimmetria esterna a forma di banana, interpretabile come un vortice. L'estremità dei bracci a spirale si trova molto vicina al centro dell'asimmetria (pannello centrale di Fig. 3.1): proponiamo quindi che i bracci a spirale siano provocati dal vortice, e non da pianeti aggiuntivi. In questa spiegazione è richiesto un solo pianeta, che scava l'anello interno. Questo scenario è in accordo con il fatto che, nonostante gli sforzi, nessun pianeta sia stato ancora identificato nelle regioni esterne dell'HD 135344B.

Il capitolo 4 presenta osservazioni del disco intorno all'HD 135344B ad una risoluzione ancora maggiore e ad una diversa lunghezza d'onda: questa volta,
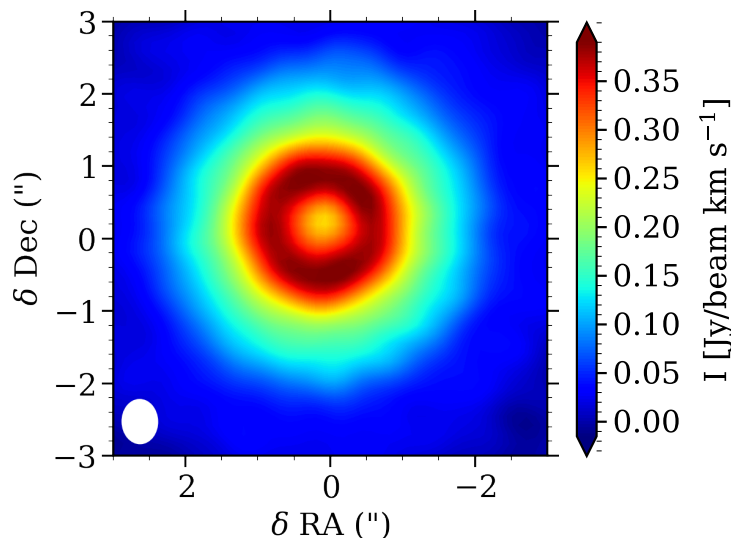
Figure 6.17: La struttura a forma di anello dell'emissione del CN osservata attorno aTW Hya.

l'anello interno e l'asimmetria esterna sono chiaramente distinguibili. Inoltre, combinando le nuove osservazioni con le precedenti, viene effettuato uno studio del vortice a più lunghezze d'onda. Questo approccio permette di ottenere informazioni su molte proprietà dei granelli di polvere all'interno del vortice. Ad esempio, è chiaro che i grani sono più grandi nel vortice rispetto al resto del disco: è quindi probabile che la polvere al suo interso stia crescendo fino a dimensioni maggiori, potenzialmente originando una popolazione di pianetesimi. Anche la massa del vortice viene misurata e, all'interno delle incertezze, risulta compatibile con lo scenario in cui è il vortice a originare le spirali.

I primi tre capitoli si concentrano principalmente sulle strutture in polvere. Il Capitolo 5 si focalizza invece sul gas, e in particolare sulle emissioni del CN. Avendo una tra le linee di emissioni più brillanti nei dischi, il CN risulta essere una molecola particolarmente interessante da studiare. Ciò che lo rende ancora più interessante è il fatto che le osservazioni spazialmente risolte di dischi protoplanetari mostrano sempre strutture ad anello (vedi Fig. 6.17). Sono anche questi anelli dovuti ad un pianeta? Esiste una correlazione con gli anelli di polvere? Per rispondere a queste domande, l'emissione del CN è stata simulata in una griglia di modelli utilizzano il codice DALI. La conclusione è che il CN mostra sempre una emissione ad anello, anche in dischi senza sottostrutture.

L'origine di questi anelli è infatti chimica. La reazione che porta a questa particolare emissione, inoltre, dipende fortemente da alcune proprietà del disco, come la sua dimensione, massa, la variazione del suo spessore con il raggio, e anche dall'emissione ultravioletta della stella centrale. Pertanto, osservando il CN nei dischi protoplanetari, quindi, le dimensioni e la luminosità dell'anello possono essere utilizzate per ottenere informazioni su queste proprietà.

Il Capitolo 6, infine, si concentra sulle osservazioni ALMA di polvere e gas non più in singoli dischi, ma in più dischi appartenenti ad una singola regione di formazione stellare, Corona Australis (CrA), mostrata in Fig. 6.15. Si ritiene che la CrA sia una regione giovane, e come tale ci si aspetta mostri dischi relativamente grandi e luminosi come altre regioni della stessa età quali Lupus. Tuttavia, nessun disco è stato rilevato nel gas, e i dischi di polvere sembrano essere deboli e piccoli, paragonabili a quelli di una regione 10 volte più vecchia del Lupus, ovvero Upper Sco. Tuttavia, nuovi spettri VLT/X-Shooter degli oggetti osservati con ALMA sembrano confermare la loro giovane età. La domanda sul motivo della bassa luminosità dei dischi resta aperta, ma due opzioni principali sono possibili. La prima possibilità è che in CrA abbiano avuto luogo due distinti eventi di formazione stellare, a distanza di alcuni milioni di anni l'uno dall'altro. In alternativa, la luminosità e le dimensioni dei dischi osservati oggi dipendono fortemente dalle condizioni iniziali (e.g. dalla rotazione del nucleo) presenti nelle primissime fasi del processo di formazione delle stelle. Ulteriori osservazioni saranno necessarie per distinguere gli scenari. In particolare, se i dischi attorno agli oggetti più giovani della regione fossero osservati e trovati anch'essi meno luminosi del solito, sarebbe un chiaro segno che le condizioni iniziali giocano un ruolo importante rendendo i dischi piccoli e meno massicci fin dall'inizio.

Ad oggi non è chiaro se le strutture osservate siano dovute a pianeti già formati o a qualche altro meccanismo. Fino ad ora solo un pianeta è stato "fotografato" all'interno di un disco, ma osservazioni future potrebbero osservare anche altri pianeti associati a queste strutture. Nel frattempo, nuovi promettenti approcci stanno diventando sempre più comuni per dedurre indirettamente la presenza di pianeti in dischi, e si riveleranno critici nel prossimo futuro. Le perturbazioni sul moto del gas indotte dai pianeti, ad esempio, sono già state utilizzate in alcuni casi, e la stessa tecnica può ora essere applicata a più sistemi. Inoltre, l'emissione proveniente da dischi circumplanetari associati a protopianeti, così come le emissioni associate al loro accrescimento sui pianeti stessi, sono state recentemente rilevate rispettivamente con ALMA e MUSE. Anche tali osservazioni potrebbero diventare più comuni in futuro.

Nel frattempo, nuovi studi a diverse lunghezze d'onda di dischi protoplan-

etari, come quello effettuato per HD135344B, possono fornire preziose informazioni sulle proprietà all'interno delle sottostrutture, inclusi i vortici. In particolare, il legame tra i vortici e le spirali devono essere studiati in maggior dettagli in un campione più ampio di dischi, anche sfruttando la sensibilità e la risoluzione spaziale di ALMA a frequenze più alte.

Questi studi sono critici per comprendere se le sottostrutture nei dischi siano o meno il luogo di nascita di nuovi pianeti. In conclusione, ci diranno se la varietà delle strutture osservate alle lunghezze d'onda del millimetrico sia legata o meno alla diversità delle proprietà dei sistemi esoplanetari e, in ultima analisi, alla nostra origine.

List of publications

First author papers

1. *ALMA survey of Class II protoplanetary disks in Corona Australis: a young region with low disk masses*
Cazzoletti, P., Manara, C. F., Baobab Liu, H., van Dishoeck, E. F., Facchini, S., Alcalà, J. M., Ansdell, M., Testi, L., Williams, J. P., Carrasco-González, C., Dong, R., Forbrich, J., Fukagawa, M., Galván-Madrid, R., Hirano, N., Hogerheijde, M., Hasegawa, Y., Muto, T., Pinilla, P., Takami, M. Tamura, M., Tazzari, M., Wisniewski, J. P., (2019), Astronomy and Astrophysics, 626, A11

2. *Evidence for a massive dust-trapping vortex connected to spirals. Multiwavelength analysis of the HD 135344B protoplanetary disk*
Cazzoletti, P., van Dishoeck, E. F., Pinilla, P., Tazzari, M., Facchini, S., van der Marel, N., Benisty, M., Garufi, A., Pérez, L. M., (2018), Astronomy and Astrophysics, 619, A161

3. *CN rings in full protoplanetary disks around young stars as probes of disk structure*
Cazzoletti, P., van Dishoeck, E. F., Visser, R., Facchini, S., Bruderer, S., (2018), Astronomy and Astrophysics, 609, A93

4. *Testing dust trapping in the circumbinary disk around GG Tauri A*
Cazzoletti, P., Ricci, L., Birnstiel, T., Lodato, G., (2017), Astronomy and Astrophysics, 599, A102

Co-authored papers

5. *Bright C2H emission in protoplanetary disks in Lupus: high volatile C/O>1 ratios*
   Miotello, A., Facchini, S., van Dishoeck, E. F., **Cazzoletti, P.**, Testi, L., Williams, J. P., Ansdell, M., van Terwisga, S., van der Marel, N., in press, Astronomy and Astrophysics

6. Observational constraints on dust disk sizes in tidally truncated protoplanetary disks in multiple systems in the Taurus region
   Manara, C. F., Tazzari, M., Long, F., Herczeg, G. J., Lodato, G., Rota, A. A., **Cazzoletti, P.**, van der Plas, G., Pinilla, P., Dipierro, G., Edwards, S., Harsono, D., Johnstone, D., Liu, Y., Menard, F., Nisini, B., Ragusa, E., Boehler, Y., Cabrit, S., (2019), Astronomy and Astrophysics, 628, A95

7. *An Inner Disk in the Large Gap of the Transition Disk SR 24S*
   Pinilla, P., Benisty, M., **Cazzoletti, P.**, Harsono, D., Pérez, L. M., Tazzari, M., (2019), Astrophysical Journal, 878, 16

8. *High gas-to-dust size ratio indicating efficient radial drift in the mm-faint CX Tauri disk*
   Facchini, S., van Dishoeck, E. F., Manara, C. F., Tazzari, M., Maud, L., **Cazzoletti, P.,** Rosotti, G., van der Marel, N., Pinilla, P., Clarke, C. J., (2019), Astronomy and Astrophysics, 626, L2

9. *Stringent limits on the magnetic field strength in the disc of TW Hya. ALMA observations of CN polarisation*
   Vlemmings, W. H. T., Lankhaar, B., **Cazzoletti, P.**, Ceccobello, C., Dall'Olio, D., van Dishoeck, E. F., Facchini, S., Humphreys, E. M. L., Persson, M. V., Testi, L., Williams, J. P., (2019), Astronomy and Astrophysics, 624, L7

10. *The ALMA Lupus protoplanetary disk survey: evidence for compact gas disks and molecular rings from CN*
    van Terwisga, S. E., van Dishoeck, E. F., **Cazzoletti, P.**, Facchini, S., Trapman, L., Williams, J. P., Manara, C. F., Miotello, A., van der Marel, N., Ansdell, M., Hogerheijde, M. R., Tazzari, M., Testi, L., (2019), Astronomy and Astrophysics, 623, A150

11. *On the secular evolution of GG Tau A circumbinary disc: a misaligned disc scenario*

Aly, H., Lodato, G., **Cazzoletti, P.**, (2018), Monthly Notices of the RAS, 480, 4738

12. *Nitrogen isotope fractionation in protoplanetary disks*
Visser, R., Bruderer, S., **Cazzoletti, P.**, Facchini, S., Heays, A. N., van Dishoeck, E. F., (2018), Astronomy and Astrophysics, 615, A75

13. *ALMA Observations of the Young Substellar Binary System 2M1207*
Ricci, L., **Cazzoletti, P.**, Czekala, I., Andrews, S. M., Wilner, D., Szűcs, L., Lodato, G., Testi, L., Pascucci, I., Mohanty, S., Apai, D., Carpenter, J. M., Bowler, B. P., (2017), Astronomical Journal, 154, 24

14. *The cool-core state of Planck SZ-selected clusters versus X-ray-selected samples: evidence for cool-core bias*
Rossetti, M., Gastaldello, F., Eckert, D., Della Torre, M., Pantiri, G., **Cazzoletti, P.**, Molendi, S., (2017), Monthly Notices of the RAS, 468, 1917

15. *Vortices and Spirals in the HD135344B Transition Disk*
van der Marel, N., Cazzoletti, P., Pinilla, P., Garufi, A., (2016), Astrophysical Journal, 832, 178

Curriculum Vitae

I was born on October 4$^{\text{th}}$, 1990 in Monza, Italy to Sergio Cazzoletti and Serena Farina. I lived for the most part of my life in Concorezzo, a small city northeast of Milan. Science and physics have always been two of my main interests. However, I have seen many different passions sprouting and growing throughout the years.

Ever since primary and secondary school, it has been clear that I had a much better aptitude for science and mathematics than for literature and humanistic subjects. Consequently, I decided to attend "Scientific" High-School (Liceo Scientifico, in italian) at Istituto Sacro Cuore in Milan. In those year, I started developing a big interest for engines and sport cars, and became an avid reader of car magazines. This passion brought me to the decision to choose to study Mechanical Engineering at the University. I therefore took the test, and was admitted to Politecnico di Milano. As a farewell to physics and astronomy, I chose "cosmological models" as a topic for my final high-school project. I enjoyed this project so much, that I ended up never registering for Mechanichal Engineering, and choosing Physics instead.

In September, 2009 I started my Bachelor's degree at Università degli studi di Milano. I enjoyed all the courses and exams, but it was only in the third year that I found the topic I was sure I wanted to keep studying: the course was "Introduction to Astronomy", and the topic was (of course) astronomy. For my Bachelor thesis, I worked at INAF with Dr. Mariachiara Rossetti and Dr. Fabio Gastaldello, studying the morphology of galaxy clusters through *Chandra* X-Ray data. For my Master's degree I chose almost all astronomy related exams, and was particularly struck by the course held by Prof. Giuseppe Lodato about the theory of accretion disks. For my master's thesis, I moved for a few months to the Harvard-Smithsonian Center for Astrophysics to work on modelling and observations of protoplanetary disks. I was supervised by Dr. Luca Ricci and Prof. Giuseppe Lodato. During the university years I developed a huge passion for cooking, and attended a number of cooking classes. This

time, however, I never really thought about becoming a Chef: even though I still love cooking, I enjoyed my first astronomy research experience so much that I immediately decided to apply for a PhD at Leiden University.

I was offered a position with Prof. Dr. Ewine van Dishoeck to work on the new exciting data that ALMA was starting to provide, and in particoular to study and help in the interpretation of the substructures that were observed more and more frequently in protoplanetary disks, both in gas and dust. I spent all four years of my PhD in München, Germany, at Max-Planck-Institut für extraterrestrische Physik. I met great scientists and had beautiful collaborations with many of them, exploiting the vicinity of the European Southern Observatory. During these years, I was member of the LOC of three international conferences, and I had the pleasure to supervise a talented high-school student during her summer project, hopefully also helping her to decide what to study after high-school.

In the last year of my PhD I also got married to Federica. Next year, we will happily move back to our home country, and I will start a whole new career path as a Data Scientist. I hope to be able to exploit all the skills I developed during my PhD also in this different field, and I want to keep putting my curiosity to good use!

Acknowledgements

A long road brought me to the end of this PhD thesis, and many people played a role and should to be thanked for it.

I can only start by thanking my mentors and supervisors. Ewine, for many things: for concretely making everything possible, for "betting" on me 4 years ago, for always pushing me to do my best, for always finding time to answer e-mails and to meet, for the masterful guidance, and most of all for being the living testimony that one can (and should) always love her/his job. You have been and are a role model. Leonardo, your passion, dedication and competence are an example to aspire to. Stefano, you been a great office companion, and your precious opinions and questions have been critical to keep me on track.

Surely I would have not started this PhD without two people. Prof. Giuseppe Lodato. Thank you for giving me strong theoretical foundations and teaching me a solid approach to the study of protoplanetary disks, and for introducing me to this world. Dr. Luca Ricci, you were the first to introduce me the observational aspects of astronomy, and you gave me the possibility to be part of my first true research projects.

As my PhD developed between Leiden and Munich, I was part of two research groups. First of all, the MPE infrared group: thank you for hosting me. The atmosphere of excellence was perceivable through the corridors. Thomas, Yao, Lisa, and Nadia (for one year), you have been great colleagues in Germany. The second group is the fantastic Leiden one, with its present and past members. I feel privileged for having been a part of it. Nienke, I am grateful to you for involving me in the first HD 135344B project, for helping with ALMA data, and in general for teaching me a lot about interferometry, from the very first days. Paola, I greatly enjoyed working with you. Thanks for the great discussions, for the interesting projects together and for your constant and sincere friendliness. Anna: thank you for introducing me to `DALI`, and thanks also to Carlo and to your amazing family for the generous dinner invitations in Leiden before and in Munich after. Those have been occasions for many conversations

that have often ended up being important for me, both from the professional and personal point of view. Daniel, your help with my ALMA data was invaluable. Simon, your support with `DALI` was irreplaceable, and your insight about jobs outside of astronomy has been really useful. Merel, Arthur and Sierk: we started together and it was great to have the three of you as companions of this trip! You have more than once been a great help to me. Also, the last ALMA proposal I am still involved in is with you, so keep me updated. Good luck with everything, I wish you all the best from my heart. Łukasz, you really are a nice person to be with. Also, thanks for helping me to accept that coffee is not only espresso. Leon, a sincere thank you for your (future) help with my PhD organisational stuff, and good luck with your applications. Margot and Martijn, it was nice meeting you. I am grateful for your help with the translation. Pooneh, in the brief time we met I liked your enthusiasm and positive attitude. Good luck with the next years! An acknowledgement goes then to the current postdocs of the group. To Alex, for always bringing enthusiasm and optimism. To Giovanni, for sharing his passion, competence and attention to details. To Alvaro and Andreas, for bringing some larger scale structures into my horizon and broadening my scientific knowledge. To Benoit, Shota: we did not get to interact much, but it was a pleasure to meet you and to hear about your research. Outside the group, I would then like to thank Marco: we shared a great and fun year in Muncih. Thanks for all the help with `GALARIO` afterwards.

Outside of science, I am first of all grateful to Guido, for coming up with a great and clever idea for the cover of this book, and for designing it.

Then Chicca: our story began at the beginning of this PhD adventure and reached its fulfilment near its end! The PhD played an important role in shaping our relation, and without any doubt our relation enriched it immensely. Thanks for the support, the trust, for being willing to move to Munich with me, and finally for bringing me back to our home country. It has been 4 great years, and I am sure we both agree that the best is yet to come!

Finally, un grazie infinito ai miei genitori. Per avermi supportato (e sopportato), spinto, spronato, aiutato, sostenuto e soprattutto per avermi sempre voluto bene. Non potrò mai sdebitarmi, spero vi basti la mia gratitudine (che spesso non traspare come dovrebbe).